

Smart X-ray optics for large and small scale applications

Thesis submitted to the University of Leicester
for the degree of Doctor of Philosophy

by

Charlotte Hannah Feldman

November 2009



Space Research Centre
Department of Physics and Astronomy
University of Leicester
UK

Smart X-ray optics for large and small scale applications

Charlotte Hannah Feldman

Abstract

The Smart X-ray Optics project is a UK based consortium of eight institutions investigating active/adaptive X-ray optics for both large and small scale applications. The consortium is funded by a basic technology grant from the Engineering and Physical Sciences Research Council (EPSRC).

The large scale application is aimed towards future high angular resolution, large X-ray telescopes for X-ray astronomy. The first prototype mirror incorporates piezoelectric devices to a standard X-ray shell to enable the surface to be actively deformed. The aim is to achieve an angular resolution better than that currently available (e.g. Chandra 0.5"). The initial design is based on a thin nickel ellipsoid segment on the back of which a series of thirty, curved piezoelectric actuators have been bonded.

The small scale application is aimed at providing an X-ray focusing device, capable of producing a focused spot of $\sim 10\mu m$, the same size as an average biological cell for cancer research and studies. Current small scale devices, zone plates, are limited by their focal length and aperture, and cannot be used at energies greater than $1keV$. In order to increase the workable X-ray energies, whilst still providing small spot sizes over short distances, a new optic was designed. Micro Optical Arrays are based on polycapillary or Micro Channel Plate optics (MCPs) and consist of a series of parallel channels, etched into silicon wafers. By the attachment of piezoelectric devices, a device with a variable focal length can be created.

The work presented within this thesis describes the design, metrology, modelling and X-ray testing of the first large adaptive X-ray optic and the theory, modelling and X-ray testing of the small scale optic. Summaries, conclusions and future work are also outlined.

Declaration

I hereby declare that no part of this thesis has been previously submitted to this or any other university as part of the requirement for a higher degree. The work described herein was conducted solely by the undersigned except for those colleagues and other workers acknowledged in the text.

Charlotte Hannah Feldman

2009

Dedication

To Brian, Cheryl, Rachel and Richard;
for all your love and support.

Acknowledgments

I wish to thank all my friends and family who have helped me during my three years as a PhD student, but there are a few people who I must thank individually.

Firstly I wish to thank EPSRC, the SXO consortium and the University of Leicester for giving me the opportunity and funding to complete this project. I would also like to thank all the members of the SXO consortium for their help and support and for the fun times we had whilst we were at conferences!

I would like to thank all the people in the SRC who have provided me with entertainment and help when I needed it and to all the postgraduate students and postdoctoral RAs in the Physics and Astronomy department for all the fun nights out and for the support and drinks you provided when I needed it. In particular Danny, Michelle, Laura, and Pippa who were always there for a rant, a chat or even a spontaneous shoe shopping trip.

I would also like to thank all the members of the University of Leicester and Leicester City Fencing clubs and the University of Leicester Cross Country club for providing stress relief which was vital during the three years.

There are a few people who without, I could not have completed this PhD and I owe so much too. First, to Dr. Richard Willingale for being the best supervisor I could have wished for, for being patient with all my questions and seeing me whenever I needed some help. Secondly, to my parents, my sister and Jim, I love you all so much and I want to thank you with all my heart for all the help and encouragement you have given me, I really could not of done this without you. Finally I would like to thank Richard for absolutely everything.

Publications

Some of the results presented in this thesis have been incorporated into the following refereed journals and conference papers:

Large Adaptive X-ray Optic

C. Atkins, P. Doel, J. Yao, D. Brooks, S. Thompson, R. Willingale, **C. Feldman**, T. Button, D. Zhang and A. James, “*Active X-ray mirror development at UCL: preliminary results*”, Advanced Optical Manufacturing and Testing Technologies: Large Mirrors and Telescopes, Proceedings of SPIE Vol. 6721 (SPIE, Bellingham, WA 2007) 67210T.

P. Doel, C. Atkins, S. Thompson, D. Brooks, J. Yao, **C. Feldman**, R. Willingale, T. Button, D. Zhang and A. James, “*Large thin adaptive X-ray mirrors*”, Advances in X-Ray/EUV Optics and Components II, Proceedings of SPIE Vol. 6705 (SPIE, Bellingham, WA 2007) 67050M.

C. Atkins, H. Wang, P. Doel, D. Brooks, S. Thompson, **C. Feldman**, R. Willingale, T. Button, D. Rodriguez-Sanmartin, D. Zhang, A. James, C. Theobald, “*Future high resolution X-ray telescope technologies: prototype fabrication and finite element analysis*”, Space Telescopes and Instrumentation 2008: Ultraviolet to Gamma Ray, Proceedings of SPIE Vol. 7011 (SPIE, Bellingham, WA 2008) 70110X.

C. Feldman, R. Willingale, C. Atkins, H. Wang, P. Doel, D. Brooks, S. Thompson, T. Button, D. Zhang, D. Rodriguez-Sanmartin, A. James, C. Theobald, “*Development of thin shell adaptive optics for high angular resolution X-ray telescopes*”, Space Telescopes and Instrumentation 2008: Ultraviolet to Gamma Ray, Proceedings of SPIE Vol. 7011 (SPIE, Bellingham, WA 2008) 70110Y.

D. Zhang, D. Rodriguez-Sanmartin, T. Button, C. Atkins, P. Doel, C. Dunare, **C. Feldman**, A. James, A. Michette, W. Parkes, S. Pfauntsch, S. Sahraei, T. Stevenson, H. Wang, R. Willingale, “*Development of Piezoelectric Actuators for Active X-ray Optics*”, Proceedings of Electroceramics, XI, 21, Springer Netherlands, 2009.

C. Atkins, H. Wang, P. Doel, D. Brooks, S. Thompson, **C. Feldman**, R. Willingale, T. Button, D. Rodriguez-Sanmartin, D. Zhang, A. James, C. Theobald, G. Willis, A. Smith, “*Active X-ray optics for the next generation of X-ray telescopes*”, Proceedings of SPIE Vol. 7360 (SPIE, Bellingham, WA 2009) 736008.

C. Feldman, R. Willingale, C. Atkins, H. Wang, P. Doel, D. Brooks, S. Thompson, T. Button, D. Zhang, D. Rodriguez-Sanmartin, A. James, C. Theobald, A. Smith, “*First results from the testing of the thin shell adaptive optic prototype for high angular resolution X-ray telescopes*”, Optics for EUV, X-ray, and Gamma-Ray Astronomy IV, Proceedings of SPIE Vol. 7437 (SPIE, Bellingham, WA 2009) in press.

C. Atkins, P. Doel, H. Wang, D. Brooks, S. Thompson, **C. Feldman**, R. Willingale, T. Button, D. Zhang, D. Rodriguez-Sanmartin, A. James, C. Theobald, A. Smith, “*Advances in active X-ray telescope technologies*”, Optics for EUV, X-ray, and Gamma-Ray Astronomy IV, Proceedings of SPIE Vol. 7437 (SPIE, Bellingham, WA 2009) in press.

D. Zhang, D. Rodriguez-Sanmartin, T. Button, C. Meggs, C. Atkins, H. Wang, P. Doel, D. Books, **C. Feldman**, R. Willingale, A. Michette, S. Pfauntsch, S. Sahraei, A. James, C. Dunare, T. Stevenson, W. Parkes, A. Smith, “*The fabrication and characterisation of piezoelectric actuators for active X-ray optics*”, Advances in X-ray/EUV Optics and Components IV, Proceedings of SPIE Vol. 7448 (SPIE, Bellingham, WA 2009) in press.

Micro Optical Arrays

A. Michette, T. Button, C. Dunare, **C. Feldman**, M. Folkard, D. Hart, C. McFaul, G. Morrison, W. Parkes, S. Pfauntsch, A. Powell, D. Rodriguez-Sanmartin, S. Sahraei, T. Stevenson, B. Vojnovic, R. Willingale, D. Zhang, “*Active micro-structured arrays for X-ray optics*”, Advances in X-Ray/EUV Optics and Components II, Proceedings of SPIE Vol. 6705 (SPIE, Bellingham, WA 2007) 670502.

A. Michette, S. Pfauntsch, S. Sahraei, M. Shand, G. Morrison, D. Hart, B. Vojnovic, T. Stevenson, W. Parkes, C. Dunare, R. Willingale, **C. Feldman**, T. Button, D. Zhang, D. Rodriguez-Sanmartin, H. Wang, A. Smith, “*Active micro-structured X-ray optical arrays*”, EUV and X-ray Optics II, Proceedings of SPIE Vol. 7360 (SPIE, Bellingham, WA 2009) 736006.

C. Dunare, W. Parkes, T. Stevenson, A. Michette, S. Pfauntsch, S. Sahraei, M. Shand, D. Zhang, D. Rodriguez-Sanmartin, T. Button, **C. Feldman**, R. Willingale, P. Doel, H. Wang, A. James, “*Microstructured optical arrays for smart X-ray optics*”, EUV and X-ray Optics II, Proceedings of SPIE Vol. 7360 (SPIE, Bellingham, WA 2009) 736015.

D. Rodriguez-Sanmartin, D. Zhang, T. Button, C. Meggs, C. Atkins, H. Wang, P. Doel, D. Brooks, **C. Feldman**, R. Willingale, A. Michette, S. Pfauntsch, S. Sahraei, A. James, C. Dunare, T. Stevenson, W. Parkes, A. Smith, “*Progress on the development of active micro-structured optical arrays for X-ray optics*”, Advances in X-Ray/EUV Optics and Components IV, Proceedings of SPIE Vol. 7448 (SPIE, Bellingham, WA 2009) 744807

R. Willingale, **C. Feldman**, A. Michette, T. Button, C. Dunare, M. Folkard, D. Hart, C. McFaul, G. Morrison, W. Parkes, S. Pfauntsch, A. Powell, D. Rodriguez-Sanmartin, S. Sahraei, T. Stevenson, B. Vojnovic, D. Zhang, *Active micro-structured optical arrays of grazing incidence reflectors*, Journal of X-ray Optics and Instrumentation (JXOI), in press, (2009).

CONTENTS

1	Introduction	1
1.1	Introduction and Justification of work	1
1.2	X-rays and current adaptive/active X-ray optics	3
1.3	Background to piezoelectric devices	5
1.4	A brief summary of X-ray physics	8
1.5	Current modelling products for X-ray optics	11
1.6	Thesis overview	14
2	Design, analysis and testing of the LAXRO	15
2.1	Chapter overview	15
2.2	Introduction and background to X-ray telescopes	16
2.2.1	A brief overview of past and present of X-ray telescopes	18
2.2.2	The future of X-ray telescopes	21
2.2.3	Methods of X-ray telescope fabrication	23
2.3	Design of the first large scale prototype optic	27
2.3.1	Background to the initial design requirements	27
2.3.2	Ellipse theory	28
2.4	Large scale prototype optic designs	30
2.5	Production of the large scale optic	31
2.5.1	Piezoelectric actuators	36
2.5.2	Mounting of the optic	40
2.6	Metrology of the large prototype optic	43
2.7	Modelling the performance of the large prototype optic	55
2.7.1	The basic ellipse model	55
2.7.2	Modelling the gravitational sag	56
2.7.3	Using the profile data from the LTP in the modelling	60
2.8	Simulation of the piezoelectric actuators and adjustment algorithm	62
2.8.1	Iterative adjustment of the real piezoelectric devices	73
2.9	The Tunnel Test Facility	73
2.10	X-ray tests carried out within the TTF	79
2.10.1	Alignment and set up	79
2.10.2	Testing plan	82
2.11	Results from the TTF	84
2.11.1	Full adjustment of the piezoelectric devices	84

2.11.2	Hartmann test	87
2.11.3	Stability of the piezoelectric devices	90
2.12	Further tests carried out at STFC Daresbury Laboratory	91
2.13	Further modelling of the large scale prototype	93
2.14	Summary and conclusions	103
3	Analysis of the MOAs	106
3.1	Chapter overview	106
3.2	Background to small scale X-ray focusing devices	107
3.3	Initial design and requirements	110
3.4	Micro Optical Arrays design	112
3.4.1	First prototype design	112
3.4.2	Prototype Micro Optical Array mount design	113
3.5	Theory of Micro Optical Arrays	116
3.5.1	Single Micro Optical Arrays	116
3.5.2	Tandem Micro Optical Arrays	117
3.5.3	Equal grazing angle tandem Micro Optical Arrays	118
3.5.4	Flat-curved tandem Micro Optical Arrays	118
3.5.5	Collimator-telescope tandem Micro Optical Arrays	118
3.5.6	Line Spread Function	119
3.6	Shadowing and scattering models	119
3.6.1	In-plane scattering	120
3.6.2	Out-of-plane scattering	121
3.6.3	Shadowing models	124
3.6.4	Conclusion of surface feature models	124
3.7	Metrology of the Micro Optical Arrays	125
3.8	Simulation of the Micro Optical Arrays	128
3.8.1	Line-to-line focusing	129
3.8.2	Collimator and telescope Micro Optical Arrays	132
3.8.3	Equal grazing angle Micro Optical Arrays	133
3.8.4	Flat-curved tandem Micro Optical Arrays	135
3.8.5	Crossed pair Micro Optical Arrays	139
3.8.6	Parabolic Micro Optical Arrays	141
3.8.7	Models of scalloping and shadowing	141
3.9	X-ray experiments using Micro Optical Arrays	144
3.9.1	Micro Optical Array reflectivity experiments	144
3.9.2	The first experimental tests at UoL	148
3.10	Simulated results of the Micro Optical Array experiments	149
3.11	Results from the X-ray experiments performed at UoL	150
3.12	Summary and conclusions	157
4	Summary, conclusions and future work	162
4.1	Large Adaptive X-ray Optic	162
4.2	Micro Optical Arrays	167
	Bibliography	170

LIST OF FIGURES

1.1	A ray reflected by an optical surface with grazing angle θ_g and reflected angle θ	3
1.2	A normal incidence adaptive optical mirror. A high quality optical mirror has had multiple piezoelectric devices attached to the reverse side. a) The mirror with the hexagonal piezoelectric devices attached to the back and b) the reflective side of the mirror. The gold leads are the electrodes which control the actuators[1].	3
1.3	An example of a synchrotron mirror which consists of a silicon mirror, ground to form, with a series of piezoelectric devices attached on the back. The surface of the silicon is finished with an X-ray reflective coating. Using the piezoelectric devices, the mirror is bent into a very precise elliptical shape which can focus the X-ray beam to a nanometre scale.	4
1.4	A graphical explanation of the Full Width Half Maximum (FWHM) of a detected image.	5
1.5	The flexibility of a piece of MFC. Image supplied by UCL.	6
1.6	Examples of piezoelectric devices created at the School of Metallurgy and Materials, University of Birmingham.	6
1.7	A PZT plate with associated axes and poling direction.	7
1.8	The change in reflectivity of a nickel substrate with a $30\mu m$ gold layer on the surface, as a function of energy and surface roughness at various grazing angles. These graphs were calculated using the Centre for X-ray Optics website[2].	11
2.1	a) A Kirkpatrick-Baez telescope and b) a grid of K-B plates[3].	18
2.2	Different forms of Wolter telescopes a) type 1, b) type 2 and c) type 3[4].	19
2.3	The XMM-Newton satellite during the solar array deployment test at ESTEC, Netherlands[5].	20
2.4	An artist's impression of the Chandra X-ray Observatory in operation[6]	21
2.5	a) An image created by combining optical data and X-ray data from Chandra of NGC4258[7] and b) an image of NGC4258 taken by XMM-Newton[8]. The detail is much less than that seen in a).	22

2.6	The XMM-Newton telescope modules. It consists of three mirror modules with each module containing fifty eight nested Wolter 1 mirrors. The mirrors are gold coated, electroformed nickel with varying radii and thickness. a) A single mirror module[9] and b) the three mirror modules being installed[10].	23
2.7	The four nested glass mirrors of NASA's Chandra X-ray observatory. These were produced by grinding large pieces of zerodur ceramic to the precise form and then coating the inside with an X-ray reflective coating, iridium. The zerodur ceramic used for the mirrors is so thick that the number of nested shells is restricted[11].	24
2.8	The glass slumping technique utilized by GSFC, USA. a) A sheet of $0.4mm$ thick commercially produced glass is thermally slumped over a quartz mandrel. b) An engineering model of NuSTAR where cylindrical glass slumped mirrors are mounted to approximate parabolic and hyperbolic segments to create a Wolter 1 telescope. c) Two completed glass segments after slumping and trimming. These mirrors have been coated with gold but in the case of NuSTAR, the mirrors are coated in iridium. Images provided by GSFC.	25
2.9	a) Glass slumping at GSFC for the NuSTAR mission. b) An artist's impression of the NuSTAR extendable deployment mast and optics[12].	26
2.10	Construction of silicon pore optics. A sheet of silicon is etched or cut to create channels. The reverse side of the sheet is then coated in either gold, iridium or a multi-layered coating. Multiple sheets are then stacked and compressed to cold weld them together which creates silicon pore optics with a large collecting area. The silicon channels are coated in a layer of SiO_2 which is etched to taper the sheets to approximate a Wolter 1 geometry, thus creating an effective X-ray optic.	26
2.11	An ellipse with two foci f_1 and f_2 . A ray produced at f_1 , and reflected off the inside surface of the ellipse, will be focused at f_2	28
2.12	An ellipse with centre C and focus F	29
2.13	The production of the mandrel for electroforming the optic. The mandrel was designed to have wasters which can be removed to improve the consistency of the thickness of the nickel and to prevent rounding of the edges due to grinding and polishing. a) The mandrel's schematic before manufacture which was cut from a block of aluminium and coated in a $100\mu m$ layer of kanigen and then ground to form by hand. b) The mandrel after it had been milled to the rough shape required. c) The mandrel after polishing and d) the mandrel after the $30nm$ gold layer has been deposited, shown with the wasters detached. Images provided by UCL.	32

- 2.14 The production technique of the LAXRO by electroforming. a) The mandrel was prepared before the electroforming by placing non conducting tape between the gaps of the wasters and main body of the mandrel to enable the removal of these areas after electroforming. Tape is also placed around the outside of the mandrel to prevent electroplating in these regions. b) The in-house electroforming tank at UCL, approximately $0.6m \times 0.6m \times 1m$ tall. c) The optic and mandrel once they had been removed from the tank after the electroforming process had been completed. d) The optic once it had been removed from the mandrel. e) The areas which were plated over the wasters can easily be removed. It is clear that this area is thicker and contains a lot of air bubbles. Images provided by UCL. 34
- 2.15 One of the pre-prototype replicated segments. a) The segment after replication shown with the wasted section which was removed after electroforming. b) The pre-prototypes reflecting surface shown with some damage from cleaning. c) The pre-prototype front and back with a few piezoelectric devices attached. d) The pre-prototype sitting on the aluminium frame showing the difference in size between the pre-prototype and the first elliptical prototype optic. Images provided by UCL. 35
- 2.16 The reverse side of the large scale adaptive optic after the actuators had been attached. a) The thirty piezoelectric actuators have been numbered in sequence. The number is shown along with the thickness of each actuator which ranges between $165\mu m$ and $265\mu m$. The thickness is not known for all of the actuators and some required re-sputtering, where the gold coating is reapplied to the outer surface. The top three rows were actually piezoelectric actuators produced for the cylindrical pre-prototype optics, but have a very similar radius of curvature to one end of the elliptical prototype mirror and so could be used over a small section of the optic. b) The attached piezoelectric actuators have been harnessed where all the electrodes for the piezoelectric devices have been soldered and wired up to the 32-pin connector which was connected to the actuator control system. Images provided by UCL. 37
- 2.17 The piezoelectric devices for the first elliptical prototype were $32mm \times 29mm$ and are $\sim 200\mu m$ thick. They were coated in gold to create a conducting surface. The piezoelectric actuator is shown with the two electrodes attached, one is the ground wire whilst the other provides the voltage for the movement. The ground wire is accessed by removing a small amount of the top layer in one corner. 38
- 2.18 a) and b) show curved piezoelectric actuators. c) The piezoelectric devices have been curved over a former with the correct radius of curvature. By using pre-curved piezoelectric devices, it was hoped that print-through and stress on the optic could be reduced. Normally a conductive glue is required to access the bonded electrode, however these piezoelectric actuators have access to the electrode as a small section of the top surface is removed. Low shrinkage glue was also used to prevent print-through. Images provided by UoB. 39

2.19	A cross section taken through one of the pre-prototype mirrors showing the optic thickness, glue layer and the actuator. Within the glue layer, several $80\mu m$ diameter glass beads are visible which were used as spacers to control the glue thickness. This image was taken using an SEM at UoB.	39
2.20	a) The schematic of the frame and b) the completed aluminium frame for the optic support during the tests. The optic rested along its axial edges as this was shown to produce the least amount of axial distortion on the optic. The edges of the support structure were coated with vacuum compatible foam produced by Upilex®[13], as this provided the support required, whilst still allowing the piezoelectric devices to operate without restriction. Images provided by UCL.	41
2.21	a) The optic support structure developed by UCL. Space foam is placed along the axial edges of the support to allow support but also allow full movement as the piezoelectric devices are actuated. b) All three sections of the support structure assembled together with the optic and attached to the flange. c) The full structure within the TTF above the flange. Images provided by MSSL.	42
2.22	The finished support structure. a) The lower section of the mount with the three height adjustable support legs. These were attached to the flange and raised the rest of the structure off the edges of the pipe. The flange provided the connection between the micrometers, the piezoelectric devices and the computer control. b) The flange section attached to the micrometre section with the plastic skis which supported the optic whilst it was passed down the facility. c) The entire mounting with the soft mount attached. Images provided by MSSL.	42
2.23	The Wyko data of the cylindrical stainless steel mandrel provided by UCL. Over this small region, the surface was found to have an RMS surface roughness of $\sim 4nm$. This was replicated on to the optics surface, giving a surface roughness of $\sim 6nm$ to $8nm$	44
2.24	The Wyko data of the elliptical kanigen mandrel provided by UCL. Over this small region, the surface was found to have an RMS surface roughness of $\sim 2nm$. This was replicated on to the optics surface and gave a surface roughness of $\sim 4nm$ to $6nm$. This was an improvement on the cylindrical mandrel, and deemed sufficient for the first series of tests.	44
2.25	Operation of a Long Trace Profiler (LTP). A Laser beam is split into two pairs of collinear beams. One of the pairs is directed through the reference arm and reflected back by the reference surface, whilst the second pair are directed towards the test surface and reflected back into the optical head. Once the beams have been reflected, they are focused onto a linear array detector by a Fourier Transform lens, creating two sets of interference fringes. The separation of the minima gives a direct measure of the slope error on the mirror[14].	46

- 2.26 a) and b) operation of a Long Trace Profiler with the addition of a Dove prism. The Dove prism removes the mechanical errors introduced by the static sag of the translation stage due to gravity and the dynamic sag due to the optical head moving along the translation stage[14]. The LTP at STFC Daresbury utilises a Pentaprism for the same purpose. 47
- 2.27 The mirror with the thirty piezoelectric devices attached to the reverse, being scanned by the LTP. The optic was set up on the aluminium frame, designed for the X-ray tests, on top of the granite table. The height and stability of the granite table is controlled precisely so that no vibrations of the granite are picked up by the LTP. The laser is on a computer controlled translation stage which also calculates the slope of the optic's surface. The whole arrangement is contained within a sealed chamber which prevents any distortions caused by air currents or temperature variations. 47
- 2.28 The measurements taken of the profile of the elliptical mandrel using the LTP at STFC Daresbury Laboratory. The top graph shows the expected theoretical form is shown in black and the sixteen axial strips taken with the LTP are shown in varying colours. The lower graph shows the difference between the theoretical profile and the axial strips. The strips were $290mm$ in length and separated by $6.25mm$. The data for the extra $10mm$ of the mandrel was extrapolated using a least squares fit of the last few points of real data. The error in the $1.75mm$ data set is a calculation error and was not a real feature on the mandrel. 49
- 2.29 The scans taken of the released ellipsoidal mirror prior to any actuators being attached. The top graph shows the scans which were measured across the optics surface are shown in various colours, with the theoretical form of the mirror shown in black. The bottom graph shows the difference between the expected mirror profile and the actual profile which was measured with the LTP. These plots show that the mirror was a lot flatter than was expected which changed the focal length of the optic and therefore its required position with respect to the source and detector. The axial strips were $270mm$ in length and separated by $7.5mm$. The measurements were extended across the full length of the mirror by extrapolation using a least squares fit method. 50
- 2.30 A comparison between the mandrel's profile and the profile of the released mirror. The plot clearly shows that the mirror was distorted due to stress during the release process and this caused it to be flatter than expected. Eleven scans have been compared to produce this plot as eleven scans of the released optic were measured. 51

- 2.31 The top graph shows axial scans along the centre of the mirror with thirty piezoelectric devices attached are plotted, with the power supply to the actuators turned off, on and the difference between the two. With the power on, all the actuators are effectively at $+100V$ even though they were set to $0V$, which is demonstrated in the plot of the difference between the power being on and off. The red vertical lines represent the positions of the piezoelectric devices along the length of the mirror. The lower graph shows the plots once the theoretical profile of the mirror has been subtracted, which accentuates the print-through effect seen on the mirror's surface. 53
- 2.32 The difference between the released optic and the addition of the piezoelectric actuators. Here the positions of the piezoelectric actuators are shown in black and the various scans are shown in different colours. The top frame is the comparison with the actuators turned off and the lower frame shows the comparison with the power turned on. The extent of the print-through from the actuators described earlier, is clearly visible in both of these plots. 54
- 2.33 An example of an illustration produced in Q. In this model, a perfect simulation of the ellipse prototype mirror was completed. The top left shows the ellipse in black and the outline of the TTF is shown in blue. The two axes on this plot are not to scale and the axis of the ellipse is tilted with respect to the TTF axis. The detector and source are at the foci of the ellipse. The change in the tunnel's width can also be seen on this plot. Top right shows the full detected image with the rays which have not been reflected by the optic at the bottom of the image. The red circle represents the area of interest which was used to calculate the HEW values. This shows the outline and shape of the optic. Bottom left is a zoomed in image of the rays being reflected by the optic and then hitting the detector. Bottom right is a zoomed in view of the focused spot. The resolution of this image is limited by the detector's pixel size, $0.21mm$ 57
- 2.34 Results from the models of the rotation in the X, θ , and Y, ϕ , axes in top and bottom respectively. It is clear from these graphs that the optic was more sensitive to rotation about the X axis, θ than the Y axis, ϕ as rotation in the θ direction is effectively a rotation around the ellipsoid's axis. 58
- 2.35 The basic ellipse model with the gravitational sag deformations added in Q. This image has the same set up as in figure 2.33. It can be seen that the focused spot has been spread out in to a fan shape. The vertical detected distribution can also be seen in the lower right hand frame of this image. For a focused spot, a single central peak would be seen. The detected image was measured by simulation using Q to have a HEW of $13.77''$, close to what was predicted using the COMSOL Multiphysics FEA data of $10.02''$ 59

- 2.36 A model produced in Q of the response of the optic without any actuators attached, with the deformation matrix set to the measured data taken using the LTP at STFC Daresbury Laboratory, as shown in figure 2.29. The top left shows the ellipse, TTF, and the position of the ellipsoidal mirror. This image also shows the X-rays from the source being reflected by the optic towards the detector. Top right shows a zoomed-in image of the central detected area. Bottom left is a vertical distribution of the detected image. The bottom right is the shape of the optic which was implemented to create the model. This shape gave a measured detected spot of 1.51'. 61
- 2.37 A model of the response of the optic with actuators attached, with the deformation matrix set to the measured data taken using the LTP at STFC Daresbury Laboratory, as shown in figure 2.31. Top left shows the ellipse, TTF and the position of the ellipsoidal mirror. This image also shows the X-rays from the source being reflected by the optic towards the detector. The top right is a zoomed-in image of the detected spot. The bottom left shows the distribution of the detected spot. The bottom right is the deformation matrix added to the optic. This shape gave a simulated HEW of 3.64'. 63
- 2.38 Set up for the piezoelectric actuator simulation. Left shows the initial optic distortion, consisting of two orthogonal sine waves across the full length of the optic, which produces a 30" image on the detector. Middle, The initial piezoelectric arrangement on the mirror with four piezoelectric devices and right, arrangement of the thirty piezoelectric actuators. 64
- 2.39 Results from the simulation of four piezoelectric actuators in Q. The top graph demonstrates the decrease in the HEW of the detected image as each full iteration of the four piezoelectric devices is completed. Each piezoelectric device was actuated in ten equal steps in the voltage range of -100V to +100V. A least squares fit was used to find the optimum voltage for each of the piezoelectric devices by plotting the voltage against the detected HEW. The graph shows a decrease in the HEW from just over 30" to just under 4". The bottom graph shows the change in the FWHM with each iteration. A single iteration in this case is all four actuators being iterated and the optimum voltage found. 65
- 2.40 The FFT patterns created by the process described in section 2.4. The first column contains the basic patterns and the subsequent columns are those which have been multiplied by the short length patterns. The patterns range from -1 to +1 and the voltage applied to each individual piezoelectric is calculated by taking these values and multiplying it by the voltage iteration value in the range of -100V to +100V. 68

- 2.41 A comparison of the Gaussian model and the influence functions of the COMSOL Multiphysics models produced at UCL, on a three by three actuator grid. The Gaussian model is on the left followed by the nickel and glass models respectively. The top images show the effect of the actuators across the entire plate, the middle images show graphs of the heights of the functions and the lower images show the 3D deformation matrix. These models have been produced by simulating optics of $0.4mm$ thickness with $0.2mm$ thick piezoelectric plates attached. 69
- 2.42 A comparison of the Gaussian models and the influence functions of the COMSOL Multiphysics models produced at UCL, on a three by three actuator grid with a glue layer. The Gaussian model is on the left followed by the nickel and glass models respectively. The top images show the effect of the actuators across the entire plate, the middle images show graphs of the heights of the functions and the lower images show the 3D deformation matrix. These models have been produced by simulating optics of $0.4mm$ thickness with $0.2mm$ thick piezoelectric plates attached and a $0.5mm$ glue layer. 70
- 2.43 The results of the iterative routine in Q using the FFT patterns and the LTP data of the optic with the power supply to the piezoelectric devices turned on. In this routine, the patterns were ordered based on their influence on the HEW. Here the HEW was reduced from $3.46'$ to $1.83'$. The top graph shows the change in HEW and the lower graph the effect on the FWHM based on the pattern iteration. 71
- 2.44 The results of the iterative routine in Q using the FFT patterns and the LTP data of the optic with the power supply to the piezoelectric devices turned on. In this routine, the patterns were ordered based on their optimum voltage. Here the HEW was reduced from $3.46'$ to $2.38'$. The top graph shows the change in HEW and the lower graph shows the effect on the FWHM based on the pattern iteration. 72
- 2.45 The results of the iterative routine in Q using the FFT patterns and the LTP data of the optic with the power supply to the piezoelectric devices turned on. a) The results with the patterns in the order of HEW influence and b) the results with the patterns in the optimum voltage order. The top images are a representation of the optical distortion, the middle images are the piezoelectric distortions and the bottom images are the combined response. 72
- 2.46 A sketch of the TTF at UoL. The facility is $28m$ in length and has an X-ray source capable of producing energies of up to $100keV$ at one end and a detector chamber containing an MCP detector system at the other. Several flanges exist along the length of the facility to allow access and for optics to be mounted. The access flange to the detector chamber, where optics can also be mounted, is inside a clean room. 74

2.47 a) The source end of the TTF at UoL. The source is contained within the blue lead lined cage at the bottom right of the image. It is capable of producing X-ray energies in the range of $0.1keV$ to $100keV$ and the copper anode can be coated in varying materials to create specific X-ray excitation lines. b) The detector tank at the other end of the facility, $28m$ from the source. Within the detector tank, the MCP detector has a movement of $825mm$, in the X axis, on an automated translation stage. It is also possible to manually move the detector in the Y and Z axes. The detector chamber opens onto a clean room to allow space instruments to be tested. Images provided by Dr. J. Pearson, UoL. 75

2.48 A diagram demonstrating the TTF axes. The $(0,0)$ point is the centre of the detector’s nominal field of view and the X axis is down the beam line away from the detector, towards the source. The detector is moved in the X axes using automated motors and can be moved manually in the Y and Z axes. 75

2.49 The set up of an MCP detector with a resistive anode where two MCPs are arranged behind a UV filter. A high voltage is applied to direct the electron cloud down the channels of the MCPs, towards the resistive anode. Two MCPs are used to multiply the signal. . . . 76

2.50 Two charged MCP plates, with channel walls in a chevron configuration at an angle of 13° , in front of a resistive anode. The X-rays which reach the detector (shown in green), interact with the walls of the first MCP plate which causes an exponential cascade of electrons. The field between the two plates is such that the electron cascade is directed from the first plate, down the corresponding channel of the secondary plate. Once the electron cloud has cascaded down the second MCP plate, it is dumped onto the anode. 77

2.51 The resistive anode behind the two MCP plates within the detector system. It consists of a resistive plate and four electrodes at the corners, which are labeled $X1$, $X2$, $Y1$ and $Y2$. Each electrode receives a proportion of the charge which has been dumped on the resistive plate. These proportions are then translated into X and Y positions using equation 2.11 77

- 2.52 An unlinearized is shown on the left and a linearized image of the regular series of pin holes is on the right. Due to the nature of the read out from the MCP detector, a pin cushion effect is created in the detected image and to correct for this, an image is taken of a series of regularly spaced pin holes whose real positions are known. These positions are compared to the detected image's positions using a local polynomial fit. A look up table is then created which is used to correct any images which have been obtained with the same detector. The linearization of the edges of the image is not very good for two reasons: firstly, there was some distortion on the original image which made it difficult to find the precise position of the centre of the holes at the edge; and secondly, the curvature is greatest at the edges and the polynomial fit therefore needs more terms. As the data obtained is within the central region of the detector, the effect at the edges is unimportant. 78
- 2.53 a) The laser in place of the X-ray source to enable alignment of the optic within the facility. b) The view of the laser from within the blue X-ray source cage. 79
- 2.54 An example of the images taken during the alignment of the optic within the TTF using the laser as the source. The exit aperture of the detector chamber was covered with paper to form the image, both the reflected beam and the mirror intersecting the straight through beam from the laser are visible. 80
- 2.55 Three images showing the change in the reflected beam. Left, the "first light" image obtained with the laser. Middle, an intermediate stage of alignment and right, the final position of the optic after alignment. The calculated position of the detector is shown as a black mark in the middle and right images. 81
- 2.56 a) The detector in it's original position and b) in the new position, raised by $141.06mm$, required for the X-ray tests. 81
- 2.57 The copper anode of the X-ray source coated in a thin layer of NaCl to excite the emission lines required for the X-ray tests. 81
- 2.58 The first X-ray image obtained during the X-ray tests. The histogram on the X axis is the total integration across the height of the plate and the histogram on the Y axis is the total integration across the width of the plate. The colour bar on the right shows the maximum number of counts detected in any one position and the graph in the bottom left corner is the pulse height of the signal received by the anode. The header of the image shows the image name, total number of counts detected in the image and the count rate. 82

- 2.59 Further examples of X-ray images obtained during the X-ray experiments carried out within the TTF. The histogram on the X axis is the total integration across the height of the plate and the histogram on the Y axis is the total integration across the width of the plate. The colour bar on the right shows the maximum number of counts detected in any one position and the graph in the bottom left corner is the pulse height of the signal received by the anode. The header of the image shows the image name, total number of counts detected in the image and the count rate. 83
- 2.60 A series of fourteen local group patterns to control the piezoelectric devices during the X-ray tests. The white areas indicate the actuators which are active (with a value of +1) whilst the rest remain passive (with a value of 0). The voltage applied to each individual piezoelectric is calculated by taking these values and multiplying it by the voltage iteration value. Patterns three to ten are each of the columns of devices actuated in turn. 84
- 2.61 HEW and FWHM results from the full adjustment of the piezoelectric devices during the X-ray tests. The pattern number refers to the patterns described in figure 2.60. The HEW or FWHM were improved by a few patterns but not in a predictable way. 85
- 2.62 Optimum voltages obtained from the full adjustment routine during the X-ray tests. The top left is a 3D representation of the shape of the optic with the voltages shown in table 2.5, top right is a colour representation of the optic shape and the bottom image is a representation of the voltages applied where black is -40V and white is +100V. 86
- 2.63 Graphs demonstrating the HEW and FWHM changes in each of the images taken with the piezoelectric devices at 0V. The HEW images are on the left and the FWHM are on the right. The top frames show the change over a period of days from the start of testing, whilst the lower frames show the changes over successive actuations of the devices. Both show a trend of decreasing HEW and increasing FWHM over time. 87
- 2.64 An illustration of the Hartmann test, designed to calculate the errors within an optical system. By reconstructing the paths of the rays between two photographic plates, it is possible to calculate the errors in the mirror's form. 88
- 2.65 The results from the Hartmann test. Histograms of the changes are shown alongside an illustration of the piezoelectric devices being actuated. Each graph consists of three panes with the top representing the left hand side of the image, the middle representing the central region and the bottom representing the right hand side. The data from the +100V images are shown in black whilst -100V are shown in red. 89
- 2.66 Results of the second piezoelectric stability tests. The actuators were held for five hours in a pattern which forced each adjacent actuator into an opposite voltage to its neighbour. The HEW results are on the left and FWHM are on the right and demonstrate a drift of 17.53". 90

2.67	The stability of the power supply for the piezoelectric devices over a five hour period tested at UCL. Data was taken every ten minutes for the first hour and every twenty minutes for a further four hours. . . .	91
2.68	Scans of the optic's surface using the LTP at STFC Daresbury Laboratory with the piezoelectric devices actuated at the optimum voltages determined during the X-ray tests. The top graph shows the single scan with the theoretical curve the optic should have had. The bottom graph shows the change in the figure of the mirror between the piezoelectric devices being actuated and not actuated. The positions of the piezoelectric devices are shown in red.	92
2.69	Scans taken along the surface of the mirror with piezoelectric 17 actuated, shown alongside the modelled data and the position of the piezoelectric devices shown in black. The difference between the measured and modelled data is due to the glue thickness which causes the kinks in between the actuators but does not appear to change the influence of the device.	93
2.70	The results of the iterative routine in Q using the local group patterns and the LTP data of the optic with the piezoelectric devices turned on. In this routine, the patterns were ordered based on their influence on the HEW. Here the HEW was reduced from 3.46' to 1.84'. The top graph shows the change in HEW and the bottom graph shows the effect on the FWHM based on the pattern iteration.	94
2.71	The results of the iterative routine in Q using the local group patterns and the LTP data of the optic with the piezoelectric devices turned on. In this routine, the patterns were ordered based on their optimum voltage. Here the HEW was reduced from 3.46' to 1.79'. The top graph shows the change in HEW and the bottom graph shows the effect on the FWHM based on the pattern iteration.	95
2.72	The top images represent the starting mirror deformation, the middle figures are the piezoelectric distortion from a) figure 2.70 and b) figure 2.71 and the lower figures are the combination of the top two. These images demonstrate that for any series of patterns and initial mirror figure deformation, there is no single solution.	95
2.73	Ray traced model in Q of the LTP data taken with the piezoelectric devices actuated at the optimum voltages found during the X-ray tests, table 2.5. The simulated HEW for this deformation matrix was found to be 2.14'.	97
2.74	Ray trace in Q of the model created with the optic fixed at the four corners and the piezoelectric devices at the optimum voltages found during the X-ray tests. The simulated HEW found with this model was 2.92'.	98
2.75	Ray trace in Q of the model created with the optic fixed at two points at the centre of the ends of the mirror and the piezoelectric devices at the optimum voltages found during the X-ray tests. The simulated HEW found with this model was 2.07'.	98

2.76	Ray traced model in Q of the curvature errors. The optic was modelled as having a radius of curvature from $155mm$ to $160mm$ as opposed to $164mm$ to $169mm$. The simulated HEW for this deformation matrix was found to be $2.44'$	99
2.77	Ray traced model in Q of the curvature errors combined with the print-through from bonding the piezoelectric devices. The simulated HEW for this deformation matrix was found to be $2.62'$	99
2.78	A simulation of the X-ray data obtained by combining errors from curvature, bonding the piezoelectric devices and pitch and yaw errors.	101
2.79	Models produced at UoB showing the reduction in the size of the kinks by a) reducing the size of the gaps between the actuators and b) filling the gaps with polyimide. All the models were produced using a three by three actuator grid in COMSOL Multiphysics and were provided by UoB.	102
3.1	An illustration of a single Fresnel zone plate used to focus X-rays via diffraction. It consists of alternating opaque and transparent zones which are arranged so that the X-rays are diffracted around the opaque zones, constructively interfere, and create the desired focus[15].	108
3.2	A point-to-point focusing device using two reflections of grazing incidence. The source is brought to a focus by consecutive reflections from two surfaces. The grazing angle with which the X-rays hit the optic, depends on the radius of curvature of the optic. By adjusting the radius of curvature, the focal length is adjusted. A device of this type, would satisfy the Abbe sine condition[16] as X-rays both on and off axis would be focused[17].	110
3.3	A cross section of a proposed system with a cylindrical profile. The channels are attached to the centre stop and outer edge via spindles. The central stop reduces the number of straight through rays which hit the detector. By bending the optic to a spherical profile, it would create a spot focus similar to that of a zone plate but using grazing incidence reflections as opposed to diffraction[17].	111
3.4	Current prototype MOA design, not to scale. The silicon chip is $20mm \times 10mm \times 0.2mm$ with a central active area. The central area is $4mm^2$ and consists of $0.01mm$ wide slots with $0.01mm$ wide walls. There is a central stop to reduce the number of X-rays which pass straight through the optic and hit the detector. The lighter grey strips are the piezoelectric actuators which are $1mm$ wide and $1mm$ from the central area to reduce stress as they are actuated.	113
3.5	The mount designed to hold the MOAs. The handles control the micrometers which allow the MOAs to be moved in the translational directions and to be aligned with each other. The electrodes from the piezoelectric actuators can be attached to the drivers via the connectors on the MOA holder. a) Half of the mount with the area where the MOA will be contained at the top. The channels for the piezoelectric actuator electrodes can be seen. b) The full mount shown with sections for two MOAs. Images provided by MSSSL.	114

3.6	The MOA holder component of the mount, shown in figure 3.5, with an MOA in place. This component holds the MOA in place as there is a cut out section which the MOA sits in and the clamp is placed over the top. The clamp has two knife edges which allow the MOA to bend without any stress being added. There are also channels cut into the holder to allow access to the piezoelectric electrodes. The electrodes are connected to the driver via the connectors at the base of the holder.	114
3.7	An image of the MOA holder for the X-ray tests at UoL. The silver surround is made from steel and acts as a baffle to prevent the rays which do not hit the MOA from travelling through to the CCD. The baffle attaches to the rotation arm to allow rotation of the MOA in one axis. The brown holder is the purpose built MOA holder and an MOA with piezoelectric strips can be seen inside. The MOA holder is attached to the baffle via four screws and the clamp which holds the MOA in place can also be seen over the top of the MOA.	115
3.8	Geometry of a single reflection from an MOA channel[18].	116
3.9	Geometry of reflections from a tandem pair of MOAs[18].	117
3.10	A channel wall shown with scallops down its length. Left, an illustration of the MOA wall as it is etched, which creates the scallops during the passivation process. Right, the in-plane scattering caused by these features due to the change in slope, the grazing angle is increased or decreased by a small factor δ	120
3.11	A channel wall with the curtain features shown down the length of the wall. Left, the entire length of the channel with the curtain effect which is orthogonal to the scallops, shown in figure 3.10, and is caused by the roughness along the edge of the mask used to etch the channels. Right, the out-of-plane scattering caused by this effect which shifts and spreads out the line focus.	120
3.12	A zoomed in image of a single scallop with radius T , height h and width d	121
3.13	A demonstration of shadowing on a reflected surface. The reflective surface is pictured with surface roughness features of length t , and height h . The X-ray is coming from the left of the image and is reflected at an angle θ_g , the grazing angle. Part of the surface is hidden from the incoming X-rays by the surface features thus reducing the efficiency of the optic[19].	124
3.14	Images of the front side of the dry etched MOA taken with the FEGSEM. a) The active area of the MOA, a few broken channels are clearly visible. b) A closer view of the broken channels within the MOA's active area. c) A view down the length of the channel wall where the curtain effect is visible. d) A wider angle view down the MOA channel wall where both scallops and the curtain effect are visible. e) A series of channels, undamaged. The quality of the etch can be seen in this image, the walls are evenly spaced and vertical. f) A view of the edges of the channels which have been curved to improve the quality and ease of the etch. The scales in these images are 500, 10, 2, 2, 20 and $20\mu m$ for a), b), c), d), e) and f) respectively.	126

- 3.15 Images of the rear side of the dry etched MOA taken with the FEGSEM.
 a) The rear side of the active area of the MOA. It can be seen that this side of the MOA is very damaged, with broken channels, chips and scratches over the entire area. b) The channels are much narrower, uneven and damaged compared with the front side of the MOA. c) A zoomed in image of the damaged area of the channel walls. d) A closer view down the length of the channel walls where the scallop and curtain effects are less visible, however, it does appear as though a substance has been dripped down the walls creating very high levels of surface roughness. e) A view of the tops of the channel walls which appear uneven and narrow. f) The corners of the channels are very misshapen and damaged and there are a large number of broken channels on this side of the MOA. The scales in these images are 200, 100, 20, 5, 20 and $50\mu m$ for a), b), c), d), e) and f) respectively. 127
- 3.16 A series of images of a wet etched MOA using the ESEM at UoL. The surfaces of the channel walls are much cleaner and show practically no surface features. The channel walls are incredibly straight and even and there are very few broken channels although some do appear to of stuck together. a) and b) show the front side of the MOA and c) and d) show the reverse side. Both sides are practically identical to one another. The scales in these images are $3mm$, $100\mu m$, $2mm$ and $20\mu m$ for a), b), c) and d) respectively. 128
- 3.17 Line-to-line focusing of a $1.04 keV$ source, with a flat MOA. The top image shows the full system with the source positioned on the right of the image and the detector on the left. The red rays are produced by the source and represent the rays which have not been reflected whilst the green rays represent those which have undergone a single reflection. It can be seen in both images that not all the rays produced at the source are reflected by the optic, some pass straight through to the detector. The axes for both frames are in mm and the source to detector distance is $40mm$. The MOA is positioned at $20mm$ and has a focal length of $20mm$. The bottom image shows a zoomed-in section of channels and shows the rays being reflected. The red rays from the source enter the channels from the right and are reflected toward the detector on the left. The MOA has been modelled with a perfect reflecting silicon surface with no deformations. 130
- 3.18 Line-to-line focusing with a curved MOA. The top image has a source to detector distance of $45mm$ and the MOA is positioned at $30mm$ with a radius of curvature of $60mm$, curved toward the source. The bottom image is a zoomed-in section of the channels which shows the rays being reflected. The red rays from the source enter the channels from the right and are reflected toward the detector on the left. The model was produced and set up in the same way as figure 3.17 131

- 3.19 A finite source of 1.04 keV being reflected by an MOA acting as a collimator. The figure is set up in the same way as figure 3.17. The focal length of the MOA is 25mm and the radius of curvature of this MOA is 50mm , positioned at 25mm , and curved toward the source. The lower image shows a zoomed-in image of the channels, where the rays enter the channels from the right at an angle, and are reflected toward the left. It can be seen that the reflected rays, in green, are parallel to the optical axis. 132
- 3.20 An MOA acting as a telescope, focusing an infinite source at an energy of 1.04keV . The formatting for this figure is the same as in figure 3.17. The focal length of the MOA is 20mm and the length of the system is 30mm . The MOA has a radius of curvature of 40mm , is positioned at 20mm and is curved toward the focus. The lower image shows a zoomed-in image showing that the parallel rays entering the channels from the right, exit the MOA at an angle on the left. . . . 133
- 3.21 Two MOAs acting as a collimator-telescope tandem system. The top image has the finite source with an energy of 1.04keV on the right of the image at 45mm and the detector is on the left at 0.0mm . The image has been produced in the same way as 3.17, with the addition of the blue rays which demonstrate rays which have been reflected twice, once by each MOA. The collimator-telescope system is operating over a distance of 45mm with the two MOAs positioned at 25mm and 20mm respectively. The first is a collimator MOA with a radius of curvature of 40mm curved toward the source. The second MOA is acting as a telescope also with a radius of curvature of 40mm curved toward the detector. The MOAs are separated by 5mm and the rays are parallel to the optical axis between them, this can be seen in the lower image. The rays enter the channels from the right, are reflected by the first MOA and are then reflected by the second MOA as they are perfectly aligned. The majority of the rays reflected by the first MOA are reflected by the second MOA. Two foci can be seen in the top image, the first is at $\sim 8\text{mm}$, the second is at 0.0mm . The first focus is created by rays which have passed through the first MOA and are only reflected and focused by the second MOA and the second focus is created by the rays which have been reflected by both MOAs. 134

- 3.22 Line-to-line focusing with an equal grazing angle tandem MOA system. The system is set up in the same way as figure 3.21. Set over $45mm$ with the source at $45mm$, the MOAs at $30mm$ and $27.5mm$ respectively, and the detector at $0.0mm$. The full system is shown in the top graph, where the rays are reflected at the same angle by both MOAs. Not all rays reflected by the first MOA are reflected by the second MOA. A zoomed-in image in the lower frame shows the rays being reflected by the two MOAs. There are two foci again in the image, caused by reflections from the first MOA and reflections from both MOAs. The second focus, from the double reflection rays, is not at $0.0mm$ due to the gap between the MOAs. The intensity of the focus spot is also less than that in figure 3.21, because fewer rays are focused by both MOAs. 136
- 3.23 Line-to-line focusing with an equal grazing angle tandem system, with no gap between the MOAs. This system is identical to figure 3.22 except the MOAs are almost touching. The number of rays which are focused by both MOAs is greatly increased and the focus has been moved to $0.0mm$ as expected. In the lower frame, it is clear how close the MOAs are, although some rays reflected by the first MOA are still not reflected by the second. 137
- 3.24 A flat-curved tandem MOA system. The source is to the right of the image and the detector is to the left and is configured in the same way as figure 3.21. In the top frame, the MOA closest to the source has an infinite radius of curvature, and the second MOA is curved toward the focus. The source is focused over a distance of $20mm$. The MOAs are positioned at $7mm$ and $6.8mm$ respectively and can be seen in the lower frame. The number of rays focused by this system is less than that shown in figure 3.23, as fewer rays reflected by the first MOA are focused by the second MOA. Some of the rays which have been reflected off one wall in the first MOA experience a secondary reflection off the opposite wall. These rays, shown in blue, are not reflected by the second MOA which reduces the efficiency of this configuration. 138
- 3.25 An illustration of a crossed pair of MOAs. These MOAs are set up so that they are orthogonal to one another. This creates a focused spot, with cross arms, as opposed to a line focus. 139
- 3.26 A crossed pair of MOAs creating a focused spot. The two MOAs are orthogonal to one another so that each produces a line focus. The point at which the two line foci cross, creates the single point focus. The left hand frame shows the whole system over $160mm$, with a gap of $5mm$ in between the two MOAs. The right hand frame shows the modelled detected image with the axes in μm and the focused spot is $\sim 3\mu m$ in diameter. 140

3.27	A crossed pair of MOAs creating a focused spot of high intensity. The two MOAs are orthogonal to one another so that each produces a line focus. The point at which the two line foci cross, creates the single point focus. The left hand frame shows the whole system over $41mm$, with a gap of $1mm$ in between the two MOAs. The right hand frame is the modelled detected image with the axes in μm and the focused spot is $\sim 15\mu m$ in diameter. The focused spot is more intense than in figure 3.26 as more rays are focused by both MOAs.	140
3.28	Ray tracing and detected images of cylindrical and parabolic MOAs. An infinite source is focused by a curved MOA over a distance of $40mm$. The MOA is positioned at $20mm$ and is curved toward the source with a radius of curvature of $40mm$. a) The ray-tracing and detected image of an MOA bent to a parabola. b) An MOA bent to a cylindrical profile. The ray-tracing in both cases is almost identical. The parabolic detected image shows a much cleaner, sharper line focus and the scattered rays are also more coherent.	141
3.29	Detected distributions of cylindrical and parabolic MOAs as modelled in figure 3.28. a) The distribution of a parabolic MOA and b) the distribution of a cylindrical MOA. The detected distributions are subtly different. The widths of the distributions are very similar, but the intensity of the parabolic line focus is ten times greater than that of a cylindrical MOA.	142
3.30	A tandem MOA system with scallops and shadowing. The left hand image shows the ray-tracing and the right hand image shows the detected image. This is the same set up as shown in figure 3.21. The number of scattered rays have been increased and the intensity of the line focus has been reduced, but a focus is still produced. The number of rays which are reflected by both MOAs is also reduced.	142
3.31	A crossed pair of MOAs with scallops and shadowing included, over a large aperture. The left hand frame shows the ray-tracing and the right hand frame shows the detected image. The MOAs are focusing over a distance of $40mm$ and the MOAs are at $19mm$ and $20mm$ and are orthogonal to one another. There are very few focused rays due to scalloping effects and no focused spot can be seen in the detected image.	143
3.32	A crossed pair of MOAs with scalloping and shadowing, but over a small aperture and longer distance. Left, The ray-tracing and right, the detected image. The MOAs are focusing over a much larger distance of $160mm$ with the MOAs at $75mm$ and $80mm$ and are orthogonal to one another. The number of scattered rays is increased and the intensity of the focused spot is much lower compared to that shown in figure 3.26.	143
3.33	The set up of the reflectivity tests performed at STFC Daresbury Laboratory. The MOA was rotated on one stage, about an angle Ω and the detector was rotated on the other, about an angle Θ . Images provided by STFC Daresbury Laboratory.	145

- 3.34 An example of the results obtained from the reflectivity tests carried out at STFC Daresbury Laboratory. These results cover an angle range of -1.0° to 8.0° with the straight through flux shown at 0.0° on the X axes and the reflection is seen at approximately 4.0° . Images provided by STFC Daresbury Laboratory. 146
- 3.35 The relationship between Θ and Ω . The black line is the expected relationship of $\Theta=2\Omega$, and the red line shows the positions of the peak number of counts at each angle. 147
- 3.36 Combination of all the results obtained during the experiments at STFC Daresbury Laboratory. The blue line indicates the transmitted component detected whilst the red line indicates the reflected component. The vertical lines show the cut or repeat in data obtained. 148
- 3.37 Image of the XMM-Newton CCD life test facility at UoL. The test facility is 3.1m long with an X-ray source, X-ray CCD and mounting at the centre, for an optic. The X-ray source is on the right hand side of the image (by the bookcase) whilst the CCD is on the far left of the image. The MOA was mounted behind the flange which is in the centre of the pipe. The rotation arm can also be seen attached to this flange. 149
- 3.38 Ray tracing of the MOA tests. The source is at an energy of $\sim 1keV$ and the detector and MOA are positioned as in the testing facility. The ray traced system and detected image are shown for four different angles. a) The initial position of the MOA where the rays passing straight through the optic was studied. b) and c) are intermediate angles between a) and d). d) The angle at which the full length of the MOA channels are illuminated. 151
- 3.39 Detected distribution of the ray-tracing of the MOA tests. The source is at an energy of $\sim 1keV$ and the detector and MOA are positioned as in the testing facility. a) The distribution of the initial position of the MOA where the majority of rays pass through the optic, b) and c) show intermediate angles between a) and d). d) The angle at which all the MOA channels are illuminated. The distributions appear off centre as the reflected rays are not in the centre of the detector as the MOA is rotated. 152
- 3.40 Ray tracing of the MOA tests, as in figure 3.38 but with additional surface features and roughness. The source is at an energy of $\sim 1keV$ and the detector and MOA are positioned as in the testing facility. The ray traced system and detected image are shown at the same four angles as in figure 3.38. Scattering of the beam is clearly visible in all four images. The width of the detected focused line is also wider due to the surface features. 153
- 3.41 Detected distribution of the ray-tracing of the MOA tests, as in figure 3.39 but with surface roughness. The source at an energy of $\sim 1keV$ and the detector and MOA are positioned as in the testing facility. The width of the distributions is wider than that shown in figure 3.39, this is due to the increased scattering of the beam due to the surface roughness. 154

- 3.42 An example of a CCD image obtained during the MOA tests within the CCD life test facility at UoL. The central bright region is the straight through flux from the MOA. 155
- 3.43 Results from the reflectivity tests using a dry etched MOA. There is an increase in the amount of reflected flux as the amount of flux in the central region decreases. The amount of reflection is very low at $\sim 3.33\%$ and has suffered from the surface roughness features as shown by the asymmetry in the left and right hand reflection. 155
- 3.44 A demonstration of why no reflection was seen using the wet etched MOA, with the path of the X-rays shown in green. The reflected flux was being blocked by one of the flanges in the facility. 156
- 3.45 The mounting for the wet etched MOA within the crystal holder. A dial on the top allows for accurate alignment of the MOA with the source and a θ , 2θ turn table allows the reflected flux to be studied. 157
- 3.46 The results from the reflectivity tests of the wet etched MOA mounted in the crystal chamber. The triangular shape is very clear and shows reflection of 5.93% 158
- 3.47 A possible new MOA prototype, made from a silicon sandwich chip of $200\mu m$ silicon, $1\mu m$ silicon oxide and $10\mu m$ silicon. The $200\mu m$ silicon layer will be wet etched with many channels over the majority of the length of the chip. The $10\mu m$ layer will have a central active area as with the previous prototype. The silicon oxide layer will act as a bonding layer between the two etched silicon layers. 160
- 3.48 A possible prototype design called the spider. A series of channels are etched to make the silicon easier to bend. The legs act as levers which move independently and can either be dry or wet etched and are designed to remove stress from the active region. Provided by UoB. 161

LIST OF TABLES

2.1	A table showing the ellipsoidal segment dimensions for the first prototype optic. The semi-major and semi-minor axes of the ellipse are governed by the dimensions of the TTF. The optic was very close to a cone in form as can be seen by the sagittal difference between a cone and the optic. The level of asymmetry can be seen in the difference in the radii of curvature at the front and the back of the optic. The grazing angle achieved allowed energies up to $\sim 5keV$ to be focused during the tests.	31
2.2	Summary of the results obtained by modelling the data from the LTP in Q. Both the simulated HEW and FWHM values are displayed in <i>mm</i> (as measured at the detector) and arcminutes.	62
2.3	Table showing the contents of the array to generate each eigenfunction and the corresponding imaginary part values required. The terms are marked as <i>ia</i> where <i>i</i> is the eigenfunction index and <i>a</i> is the sign of the corresponding imaginary part.	67
2.4	Table showing the four patterns in the shorter direction. The basic patterns created using the FFT method are copied into the adjoining rows and then multiplied by these patterns to create the sixteen FFT patterns, all of which are orthogonal to one another.	67
2.5	Optimum voltages calculated for each of the piezoelectric devices, from the full adjustment routine during the X-ray tests.	86
2.6	Summary of all the results from both the models and the X-ray data. The size of the reflection on the detector is shown in <i>mm</i> as well as the results in arcminutes for both the HEW and FWHM of the images.100	

CHAPTER 1

INTRODUCTION

1.1 Introduction and Justification of work

The Smart X-ray Optics (SXO) project is a UK based consortium funded by a basic technology research grant from the Engineering and Physical Sciences Research Council (EPSRC[20], PI. Dr. P. Doel). The project had one proof-of-concept year (2005) and has since run for three years, of a four year project (2006-2010). The consortium consists of eight UK institutions investigating the application of adaptive/active optics in both the macro and micro scales for the next generation of X-ray optics. Previously, adaptive optics have only been used in optical astronomy and on focusing mirrors for synchrotron radiation sources, however, it is hoped that this technology can be adapted for other X-ray instruments. The large scale optic is aimed towards developing technologies to produce an X-ray telescope with in-situ surface manipulation to improve the resolution of the telescope. The small scale application is aimed towards an X-ray focussing device, with a variable focal length to produce a focused spot on the scale of a single biological cell for radiation induced cancer research and studies. Both applications will achieve these goals by the addition of piezoelectric actuators which have been bonded to the surface.

As the SXO project is a collaboration between eight institutions, the work presented within this thesis forms a small part of the achievement of the project and could not have been undertaken without the results, analysis and assistance from the other institutions. Some of the work outlined has developed due to results from

other institutions or with the inclusion of data from those institutions. Below is a brief description of each institutions role.

University College London (UCL) and the Mullard Space Science Laboratory (MSSL) have been project managing and leading the project since its conception in 2005. UCL have provided modelling of the piezoelectric actuators and have manufactured the large scale adaptive prototype. MSSL have provided vital engineering for the production of the mounting for both devices.

Kings College London (KCL) have designed and modelled the small scale device, and are designing and manufacturing the micro-focus source. Some modelling of the piezoelectric devices for the small scale optic and investigation into bending techniques has also been undertaken.

The School of Metallurgy and Materials at the University of Birmingham has developed, designed and manufactured the piezoelectric devices used for both the large and small scale prototype optics. Extensive modelling of the piezoelectric devices in order to optimise the designs has also been completed and the conception and modelling of the new small scale optic designs.

The Scottish Micro-electronic Centre (SMC) at the University of Edinburgh have been involved in the design and investigation of the production methods of the small scale device. This has included both dry and wet etching techniques and they have produced prototypes of the small scale device using both methods.

The Science and Technologies Facilities Council (STFC) Daresbury Laboratory have completed reflectivity tests on the small scale optic and have carried out a large amount of metrology using the Long Trace Profiler (LTP) on the large scale optic and mandrel. STFC Daresbury Laboratory has also been involved in the design concepts of both devices.

The work undertaken and described within this thesis is concerned with the design, modelling and testing of the large scale prototype optic and with the modelling and preliminary reflection tests of the small scale optic.

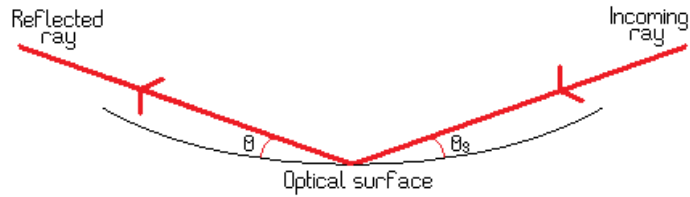


Figure 1.1: A ray reflected by an optical surface with grazing angle θ_g and reflected angle θ

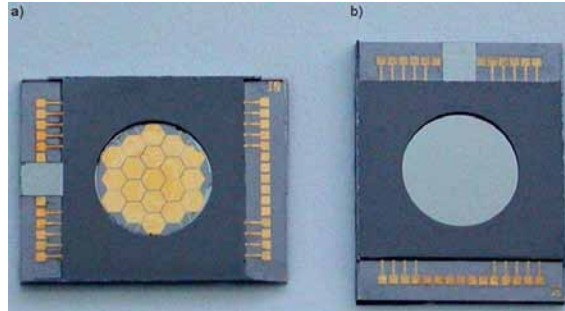


Figure 1.2: A normal incidence adaptive optical mirror. A high quality optical mirror has had multiple piezoelectric devices attached to the reverse side. a) The mirror with the hexagonal piezoelectric devices attached to the back and b) the reflective side of the mirror. The gold leads are the electrodes which control the actuators[1].

1.2 X-rays and current adaptive/active X-ray optics

X-rays were first discovered in 1895[21] and were initially described in detail by Wilhelm Conrad Röntgen, where X signified the unknown origin of this new form of radiation. X-rays are defined as being within the energy range of $0.12keV$ to $120keV$ [22] and although they are most commonly used for medical applications[23], the regions of the Universe which are under extreme conditions, e.g. within black holes, can also be imaged in this energy range[21].

As X-rays are absorbed by almost all materials, and at normal incidence, transmitted rays do not get bent as they pass through the medium and so cannot be focused by standard lenses. Grazing incidence optics have to be used to produce a focused image of an X-ray source. This is a reflection at an extremely shallow angle, usually $\leq 3^\circ$ (angle θ_g in figure 1.1) but higher energy X-rays need smaller angles to be reflected than soft X-rays[16] (see section 1.4 for a more detailed explanation).

Adaptive/active optics have been used for many years in both optical astronomy[24], using normal incidence mirrors, and in synchrotron radiation sources[25]. In the field

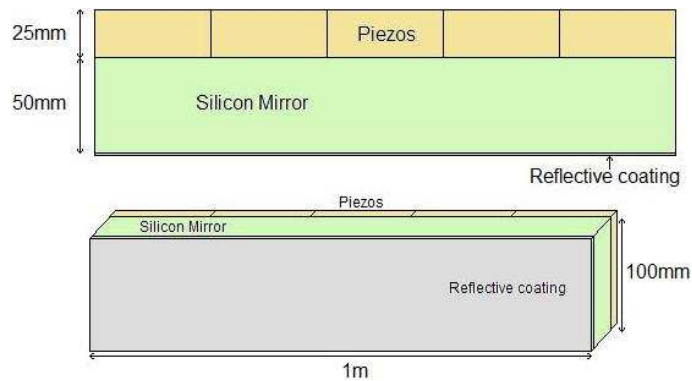


Figure 1.3: An example of a synchrotron mirror which consists of a silicon mirror, ground to form, with a series of piezoelectric devices attached on the back. The surface of the silicon is finished with an X-ray reflective coating. Using the piezoelectric devices, the mirror is bent into a very precise elliptical shape which can focus the X-ray beam to a nanometre scale.

of optical astronomy, hundreds of actuators (as shown in figure 1.2) are used at a time on several mirrors to remove aberrations and distortions on the image such as blurring, caused by the Earth's atmosphere. Using reflecting lasers the atmosphere's effect on the image can be calculated and by a simulated annealing method these distortions are removed. Simulated annealing is a process which improves the Half Energy Width (HEW) or Full Width Half Maximum (FWHM) of an image by applying a series of voltage patterns to the actuators. Each image is compared to all previous images and using a probability function the next pattern, which will improve the image, is calculated in real time. The composite mirror, optical mirror with the addition of piezoelectric actuators, have typical values of between $1.5mm$ and $2.5mm$ in thickness. The FWHM of an image is defined in terms of the surface brightness flux and it is the width at which the flux at the peak drops to half the peak value (see figure 1.4). The HEW of an image is defined in terms of the integrated flux, energy or power and is the width at which the total integral is half. The FWHM describes the size of the central region of the image and the HEW contains information on the scattering.

In synchrotron radiation sources, the focusing mirrors tend to be very large flat mirrors, with radii of curvature from $2km$ to $5km$ [26] or more. Piezoelectric actuators are used to bend the mirror very precisely in to an elliptical shape to focus the beam from the source, and thus achieve the best focused spot size. Synchrotron mirrors tend to be very thick silicon (with typical values of approximately $50mm$),

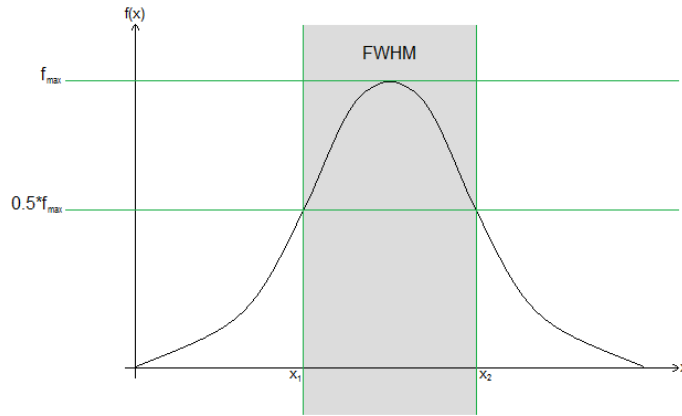


Figure 1.4: A graphical explanation of the Full Width Half Maximum (FWHM) of a detected image.

ground to a surface quality of a few atoms and then coated with an X-ray reflective material. The piezoelectric devices tend to be around 25mm in thickness and are attached along the rear surface, such that there is a single row of actuators along the length of the mirror, as demonstrated in figure 1.3. Due to the thickness of the mirrors, to provide the actuation required, the piezoelectric devices have to be around 25mm thick so the composite mirrors are approximately 75mm thick in total, making them much thicker than the optical mirrors. Several algorithms for this application have been written in order to be able to optimize the piezoelectric configuration, but no standard method exists. These form corrections are usually performed prior to any experiments being carried out and are adjusted as required during the lifetime of the mirror. A combination of both the systems described above are required for this project.

1.3 Background to piezoelectric devices

Piezoelectric actuators have been used for many years in optical adaptive optics, synchrotron radiation sources (as described above) and other commercial applications. When subjected to an electric field, they develop a strain and when subjected to a force, they produce an electrical charge, which makes them suitable as both actuators and sensors. Many materials display a small amount of natural piezoelectric properties such as quartz, tourmaline and Rochelle salt, but this effect can be amplified by using PZT (lead zirconate titanate, $\text{Pb}[\text{Zr}_x\text{Ti}_{1-x}]\text{O}_3$ where $0 < x < 1$ [27])



Figure 1.5: The flexibility of a piece of MFC. Image supplied by UCL.



Figure 1.6: Examples of piezoelectric devices created at the School of Metallurgy and Materials, University of Birmingham.

ceramics for actuators and PVDF (polyvinylidene fluoride polymer) for sensing[28].

Two forms of piezoelectric actuator design are being investigated for the purposes of this project, piezoelectric plates and Macro Fiber Composites (MFCs)[29]. A piezoelectric plate consists of PZT material, sandwiched between a pair of electrodes. In comparison, MFCs use piezoelectric fibres in parallel lines, on the top of which is laid an interlaced electrode pattern which is then sandwiched between two layers of polyamide. Piezoelectric plates experience motion in all three spatial axes, however, due to their fibre structure, MFCs experience motion in primarily one direction. MFCs are extremely flexible, as shown in figure 1.5, compared to PZT plates, allowing them to be bent to fit curved surfaces. However, PZT plates can be produced in different shapes and sizes by using moulds during production (figure 1.6).

The School of Metallurgy and Materials at the University of Birmingham provided the piezoelectric actuators for both areas of the project. They are capable of fabricating their own actuators[30] which can either be a PZT plate or a fibre based device similar to an MFC called an Active Fibre Composite (AFCs)[31]. For the

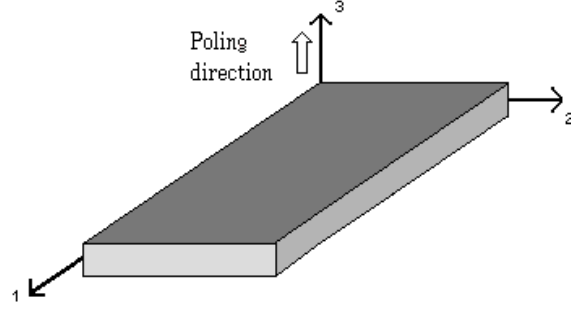


Figure 1.7: A PZT plate with associated axes and poling direction.

purposes of both the large and small scale applications, the piezoelectric actuators used had to be able to move the surfaces of the devices by several microns. The piezoelectric devices are intrinsic to both the small scale device and the large scale optic and an understanding of them is essential to understand how they will affect the two devices as they are actuated. Piezoelectric materials are characterised by their d_{33} and d_{31} properties which describe the degree of contraction or expansion they experience when an electrical potential difference is applied[28].

The relationship between stress, $[e]$, and strain, $[d]$, in piezoelectric material is given by equation 1.1.

$$[e]^T = [c^E][d]^T \quad (1.1)$$

where T is the stress vector and $[c^E]$ is the stiffness matrix of the material being used[28]. The most common material used for actuators is PZT ceramic, but PZT crystals have a dielectric nature and must be poled using a potential difference to align the crystals to the same direction, prior to the material being used as an actuator or a sensor. The poling direction is usually aligned normal to the surface with the largest area. This axis is traditionally labelled 3 and the other two axes within the plane are labelled 1 and 2 (see figure 1.7). As d represents the strain on the PZT plate, the value of d_{33} is the strain in the 3-axis caused by the electric field in that axis. Similarly, d_{31} is the strain in the 1-axis due to the electric field present in the 3-axis. In general, d_{33} is positive and represents expansion and d_{31} is negative and represents the contraction.

Using these values it is possible to calculate the optimum characteristics of the actuator required and therefore what proportions of lead, zirconate and titanate are needed. It is also possible to calculate the influence functions of the actuators and

produce models to predict the response of the surfaces.

1.4 A brief summary of X-ray physics

James[32], Compton and Allison[33] and Henke[34] give a complete description of the nature of X-rays interacting with matter and this is briefly summarised below. The reflection of electromagnetic waves can be described by the complex index of refraction, n , of the reflectivity material given by equation 1.2:

$$n = (1 - \delta) - i\beta \quad (1.2)$$

where both δ and β are positive and they can be calculated using atomic physics. δ is the phase change and β describes the absorption of a material at the specific wavelength and is related to the mass absorption coefficient μ by the equation:

$$\beta = \frac{\lambda\rho}{4\pi}\mu \quad (1.3)$$

where λ is the wavelength of the electromagnetic wave, ρ is the mean mass density of the reflecting material. β can then be calculated from equation 1.3 and absorption measurements of μ or calculations from first principles. For X-ray wavelengths sufficiently apart from absorption edge, δ can be calculated from equation 1.4 which is derived from dispersion theory.

$$\delta = N_0 \frac{Z}{A} \frac{e^2}{2\pi m_e c^2} \rho \lambda^2 \quad (1.4)$$

where N_0 is Avogadro's number and Z and A are the atomic number and weight respectively. Near to absorption edges, δ becomes complex and has to be calculated using the Kramers and Kroenig equations. At X-ray wavelengths, $\beta \ll 1$ and $\delta \ll 1$, which means that the real part of the reflective index is less than 1.

Total reflection will occur at a grazing angle of θ_g measured off the surface plane and given by:

$$\cos \theta_g = 1 - \delta \quad (1.5)$$

or

$$\theta_g = \sqrt{2\delta} \quad (1.6)$$

but due to β , reflection at this angle will not be total.

By combining 1.6 and 1.4, for heavy elements with $\frac{Z}{A} \sim 0.5$, we get:

$$\theta_{g(arcmin)} = 5.6\lambda_{(A)} \rho_{(g/cm^3)}^{1/2} \quad (1.7)$$

and for gold:

$$\theta_g = 25_{(arcmin)}\lambda_{(A)} \quad (1.8)$$

This angle is equivalent to the critical angle, θ_c where total internal reflection will occur. As θ_c is the ratio of the refractive indices of the two materials:

$$\theta_c = \frac{n_2}{n_1} \quad (1.9)$$

at X-ray wavelengths this angle will be the point at which total external reflection will occur as n_2 is slightly less than 1.

The Fresnel equations give the amplitude reflection coefficients as[16]:

$$r_{\parallel} = \frac{Z_2 \cos \theta_2 - Z_1 \cos \theta_1}{Z_2 \cos \theta_2 + Z_1 \cos \theta_1} \quad (1.10)$$

and

$$r_{\perp} = \frac{Z_2 \cos \theta_1 - Z_1 \cos \theta_2}{Z_2 \cos \theta_1 + Z_1 \cos \theta_2} \quad (1.11)$$

where r_{\parallel} and r_{\perp} are the polarisation of the ray and Z is the complex impedance given by:

$$Z = \frac{C\mu}{n} \quad (1.12)$$

The reflectance of a ray is given by $R = r^2$, at normal incidence $\theta_1 = \theta_2 = 0$ and taking the real parts, R becomes:

$$R = \left(\frac{n_1 - n_2}{n_1 + n_2} \right)^2 \quad (1.13)$$

At X-ray wavelengths and with $n_1 = 1$ (within a vacuum), R is incredibly small which leads to no reflection at normal incidence angles. The rays which are transmitted do not get bent as they pass through the medium and so cannot be focused.

Scalar scattering theory in Beckmann and Spizzichino[35] describes the scattering of rays from randomly rough surfaces.

$$\frac{1}{I_0} \frac{dI_s}{d\omega} = \frac{2\pi F^2 \alpha}{\lambda^2} \exp(-g) \sum_{m=1}^{\infty} \frac{g^m}{m!} \int J_0(V_{xy}\tau) \cdot C^m(\tau) \tau d\tau \quad (1.14)$$

where I_0 is the totally reflected flux, I_s is the scattered flux, ω is the scattering solid angle, J_0 is the 0th order Bessel function, C^m is the auto correlation function and

$$F = 1 + \frac{\phi}{2\alpha} \quad (1.15)$$

where ϕ is the scattering angle in the plane of incidence given by:

$$\phi = \frac{\lambda}{d \sin \alpha} \quad (1.16)$$

and d is the particular spatial wavelength of the surface roughness. From equation 1.14:

$$g = \left(\frac{2\pi}{\lambda} \sigma (2\alpha + \phi) \right)^2 \quad (1.17)$$

and

$$V_{xy} = \frac{2\pi}{\lambda} \left(\left(\phi \left(\alpha + \frac{\phi}{2} \right) \right)^2 + \epsilon^2 \right)^{\frac{1}{2}} \quad (1.18)$$

and σ is the RMS surface roughness and ϵ is the scattering angle perpendicular to the plane of incidence. Solving for equation 1.14 gives the ratio between the amount of reflected flux and the scattered flux given an RMS surface roughness.

$$\frac{I_s}{I_0} = 1 - \exp \left(- \left(\frac{4\pi\sigma \sin \alpha}{\lambda} \right)^2 \right) \quad (1.19)$$

The same results can be obtained using vector theory as described in Rice[36]. At small grazing angles, $\sin \alpha$ becomes θ_g and so equation 1.19 becomes the Total Integrated Scatter (TIS) and is used to calculate the 1st order diffraction.

$$TIS = 1 - \exp \left(- \left(\frac{4\pi\theta_g\sigma}{\lambda} \right)^2 \right) \quad (1.20)$$

where σ is the RMS surface roughness and θ_g is the grazing angle, at a wavelength λ . Using the exponential expansion, equation 1.20 becomes

$$TIS \simeq \left(\frac{4\pi\theta_g\sigma}{\lambda} \right)^2 \quad (1.21)$$

This is a first order approximation and gives the percentage of the rays that are scattered due to the surface roughness of the optic. In order to not be dominated by scattering, this value must be kept below $\sim 10\%$.

Figure 1.8 shows the change in reflectivity as a function of energy (top) and of surface roughness (bottom) calculated using the CXRO[2] website. A nickel

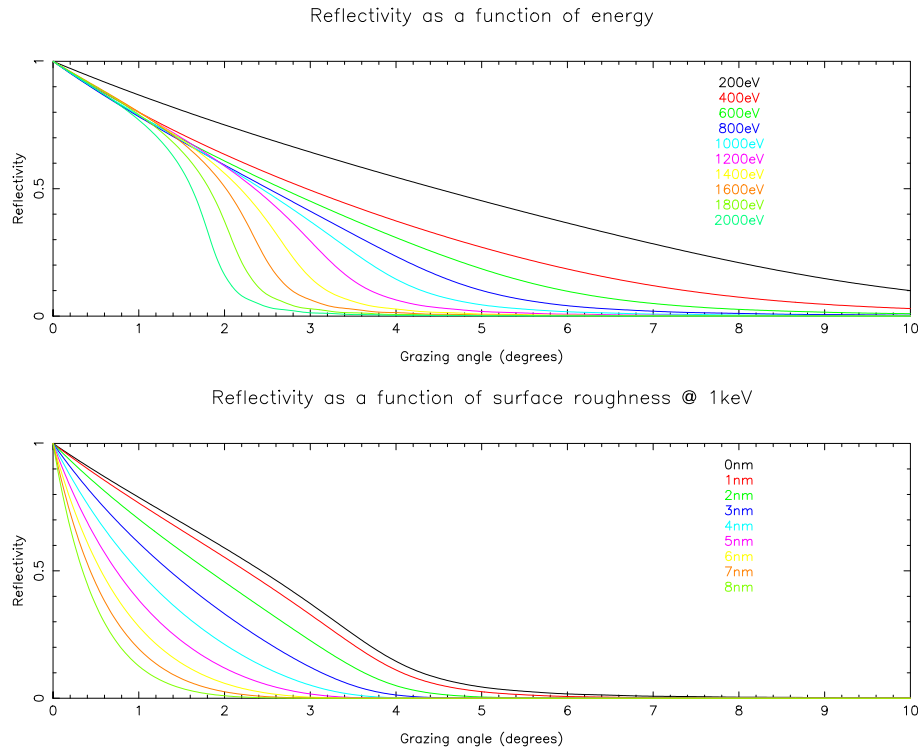


Figure 1.8: The change in reflectivity of a nickel substrate with a $30\mu m$ gold layer on the surface, as a function of energy and surface roughness at various grazing angles. These graphs were calculated using the Centre for X-ray Optics website[2].

substrate with a $30\mu m$ gold layer on the surface was modelled to demonstrate the effect on the reflectivity at various grazing angles as described above. The reflectivity of a given material would be a sharp cut off but the absorption of the material, as given by β smoothes the curve as shown in figure 1.8.

1.5 Current modelling products for X-ray optics

Many software packages exist designed to model either X-ray wavefronts or provide ray-tracing from a specified source. Some have been designed for a specific purpose whilst others are modelling packages which have a facility to model mirrors or lenses with a reflective surface of a user defined design. There have also been many methods used for computing the ray's path from the source.

SHADOW is a ray-tracing program and was created for the XUV optics range but was extended in 1986 to be more general[37]. SHADOW simulates the photon flux in a synchrotron radiation beam line and can trace up to 5,000 rays with satellite programs analysing the data produced. Each ray is given a starting position and

direction, it will then either hit the optic and be reflected or miss it completely and move on to the next surface. All settings within the program, e.g. surface type and quality, source type etc. can be set by the user allowing for accurate models to be created. Outputs created include a cross section of the beam along the length of the beam line, position of the focus, vignetting and mirror illumination. X-ray Oriented Programs (XOP) is a front end interface for synchrotron radiation programs used to model X-ray sources, optical devices and analysis of data[38]. It is often used with SHADOW to expand the functionality and provide data analysis of the results from SHADOW. As these programs were specifically designed for synchrotron radiation sources, they were not capable of simulating all of the situations required for this project and so were not used in this instance.

J. Bahrtdt from Bessy[39] has developed software called PHASE, which uses ray-tracing for the first estimation and “physical optic code” for detailed beam studies in order to model X-rays through a synchrotron detector. The models follow a process of creating the X-ray sources, defining the beam-line, tracing the rays and producing a graphical representation of the rays. Once the graphic output has been checked for consistency the system switches to the physical optic and models the wavefront propagation and produces a final graphic output of the wavefront’s path. In order to model the wavefronts, the amplitude, phase and energy of each wave is calculated and a Fourier Transform method is completed to calculate the path. Diffraction effects on long mirrors in grazing incidence geometry are not exactly simulated and as the grazing incidence angle is required to model X-ray telescopes, the software was not suitable for this application.

PHASE was adapted in order to model the transverse coherence properties of X-ray beams in 3rd generation synchrotron radiation sources[40]. The wavefront propagation is calculated using the propagation of the EM field and specifically the electric field. In order to complete this, the probability of the field being at a specific point along the path is calculated (using ray-tracing) and then summed to produce the most probable propagation of the wavefront. Spectral coherence in the soft X-ray region was used for testing the model.

A commercially available product called ZEMAX[41] uses a function called Physical Optics Propagation, which models the wavefronts via ray-tracing but only models

rays from a defined source in a specific direction and does not allow the interaction of an optic with the rays from the source or simulated detector output.

Another commercially available product is Oslo Premium[42] which computes the wavefronts in several ways depending on which method the program decides is the best for the situation described by the user. The optics are designed by the user who specifies the size, radius, aperture size, number of apertures, tilt etc. as well as the surface of the optic. The program works with lenses and not mirrors, although the lens can be designed to have a reflective surface thus creating a mirror. The outputs created from the data include the amplitude, phase and intensity of the waves after interaction with the optic. There is only a small catalogue of lenses available and thus a system such as a Wolter 1 mirror would have to be designed and created from scratch. This would be a very long process for modelling X-ray telescopes and also does not include the response from a detector.

For the purposes of modelling piezoelectric actuators, the best program to use is COMSOL Multiphysics[43] as it allows source and surface creation, and the changes to the surface due to the actuators to be modelled. It demonstrates the changes to the surface by ray-tracing the EM field from the source to the surface. Although this is perfect for modelling the effects to a surface, it is not a suitable program to model the surface interaction with the wavefronts on to a detector.

None of the systems or products described above provided the necessary facilities to accurately model and describe the optics via interactions with X-rays. For this reason, in-house software called Q was used for the purposes of modelling both of the adaptive X-ray optics.

Q has been developed by R. Willingale, Dept. of Physics and Astronomy, at the University of Leicester. By using the sequential ray-tracing code in Q, the optics behaviour as it interacts with X-rays at different wavelengths can be modelled and studied. Q works by taking each ray individually and calculating the angles and direction of the ray after reflection, based on the optic type and surface. Different forms of calculation can be selected so that either counting statistics or reflectivity look-up tables can be used and probability functions are used to allow for non-reflected rays and rays which do not reach the detector. In Q the user specifies the size, direction and type of the optic, source and detector to enable them to

be modelled. The optic is described by setting the type, axis, normal, the radius of curvature if required, and surface type and quality. The source can be either infinite or finite and the detector can be any size and shape. The detector within the program is not a specific type and just produces an image of the rays which have reached its position. Deformation matrices can be used to alter the shape of the optic, source or detector and can be created by, and then read in from, an external source or calculated within Q. Using these values, the software can predict how the X-rays will react with the optic and therefore what results would be seen by a detector. Plots can be produced showing the X-rays interacting with the surface, the detected image, detected distribution, a profile of the detected image, histogram of the point or line spread function or the positions of the rays as they exit the optic. Using this software, extremely accurate models and predictions can be created for almost any optic. Routines can be added to the software in order to model any new optic, mirror or device design needed.

1.6 Thesis overview

The work contained and described within this thesis outlines the work completed at the University of Leicester. Chapter 2 describes the processes employed to produce the first large scale adaptive X-ray prototype, including design, production, metrology, modelling and testing of the optic. Chapter 3 outlines the development of the small scale optic, focusing on the theory, modelling and preliminary reflectivity tests carried out. Finally chapter 4 gives the summaries, conclusions and future work of the project and the work described within this thesis.

CHAPTER 2

DESIGN, MODELLING AND TESTING OF THE LARGE ADAPTIVE X-RAY OPTIC PROTOTYPE

2.1 Chapter overview

An X-ray telescope with a better angular resolution combined with a larger collecting area than that currently available is required in order to study the regions of the Universe under extreme conditions in detail, such as Active Galactic Nuclei (AGN), black holes and neutron stars. This is the aim of NASA's Generation-X mission for which new technology needs to be developed to achieve the required resolution of 0.1" and a collecting area of $50m^2$ [44]. The aim of the Large Adaptive X-ray Optic (LAXRO) is to investigate whether the angular resolution and the figure quality of the surface of a standard X-ray mirror could be improved by the addition of piezoelectric actuators, in order to provide in-situ manipulation of the reflecting surface.

This chapter outlines the design, production and testing of the LAXRO. The first section of this chapter, section 2.2 gives an introduction and background to X-ray telescopes. Section 2.3 describes the processes used to design the prototype optic and the LAXRO design is outlined in section 2.4. Production of the optic is described in section 2.5, including mirror manufacture and the mounting designed and produced for the prototype during the X-ray tests. Metrology of the optic along with modelling and simulation of the piezoelectric actuators is described in sections

2.6, 2.7 and 2.8 respectively. The Tunnel Test Facility (TTF), which was used to carry out the X-ray tests, is outlined in section 2.9 and the X-ray test procedures and results are detailed in sections 2.10 and 2.11. Further metrology and modelling based on the results is outlined in sections 2.12 and 2.13 with the summaries and conclusions of the chapter given in section 2.14.

The work described in this chapter has been published in the conference proceedings, journals and articles described in the publications section.

2.2 Introduction and background to X-ray telescopes

Emissions from regions of the Universe under extreme conditions, such as temperature and pressure in AGN, black holes etc., are best studied at the X-ray wavelengths. The X-rays emitted by astronomical sources may be either thermal radiation, produced by gas at temperatures above $10^6 K$, or non-thermal radiation in the form of high-energy electrons interacting with either a magnetic field or with low energy photons[21]. An example of this form of radiation is in binary star systems where the accretion of matter on to a compact object, such as a black hole, neutron star or white dwarf, releases energy at X-ray wavelengths[45]. X-ray telescopes enable the study and analysis of these high-energy regions and provide a view of the most violent areas of the Universe. Current X-ray telescope technology has enabled us to look deeper into space, further back in time and as close as $\sim 90km$ from the event horizon of a black hole. However, if we are to solve some of the fundamental questions of the evolution of the Universe, the sensitivity and resolution of space based telescopes needs to be improved.

X-ray telescopes are described by their collecting area and their resolution; the larger the collecting area, the further back in time we can view the Universe as more photons can be collected from dimmer objects and the better the resolution of the optic, the easier it is to distinguish between individual objects and the sharper the image. These two features are not independent of each other as a telescope with a large collecting area would suffer from source confusion if it did not have a high angular resolution. A very large collecting area combined with high angular

resolution would provide a very high sensitivity to distant sources.

As the Earth's atmosphere absorbs X-rays, telescopes looking at this region have to be launched and operated in space and this was first suggested by Giacconi et al. in 1960[46]. Launch weight limitations and the cost of launch, \$50,000/*kg*, restricts the mass and therefore the collecting area of any telescope put into space. In order to create a telescope with an improved angular resolution than that currently available and to increase the collecting area of the optics, thinner lighter mirrors are being developed. These mirrors are easily deformed by gravity and handling, as well as the severe conditions imposed during launch. In-situ manipulation of the surfaces of the mirrors would allow these deformations to be removed and thus improve the angular resolution and overall functionality of the telescope.

In order to answer some of the most fundamental questions of the evolution of the Universe, new technologies need to be developed. The large scale application is geared towards developing possible technologies to create a telescope with an increased collecting area and an improved angular resolution.

The current telescopes, Chandra and XMM-Newton, have resolutions of $\sim 0.5''$ [47] and $\sim 12-13''$ [48] respectively. Planned future telescopes, such as NASA, ESA and JAXA's combined International X-ray Observatory (IXO)[49] and NASA's Generation-X mission[50], hope to reach angular resolutions of $\sim 5''$ and $\sim 0.1''$ respectively and collecting areas of over $3m^2$.

There are four main types of X-ray telescope, Kirkpatrick-Baez and Wolter types 1, 2 and 3. A Kirkpatrick-Baez telescope consists of two orthogonal reflecting surfaces to create a double reflection and was suggested in 1948[3]. To increase efficiency and reflecting area, a grid of these plates can be used (figure 2.1) and the efficiency can be improved further still if the plates have a parabolic shape. However, focusing X-rays in this way does have a few problems such as small aperture, poor resolution and geometric aberrations.

In 1952 Wolter[51] produced a study of concentric figures of revolution, such as paraboloids, hyperboloids and ellipsoids, and showed that to achieve a true image over an extended field of view, the X-rays must undergo double reflections from either paraboloid/hyperboloid or paraboloid/ellipsoid combinations. A Wolter 1 (figure 2.2 a)) telescope has two surfaces of revolution, normally a paraboloid followed by

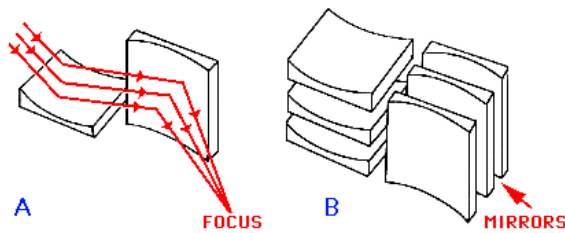


Figure 2.1: a) A Kirkpatrick-Baez telescope and b) a grid of K-B plates[3].

a hyperboloid and the collecting area can be increased by having nested shells, like the XMM-Newton telescope[48]. Wolter 2 telescopes have a paraboloid shell with a hyperboloid block behind the mirror shells, as shown in figure 2.2 b). These are not as widely used as Wolter 1 as they cannot be nested due to the design of the hyperboloid, which limits the collecting area of the telescope. A Wolter 3 telescope (figure 2.2 c)) consists of a paraboloid surface followed by an ellipsoidal surface but as with the Wolter 2 geometry, it is very difficult to nest this form of telescope and so it has a restricted collecting area.

2.2.1 A brief overview of past and present of X-ray telescopes

The Sun was the first object in astronomy to be imaged using an X-ray telescope on a V2 rocket, in 1949[52], as it was found to have a strong X-ray signal which could be measured and the first X-ray images of the sky were taken in 1962 by rocket-borne telescopes[53]. High Energy Astronomy Observatories (HEAO) were designed to be the first specific X-ray devices launched by NASA. The first HEAO-1, which was launched in 1977, was designed to study and survey the X-ray sky over a range of $0.2keV$ to $10MeV$. The mission lasted eighteen months and detailed readings of a few objects were taken over three to six hour periods. HEAO-2, which was renamed the Einstein X-ray Observatory, was launched in 1978 as the first imaging X-ray mission[54] and had a resolution of $\sim 1'$ [53] and a collecting area of $200cm^2$.

Many developments have occurred in the harder X-ray region ($10keV$ to $80keV$), however, this thesis is concerned with the softer region ($0.1keV$ to $10keV$) and associated telescopes. Since the Einstein X-ray Observatory, there have been several X-ray missions including ROSAT (Roentgensatellit) and EXOSAT (European Space

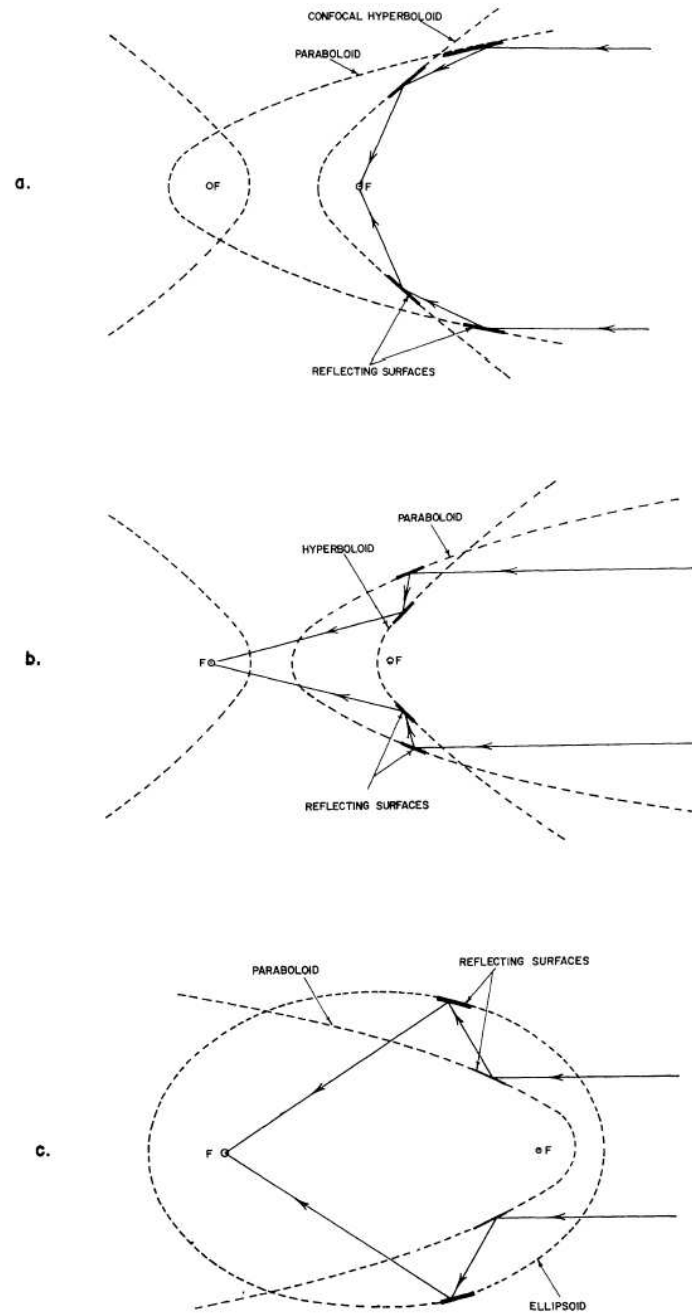


Figure 2.2: Different forms of Wolter telescopes a) type 1, b) type 2 and c) type 3[4].



Figure 2.3: The XMM-Newton satellite during the solar array deployment test at ESTEC, Netherlands[5].

Agency's X-ray Observatory) and the most recent are described below.

2.2.1.1 XMM-Newton

The XMM-Newton telescope was launched on December 10th 1999 by ESA as a complementary optic to Chandra[48]. The XMM-Newton telescope consists of three X-ray mirror modules formed by fifty eight nested Wolter 1 shells. The outer diameter of the shells is 700mm and the mirrors were formed by electroplating nickel of between 0.66mm and 0.9mm thickness on to a highly polished ceramic mandrel. The mandrel was coated with a thin layer of gold to create the reflective surface, onto which the nickel was electroplated and the shell was removed by thermal shock. The satellite is 11m in length, 4m in diameter and the solar array powering the satellite has a span of 16.1m and a total weight of 4tons , making it the largest satellite ever built by ESA. Figure 2.3 shows an image of the XMM-Newton satellite during the solar array deployment tests at ESTEC, Netherlands. It is the most sensitive instrument within the energy range of 250eV to 12keV . At 1.5keV , the collecting area of the telescope is 1650cm^2 making it almost four times the size of Chandra. The angular resolution of the telescope is $\sim 12\text{-}13''$, therefore the detail of the images is much less than that of Chandra (figure 2.5), but it can take pictures of objects further back in time and carry out spectroscopy.



Figure 2.4: An artist's impression of the Chandra X-ray Observatory in operation[6]

2.2.1.2 Chandra

The Chandra X-ray telescope was launched by NASA on July 23rd 1999 by a space shuttle[47] and an artist's impression of the Chandra X-ray observatory is shown in figure 2.4. The mirrors are the largest, smoothest and most accurately formed X-ray mirrors ever manufactured. The images produced improved the quality of previous images by up to 25% in both detail and sharpness (see figure 2.5). The telescope is 13.8m in length and is powered by two solar arrays with a total span of 19.5m each and its original lifespan was only 5 years but this has been extended and it is still fully operational. The telescope itself is made up of 4 nested Wolter 1, 833mm long, zerodur shells with the inner mirror coated in 600Å of iridium and the others coated in gold. This creates a collecting area of 400cm² at 2keV to 5keV and 800cm² below 2keV[55]. The average angular resolution of the telescope is 0.5" with a pointing accuracy of 30", 99% of the time, which is achieved by removing the known variation in pointing from the images.

2.2.2 The future of X-ray telescopes

There has always been a trade off between angular resolution and collecting area, however, the aim of future missions is to combine the two to create highly sensitive optics.

2.2.2.1 The International X-ray Observatory (IXO)

Both ESA and NASA planned mid resolution, moderate collecting area X-ray telescopes with the aim to be launched in ~ 2020 , XEUS (X-ray mission for Evolving

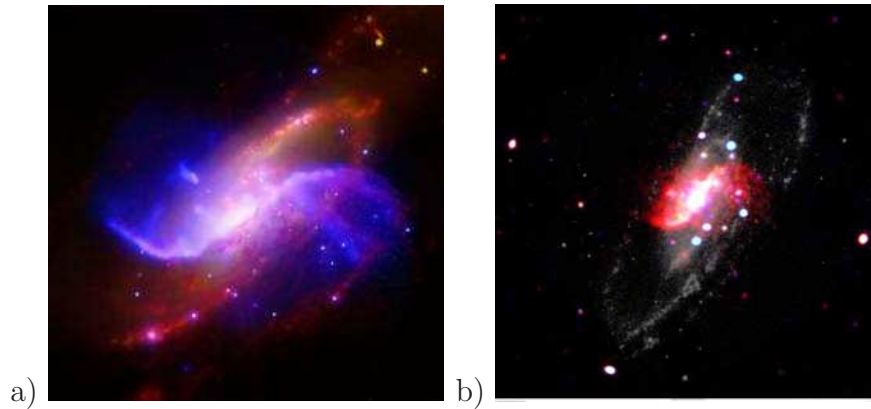


Figure 2.5: a) An image created by combining optical data and X-ray data from Chandra of NGC4258[7] and b) an image of NGC4258 taken by XMM-Newton[8]. The detail is much less than that seen in a).

Universe Spectroscopy) and Constellation-X respectively. However, both realised that the requirements for the telescopes were almost identical and although they would be made in very different ways, it would be beneficial to combine the two efforts and incorporate the JAXA (Japan Aerospace Exploration Agency), to create the International X-ray Observatory (IXO). To date, the schematics and optical design for IXO have yet to be confirmed but it is likely to be either slumped glass, Wolter 1 nested shells, or silicon pore optics in a Wolter 1 approximation (see section 2.2.3). The aims of IXO are to create a telescope with a $3m^2$ collecting area, a twenty fold improvement on XMM-Newton, an angular resolution of $5''$ and to be launched ~ 2021 [56]. The main drive is the increase in collecting area which will enable the study of super massive black hole evolution and objects up to a redshift of $z=6$. It is likely that IXO will be operated on an extendable boom, as was designed for Constellation-X, opposed to two separate spacecraft, which was planned for XEUS.

2.2.2.2 Beyond IXO

After IXO, NASA are planning an ambitious project, called Generation-X[57], to create an X-ray telescope with an angular resolution of $0.1''$ and a collecting area of $50m^2$. With this collecting area, so many sources would be visible that a resolution of $\sim 0.1''$ would be essential in order to differentiate between them. Generation-X would be a huge improvement in both collecting area and resolution. In order to

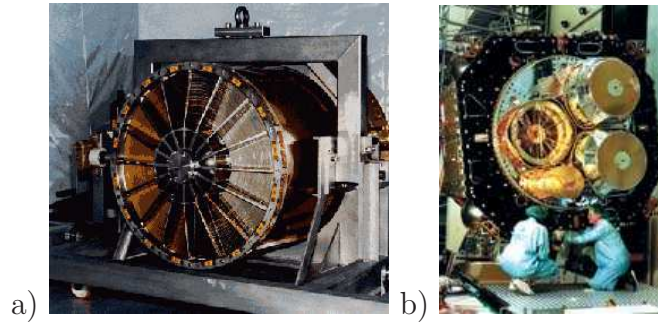


Figure 2.6: The XMM-Newton telescope modules. It consists of three mirror modules with each module containing fifty eight nested Wolter 1 mirrors. The mirrors are gold coated, electroformed nickel with varying radii and thickness. a) A single mirror module[9] and b) the three mirror modules being installed[10].

create such a telescope many suggestions have been made, but a large majority have included adaptive/active optics. This is the aim of the SXO consortium; to investigate this form of technology. If such a telescope could be created then it would be possible to detect and study the first black holes, stars and galaxies[58] at redshifts beyond $z=6$. In order to be able to detect the first black holes at a redshift of $z=15$, a flux sensitivity of $3 \times 10^{-20} \text{ erg cm}^{-2} \text{ s}^{-1}$ is required, which can only be achieved with a collecting area of 50 m^2 and an angular resolution of $0.1''$. The hunt for the missing baryon mass could also be achieved with this type of telescope as well as detailed study of stellar formation and galactic evolution. Using such a telescope would greatly reduce observing times and therefore more people could access the data and use the telescope to perform vital research to significantly increase our understanding of the evolution and origin of the Universe. Long observations of single objects such as supernovae explosions and Gamma Ray Bursts (GRBs) could also be carried out without interrupting other observing programmes.

2.2.3 Methods of X-ray telescope fabrication

In the past the majority of X-ray telescopes have been built using two different methods. One is to electroform the mirror shells from a material such as nickel, whilst the other is to use high precision glass, which is ground to form. ESA's XMM-Newton mission consisted of three telescope modules, each containing fifty eight nested Wolter 1 mirror shells, as shown in figure 2.6[59]. These shells were produced using ceramic mandrels and electroformed nickel. Ceramic mandrels were

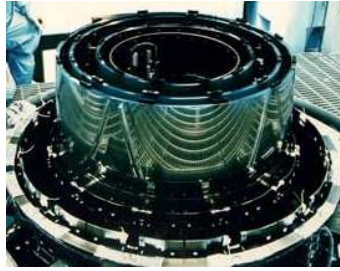


Figure 2.7: The four nested glass mirrors of NASA's Chandra X-ray observatory. These were produced by grinding large pieces of zerodur ceramic to the precise form and then coating the inside with an X-ray reflective coating, iridium. The zerodur ceramic used for the mirrors is so thick that the number of nested shells is restricted[11].

ground to high precision to create high quality surfaces, which were coated in a vacuum deposited layer of gold and placed in the electroforming bath. The nickel was electroformed onto the gold coating and the shell, once completed, was removed by cooling both the shell and the mandrel. Due to the different temperature coefficients of the ceramic and nickel, the shell easily popped off the mandrel. In order to prevent too many handling deformations, the mirror had a series of small holes drilled along the edge and was lifted off the mandrel using a suspended wire frame. A nickel mirror with a gold coating, which is flat to $\sim 10\text{\AA}$ and has an accurate form, is left. Finally the mandrel was cleaned and could then be reused. This method creates thin nickel shells with accurate forms which can be nested (figure 2.6) thus creating a large collecting area. The gold coating acts as both a release layer and a reflective coating to improve the reflectivity of the mirrors. This process was also used to create the mirrors on NASA's Swift telescope, which is a three instrument device designed to detect and monitor Gamma-Ray Bursts (GRBs)[60]. The X-ray Telescope (XRT) on Swift is a Wolter 1 telescope with a collecting area of 135cm^2 at 1.5keV , an angular resolution of $18''$ and operates in the range of 0.2keV to 10keV .

The other method to produce the mirrors is to grind zerodur ceramic very precisely into the required shape, and then apply a reflective coating such as gold or iridium. These mirrors tend to be very thick and so only a few shells can be nested, reducing the collecting area. An example of this form of telescope is NASA's Chandra X-ray observatory[61] which consists of four nested zerodur mirrors, shown in figure 2.7. These mirrors have been produced so precisely that Chandra has an average angular resolution of $0.5''$, the best angular resolution achieved in X-ray

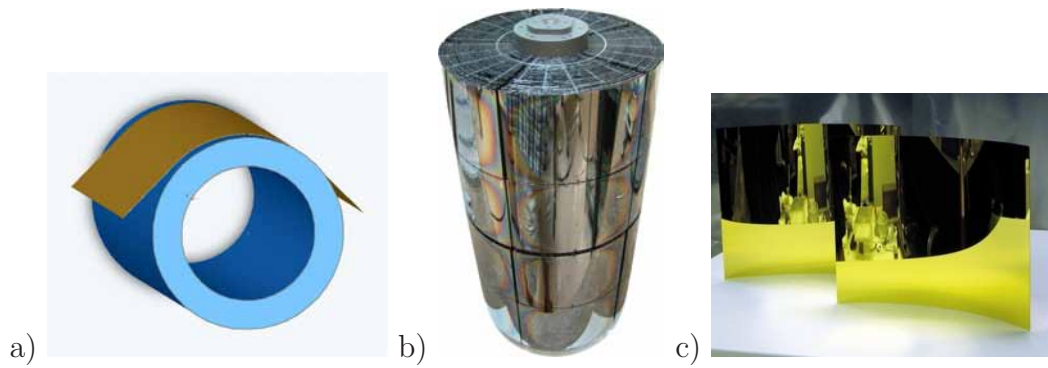


Figure 2.8: The glass slumping technique utilized by GSFC, USA. a) A sheet of 0.4mm thick commercially produced glass is thermally slumped over a quartz mandrel. b) An engineering model of NuSTAR where cylindrical glass slumped mirrors are mounted to approximate parabolic and hyperbolic segments to create a Wolter 1 telescope. c) Two completed glass segments after slumping and trimming. These mirrors have been coated with gold but in the case of NuSTAR, the mirrors are coated in iridium. Images provided by GSFC.

astronomy to date.

Due to the cost and weight restrictions of launching telescopes, new methods of producing X-ray mirrors are being developed. In recent years, a few institutions in America[62] and Italy[63] have started working on glass slumping. Glass slumping is where a sheet of commercially produced glass is thermally slumped over a quartz mandrel. The sheet is then trimmed to create thin glass segments which can be combined in order to create full shells. Usually, a hyperbolic segment and a parabolic segment are created separately and then mounted in pairs to create a Wolter 1 geometry. The sheets used for slumping are usually around 0.4mm thick or less, so it is easy to create nested shells and thus increase the collecting area of the telescope whilst reducing the mass. It is hoped that by using this method a combination of a large collecting area and high angular resolution could be achieved. This was the aim of NASA's Constellation-X mission (figure 2.8), however, it has now been combined with ESA's XEUS mission to produce the International X-ray Observatory (IXO).

The Nuclear Spectroscopic Telescope Array (NuSTAR), a high energy X-ray telescope being developed at CalTech, USA and the University of Columbia, USA, will consist of slumped glass mirror segments produced at Goddard Space Flight Center (GSFC), USA. The mirror segments are conic sections which are mounted into a Wolter 1 approximation. NuSTAR will be the first focusing high energy X-ray mission to look at black holes, supernovae explosions and AGN. It will operate

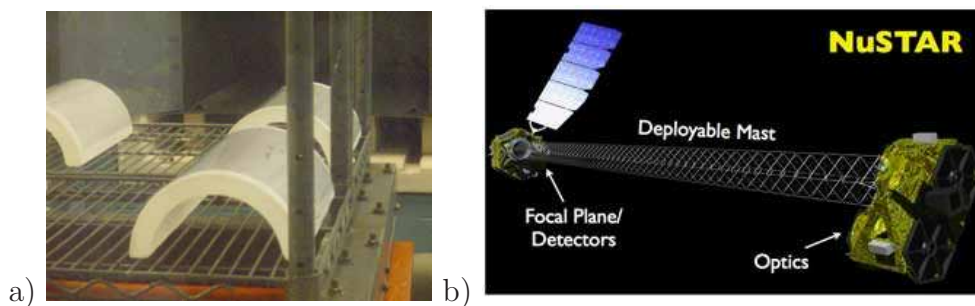


Figure 2.9: a) Glass slumping at GSFC for the NuSTAR mission. b) An artist's impression of the NuSTAR extendable deployment mast and optics[12].

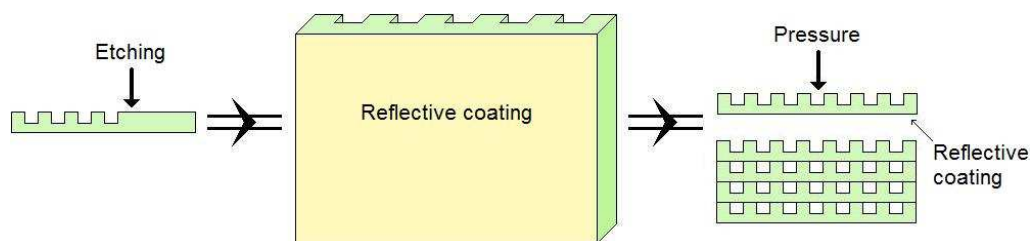


Figure 2.10: Construction of silicon pore optics. A sheet of silicon is etched or cut to create channels. The reverse side of the sheet is then coated in either gold, iridium or a multi-layered coating. Multiple sheets are then stacked and compressed to cold weld them together which creates silicon pore optics with a large collecting area. The silicon channels are coated in a layer of SiO_2 which is etched to taper the sheets to approximate a Wolter 1 geometry, thus creating an effective X-ray optic.

in the energy range of 6keV to 79keV and should achieve a resolution of $\sim 1'$ over a 10m focal length. It is due to be launched into a low Earth orbit in August of 2011[12]. Figure 2.9 shows an artist's impression of NuSTAR and glass sheets being thermally slumped at GSFC, whilst figure 2.8 b) shows an engineering model of the telescope.

Another developing technology is the use of silicon pore optics, which were planned for ESA's XEUS mission[64]. Sheets of silicon are etched or cut to create a series of channels and a layer of SiO_2 is applied which is etched to taper the sheets to approximate a Wolter 1 geometry. The reverse side of the sheet is then coated with either gold, iridium or a multi-layered coating to create a reflective surface. The reflective surface is then cold welded to the top of the channel walls to create square, silicon pores (figure 2.10). A very large collecting area can be achieved with this method.

Another form of X-ray telescope technology is the Micro Channel Plate (MCP)

which have been used as detectors in previous missions (e.g. Chandra), but are now being used as X-ray focusing devices for the Bepi-Colombo mission to Mercury[65]. The MIXS-T and MIXS-C instruments on Bepi-Colombo will use the fluorescence emission of Mercury's surface, due to the interaction with X-rays produced by the Sun, to create a complete map of the elements on the surface. MCPs are created by forming tubes of glass with a square profile and a soluble support core, which are then drawn out and stacked. The stack is then drawn and stacked and cut to create 1.5mm thick plates containing $\sim 10^7$ precise square pores[66]. The pores are coated with iridium to provide reflections at various energies. These plates are then mounted as a tandem pair to provide double reflections. By slumping the plates it is possible to approximate a Wolter 1 geometry but with a reduced mass, as the MIXS-T optics will weigh just 2kg , in comparison the XMM-Newton optics weighed $\sim 1000\text{kg}$.

2.3 Design of the first large scale prototype optic

2.3.1 Background to the initial design requirements

In order to remain within the weight limit but at the same time increase the size of telescopes, thinner, lighter mirrors or shells are required. Unfortunately, these are prone to deformations and distortions due to gravity, handling and the stresses and excessive vibrations of launch conditions, all of which can damage and distort the mirror and compromise the angular resolution. One solution is to create an optic capable of active adjustment to overcome and correct the deformations introduced during manufacture and launch whilst maintaining a large collecting area. Active alignment of the telescope's various components would also be achievable thus improving the overall performance of the telescope.

The LAXRO, which is at an initial stage of development, is aimed at providing the necessary active X-ray optics to realise future telescopes such as the Generation-X concept. The design, modelling and testing of the LAXRO was completed at the University of Leicester (UoL); manufacture of the mirror was completed at University College London (UCL); the mounting for the optic during the X-ray tests was designed and engineered at the Mullard Space Science Laboratory (MSSL) and the

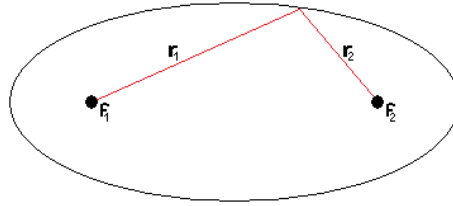


Figure 2.11: An ellipse with two foci f_1 and f_2 . A ray produced at f_1 , and reflected off the inside surface of the ellipse, will be focused at f_2 .

piezoelectric devices were designed and manufactured at the School of Metallurgy and Materials at the University of Birmingham (UoB).

2.3.2 Ellipse theory

Traditionally, X-ray telescopes utilise two reflections off consecutive conic sections (paraboloid and hyperboloid in the case of a Wolter 1 telescope, section 2.2). An ellipse is a very basic example of a single reflection surface telescope. As an ellipse has two foci, if a ray or source is placed at one focus, and is reflected off the inside of the ellipse surface, then a perfect image will be formed at the other focus (see figure 2.11). This is because the sum of the angles from the tangent to the rays always equal a constant i.e. $a + b = c$.

Ellipses are conic in shape and have an eccentricity of less than 1 and in the case of a circle, the eccentricity is 0. The quadratic equation to describe an ellipse is given by equation 2.1

$$ax^2 + bxy + cy^2 + dx + ey + f = 0 \quad (2.1)$$

but it can also be paramatised as shown below. For example, the radii from the two foci add to give double the semi-major axis and the semi-major and semi-minor axes can be used to give the eccentricity, e , as shown in equation 2.2:

$$e = \sqrt{1 - \frac{B^2}{A^2}} \quad (2.2)$$

and

$$r_1 + r_2 = 2A \quad (2.3)$$

where A and B are the semi-major and semi-minor axes respectively. Although integration should be used to find the circumference, a good approximation can be

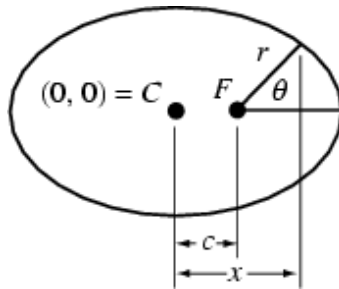


Figure 2.12: An ellipse with centre C and focus F

found by using

$$Circumference \simeq 2\pi \sqrt{\frac{A^2 + B^2}{2}} \quad (2.4)$$

The radius of the ellipse (as shown in figure 2.12) can be found using the angle from the semi-major axis to a point on the ellipse and using the equation

$$r = \frac{A(1 - e^2)}{1 + e \cos \theta} \quad (2.5)$$

This can then be used to give the x and y positions of the point on the ellipse and is demonstrated in figure 2.12.

$$x = C + r \cos \theta \quad (2.6)$$

$$y = r \sin \theta \quad (2.7)$$

The x and y positions can also be found using the semi-major and semi-minor axes.

$$\frac{x^2}{A^2} + \frac{y^2}{B^2} = 1 \quad (2.8)$$

Equation 2.8 was utilised to define the radii of curvature and vertical position of the prototype based on its location within the testing facility.

An ellipsoidal segment can be produced by turning an ellipse into a surface of revolution and by using such a segment, a simple single reflection, point-to-point focusing device is formed. The above equations were used to design the first prototype optic and therefore create a simplified example and test of an adaptive X-ray optic with the application of piezoelectric actuators to provide in-situ manipulation of the optical surface. As only one surface was used i.e. a single reflection, only on-axis rays were focused but this simplified the design of the mirror of the first prototype and testing of the optic.

2.4 Large scale prototype optic designs

The initial concept was to take a standard X-ray optic, apply piezoelectric devices to it to actively manipulate the reflecting surface and then examine the effects. In order to simplify the initial test concept, it was decided that the first mirror would be an ellipsoidal segment to provide a single reflection, point-to-point, focusing device. If the X-ray source and the detector of the testing facility, are placed at each of the foci of the ellipse and the mirror is a section of that ellipse, then the X-rays produced at the source will be focused at the detector (see section 2.3). The optic's size and shape was governed by the size of the testing facility and the position of the access flanges in the TTF. The TTF is a 28m long X-ray beam line within UoL with an X-ray source, capable of producing energies in the range of 0.1keV to 100keV, and an MCP detector. Along the length of the beam line is a series of access flanges to allow for easy mounting of optics. A full description of the testing facility can be found in section 2.9. The LAXRO was placed close to the detector to allow easy installation, which made the optic asymmetrical and in order to make manufacture of the mirror easier but retain a larger surface area, the axis of the ellipse was tilted compared to the axis of the TTF. This required the detector position to be raised in the Z direction by 141.06mm in order to detect the reflected beam, but allowed the semi-minor axis of the ellipse to be increased and thus the ellipsoidal segment to be flatter and closer to a cone in form.

Approximately 4m away from the detector are three access flanges spaced 0.5m apart and to accommodate a reasonable distance between the optic and the detector, the optic was sited at the second access flange. Although the optic was not placed in the facility via the flanges, access was required for the piezoelectric actuator electronics and controls. The optic was designed to be placed in the central flange, as this would allow easy access to the optic from the other two flanges and also room for manoeuvre if the optic's form was not quite to specification. The geometric design of the mirror was carried out by the author at UoL by using the equations described in section 2.3.2 and the dimensions of the TTF, the ellipse parameters were calculated and are shown in table 2.1.

Parameter	Value
Optic width (radial)	100mm
Optic length (axial)	300mm
Ellipse semi-major axis	14145mm
Ellipse semi-minor axis	228mm
Distance of the optic from the detector (centre of travel)	4402.5mm
Radius of curvature at the front of the optic	169.8mm
Radius of curvature at the rear of the optic	165.3mm
Grazing angle	1.163°
Sagittal distance from a cone	0.03mm

Table 2.1: A table showing the ellipsoidal segment dimensions for the first prototype optic. The semi-major and semi-minor axes of the ellipse are governed by the dimensions of the TTF. The optic was very close to a cone in form as can be seen by the sagittal difference between a cone and the optic. The level of asymmetry can be seen in the difference in the radii of curvature at the front and the back of the optic. The grazing angle achieved allowed energies up to $\sim 5keV$ to be focused during the tests.

2.5 Production of the large scale optic

The ellipsoidal segment was manufactured in a similar way to the production of the XMM-Newton mirror shells. The mirror was produced by electroforming a nickel shell using a mandrel of inverse form. The mandrel was designed (figure 2.13 a)) and produced at UCL by taking a solid block of aluminium which was milled to the correct form (figure 2.13 b)) and was then coated with a $100\mu m$ layer of kanigen, a nickel alloy. This made it easier to hand polish the surface to the correct figure with low surface roughness ($\sim 2nm$), as shown in figure 2.13 c). The mandrel was designed with a series of wasters to avoid curving of the edges due to the polishing process. As kanigen is a nickel alloy, to prevent the nickel bonding directly to the kanigen and to allow easy release of the mirror after electroforming, a passivation layer was required. As the nickel would bond directly to the release layer, it needed to be a material with a high X-ray reflectivity such as gold (as used in XMM-Newton) or iridium (Chandra). Gold was selected as it was shown to be both an effective release layer and would reflect a high percentage of X-rays. To create the release layer, a $30nm$ layer of gold was vacuum deposited onto the mandrel's surface prior to the electroforming process. The processes used to create the mandrel are displayed in figure 2.13.

UCL are able to electroform small segments and mirrors in an in-house facility

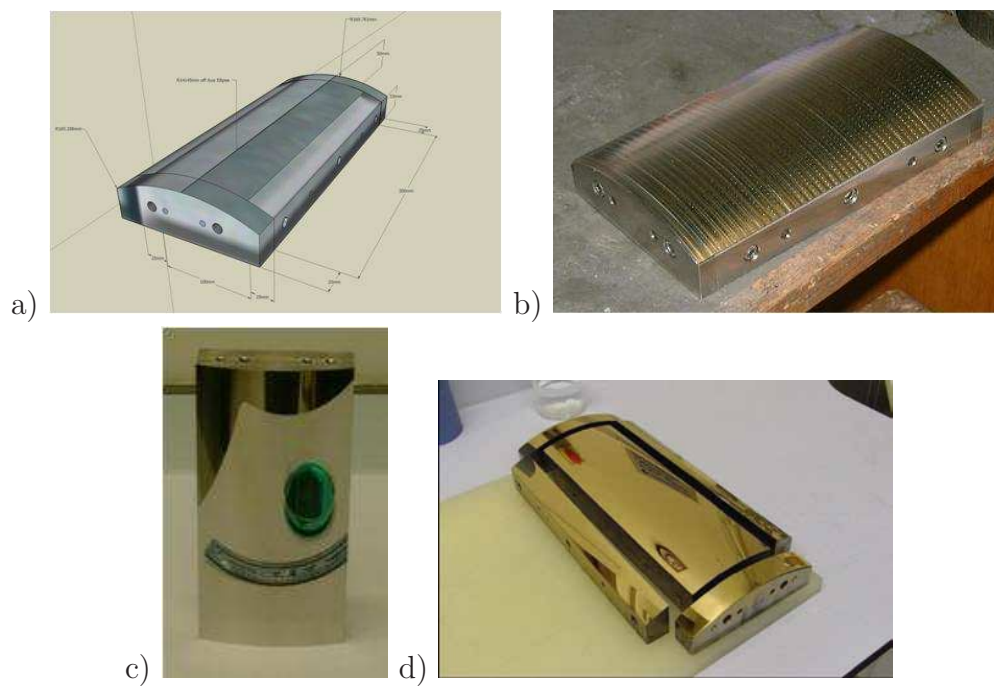


Figure 2.13: The production of the mandrel for electroforming the optic. The mandrel was designed to have wasters which can be removed to improve the consistency of the thickness of the nickel and to prevent rounding of the edges due to grinding and polishing. a) The mandrel's schematic before manufacture which was cut from a block of aluminium and coated in a $100\mu\text{m}$ layer of kanigen and then ground to form by hand. b) The mandrel after it had been milled to the rough shape required. c) The mandrel after polishing and d) the mandrel after the 30nm gold layer has been deposited, shown with the wasters detached. Images provided by UCL.

which is approximately $0.6m \times 0.6m \times 1m$ tall and is shown in figure 2.14 b). Due to the electron currents within the tank, the shell was thicker towards the edges than in the middle. Several methods exist to reduce this problem, the mandrel can be rotated during electroforming, wasters can be used to increase the size of the shell and the edges can then be removed after replication, or a sacrificial electrode can be used. Due to the size of the facility at UCL, spinning the mandrel would have been difficult so wasters and a sacrificial electrode were used. COMSOL Multiphysics was used to calculate the electron currents within the tank to optimise the thickness of the mirror. Extra electrodes were placed around the mandrel in order to attract the thicker nickel deposits to the edges which could then be removed with the wasters. The electroforming process is displayed in figure 2.14.

Several initial cylindrical nickel prototype optics of varying thickness were produced, with a radius of curvature of $154mm$, and size $200mm$ by $100mm$, slightly smaller than the full elliptical prototype. The purpose of these pre-prototypes was to investigate the electroforming process and the techniques required to bond the piezoelectric devices to the mirror. Figure 2.15 shows one of the cylindrical pre-prototypes after replication and with a few actuators bonded onto the back.

Full details of the manufacture processes of the mirror are described in “Future high-resolution X-ray telescope technologies: prototype fabrication methods and finite element analysis” by Atkins et al.[67]. This method produced a gold coated, nickel, ellipsoidal segment of $100mm \times 300mm \times 0.4mm$ thick.

The School of Metallurgy and Materials at UoB investigated and produced curved piezoelectric actuators to reduce the stress on the optic due to bonding (section 2.5.1). Thirty curved piezoelectric actuators were attached to the reverse side of the mirror, to provide the active adjustment of the surface. To bond the actuators to the mirror, low shrinkage glue of $\sim 0.1\%$ was used to further reduce the stress due to bonding and to prevent print-through, where the shape of the device can be seen on the mirror’s reflecting surface. Unfortunately the radius of curvature of the piezoelectric actuators did not completely match the radius of curvature of the optic. In order to prevent air bubbles from forming under vacuum and to ensure that the entirety of each actuator was attached to the optic, the gaps were filled with excess glue. Figure 2.16 a) shows the reverse side of the optic after the actuators

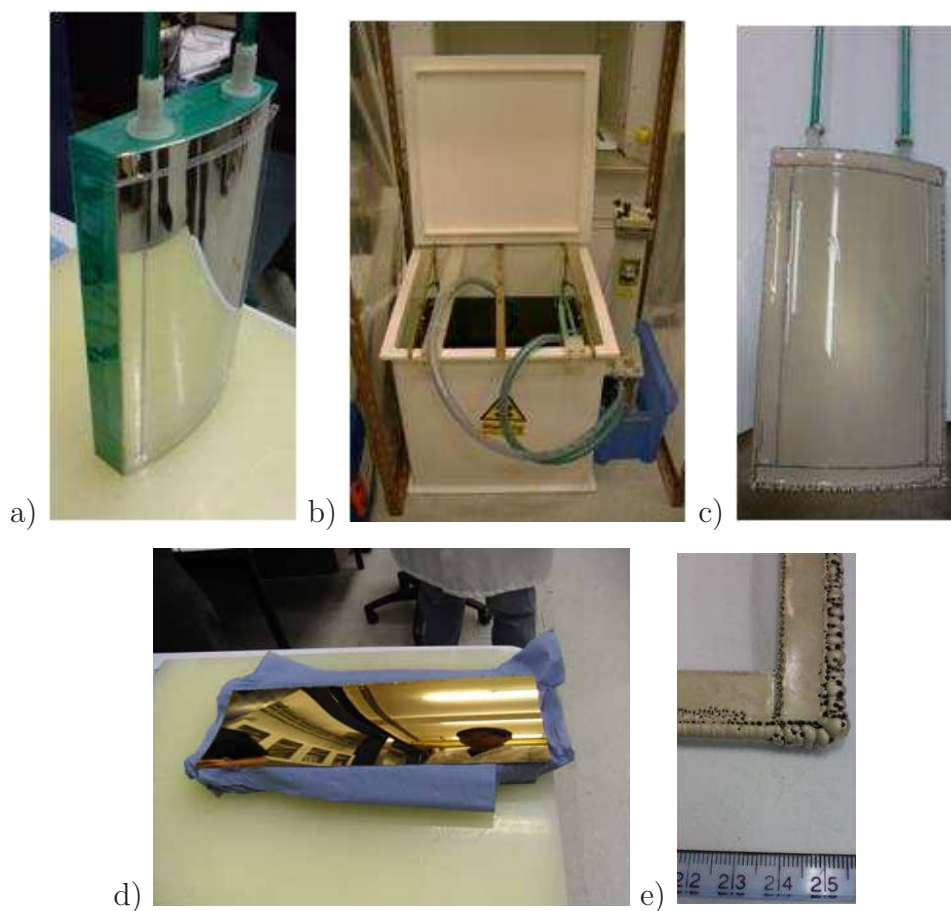


Figure 2.14: The production technique of the LAXRO by electroforming. a) The mandrel was prepared before the electroforming by placing non conducting tape between the gaps of the wasters and main body of the mandrel to enable the removal of these areas after electroforming. Tape is also placed around the outside of the mandrel to prevent electroplating in these regions. b) The in-house electroforming tank at UCL, approximately $0.6m \times 0.6m \times 1m$ tall. c) The optic and mandrel once they had been removed from the tank after the electroforming process had been completed. d) The optic once it had been removed from the mandrel. e) The areas which were plated over the wasters can easily be removed. It is clear that this area is thicker and contains a lot of air bubbles. Images provided by UCL.

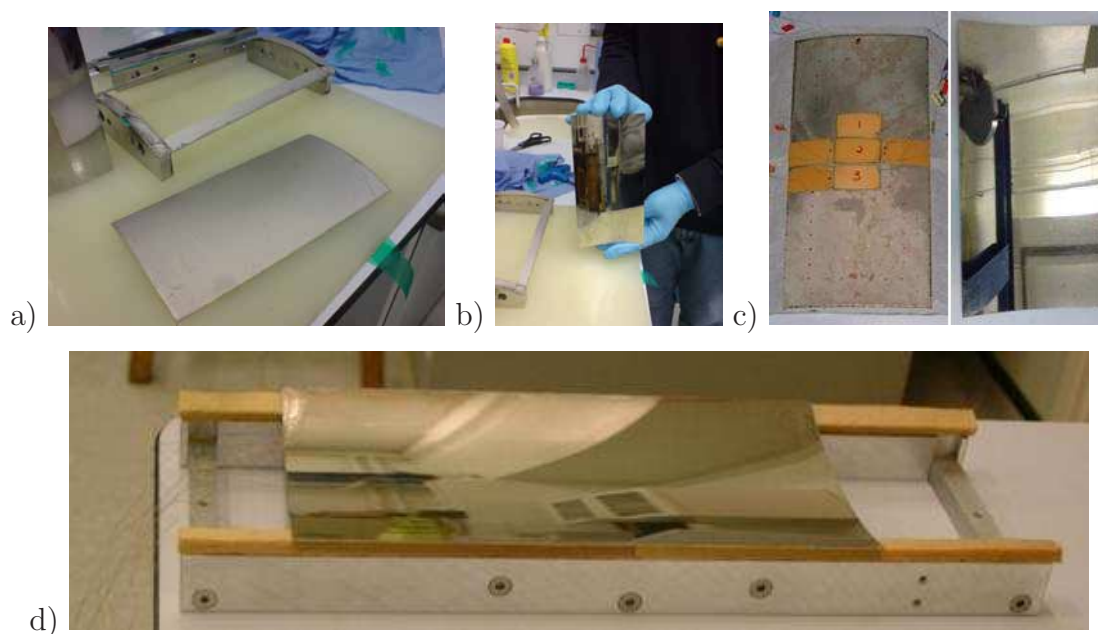


Figure 2.15: One of the pre-prototype replicated segments. a) The segment after replication shown with the wasted section which was removed after electroforming. b) The pre-prototypes reflecting surface shown with some damage from cleaning. c) The pre-prototype front and back with a few piezoelectric devices attached. d) The pre-prototype sitting on the aluminium frame showing the difference in size between the pre-prototype and the first elliptical prototype optic. Images provided by UCL.

were attached. The thirty piezoelectric actuators were numbered in sequence and the piezoelectric device number is shown with the thickness of that actuator. The thicknesses of the devices ranged from $165\mu\text{m}$ to $265\mu\text{m}$ but is not known for all the actuators and some required resputtering to the outer surface (where the gold coating is reapplied). The top three rows of piezoelectric devices used were produced for the cylindrical pre-prototype optics. Due to the error margins in the radii of curvature of the actuators, these actuators had a very similar radius of curvature to one end of the elliptical prototype mirror and so could be used over a small section of the optic. In figure 2.16 b), the attached piezoelectric actuators have been harnessed where all the electrodes for the piezoelectric devices have been soldered and wired up to the 32-pin connector, which was then connected to the actuator control system. The actuator electrodes were harnessed along the gaps between the piezoelectric devices to limit and reduce the thickness of the composite mirror as the aim of the project is to create a thin adaptive X-ray optic. The composite mirror, optic, variable glue layer and the actuators, is approximately 1mm thick, comparable to the thicker XMM-Newton shells.

2.5.1 Piezoelectric actuators

The School of Metallurgy and Materials at UoB fabricate their own piezoelectric actuators; both piezoelectric plates and Active Fibre Composites (AFCs)[30][31]. The production of curved piezoelectric actuators was investigated, to reduce the stress on the optic during and after bonding, and were designed to match the radius of curvature of the large scale prototype. The surface quality of these actuators is better than those that are currently commercially available, which further reduced the effect of print-through on the optical surface. Thirty curved piezoelectric actuators were bonded directly to the back of the ellipsoidal nickel shell in a ten by three arrangement.

The adhesives used to bond the piezoelectric devices were required to be of extremely low shrinkage ($<1\%$), because shrinkage can easily warp and damage the optic's surface and cause print-through. In the past this problem has been solved by the use of UV curing adhesives, however, UV curing was not practical for the prototype design because both of the bonding surfaces were opaque. Conductive glue

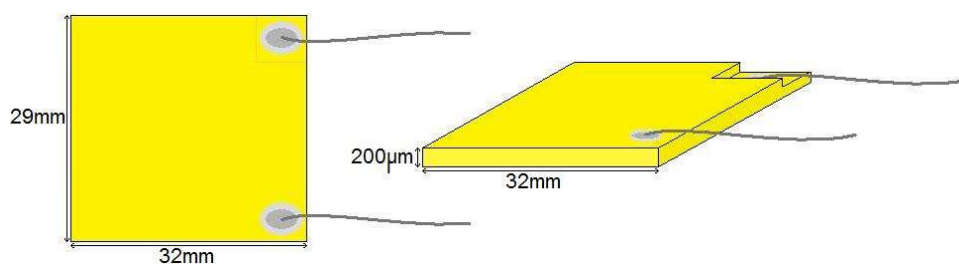


Figure 2.17: The piezoelectric devices for the first elliptical prototype were $32\text{mm} \times 29\text{mm}$ and are $\sim 200\mu\text{m}$ thick. They were coated in gold to create a conducting surface. The piezoelectric actuator is shown with the two electrodes attached, one is the ground wire whilst the other provides the voltage for the movement. The ground wire is accessed by removing a small amount of the top layer in one corner.

was also not required because the piezoelectric plates produced by UoB provided access to the base electrode directly, as a small section of the top surface is removed (figure 2.17). Several curved piezoelectric actuators were developed (as shown in figure 2.18) with the same cylindrical profile as the pre-prototypes, to investigate various types of adhesives and the thickness of the glue layer. The thickness of the glue was controlled by mixing glass beads, with a diameter of $80\mu\text{m}$, in to the glue to act as spacers. One of the pre-prototype optics was cut in to sections after several piezoelectric devices had been bonded in order to study the quality of the bonding between the optic and the actuators. Figure 2.19 shows the cross section (taken with an SEM at UoB) of the optic, glue layer, and the actuator, with some of the glass beads visible within the glue layer. The bonding between the actuators and the mirror was reasonably consistent and the thickness of the glue was also quite regular. Some areas of the mirror appear to have bonded slightly better, but overall the bonding was quite successful.

For the first elliptical prototype design, the thirty piezoelectric devices were roughly square in shape, 32mm by 29mm , to give almost the same amount of movement in both directions. The size of the actuators was determined by the need to allow for a $\sim 1\text{mm}$ gap in between each of the piezoelectric devices. Although the gaps were predicted to and were shown to cause junction effects on the mirrors surface (see section 2.6), the low shrinkage glue and shape of the piezoelectric devices limited the effect. FEA modelling at UoB determined the optimum thickness of the piezoelectric devices to be $200\mu\text{m}$, in order to give the maximum amount of

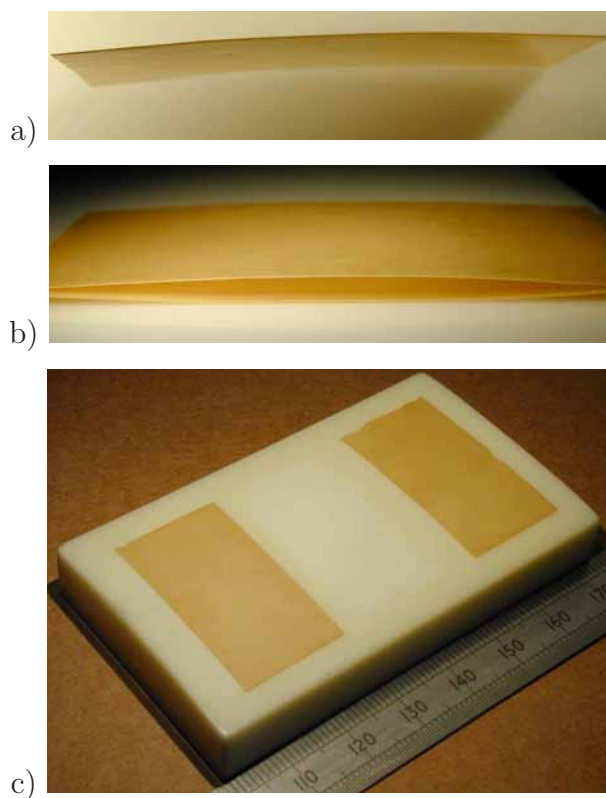


Figure 2.18: a) and b) show curved piezoelectric actuators. c) The piezoelectric devices have been curved over a former with the correct radius of curvature. By using pre-curved piezoelectric devices, it was hoped that print-through and stress on the optic could be reduced. Normally a conductive glue is required to access the bonded electrode, however these piezoelectric actuators have access to the electrode as a small section of the top surface is removed. Low shrinkage glue was also used to prevent print-through. Images provided by UoB.

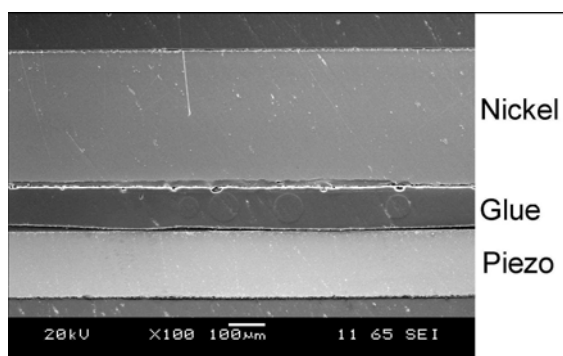


Figure 2.19: A cross section taken through one of the pre-prototype mirrors showing the optic thickness, glue layer and the actuator. Within the glue layer, several $80\mu\text{m}$ diameter glass beads are visible which were used as spacers to control the glue thickness. This image was taken using an SEM at UoB.

movement of the nickel, thicker than this restricted the actuator's movement due to stiffness whilst thinner reduced the effect of the actuator. Figure 2.17 shows the dimensions of the piezoelectric devices and also shows the two electrodes which were attached to the actuator, where one was the ground electrode whilst the other provided the voltage to the actuator. The electrodes used were $100\mu m$ thick enamelled copper wire, which were soldered to the actuators post cure using indium solder, as it bonds to both copper and the gold surface of the actuator and has a low melting point.

The thirty piezoelectric devices were operated by a high voltage amplifier which in turn was controlled by a computer. The controller provides a $10V$ range from $-5V$ to $+5V$, with the common ground set to $+5V$, which was then amplified by twenty to create the voltage range of $-100V$ to $+100V$. The electrodes were harnessed to the back of the optic using vacuum compatible acrylic tape and were attached to a 32-pin connector which connected directly to the actuator controller (figure 2.16).

2.5.2 Mounting of the optic

A structure to support the mirror during the X-ray and metrology tests was designed jointly at MSSL and UCL. The support structure consisted of three individual sections which were connected together. The first section was designed at UCL and supported the optic along its axial edges which allowed it to move as the piezoelectric devices were actuated. It consisted of a simple rectangular aluminium frame, the edges of which were coated in foam developed for space missions and created by Upilex®[13]. This allowed for the movement of the mirror, due to the piezoelectric devices, without restriction, whilst still providing the support needed. Details of the specification and manufacture of this section of the mounting can be found in Atkins et al.[67].

The schematic and manufactured frame are shown in figure 2.20. The optic was supported along the axial edges as it was shown, through FEA modelling performed at UCL, that this would create the minimum axial distortion, due to gravity and stress, on the optic.

The second section of the mounting attached to the base of the first section and contained the micrometers for the pitch and yaw (θ and ϕ in figure 2.48) adjustments

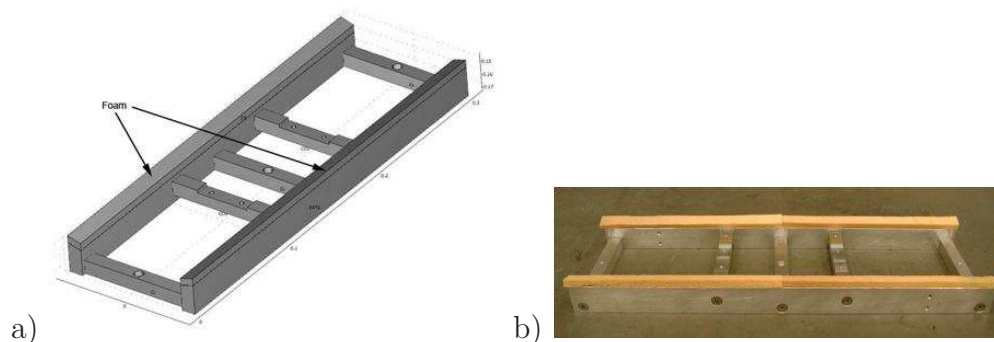


Figure 2.20: a) The schematic of the frame and b) the completed aluminium frame for the optic support during the tests. The optic rested along its axial edges as this was shown to produce the least amount of axial distortion on the optic. The edges of the support structure were coated with vacuum compatible foam produced by Upilex®[13], as this provided the support required, whilst still allowing the piezoelectric devices to operate without restriction. Images provided by UCL.

of the optic. This section was also used to manoeuvre the optic to the correct position within the tunnel which was passed down the facility from the clean room at the detector end to the required position within the pipe. Plastic skis were placed on this section of the mount to enable the support structure to be moved down the pipe without damaging the optic, micrometers or the pipe and to keep the optic balanced in the centre of the pipe. The final section attached to the base of the second section of the support structure and supported the entire structure off the access flange. Three height adjustable support legs attached to the flange and raised the structure off the skis and into the correct position within the pipe. The flange had connectors attached to be able to connect the electronics for both the piezoelectric actuators and the micrometers to the computer control system. A CAD diagram of the structure can be seen in figure 2.21 and figure 2.22 shows the finished mounting and how it was built up.

As the optic was only supported along the axial edges by the support structure, the mirror sagged slightly due to gravity. This error introduced to the mirror was removed by adjusting the height of the support legs and therefore the radius of curvature of the ellipsoid. This process was completed during the alignment of the optic within the TTF and required an adjustment of approximately $1mm$.

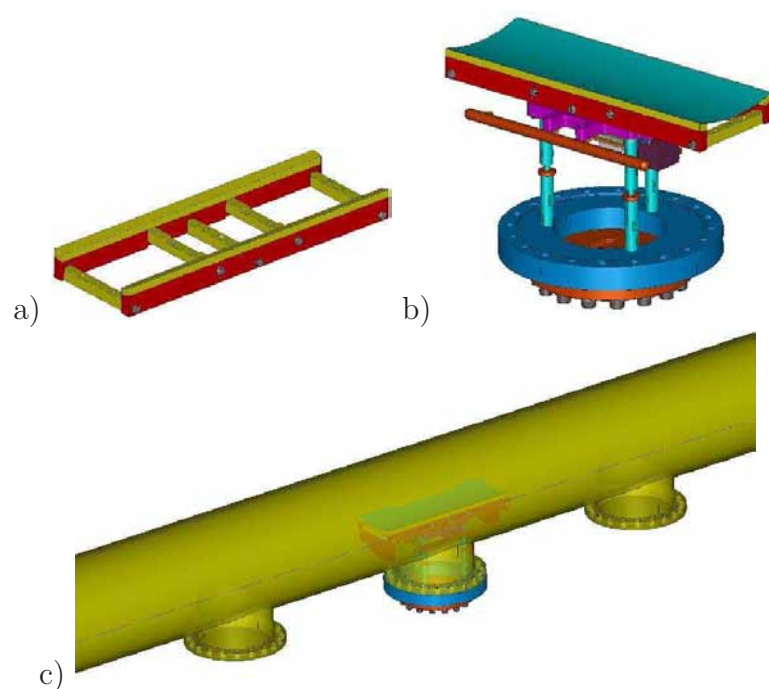


Figure 2.21: a) The optic support structure developed by UCL. Space foam is placed along the axial edges of the support to allow support but also allow full movement as the piezoelectric devices are actuated. b) All three sections of the support structure assembled together with the optic and attached to the flange. c) The full structure within the TTF above the flange. Images provided by MSSL.

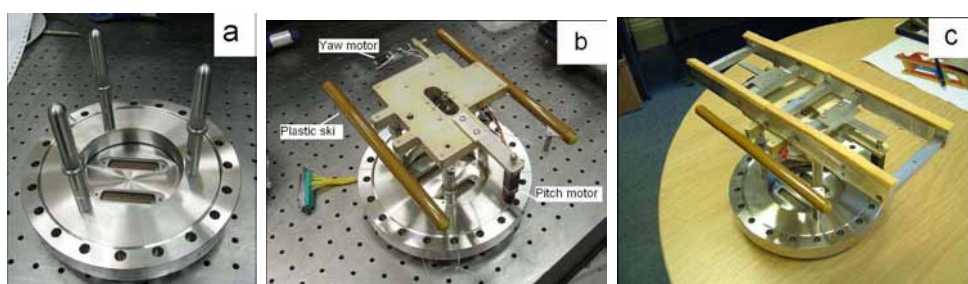


Figure 2.22: The finished support structure. a) The lower section of the mount with the three height adjustable support legs. These were attached to the flange and raised the rest of the structure off the edges of the pipe. The flange provided the connection between the micrometers, the piezoelectric devices and the computer control. b) The flange section attached to the micrometre section with the plastic skis which supported the optic whilst it was passed down the facility. c) The entire mounting with the soft mount attached. Images provided by MSSL.

2.6 Metrology of the large prototype optic

A series of metrology tests were carried out on the prototype optic and mandrel at both STFC Daresbury Laboratory and UCL, before the X-ray testing. Prior to the shell replication, Wyko measurements of the mandrel's surface were taken at UCL, these gave an indication of the expected surface roughness for the mirror as it was found that an electroformed shell will replicate approximately double the surface roughness of the mandrel. A Wyko interferometer uses white light instead of a laser, and matches the paths of the various wavelengths to create the interference fringes. The short coherence length results in a good contrast in fringes if the two paths are close in length and there is no ambiguity in the fringe order number[68].

The cylindrical mandrel, made from polished stainless steel, was tested first and the elliptical mandrel, made from polished kanigen, was tested subsequently. Kanigen was found to be easier to polish and this was reflected in the higher quality of the surface finish. The Wyko measurement of the cylindrical mandrel, figure 2.23, showed an RMS surface roughness of around $\sim 4nm$ which lead to an optic with an RMS surface roughness of between $\sim 6nm$ and $8nm$. The elliptical mandrel was also tested in the same way and was found to have an RMS surface roughness of $\sim 2nm$ (figure 2.24). This was deemed to be sufficient for the first series of tests, although in order to keep the total integrated scatter (TIS) to a few %, the surface should have an RMS roughness of $\sim 1nm$ or less.

$$TIS = 1 - \exp\left(-\left(\frac{4\pi\theta_g\sigma}{\lambda}\right)^2\right) \quad (2.9)$$

As described in section 1.4, equation 2.9 describes the percentage of rays which are scattered by an RMS surface roughness of σ , at a grazing angle of θ_g and wavelength λ . Using this equation, at $1keV$, a grazing angle of 1.163° (table 2.1) and an RMS roughness of $2nm$, 15.58% of rays would be scattered. To reduce this to below 10% at the same wavelength and grazing angle, the RMS surface roughness would need to be less than $1.5nm$. With a surface roughness of $4nm$, $6nm$ and $8nm$, the TIS would be 49.2%, 78.2% and 93.3% respectively making it essential to reduce the RMS surface roughness to prevent the X-ray images being dominated by scatter.

The Long Trace Profiler (LTP) at STFC Daresbury Laboratory was used to

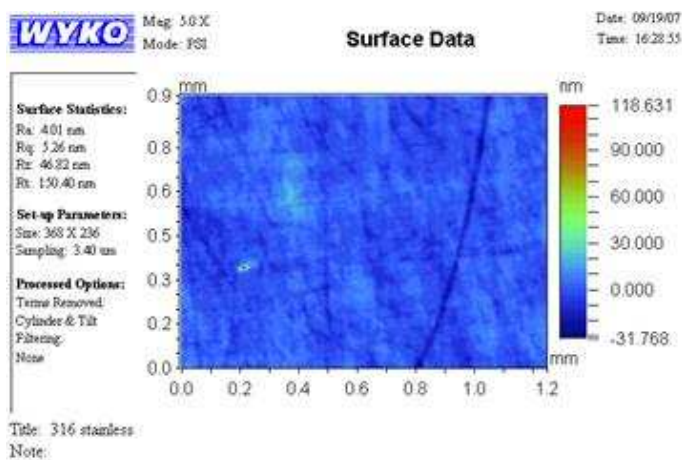


Figure 2.23: The Wyko data of the cylindrical stainless steel mandrel provided by UCL. Over this small region, the surface was found to have an RMS surface roughness of $\sim 4\text{nm}$. This was replicated on to the optics surface, giving a surface roughness of $\sim 6\text{nm}$ to 8nm .

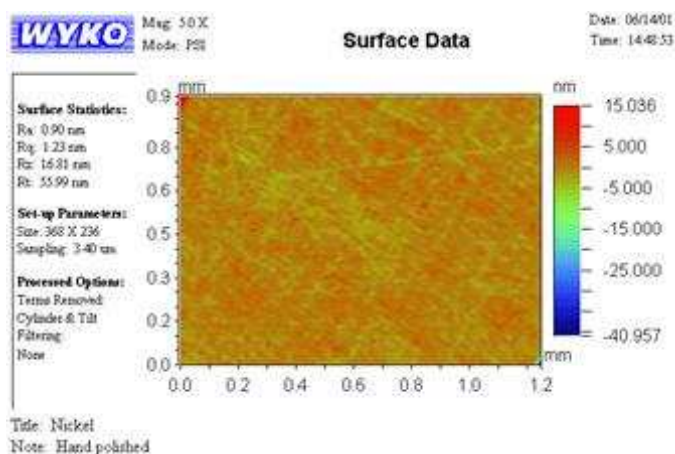


Figure 2.24: The Wyko data of the elliptical kanigen mandrel provided by UCL. Over this small region, the surface was found to have an RMS surface roughness of $\sim 2\text{nm}$. This was replicated on to the optics surface and gave a surface roughness of $\sim 4\text{nm}$ to 6nm . This was an improvement on the cylindrical mandrel, and deemed sufficient for the first series of tests.

measure the profile of the mandrel, the mirror shell after release but before the attachment of the piezoelectric actuators and finally the mirror after the actuators had been bonded. These measurements were then used to assess the quality of the electroforming and the degradation introduced by the attachment of the piezoelectric devices.

The LTP is an optimized non-contact profiling instrument, which measures the slope and the absolute surface figure of mirrors with very large radii of curvature[14] and is based on the principle of the pencil beam interferometer developed by von Bieren[69]. The local slope profile along the length of a mirror is measured by the change in the angle of a reflected laser beam and the only criterion for measurability of an optic is that the reflected beam from the test surface reaches the optical system to be focused on the detector. The LTP is most commonly used to measure the accuracy of the large mirrors with large radii of curvature used in synchrotron radiation sources to focus the beam. The tolerances on the synchrotron mirrors are such that the LTP can measure less than $1\mu rad$ slope error on the surface of the mirror.

Figure 2.25 demonstrates how an LTP works, where an optical head is moved along a translation stage across the length of the mirror. A laser is split into a pair of collinear beams which are then split again into two pairs by a polarising beam splitter (PBS). One pair is directed into the reference beam arm (REF) and the other is directed to the test surface arm (SUT). Once the beams have been reflected from the test and reference surfaces, both sets are directed back into the optical head and into a Fourier Transform lens. This then focuses the beams onto the linear detector array, creating two sets of interference fringes. The difference between the positions of the minima is a direct measure of the slope of the surface. Figure 2.26 shows the inclusion of a Dove prism in the reference beam arm to remove any measurement errors due to static sag of the translation stage due to gravity, and dynamic sag caused by the shifting load of the moving optical head. In the LTP at STFC Daresbury Laboratory a Pentaprism is used instead of a Dove prism to achieve the same goals.

The measurements are extremely sensitive to the temperature fluctuations of the surrounding atmosphere which causes a slow drift of fringe position of several

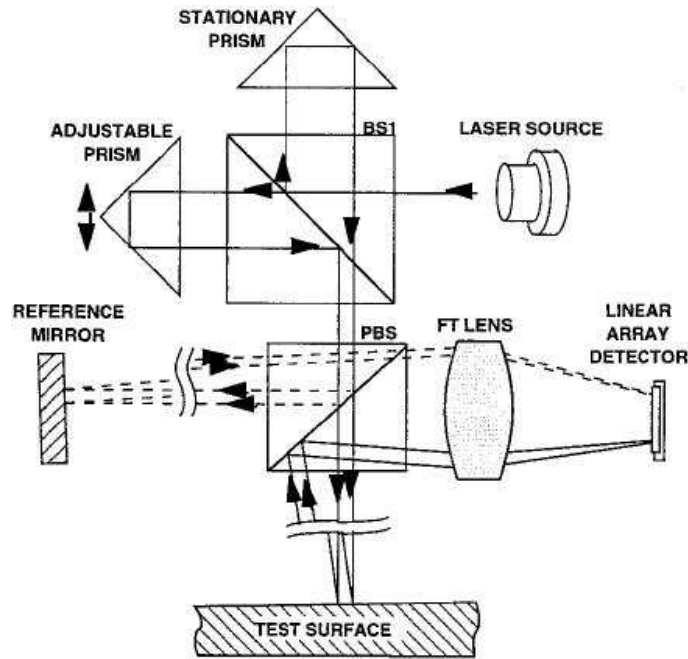


Figure 2.25: Operation of a Long Trace Profiler (LTP). A Laser beam is split into two pairs of collinear beams. One of the pairs is directed through the reference arm and reflected back by the reference surface, whilst the second pair are directed towards the test surface and reflected back into the optical head. Once the beams have been reflected, they are focused onto a linear array detector by a Fourier Transform lens, creating two sets of interference fringes. The separation of the minima gives a direct measure of the slope error on the mirror[14].

micro radians over time periods of minutes to hours. Temperature fluctuations are reduced by mounting the LTP within a sealed unit where the temperature and atmosphere can be controlled using sensors. Errors induced by vibrations are removed by mounting the LTP on a solid granite block which is placed on legs, which in turn are resting on solid concrete foundations. Figure 2.27 shows the optic with piezoelectric devices attached to the back, set up on the LTP. The optic was set up on the aluminium frame, designed for the X-ray tests on top of the granite table.

Due to the high radii of curvature of the mandrel and prototype optic compared to the curvature of the synchrotron mirrors, limited axial strips of the surfaces were taken and then stitched together to approximate the surface form.

The mandrel was tested first; sixteen axial strips were measured, along 290mm and approximately 6.25mm apart, across the surface and are shown in figure 2.28. It was found that the mandrel's profile was close to the theoretical form in terms of the maximum displacement, however it was misaligned leading to a hump having been

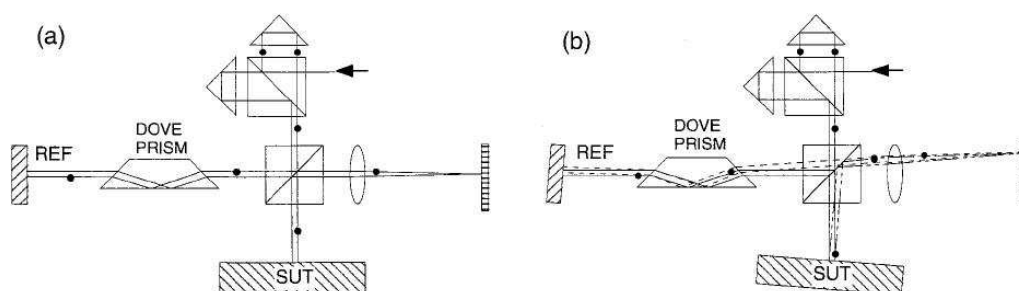


Figure 2.26: a) and b) operation of a Long Trace Profiler with the addition of a Dove prism. The Dove prism removes the mechanical errors introduced by the static sag of the translation stage due to gravity and the dynamic sag due to the optical head moving along the translation stage[14]. The LTP at STFC Daresbury utilises a Pentaprism for the same purpose.

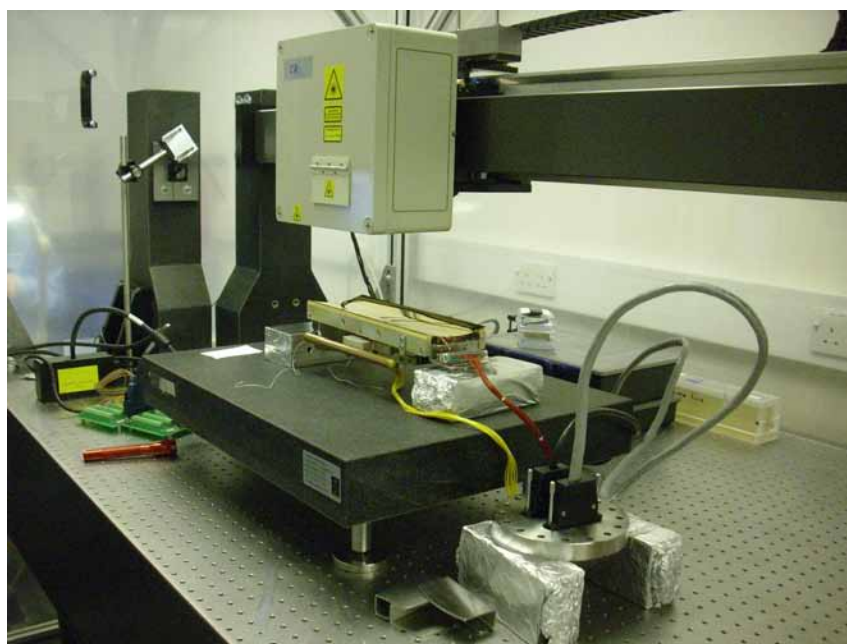


Figure 2.27: The mirror with the thirty piezoelectric devices attached to the reverse, being scanned by the LTP. The optic was set up on the aluminium frame, designed for the X-ray tests, on top of the granite table. The height and stability of the granite table is controlled precisely so that no vibrations of the granite are picked up by the LTP. The laser is on a computer controlled translation stage which also calculates the slope of the optic's surface. The whole arrangement is contained within a sealed chamber which prevents any distortions caused by air currents or temperature variations.

created at one end. The top frame of figure 2.28 shows the measurements taken (in varying colours) and the theoretical profile, i.e. the form the mandrel should have had, in black. The lower frame demonstrates the difference between the actual measurements taken using the LTP and the theoretical form. All of the graphs showing the subtraction of the perfect optic have been shifted and centred around the 0 point. Due to the length of the axial strips which were measured, the data covering the ends of the mandrel were extrapolated to cover the full length. This extension was only required for the last 10mm of the surface and was calculated using a least squares fit to the last few points of measured data. One of the axial strips had a large error around 220mm along the length of the mandrel, which was due to a calculation error and was not a real feature on the surface of the mandrel.

The released mirror was measured by taking eleven axial strips, 270mm long and 7.5mm apart, across the surface. Figure 2.29 shows plots of the theoretical data and the measured data. In the top frame the theoretical profile is shown in black and each individual strip of measured data are shown in various colours. The lower frame shows the difference between the theoretical profile and each of the measured data. This difference gives a clear indication of the shape of the released mirror. During the measurements, the mirror was mounted on the aluminium frame so the shape measured was as close to the shape the mirror had during the X-ray tests. As the scans were only 270mm in length, a least squares fit was used to extrapolate the data to cover the full 300mm of the mirror. It is clear from the plots that the optic was a lot flatter than it should have been, which changed the focal length and its required position with respect to the source and detector.

Figure 2.30 shows a comparison between the expected profile of the mirror, based on the scans taken of the mandrels form, and the actual profile of the released optic. The eleven scans taken of the released mirror were compared to eleven scans of the mandrel. The nature of the plot demonstrates that the mirror was distorted due to stress during the release process and thus created a flatter optic than expected.

The optic with the piezoelectric actuators was scanned in single axial strips over a length of 290mm across the centre. It was tested with the power supply to the actuators turned off and then with the power supply turned on to illustrate the reaction of the piezoelectric devices. When the power supply was switched on, the

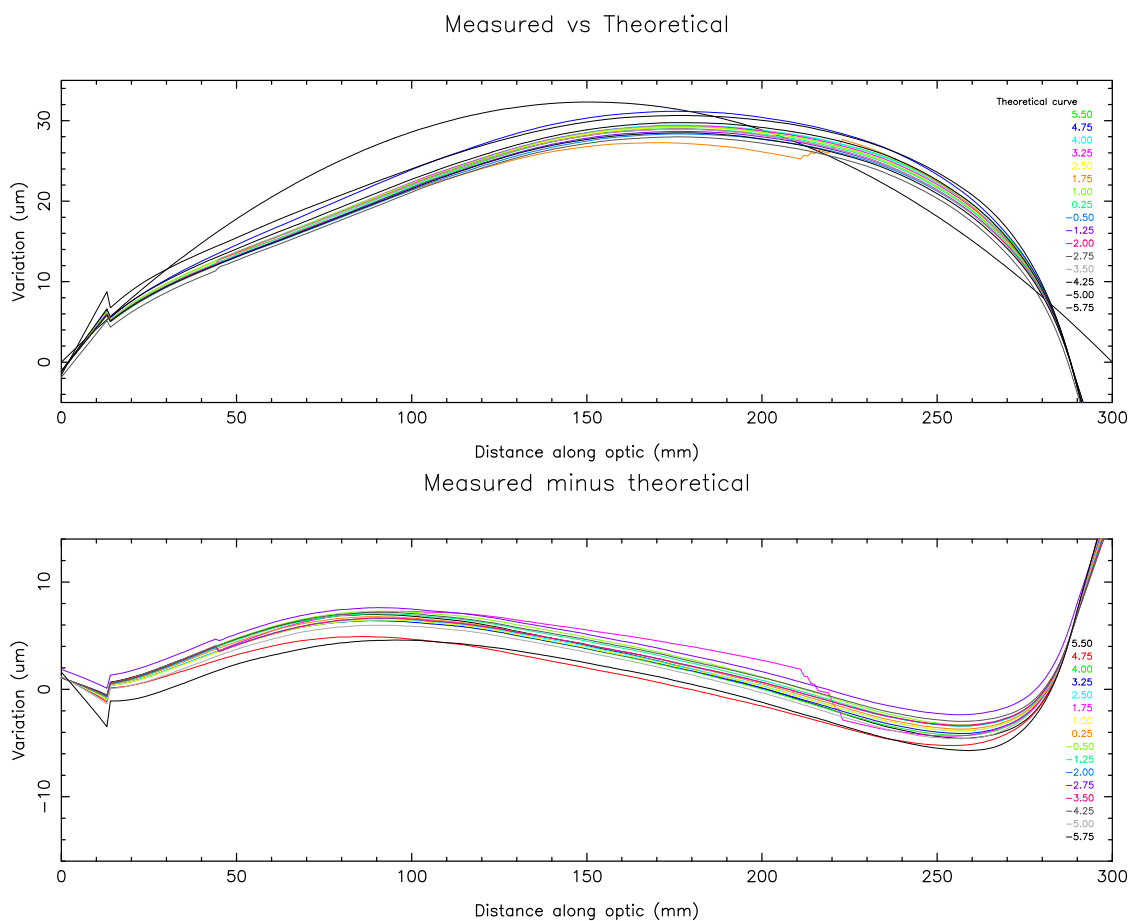


Figure 2.28: The measurements taken of the profile of the elliptical mandrel using the LTP at STFC Daresbury Laboratory. The top graph shows the expected theoretical form is shown in black and the sixteen axial strips taken with the LTP are shown in varying colours. The lower graph shows the difference between the theoretical profile and the axial strips. The strips were 290mm in length and separated by 6.25mm. The data for the extra 10mm of the mandrel was extrapolated using a least squares fit of the last few points of real data. The error in the 1.75mm data set is a calculation error and was not a real feature on the mandrel.

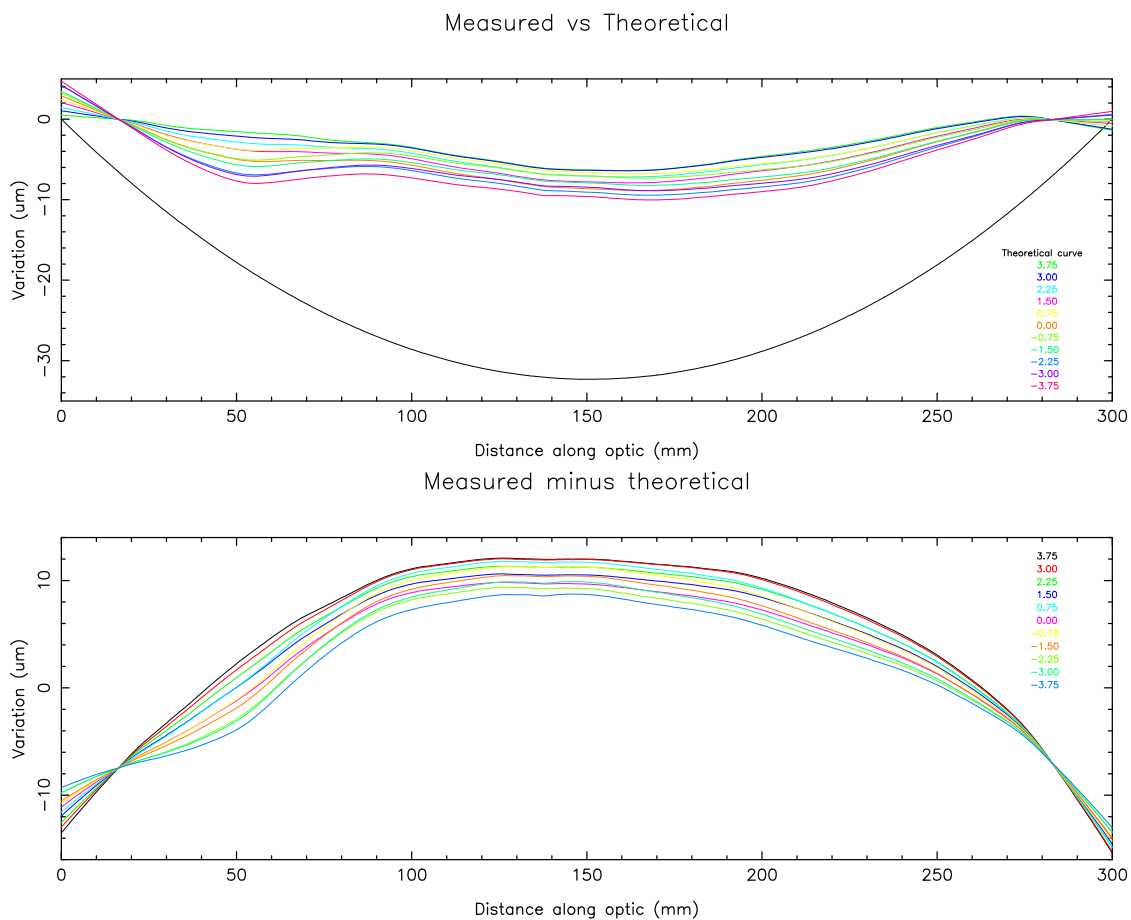


Figure 2.29: The scans taken of the released ellipsoidal mirror prior to any actuators being attached. The top graph shows the scans which were measured across the optics surface are shown in various colours, with the theoretical form of the mirror shown in black. The bottom graph shows the difference between the expected mirror profile and the actual profile which was measured with the LTP. These plots show that the mirror was a lot flatter than was expected which changed the focal length of the optic and therefore its required position with respect to the source and detector. The axial strips were 270mm in length and separated by 7.5mm . The measurements were extended across the full length of the mirror by extrapolation using a least squares fit method.

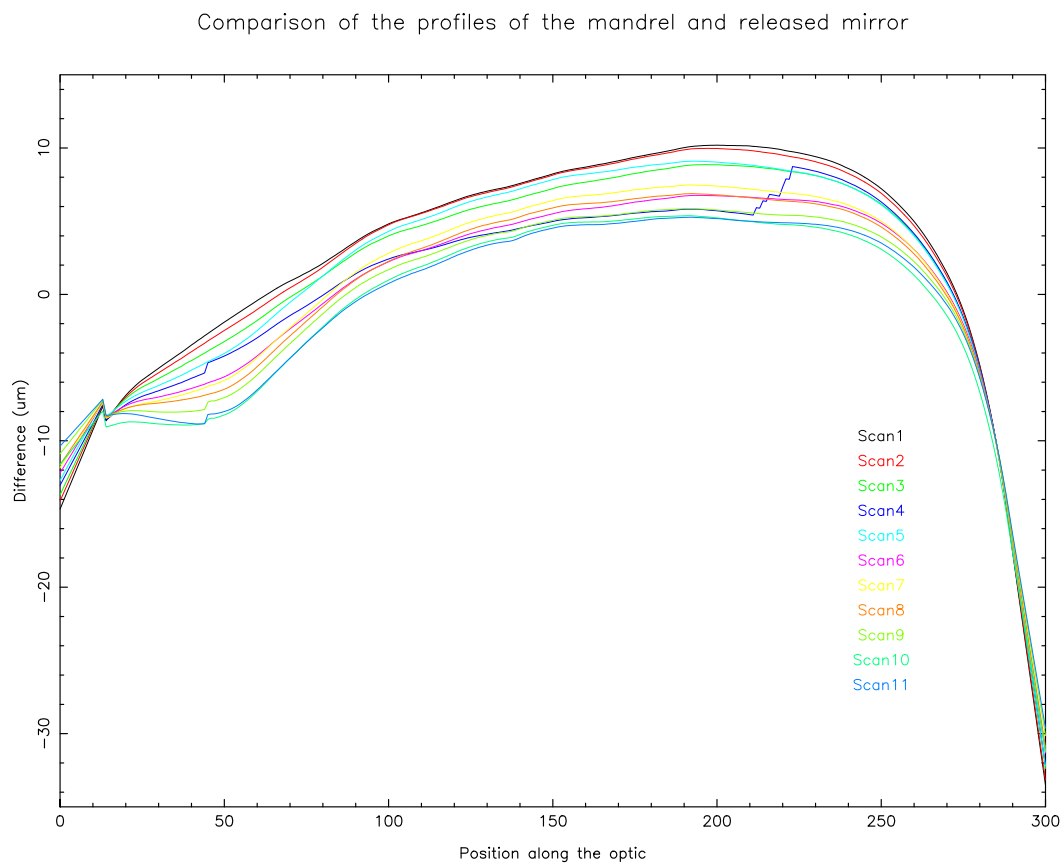


Figure 2.30: A comparison between the mandrel's profile and the profile of the released mirror. The plot clearly shows that the mirror was distorted due to stress during the release process and this caused it to be flatter than expected. Eleven scans have been compared to produce this plot as eleven scans of the released optic were measured.

actuators were set to $0V$, however, due to the nature of the actuator control system this is equivalent to $+100V$ on all the actuators. This is evident in the scans shown in figure 2.31, where the difference between the power supply being switched on and off is plotted along with the theoretical measurements. When the power supply was switched off, the PZT plates are allowed to relax, stretch and contract which also contributes to the differences in the measured profiles. As with the previous plots, the data were extended to cover the full $300mm$ of the optic using a least squares fit method. The red vertical lines, in both plots, illustrate the positions of the actuators along the length of the optic and at several of these positions it is clear that print-through has occurred on the optic. Once the theoretical form of the optic had been removed from the scans, this effect was accentuated and is shown in the lower frame of the plot. It is believed that this effect was caused by the variable glue layer thickness between the actuators and the optic. There was a considerable amount of variance in the radii of curvature of the actuators which led to a mismatch between the actuators and the mirror. Due to time constraints, the radius of curvature of each individual piezoelectric device could not be measured to find its optimum position on the optic. The gaps created by the mismatch were filled with excess glue to prevent air pockets which could have led to actuators being removed from the mirror when within a vacuum. It was also essential that the whole of each actuator was completely bonded to the optic. This excess glue probably caused a glue layer of up to $500\mu m$ thickness instead of the optimum of $80\mu m$, which led to the print-through on the mirrors reflecting surface. The gaps in between the individual actuators added to this effect as predicted and unfortunately this could not be removed by the actuators.

The difference between the scans taken of the released mirror and the scans of the actuators with the power on and off, were calculated and plotted to produce figure 2.32. This illustrates how the addition of the piezoelectric devices has affected the form of the mirror and also shows the extent of the print-through effect on the mirrors surface as described previously. The positions of the actuators are shown here in black with the differences between the scans shown in various colours. As with the above plots, the data has been extended to cover the full length of the mirror using a least squares fit method.

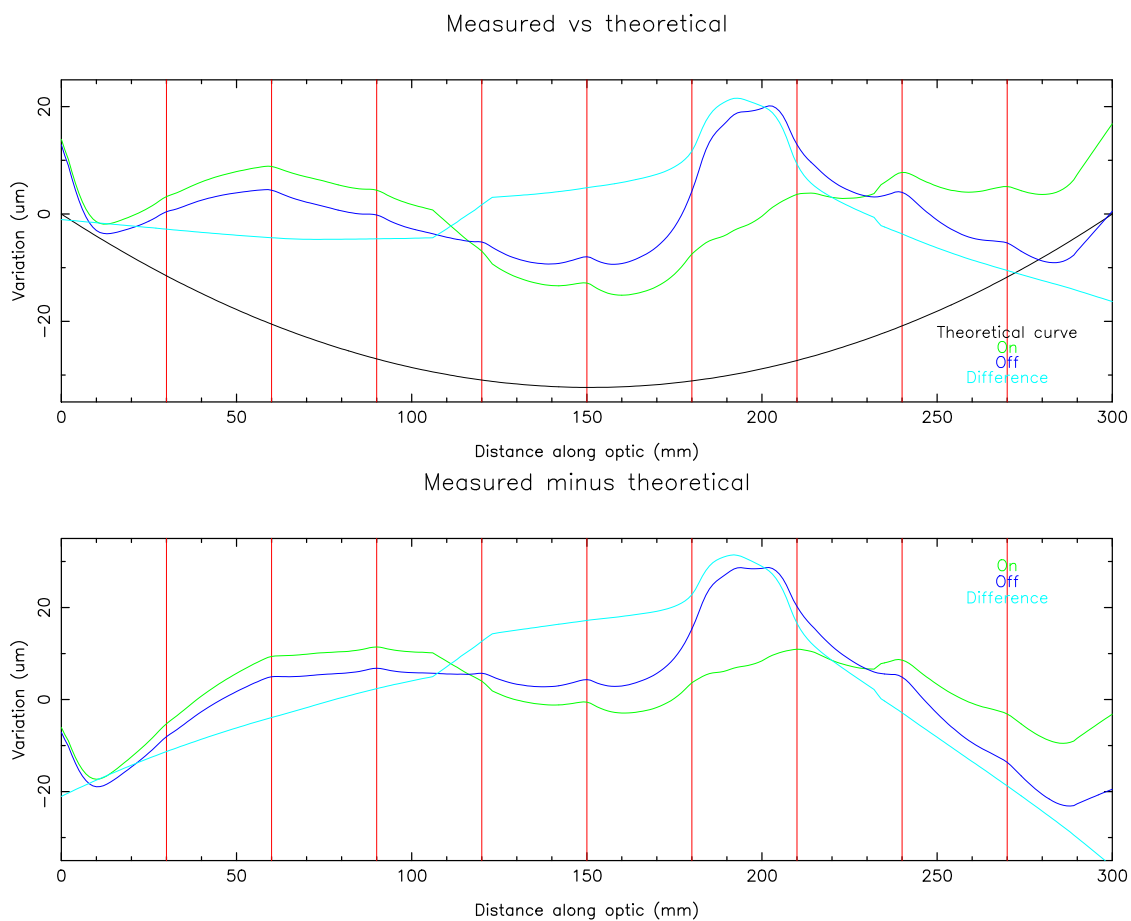


Figure 2.31: The top graph shows axial scans along the centre of the mirror with thirty piezoelectric devices attached are plotted, with the power supply to the actuators turned off, on and the difference between the two. With the power on, all the actuators are effectively at +100V even though they were set to 0V, which is demonstrated in the plot of the difference between the power being on and off. The red vertical lines represent the positions of the piezoelectric devices along the length of the mirror. The lower graph shows the plots once the theoretical profile of the mirror has been subtracted, which accentuates the print-through effect seen on the mirror's surface.

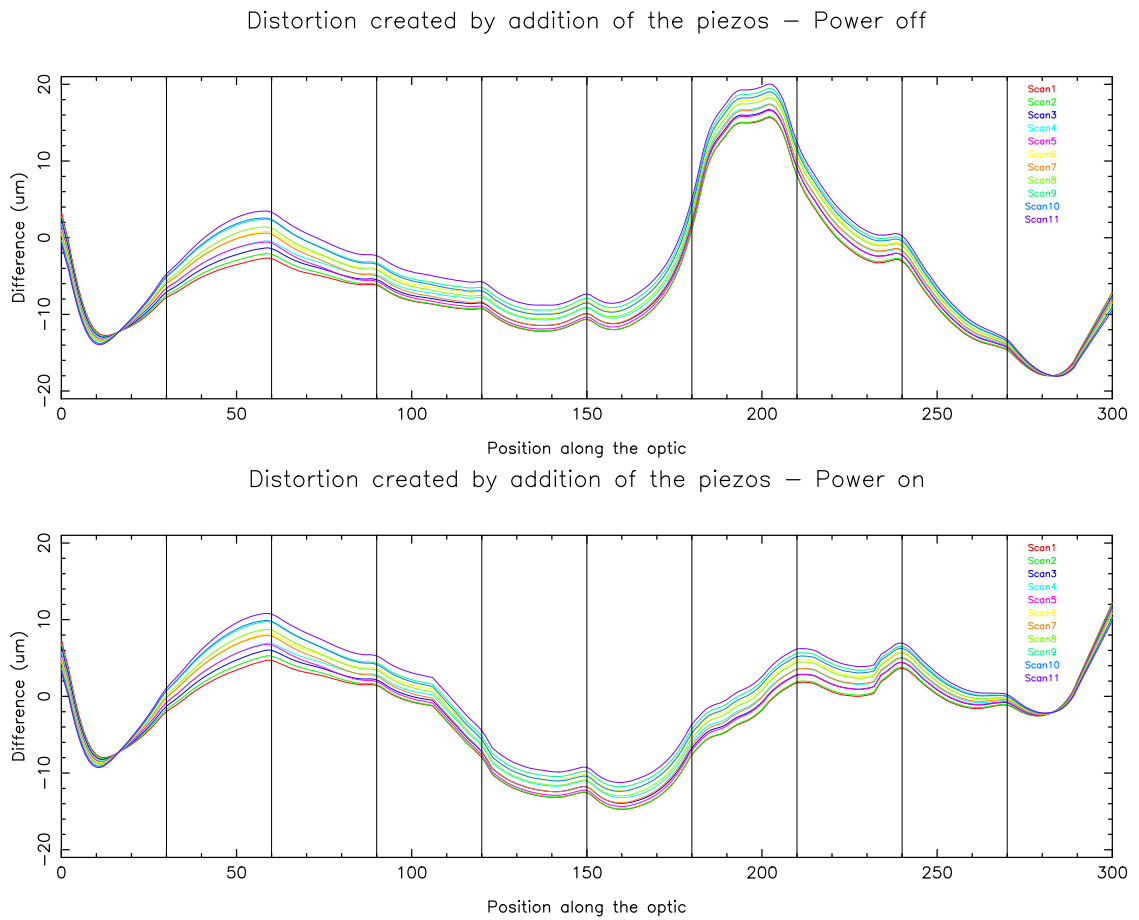


Figure 2.32: The difference between the released optic and the addition of the piezoelectric actuators. Here the positions of the piezoelectric actuators are shown in black and the various scans are shown in different colours. The top frame is the comparison with the actuators turned off and the lower frame shows the comparison with the power turned on. The extent of the print-through from the actuators described earlier, is clearly visible in both of these plots.

2.7 Modelling the performance of the large prototype optic

All the modelling of the prototype mirror was performed in a ray-tracing program called Q (see section 1.5). Several aspects of the LAXRO were researched and modelled using this software. Firstly, a model of the perfect prototype optic was produced to check that the optic would perform as expected and to also provide a base model to which other features could be added. These included:

- surface roughness
- the effect of gravitational sag on the optic
- the figure error of the mandrel and subsequent release
- the influence of integration of the piezoelectric devices
- the activation of the piezoelectric actuators
- the adjustment algorithm - similar to simulated annealing

2.7.1 The basic ellipse model

The model was set up with the dimensions of the TTF, with the source and detector at the foci of the ellipse and the segment $\sim 4.4m$ from the detector, in line with the centre of the three flanges. The mirror was also specified to be $300mm$ in length and $100mm$ in width and initially a perfect gold surface was modelled. An image was produced which represented the rays originating from the source, hitting the mirror's surface and finally reaching the detector. In addition, the expected response of the detector to the X-rays was simulated and multiple models were produced by varying the mirror's surface roughness. Deformation matrices were also included to create rotation of the optic about its axes.

The source was set at an energy of $1.25keV$ and the detector was chosen to be $250mm^2$ so that all the rays, even those which missed the optic, would be displayed. Two apertures were specified, one in front of the source and one in front of the optic so that only the optic would be illuminated by the X-rays. Figure 2.33 shows the

image of the model described. Figure 2.33 top left, shows the X-rays which were produced by the source and either hit the mirror and been reflected towards the detector or have missed the optic completely. The ellipse, on which the segment was based, is shown in black whilst the TTF outline is shown in blue, which illustrates the tilt of the ellipse axis in relation to the axis of the TTF. Figure 2.33 top right, is the simulated detector response and the reflected rays are surrounded by a red circle whilst the rays which did not hit the optic can be seen at the bottom of this image. The lower frames are zoomed in images of the top frames. The bottom left of figure 2.33 shows the rays hitting the mirror and being reflected to the detector and the bottom right of figure 2.33 is an enlarged view of the detected reflected rays. It should be noted that for a perfect optic, the resolution is limited by the detector's pixel size, in this case $0.21mm$. Similar images were produced for the rough surfaces and for small amounts of rotation and deformations that were added.

In order to model the rotation of the optic in both θ and ϕ (figure 2.48), the axes of the optic were rotated by small steps in each direction. The Half Energy Width (HEW) of the detected image was measured by simulation at each increment and graphs were drawn to give an indication of the sensitivity of the optic. The plots are shown in figure 2.34, with the graphs for θ and ϕ on the top and bottom respectively. From these graphs it is clear that the optic was more sensitive to rotation about the Y axis, ϕ , than rotation about the X axis, θ , as this is effectively rotating the optic around the ellipse.

2.7.2 Modelling the gravitational sag

As described in section 2.9, the optic was supported along the axial edges in order to allow for full movement of the mirror as the piezoelectric devices were actuated. Therefore, there was a small amount of gravitational sag on the optic due to the lack of support along the centre of the mirror. The $300mm \times 100mm \times 0.4mm$ nickel prototype optic was modelled, at UCL using COMSOL Multiphysics, sitting within the support structure with thirty piezoelectric actuators attached to the back. The results of this model were then included as a deformation matrix in the base model of the prototype in Q. The maximum displacement, over the length of the optic due to gravity, predicted by the data from the COMSOL Multiphysics model was

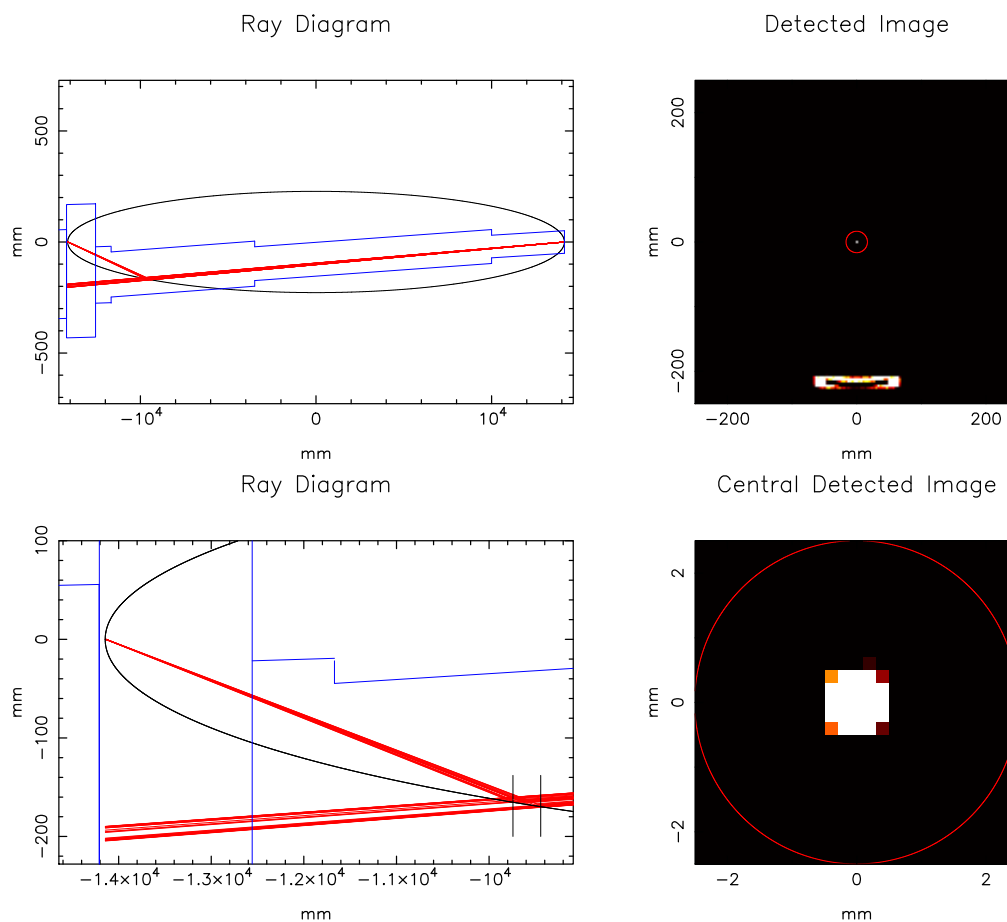


Figure 2.33: An example of an illustration produced in Q. In this model, a perfect simulation of the ellipse prototype mirror was completed. The top left shows the ellipse in black and the outline of the TTF is shown in blue. The two axes on this plot are not to scale and the axis of the ellipse is tilted with respect to the TTF axis. The detector and source are at the foci of the ellipse. The change in the tunnel's width can also be seen on this plot. Top right shows the full detected image with the rays which have not been reflected by the optic at the bottom of the image. The red circle represents the area of interest which was used to calculate the HEW values. This shows the outline and shape of the optic. Bottom left is a zoomed in image of the rays being reflected by the optic and then hitting the detector. Bottom right is a zoomed in view of the focused spot. The resolution of this image is limited by the detector's pixel size, 0.21mm .

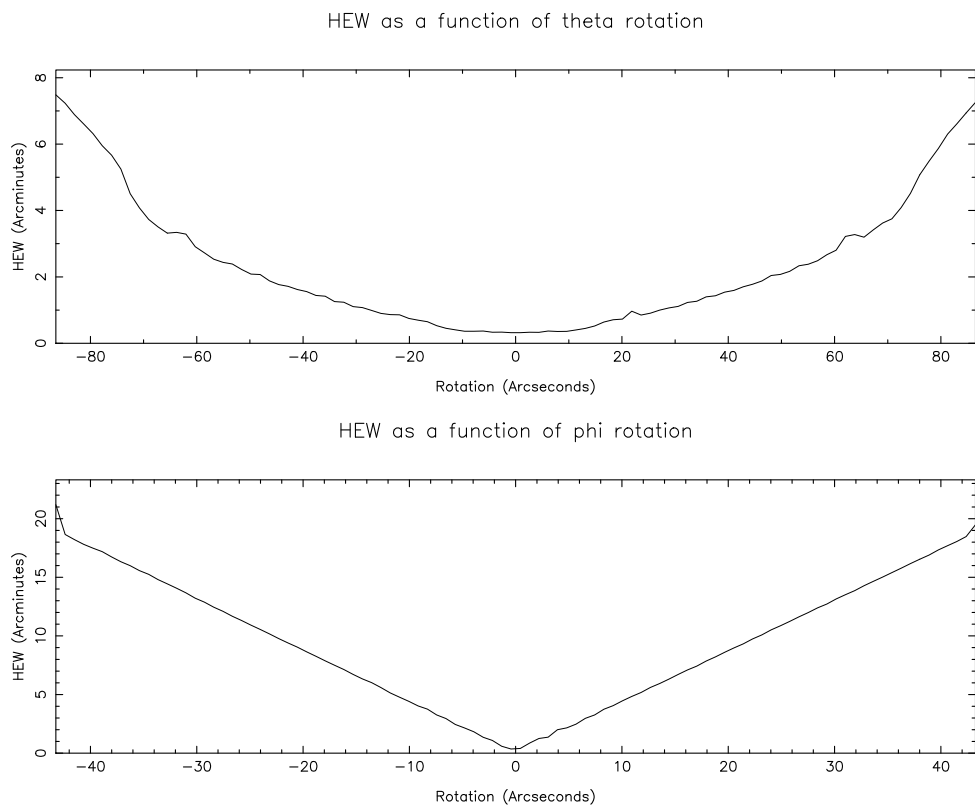


Figure 2.34: Results from the models of the rotation in the X, θ , and Y, ϕ , axes in top and bottom respectively. It is clear from these graphs that the optic was more sensitive to rotation about the X axis, θ than the Y axis, ϕ as rotation in the θ direction is effectively a rotation around the ellipsoid's axis.

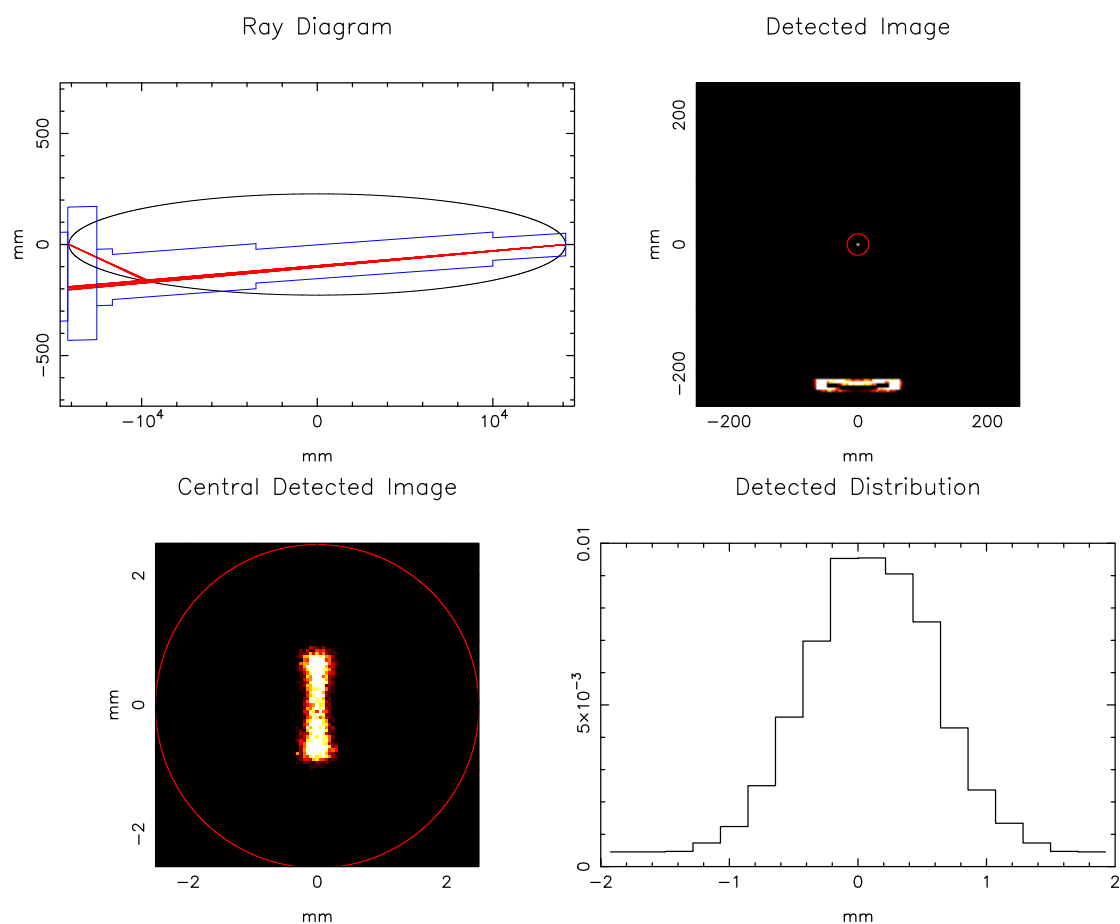


Figure 2.35: The basic ellipse model with the gravitational sag deformations added in Q. This image has the same set up as in figure 2.33. It can be seen that the focused spot has been spread out in to a fan shape. The vertical detected distribution can also be seen in the lower right hand frame of this image. For a focused spot, a single central peak would be seen. The detected image was measured by simulation using Q to have a HEW of $13.77''$, close to what was predicted using the COMSOL Multiphysics FEA data of $10.02''$.

used to calculate that the gravitational sag would create a $10.02''$ distortion on the detector. Figure 2.35 shows the model of the gravitational sag in Q.

It can be seen in this image that the detected spot has fanned out to approximate a bow tie shape. The HEW value, measured by simulation in Q, of the detected image was found to be $13.77''$, which is close to the predicted calculated value, using the COMSOL Multiphysics FEA data, of $10.02''$. The vertical detected distribution is shown in the lower right hand frame and demonstrates the fanning out of the detected spot as a single central peak would have been seen if a single spot had been detected.

It was possible to reduce the gravitational sag error using the height adjustable legs on the support structure. This is because the gravitational sag is essentially just

changing the radius of curvature of the optic and therefore the ellipse. By raising the optic slightly, $\sim 1\text{mm}$, the error should have been reduced to $\sim 0.5''$, which was confirmed by the ray-tracing. In practice this small adjustment was made by default when mounting and positioning the optic in the TTF.

2.7.3 Using the profile data from the LTP in the modelling

As described in section 2.6, the LTP at STFC Daresbury Laboratory was used to measure the shape of the optic. This was compared to the theoretical shape of the mirror and the difference was found, as shown in figure 2.29 and figure 2.31. Because it was only possible to measure 270mm and 290mm of the 300mm axial profile of the optic respectively, the ends were extrapolated to cover the full length of the optic for the purposes of the model. For the optic without any piezoelectric devices, the eleven scans taken were equally spread over the width of the optic. For the optic with the piezoelectric devices attached, only one axial strip along the central section was measured, this data was expanded over the entire width of the optic. Figure 2.36 shows the results of the model, produced using Q, of the optic prior to any actuators being attached. As with the previous models, the ray-traced image is shown in the top left. A zoomed-in image of the detected spot is shown in the top right, the bottom left is a histogram of a vertical cut across the detected spot and the diagram in the bottom right represents the deformation which has been applied to the optic. The deformation matrix displayed is an alternative representation of the data shown in figure 2.29. The model predicts that the angular resolution limit, imposed by the optic without piezoelectric devices attached, is $1.51'$. This simulated value was achieved by slightly adjusting the position of the detector and adjusting the rotation of the optic to optimise its position, which removed some of the error caused by the optic being flatter than expected.

The method described was repeated for the data collected for the optic to which the piezoelectric devices had been attached, both with the actuators turned on and off. The results of the model with the power supply to the piezoelectric devices switched on are shown in figure 2.37. The results of the simulated HEW were $4.15'$ and $3.46'$ for the power supply turned off and on respectively. This shows that by adding the piezoelectric devices, the print-through and kinks added to the

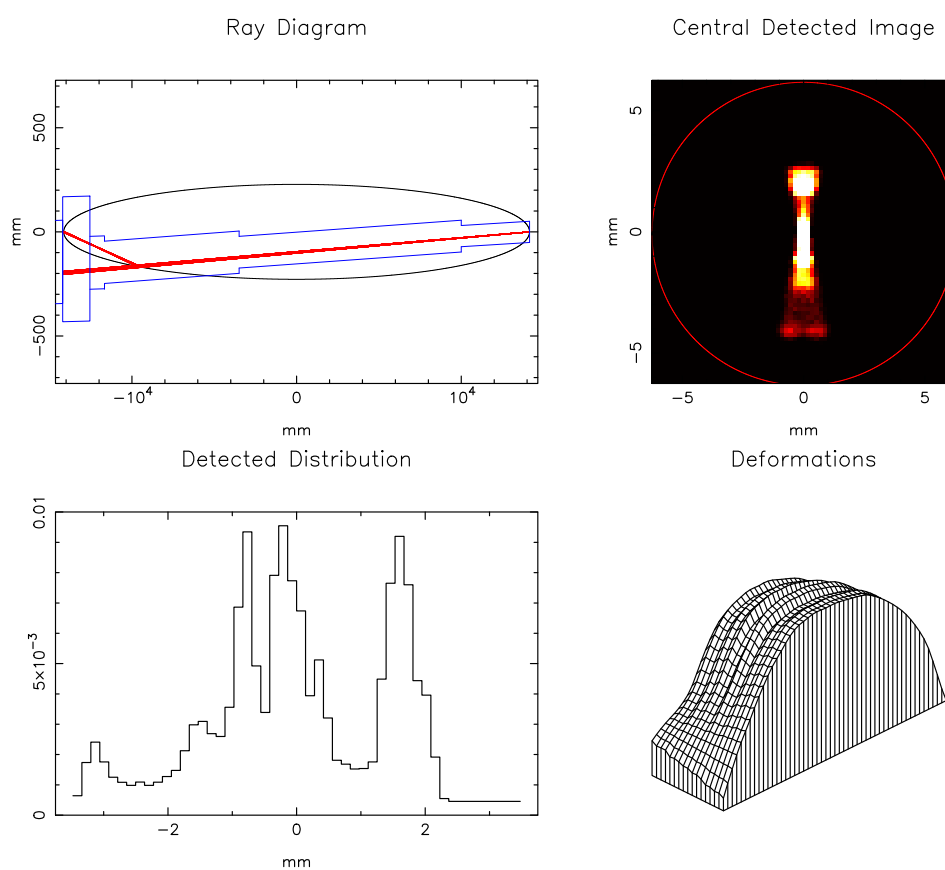


Figure 2.36: A model produced in Q of the response of the optic without any actuators attached, with the deformation matrix set to the measured data taken using the LTP at STFC Daresbury Laboratory, as shown in figure 2.29. The top left shows the ellipse, TTF, and the position of the ellipsoidal mirror. This image also shows the X-rays from the source being reflected by the optic towards the detector. Top right shows a zoomed-in image of the central detected area. Bottom left is a vertical distribution of the detected image. The bottom right is the shape of the optic which was implemented to create the model. This shape gave a measured detected spot of $1.51'$.

optical surface have caused deformations which have made the resolution of the optic worse by almost 4'. These deformations would not be removable using the piezoelectric devices as they are on the same scale. The mandrel was also modelled in this way and the result measured by simulation using Q was 1.12', which suggests that the optic experienced some form of stress after its release. The results, both HEW and Full Width Half Maximum (FWHM), of all these models produced in Q are summarized in table 2.2. The degradation of the optical performance due to the different production processes is clear in this table and demonstrates the need to improve each area for the next prototype, in particular the bonding of the actuators. The stress on the optic after its release from the mandrel is inherent in the electroforming process, however, techniques for controlling the electroforming solution are being investigated.

Model	HEW		FWHM	
	Actual size (mm)	Arc minutes	Actual size (mm)	Arc minutes
Gravitational sag	0.22	0.17	0.15	0.11
Mandrel	1.43	1.12	1.59	1.24
Optic	1.93	1.51	0.40	0.31
Actuators bonded (off)	5.31	4.15	0.90	0.70
Actuators bonded (on)	4.44	3.46	0.55	0.43

Table 2.2: Summary of the results obtained by modelling the data from the LTP in Q. Both the simulated HEW and FWHM values are displayed in *mm* (as measured at the detector) and arcminutes.

2.8 Simulation of the piezoelectric actuators and adjustment algorithm

In order to be able to adjust the surface of the mirror, by simulation and during the tests within the TTF, a routine had to be devised to control the piezoelectric actuators so that the detected image could be improved with each actuation. Ultimately, the algorithm used for space based telescopes would be similar to simulated annealing which is the technique used in optical adaptive optics. For this method to work, the piezoelectric devices are put in a series of random patterns which are then combined to improve the mirror's surface. A probability function is used to find the next closest random pattern as the image is improved with each iteration.

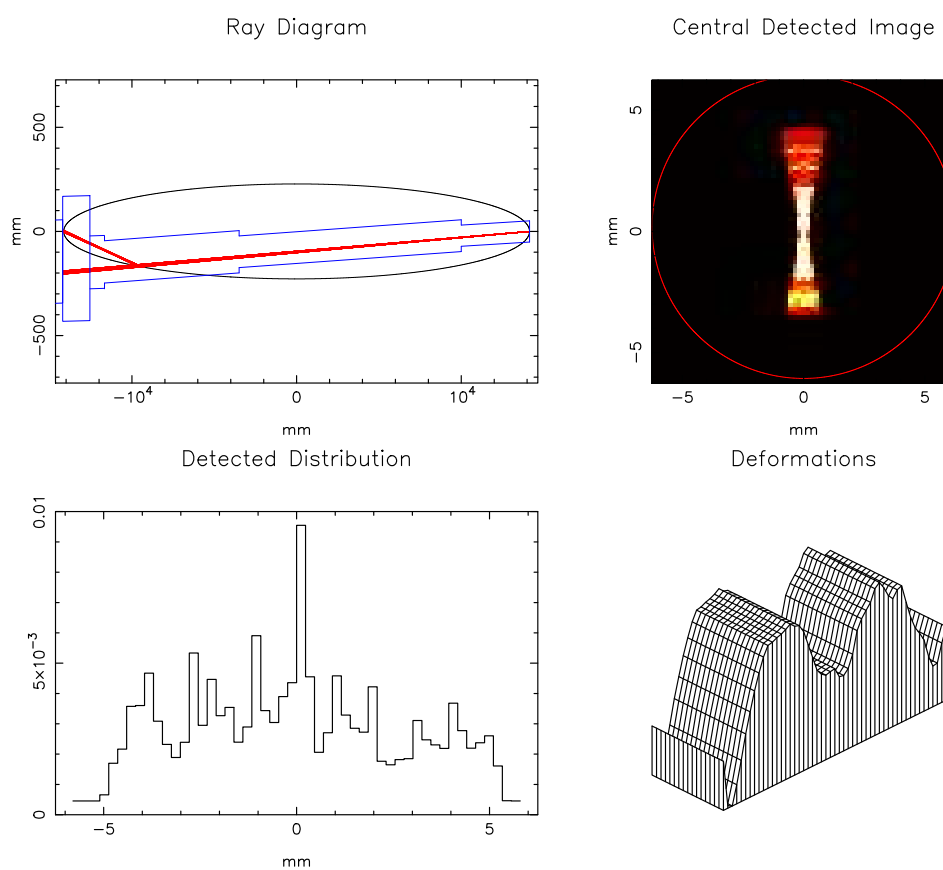


Figure 2.37: A model of the response of the optic with actuators attached, with the deformation matrix set to the measured data taken using the LTP at STFC Daresbury Laboratory, as shown in figure 2.31. Top left shows the ellipse, TTF and the position of the ellipsoidal mirror. This image also shows the X-rays from the source being reflected by the optic towards the detector. The top right is a zoomed-in image of the detected spot. The bottom left shows the distribution of the detected spot. The bottom right is the deformation matrix added to the optic. This shape gave a simulated HEW of 3.64'.

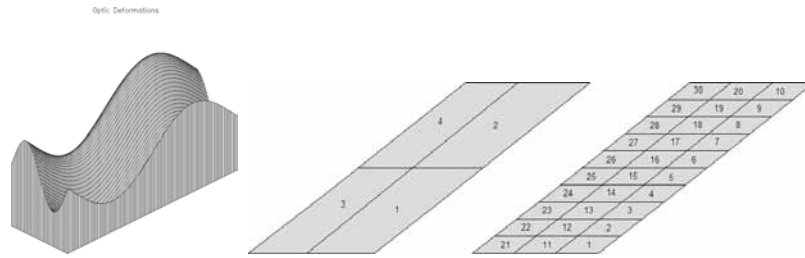


Figure 2.38: Set up for the piezoelectric actuator simulation. Left shows the initial optic distortion, consisting of two orthogonal sine waves across the full length of the optic, which produces a 30” image on the detector. Middle, The initial piezoelectric arrangement on the mirror with four piezoelectric devices and right, arrangement of the thirty piezoelectric actuators.

In optical astronomy, hundreds of actuators are put into hundreds of patterns which are implemented in seconds[24]. However, for X-ray adaptive optics, this process will take much longer as the flux available is typically much lower. It was found that a single image takes tens of minutes to accumulate and many hours were required to observe a complete series of images.

For the purposes of the initial model, the piezoelectric devices were modelled as two, 3D Gaussian bumps, one caused by the piezoelectric device being actuated and the other being the reaction of the mirror surface to the actuation. The combined response of the two Gaussians, with different heights and widths, gave a displacement with positive and negative lobes. The sizes and widths of each Gaussian was estimated based on results from experimental tests carried out at UoB.

The basic optic was set up as described in section 2.7.1. To start with a series of four piezoelectric devices in a two by two arrangement, were set up (figure 2.38 middle). Each piezoelectric device was simulated by the two Gaussians as described above. A simple “ripple” was set up on across the full length and width of the optic surface consisting of two orthogonal sine waves, as shown in figure 2.38 on the left, and the size of this ripple was set so that it gave approximately a 30” distortion on the simulated detector image. This distortion was used as a base as it was a simple deformation that a two by two arrangement of piezoelectric devices should be able to remove.

Each simulated piezoelectric device was actuated several times between a voltage range of $-100V$ to $+100V$ in ten equal steps. This deformation was then added to the optic and ray-traced in Q, the resultant simulated HEW on the detected image

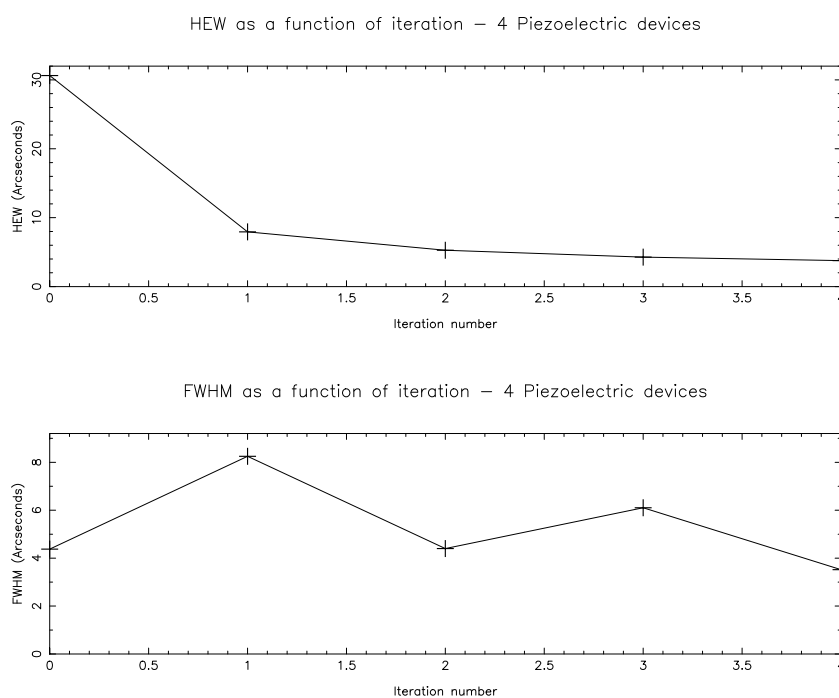


Figure 2.39: Results from the simulation of four piezoelectric actuators in Q. The top graph demonstrates the decrease in the HEW of the detected image as each full iteration of the four piezoelectric devices is completed. Each piezoelectric device was actuated in ten equal steps in the voltage range of $-100V$ to $+100V$. A least squares fit was used to find the optimum voltage for each of the piezoelectric devices by plotting the voltage against the detected HEW. The graph shows a decrease in the HEW from just over $30''$ to just under $4''$. The bottom graph shows the change in the FWHM with each iteration. A single iteration in this case is all four actuators being iterated and the optimum voltage found.

was then plotted against the corresponding voltage. Using a least squares fit, the optimum voltage for that piezoelectric device was found and then the device was set to that voltage and the next piezoelectric device was iterated as the first had been. This was repeated for each piezoelectric actuator in turn and the whole process was repeated several times. Each time the routine was completed, the range of voltages was reduced to a smaller range, around the optimum voltage for each device in order to home in on the true optimum. Using this method the initial simulated HEW of $30''$ was reduced to $\sim 4''$. The top graph in figure 2.39 shows the decrease in the HEW with each iteration and the bottom graph in figure 2.39 shows the change in the FWHM. A single iteration in this case is all four actuators being iterated and the optimum voltage found.

The prototype ellipsoidal segment had thirty piezoelectric devices attached to the back in a ten by three arrangement (figure 2.38.c). A new routine was created

to be able to deal with any series of patterns and an increase in the total number of piezoelectric actuators. A simulated run was completed where each piezoelectric actuator was individually iterated, as with the simulation of the four piezoelectric actuators, to see how well the initial deformation could be removed.

The routine in Q reduced the simulated HEW from 30" to ~4". Due to the fact that the distortion is of a low order, thirty piezoelectric devices are not required, the distortion can be effectively removed by just four actuators. This routine, whilst successful, was very slow. In order to achieve this decrease in the HEW, approximately 300 individual adjustments and HEW measurements had to be made.

In a real system, this process would take a long time and so a series of patterns were devised to actuate all thirty devices at once, in order to speed up the routine and create a fast way to remove the initial optic distortion, both during the simulation and the X-ray tests. It was decided that a Fast Fourier Transform (FFT) method would be employed as this would provide several orthogonal patterns and any distortion of the optic (excluding higher orders at a frequency greater than the size of the actuators) could be expressed as a linear sum of the FFT patterns. Using these patterns reduces the number of adjustments required and HEW measurement cycles as each adjustment is moving all thirty piezoelectric devices at once.

Starting with an array of thirty piezoelectric devices, in a ten by three arrangement, the Fourier eigenfunctions were set up by using the Discrete Fourier Transform routine (using a standard DFT algorithm) in Q. Since the displacements are of the real piezoelectric devices, only the eigenfunctions which have a real part and no imaginary part, were required and conjugate symmetry was applied in the Fourier Domain to account for this. If the 1D index runs from 0 to $N - 1$ then we have:

$$A(i) = A(N - i)^* \quad (2.10)$$

where * represents the complex conjugate. It is also required that the eigenfunctions are shifted so that zero phase is at the edge of the plate not the centre of the 1st sample, where $i = 0$. This was achieved by multiplying the element by $exp(i\theta)$ where $\theta = \pi/N$. For the short dimension, no shift was required as there was an odd number of samples, M=3. The values shown in table 2.3 were set within an array and then the inverse FFT was taken to obtain the eigenfunctions, for each eigenfunction two elements were set. Terms were marked ia where i is the running

	1+	2+	3+	4+		4-	3-	2-	1-
0	1	2	3	4	5	6	7	8	9

Table 2.3: Table showing the contents of the array to generate each eigenfunction and the corresponding imaginary part values required. The terms are marked as ia where i is the eigenfunction index and a is the sign of the corresponding imaginary part.

Pattern number	Row number		
	1	2	3
1	+	+	+
2	-	+	+
3	+	-	+
4	+	+	-

Table 2.4: Table showing the four patterns in the shorter direction. The basic patterns created using the FFT method are copied into the adjoining rows and then multiplied by these patterns to create the sixteen FFT patterns, all of which are orthogonal to one another.

index of the eigenfunction (1,2,3 etc) and a is the sign of the imaginary part. Note that the eigenfunction 0,0 is not required since it is the DC (constant level) term which represents a simple offset. The nyquist term is also missing because this term cannot be phase shifted, and was not required for this model. For each pattern, all other elements of the array were set to zero.

This process created the pattern for the first row of the piezoelectric devices and the other two rows were filled by copying the first row and this produced the four basic patterns. These patterns were then multiplied by the patterns in the shorter direction, which are given in table 2.4.

This created a total of sixteen patterns which were all orthogonal to one another and are shown in figure 2.40. The first column contains the 4 patterns which have been generated using the FFT program and the subsequent columns are the basic patterns multiplied by the short direction patterns in table 2.4.

These patterns range from -1 to +1 in value and were then multiplied by the incremental voltage to calculate the voltage of each individual piezoelectric device. These patterns were used instead of actuating the thirty piezoelectric devices individually and it reduced the number of iterations required from over 300 iterations and HEW measurements to just 160.

The FFT patterns were modelled with the initial distortion in Q and it was reduced from a simulated HEW value of $\sim 30''$ to $9.62''$. Each of the sixteen patterns

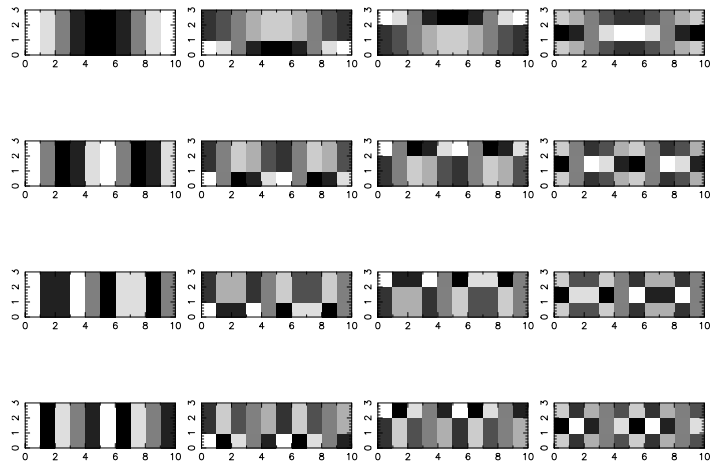


Figure 2.40: The FFT patterns created by the process described in section 2.4. The first column contains the basic patterns and the subsequent columns are those which have been multiplied by the short length patterns. The patterns range from -1 to $+1$ and the voltage applied to each individual piezoelectric is calculated by taking these values and multiplying it by the voltage iteration value in the range of -100V to $+100\text{V}$.

were iterated at ten voltage steps equally spread over the voltage range. Using the four piezoelectric devices, the same result took four full iterations of all four piezoelectric devices, but using this method, each pattern was only iterated once.

Using COMSOL Multiphysics, UCL were able to simulate the influence function of the type of piezoelectric device designed for this experiment on nickel and glass optics of 0.4mm thickness. Influence functions were also produced with a 0.5mm glue layer in between the optic and the piezoelectric actuators. Comparisons of the Gaussian models and the FEA models of the two different optics (nickel and glass) on a three by three actuator grid are shown in figure 2.41 and the influence functions with the glue layer are shown in figure 2.42. The Gaussian models are the same in both graphs as a glue layer was not added whilst the nickel and glass models show a decrease in the piezoelectric device's influence due to the thick glue layer. Only the Gaussian representing the actuation of the piezoelectric device is visible in these plots as the three by three actuator grid is not large enough to show the reaction of the surface to the actuation.

Using these influence functions, instead of the Gaussian bumps, and the LTP data of the optic with the piezoelectric devices attached, the routine was run again. The patterns were run individually and the change in the simulated HEW for each pattern was recorded. The patterns were then put into the order to which they were

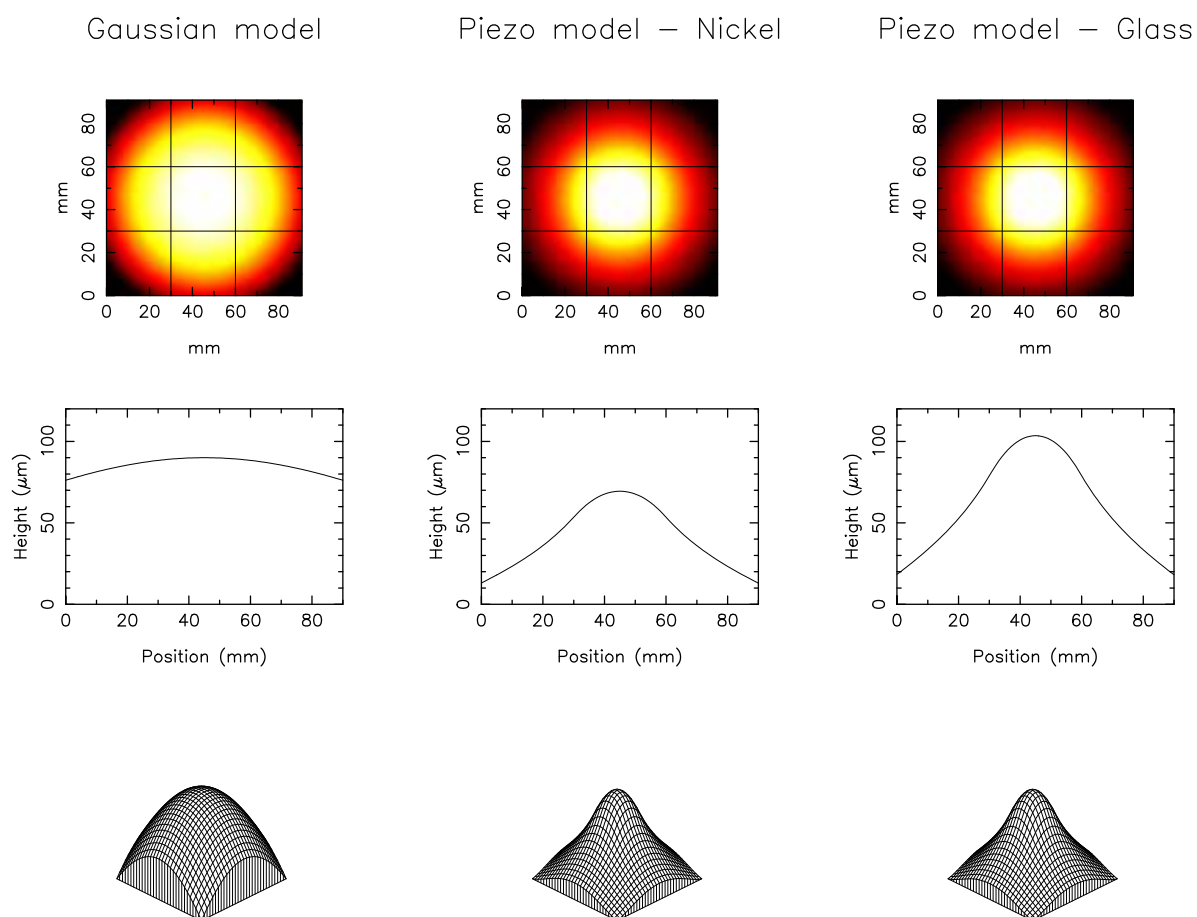


Figure 2.41: A comparison of the Gaussian model and the influence functions of the COMSOL Multiphysics models produced at UCL, on a three by three actuator grid. The Gaussian model is on the left followed by the nickel and glass models respectively. The top images show the effect of the actuators across the entire plate, the middle images show graphs of the heights of the functions and the lower images show the 3D deformation matrix. These models have been produced by simulating optics of 0.4mm thickness with 0.2mm thick piezoelectric plates attached.

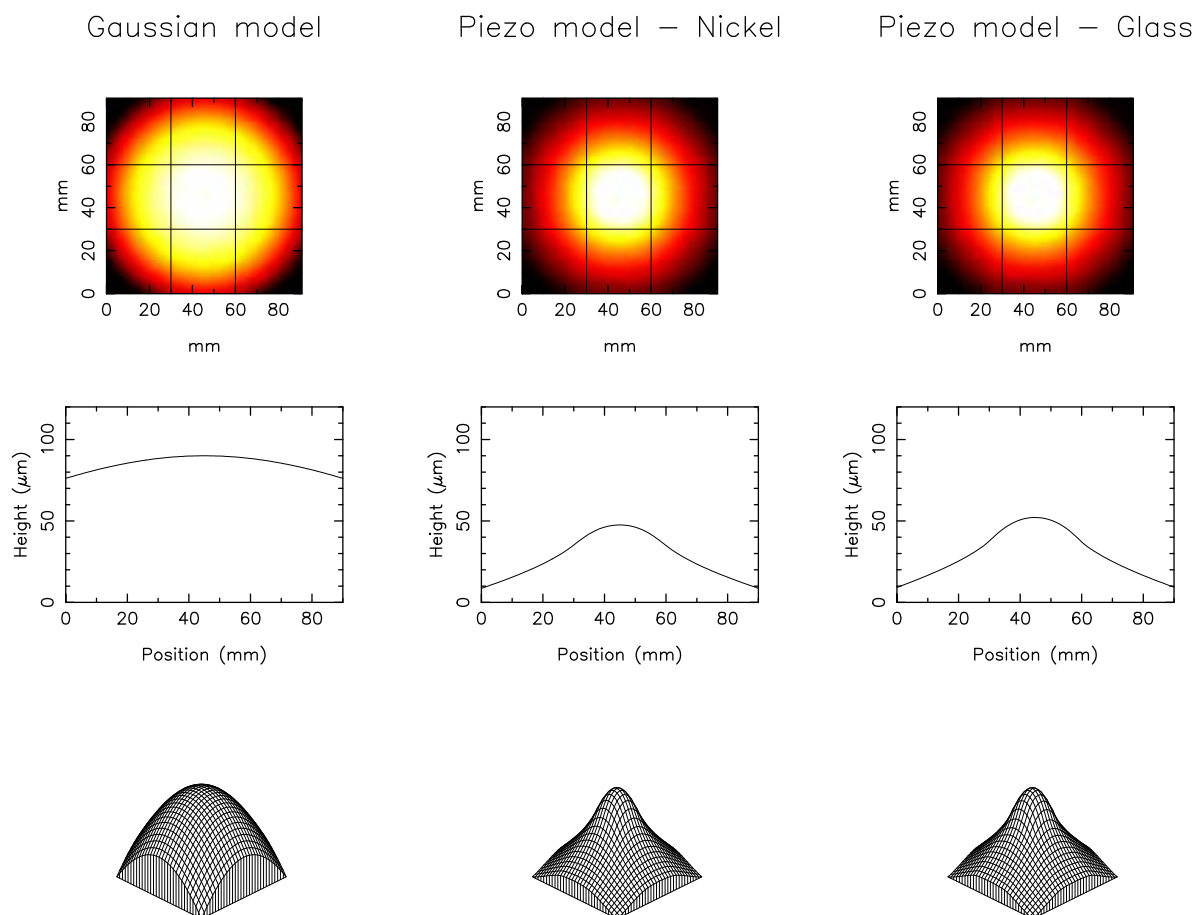


Figure 2.42: A comparison of the Gaussian models and the influence functions of the COMSOL Multiphysics models produced at UCL, on a three by three actuator grid with a glue layer. The Gaussian model is on the left followed by the nickel and glass models respectively. The top images show the effect of the actuators across the entire plate, the middle images show graphs of the heights of the functions and the lower images show the 3D deformation matrix. These models have been produced by simulating optics of 0.4mm thickness with 0.2mm thick piezoelectric plates attached and a 0.5mm glue layer.

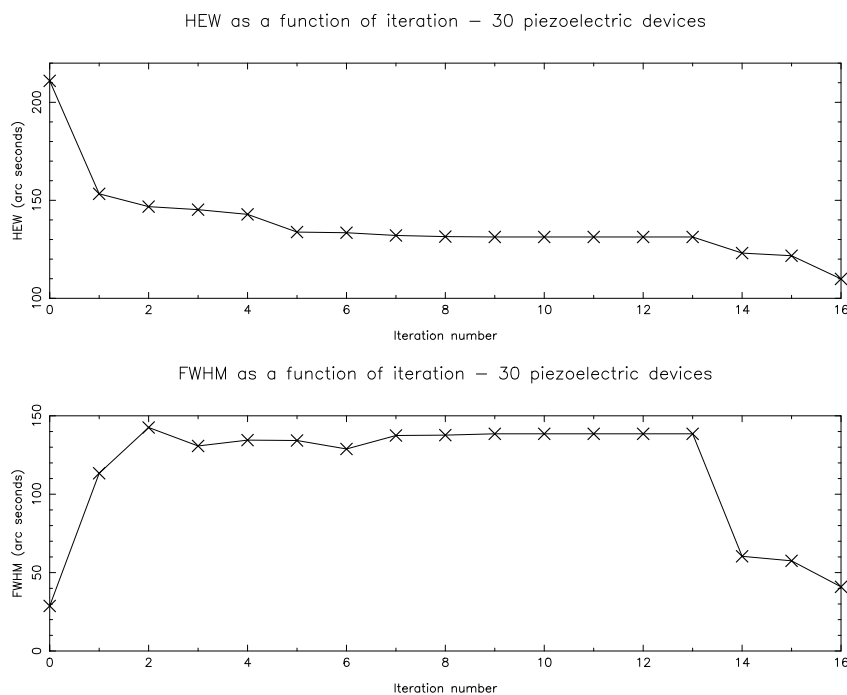


Figure 2.43: The results of the iterative routine in Q using the FFT patterns and the LTP data of the optic with the power supply to the piezoelectric devices turned on. In this routine, the patterns were ordered based on their influence on the HEW. Here the HEW was reduced from 3.46' to 1.83'. The top graph shows the change in HEW and the lower graph the effect on the FWHM based on the pattern iteration.

most effective on the HEW and the routine was repeated. Using this method the HEW was reduced from 3.46' to 1.83', nearly a 50% reduction, and the results of the model are shown in figure 2.43. This was repeated, but by putting the patterns in the order of the optimum voltages instead of the influence on the HEW. Using this method, the simulated HEW value was reduced from 3.46' to 2.38' and the results are shown in figure 2.44.

The two solutions to the optical distortion are shown in figure 2.45. The results from the HEW order are shown in a) and the results from the optimum voltage order are shown in b). The top images are a representation of the optical distortion, the middle images are the piezoelectric distortions and the bottom images are the combined response. Both of these are quite clearly different which indicates that for any optical distortion, there is no single solution and that there are only a few patterns which actually have an effect on the distortion. In this case, 16 patterns may be too many and the optimum may be to have less than thirty piezoelectric devices in order to remove the types of distortions that the optic had.

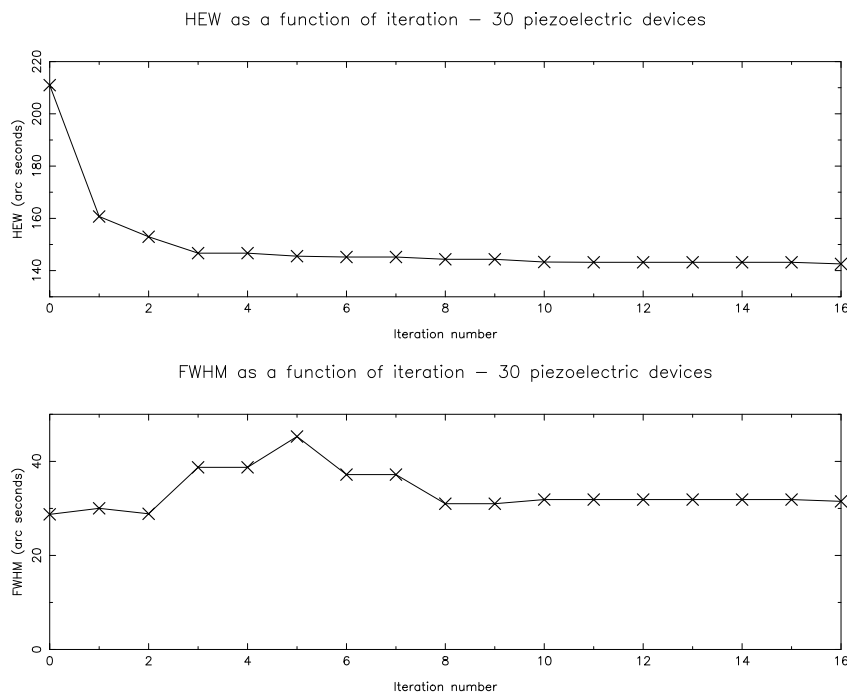


Figure 2.44: The results of the iterative routine in Q using the FFT patterns and the LTP data of the optic with the power supply to the piezoelectric devices turned on. In this routine, the patterns were ordered based on their optimum voltage. Here the HEW was reduced from 3.46' to 2.38'. The top graph shows the change in HEW and the lower graph shows the effect on the FWHM based on the pattern iteration.

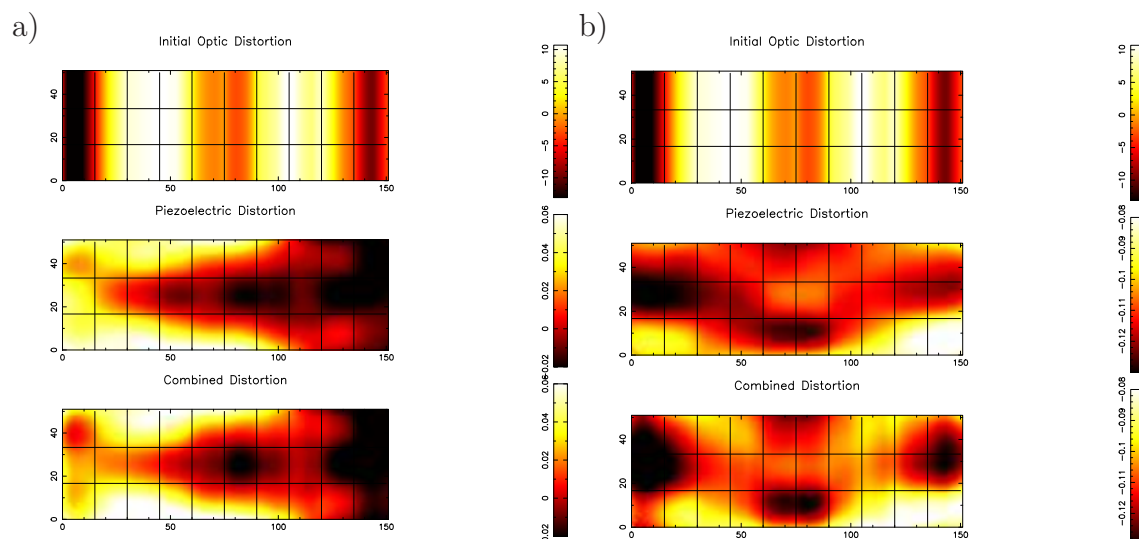


Figure 2.45: The results of the iterative routine in Q using the FFT patterns and the LTP data of the optic with the power supply to the piezoelectric devices turned on. a) The results with the patterns in the order of HEW influence and b) the results with the patterns in the optimum voltage order. The top images are a representation of the optical distortion, the middle images are the piezoelectric distortions and the bottom images are the combined response.

2.8.1 Iterative adjustment of the real piezoelectric devices

The simulated routine was adapted to be able to control the piezoelectric devices during the X-ray tests. The routine calculates the voltages of each of the individual piezoelectric devices and creates a text file containing each of the voltages. A separate algorithm, which drives the high voltage amplifier and therefore controls the piezoelectric devices, was developed at UCL. The text files were then inputted into the piezoelectric control routine which actuated the piezoelectric devices as required. An image was then taken using the MCP detector within the testing facility and analyzed with in-house software. The HEW and FWHM for each image was inputted into the piezoelectric pattern routine software and the next series of voltages were calculated. A least squares fit was used to locate the most suitable voltage for each pattern and a graph was also produced in case the least squares fit was effected by anomalous results so that the best voltage could be determined by eye or by a refit.

2.9 The Tunnel Test Facility

The Tunnel Test Facility (TTF) is a $28m$ X-ray beam line at UoL (see figure 2.46). It has been used to test many space flight missions, including ROSAT, and is currently being used to test the MIXS optics for Bepi-Colombo. The facility has an X-ray source at one end and a detector chamber at the other.

The X-ray source is capable of producing X-ray energies in the range of $0.1keV$ to $100keV$ (figure 2.47 a.) and the copper anode can be coated with different materials to create specific excitation lines. A collimator and pin hole are used to create a source spot size of between $3mm$ and $5mm$ and a flux of ~ 400 counts per second was used during the experiment. A $2\mu m$ makrofol filter to filter the carbon K line was used creating a broad band source made up of bremsstrahlung radiation and the excitation line. The beam line has a varying diameter of $100mm$ nominal at the source end to $200mm$ nominal at the detector end. There are several access flanges along the length of the tunnel which allow access to the pipe so that optics can be placed and mounted within the facility. It is also possible to mount optics within the detector tank at the other end of the facility. Once an optic has been installed in the facility, either via the detector chamber or via a flange, it can be aligned using a

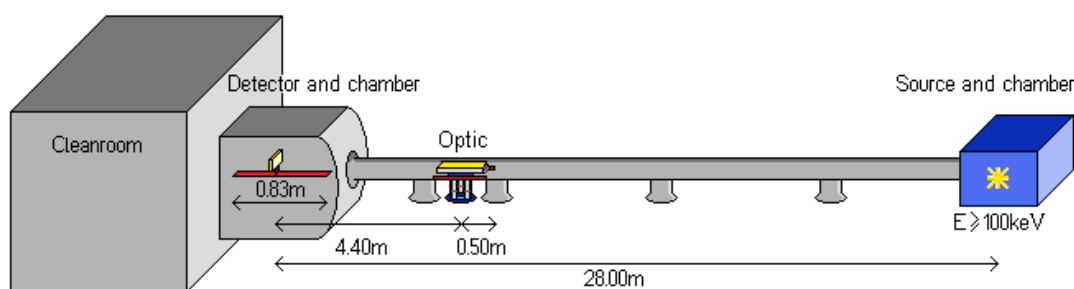


Figure 2.46: A sketch of the TTF at UoL. The facility is 28m in length and has an X-ray source capable of producing energies of up to 100keV at one end and a detector chamber containing an MCP detector system at the other. Several flanges exist along the length of the facility to allow access and for optics to be mounted. The access flange to the detector chamber, where optics can also be mounted, is inside a clean room.

laser, which can replace the source in the source chamber. The facility is normally operated under a vacuum of $\sim 10^{-6}$ mbar unless the laser is being used or the tests need to be performed at air pressure.

The access flange for the detector chamber opens onto a clean room to allow space instruments to be tested. The detector chamber (figure 2.47 b)) contains a 93mm square, Micro Channel Plate (MCP) detector on an automated translation stage, which allows it to move 825mm in and out of the focus of any optic, the X axis. It is also possible to manually move the detector in the Y and Z axes if required. Figure 2.48 shows the set up for the detector and tunnel axes where the (0,0) point is at the centre of the detector's nominal field of view and the X axis comes away from the detector, down the beam line, towards the source.

The MCP detector consists of two MCP plates (to multiply the signal) with a resistive anode positioned behind them (figure 2.49). The channels of the MCPs are tilted in a chevron configuration, at an angle of 13° , so that all X-rays will hit the walls of the channels as they enter the detector, as shown in figure 2.50. Voltages are applied to the plates so that across the plates there is 1650V, -50V between the two plates and 300V between the rear plate and the anode. There is a huge gain on the MCP detector and so the voltages are chosen to create a low voltage across the gap to reduce the gain by a factor of ten. The interaction of the X-rays with the channel walls causes a small electron cloud to be formed. A large potential applied across the plates (down the channels) results in an exponential cascade of the electrons within the cloud. The charge across the small gap between the two plates is set

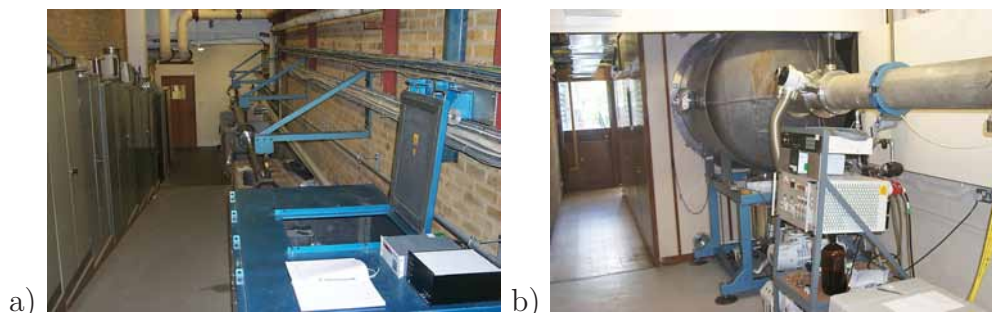


Figure 2.47: a) The source end of the TTF at UoL. The source is contained within the blue lead lined cage at the bottom right of the image. It is capable of producing X-ray energies in the range of 0.1keV to 100keV and the copper anode can be coated in varying materials to create specific X-ray excitation lines. b) The detector tank at the other end of the facility, 28m from the source. Within the detector tank, the MCP detector has a movement of 825mm , in the X axis, on an automated translation stage. It is also possible to manually move the detector in the Y and Z axes. The detector chamber opens onto a clean room to allow space instruments to be tested. Images provided by Dr. J. Pearson, UoL.

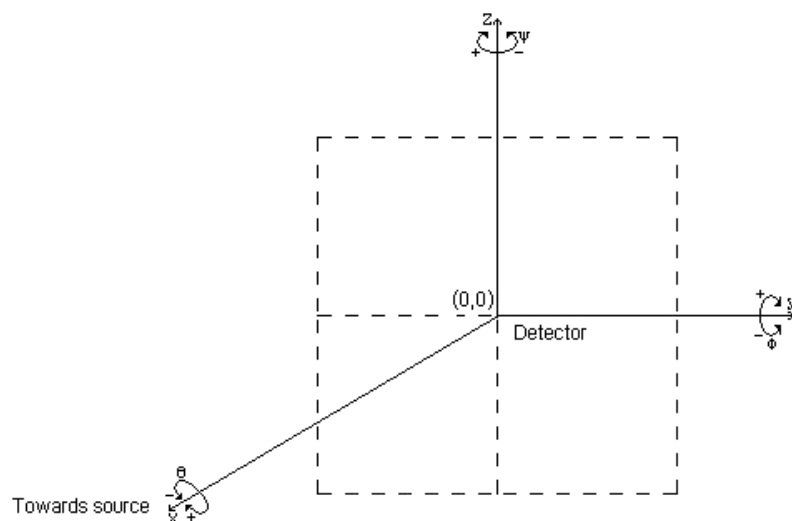


Figure 2.48: A diagram demonstrating the TTF axes. The $(0,0)$ point is the centre of the detector's nominal field of view and the X axis is down the beam line away from the detector, towards the source. The detector is moved in the X axes using automated motors and can be moved manually in the Y and Z axes.

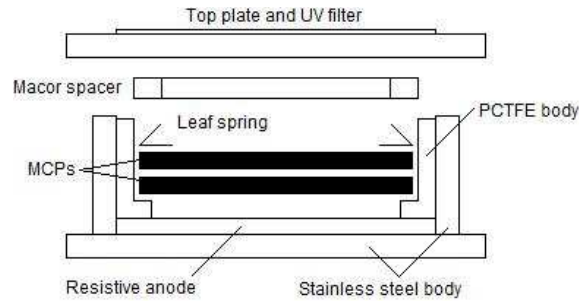


Figure 2.49: The set up of an MCP detector with a resistive anode where two MCPs are arranged behind a UV filter. A high voltage is applied to direct the electron cloud down the channels of the MCPs, towards the resistive anode. Two MCPs are used to multiply the signal.

such that the electrons exiting the first plate are directed towards the corresponding channels in the second plate thus multiplying the signal. As the electron cloud moves down the secondary plate, a second exponential cascade is created which eventually lands on the resistive anode as a charge dump. The four electrodes at the corners of the resistive plate each receive a proportion of the total charge dumped on the anode, as shown in figure 2.51 and these proportions are then translated back into X and Y positions using equation 2.11. The computer which controls the automated translation stage also collects the information from the resistive anode and converts the data into an image.

$$X = \frac{X_2}{(X_1 + X_2)}, Y = \frac{Y_2}{(Y_1 + Y_2)} \quad (2.11)$$

Unfortunately, the way the data are read from the detector causes a pin cushion effect on the detected image, where the edges of the image are compressed. The detected image is linearized to correct for this by taking another image of a regular series of pin holes whose actual positions are known. A local polynomial fit is completed between the detected positions and the actual positions of the pin holes creating a look up table and the image is linearized by linear interpolation within the cells of the table. An unlinearized image and a corrected image of the pin holes are shown in figure 2.52.

The linearization routine works well for most of the image, however, it loses accuracy towards the edges. This is due to some distortion in the original image which made the precise centre of each of the holes difficult to locate. In addition, the curvature of the distortion is highest at the edges so the polynomial fit requires

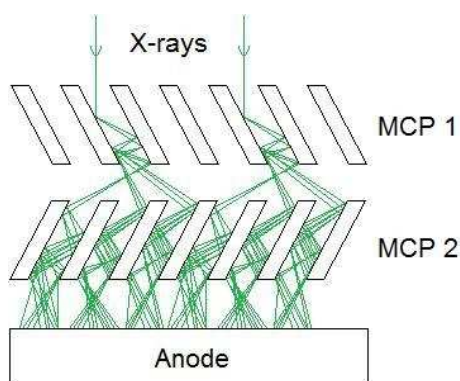


Figure 2.50: Two charged MCP plates, with channel walls in a chevron configuration at an angle of 13° , in front of a resistive anode. The X-rays which reach the detector (shown in green), interact with the walls of the first MCP plate which causes an exponential cascade of electrons. The field between the two plates is such that the electron cascade is directed from the first plate, down the corresponding channel of the secondary plate. Once the electron cloud has cascaded down the second MCP plate, it is dumped onto the anode.

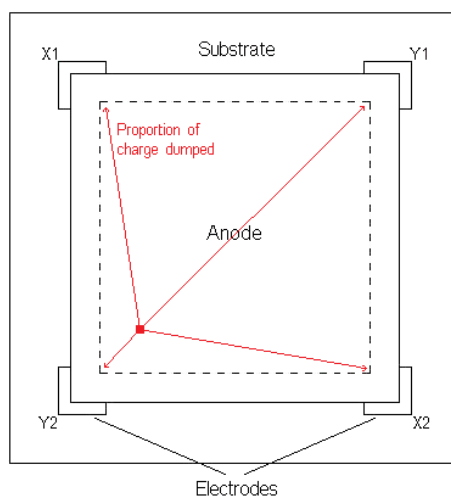


Figure 2.51: The resistive anode behind the two MCP plates within the detector system. It consists of a resistive plate and four electrodes at the corners, which are labeled $X1$, $X2$, $Y1$ and $Y2$. Each electrode receives a proportion of the charge which has been dumped on the resistive plate. These proportions are then translated into X and Y positions using equation 2.11

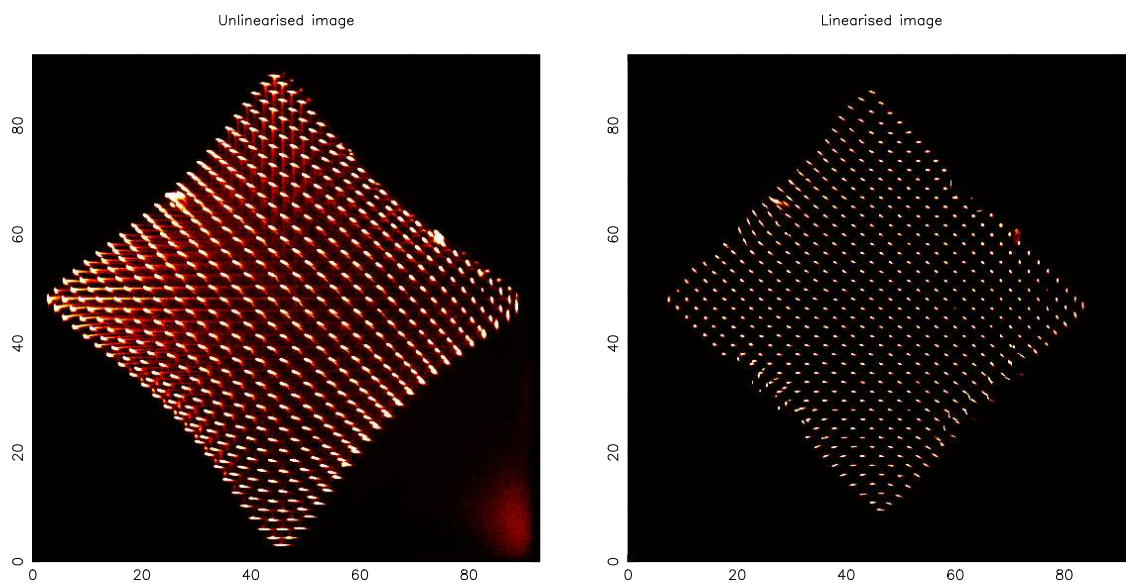


Figure 2.52: An unlinearized is shown on the left and a linearized image of the regular series of pin holes is on the right. Due to the nature of the read out from the MCP detector, a pin cushion effect is created in the detected image and to correct for this, an image is taken of a series of regularly spaced pin holes whose real positions are known. These positions are compared to the detected image's positions using a local polynomial fit. A look up table is then created which is used to correct any images which have been obtained with the same detector. The linearization of the edges of the image is not very good for two reasons: firstly, there was some distortion on the original image which made it difficult to find the precise position of the centre of the holes at the edge; and secondly, the curvature is greatest at the edges and the polynomial fit therefore needs more terms. As the data obtained is within the central region of the detector, the effect at the edges is unimportant.

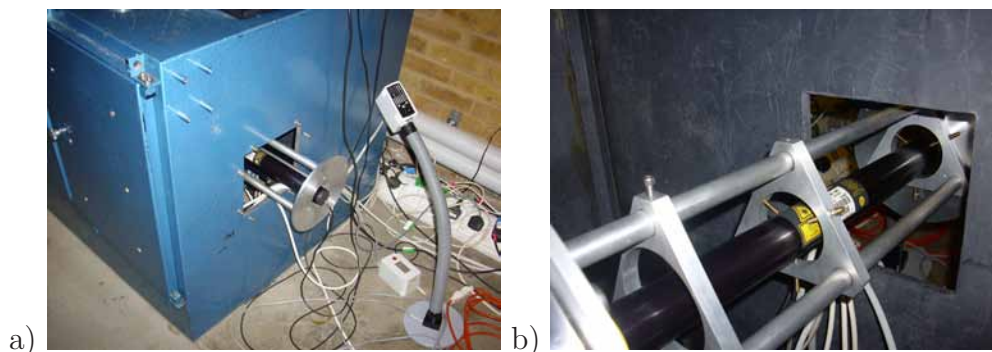


Figure 2.53: a) The laser in place of the X-ray source to enable alignment of the optic within the facility. b) The view of the laser from within the blue X-ray source cage.

a larger number of terms which take longer to calculate, but this did not cause a problem as the area of interest was the centre of the detector which is effectively linearized with this routine.

2.10 X-ray tests carried out within the TTF

2.10.1 Alignment and set up

Once the mirror had been positioned within the facility, the X-ray source was replaced with a laser in order to be able to align the mirror. Figure 2.53 shows the laser in place of the source within the source chamber. The detector was shielded and a piece of paper was used to monitor the reflected beam. Images were taken with a standard, $6Mpixel$ digital camera to record the changes produced by moving the optic. Figure 2.54 is an example of such an image, where the exit aperture of the detector chamber was covered with paper to show the reflection from the mirror and the optic intersecting the straight through beam.

A piece of paper with a mark on it was used to indicate the calculated position of the detector. As the optic was aligned, it was possible to move the reflected beam to be in line with that mark and therefore the optic would be in the correct position. Figure 2.55 shows three images of the change in the reflected beam as the optic was aligned. The mark used for alignment is visible in the second and third images and the size of the reflection was also reduced during this process. During the alignment tests of the optic, it was found that the motors controlling the pitch and yaw of the mirror occasionally stuck and would not be capable of moving the

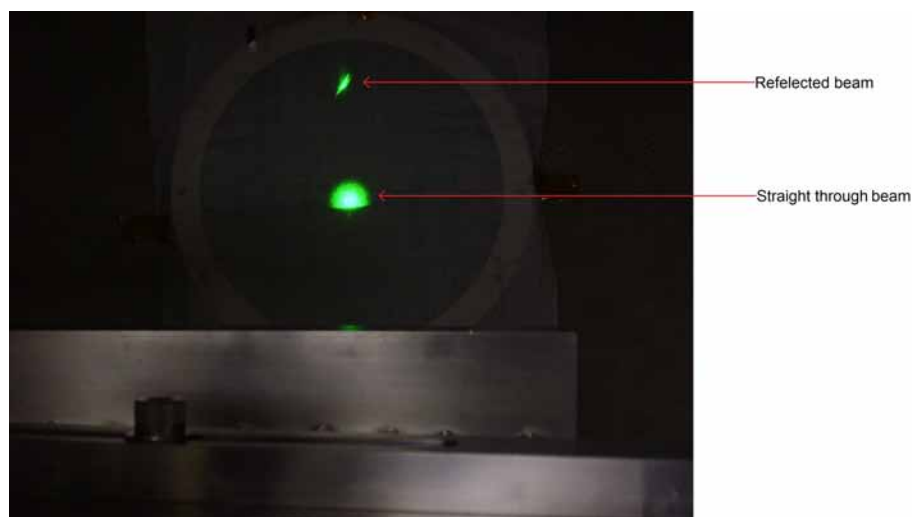


Figure 2.54: An example of the images taken during the alignment of the optic within the TTF using the laser as the source. The exit aperture of the detector chamber was covered with paper to form the image, both the reflected beam and the mirror intersecting the straight through beam from the laser are visible.

optic in a predictable or repeatable way. This combined with time constraints within the facility, led to the decision that the optic would remain in the position shown in figure 2.55 c), instead of trying to locate the optimum position.

In order to be able to locate the reflected beam from the X-ray source, the detector needed to be moved in the positive Z axes by 141.06mm , due to the tilt in the ellipse axes from the TTF axes (section 2.4 and shown in figure 2.48). Two steel rods were manufactured to support the detector during the X-ray tests (figure 2.56).

So as to excite the required X-ray emission lines, the copper anode of the source was coated in a thin layer of NaCl in order to excite the sodium K line at 1.04keV and the chlorine K line at 2.62keV . Figure 2.57 shows the copper anode coated in the thin layer of NaCl.

Once the optic was in position; the detector had been put in place and the laser had been replaced by the X-ray source coated in NaCl, the TTF was pumped down to a vacuum. The motors and piezoelectric devices had also been connected up to the computer control at this point. A series of thirteen images were taken whilst moving the detector in and out of the focus of the optic to determine the best position in the X axes for the detector. The X-ray first light image is shown in figure 2.58 and further examples of X-ray images obtained during the experiments

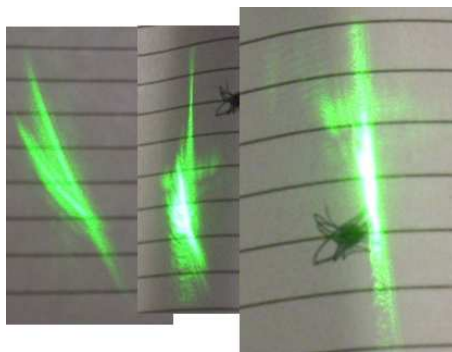


Figure 2.55: Three images showing the change in the reflected beam. Left, the “first light” image obtained with the laser. Middle, an intermediate stage of alignment and right, the final position of the optic after alignment. The calculated position of the detector is shown as a black mark in the middle and right images.

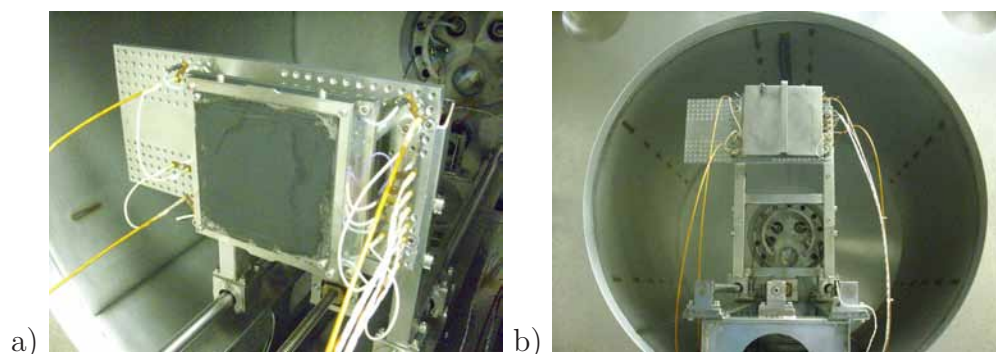


Figure 2.56: a) The detector in its original position and b) in the new position, raised by 141.06mm , required for the X-ray tests.



Figure 2.57: The copper anode of the X-ray source coated in a thin layer of NaCl to excite the emission lines required for the X-ray tests.

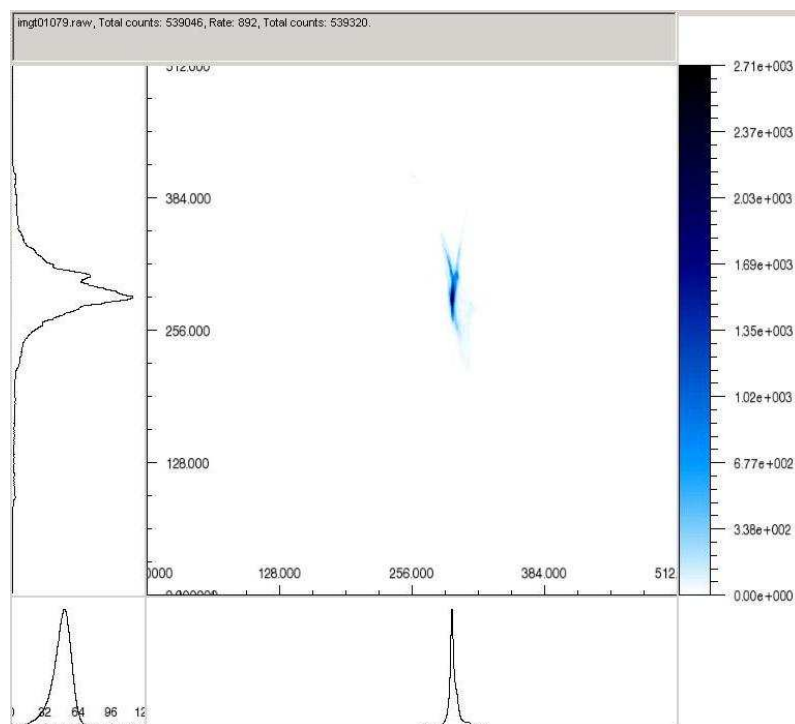


Figure 2.58: The first X-ray image obtained during the X-ray tests. The histogram on the X axis is the total integration across the height of the plate and the histogram on the Y axis is the total integration across the width of the plate. The colour bar on the right shows the maximum number of counts detected in any one position and the graph in the bottom left corner is the pulse height of the signal received by the anode. The header of the image shows the image name, total number of counts detected in the image and the count rate.

are shown in figure 2.59. In all of these images, the histogram on the X axis is the total integration across the height of the plate and the histogram on the Y axis is the total integration across the width of the plate. The colour bar on the right shows the maximum number of counts detected in any one position and the graph in the bottom left corner is the pulse height of the signal received by the anode. The header of the image shows the image name, total number of counts detected in the image and the count rate.

2.10.2 Testing plan

A series of X-ray tests were designed to test the theory of the LAXRO and to examine the influence of the piezoelectric devices and the condition of the mirror. A new set of fourteen local group patterns were also designed to control the piezoelectric devices during these tests as they were simple and represented the deformation seen

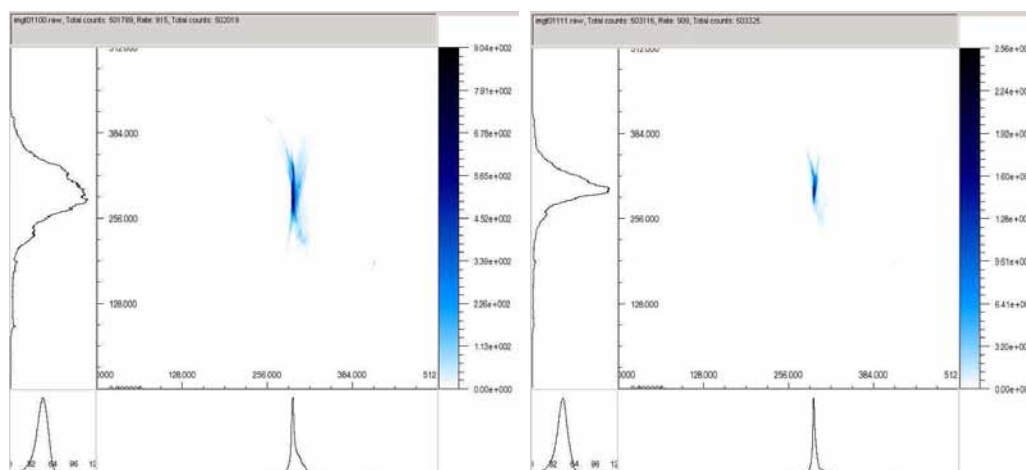


Figure 2.59: Further examples of X-ray images obtained during the X-ray experiments carried out within the TTF. The histogram on the X axis is the total integration across the height of the plate and the histogram on the Y axis is the total integration across the width of the plate. The colour bar on the right shows the maximum number of counts detected in any one position and the graph in the bottom left corner is the pulse height of the signal received by the anode. The header of the image shows the image name, total number of counts detected in the image and the count rate.

on the optical surface. Figure 2.60 shows the series of patterns described. Patterns three to twelve are just actuating the individual columns of piezoelectric devices in turn. These patterns were actuated between $-100V$ and $+100V$ at eight voltage steps with approximately 500,000 counts in each image. During this period, images with the piezoelectric devices set to $0V$ were also taken for comparison and to show the stability of the total system over time.

The detector was then moved to a position intra focus of the optic, to complete an experiment similar to the Hartmann test (section 2.11.2), and a series of patterns actuating the devices in groups of four were used to determine which areas of the mirror influenced the reflected beam. These patterns were actuated at voltages of $-100V$ and $+100V$ only.

The stability of the devices were also tested by setting the actuators in to a pattern which forced neighbouring devices into opposite voltages for long periods of time. This was repeated twice, once with the devices held for one hour with images taken every ten minutes and secondly held for five hours with images taken every twenty minutes. All the images were compared to determine the stability of the devices. The stability of the piezoelectric device's power source was also tested at UCL.



Figure 2.60: A series of fourteen local group patterns to control the piezoelectric devices during the X-ray tests. The white areas indicate the actuators which are active (with a value of +1) whilst the rest remain passive (with a value of 0). The voltage applied to each individual piezoelectric is calculated by taking these values and multiplying it by the voltage iteration value. Patterns three to ten are each of the columns of devices actuated in turn.

2.11 Results from the TTF

Several problems were encountered during the first prototype tests in the TTF at UoL. The first involved the motors which were designed to adjust the pitch and yaw of the optic. The specification of the motors was incorrect which led to them being ineffective during the tests so the results could not be corrected for in these two directions. The second problem involved the measurements of the centroid position of the flux which had to be found by eye. This led to incorrect optimisation, i.e. not finding the true optimum voltage of each pattern. Subsequently, it has been found that all calculations of the centroid position and therefore the HEW or FWHM of the image have to be completely calculated within the software.

2.11.1 Full adjustment of the piezoelectric devices

For the purposes of the first X-ray tests, the series of local group patterns (figure 2.60) were used to control the piezoelectric devices due to the nature of the figure of the mirror's surface. Even though the optic had a lot of print-through from the attachment of the actuators, which could not be removed, the detected image was easily influenced by the piezoelectric devices. Figure 2.61 shows the HEW and FWHM results of the full iteration of the fourteen local group patterns. The HEW

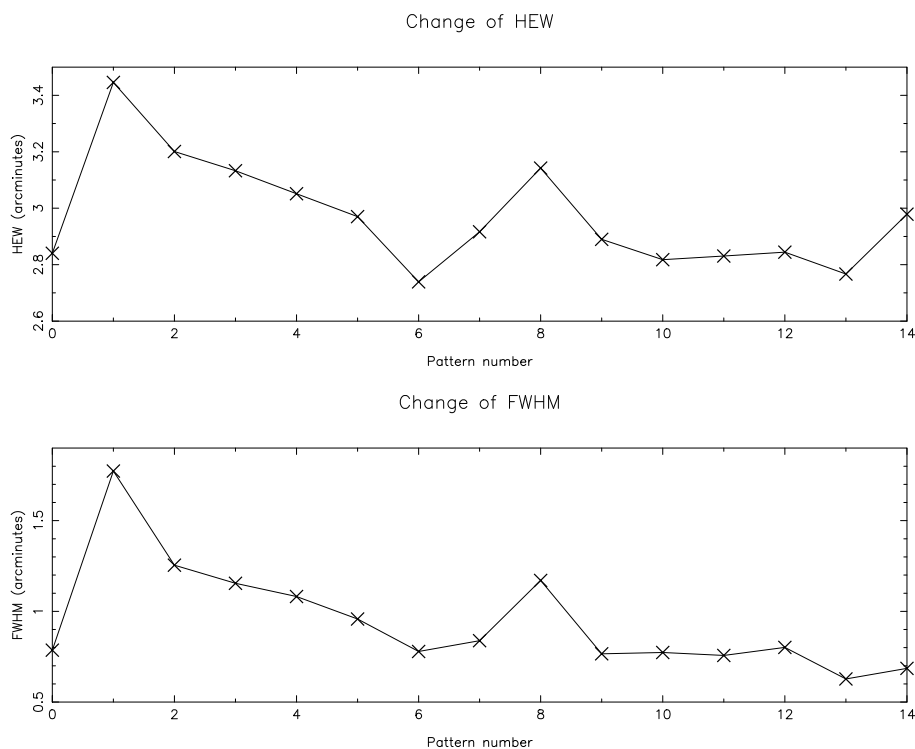


Figure 2.61: HEW and FWHM results from the full adjustment of the piezoelectric devices during the X-ray tests. The pattern number refers to the patterns described in figure 2.60. The HEW or FWHM were improved by a few patterns but not in a predictable way.

and FWHM values have been calculated from the original data and using the Q software. Here, the a circle is specified around the area of interest and the HEW and FWHM are then calculated by taking the flux from within the area of that circle. In a few cases both the HEW and FWHM were improved although this was not in a predictable way as the pitch and yaw errors could not be removed and the optimisation routine was not fully controlled by the software.

The optimum voltages obtained for each of the piezoelectric devices are shown in table 2.5 and graphic representations are shown in figure 2.62. Although it has since been shown that this was not in fact the true optimum, these voltages were used for the experiments at STFC Daresbury Laboratory as described in section 2.12.

Multiple images with the piezoelectric devices set at $0V$ were taken at the start and end of each day and during the adjustment routine. This also included images where the power supply to the piezoelectric devices was switched on and off, as demonstrated by the LTP data shown in figure 2.31. The HEW and FWHM of these images were plotted against the time in days and the total number of actuations completed and are shown in figure 2.63. The HEW results (on the left hand side)

Device 21	Device 22	Device 23	Device 24	Device 25	Device 26	Device 27	Device 28	Device 29	Device 30
40.000	40.000	100.00	100.00	52.663	52.663	52.663	52.663	22.663	67.663
Device 11	Device 12	Device 13	Device 14	Device 15	Device 16	Device 17	Device 18	Device 19	Device 20
40.000	100.00	100.00	100.00	70.118	70.118	70.118	70.118	40.118	25.118
Device 1	Device 2	Device 3	Device 4	Device 5	Device 6	Device 7	Device 8	Device 9	Device 10
100.00	100.00	100.00	100.00	52.663	52.663	52.663	52.663	-37.34	7.6630

Table 2.5: Optimum voltages calculated for each of the piezoelectric devices, from the full adjustment routine during the X-ray tests.

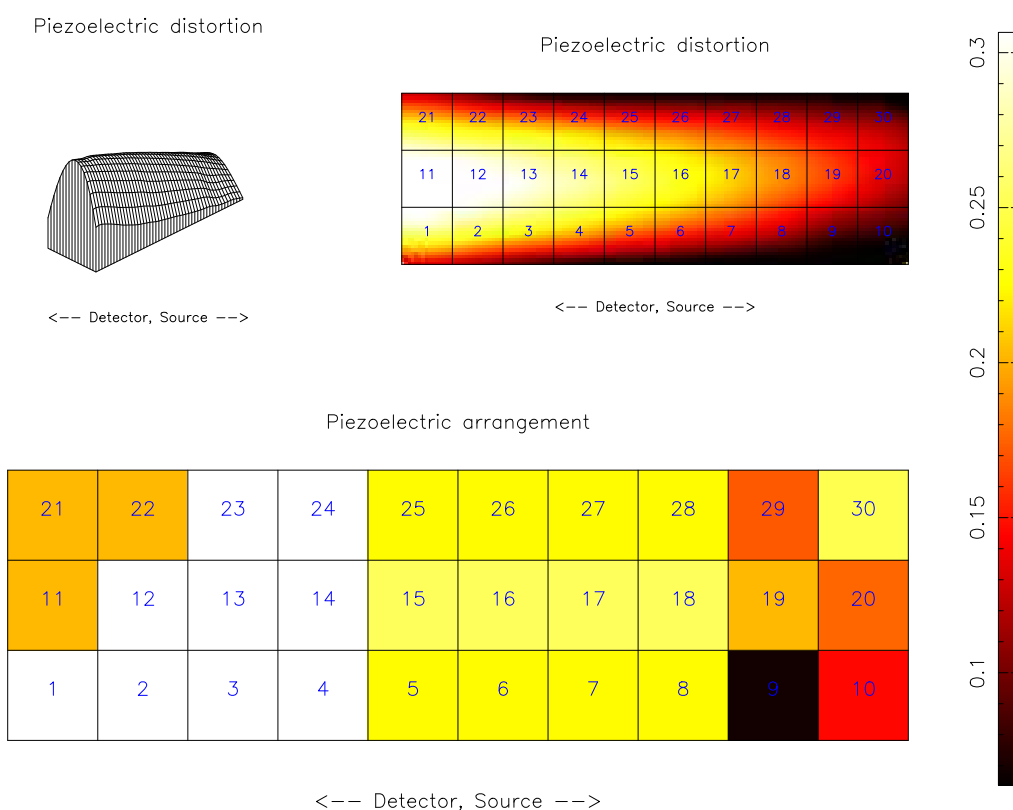


Figure 2.62: Optimum voltages obtained from the full adjustment routine during the X-ray tests. The top left is a 3D representation of the shape of the optic with the voltages shown in table 2.5, top right is a colour representation of the optic shape and the bottom image is a representation of the voltages applied where black is -40V and white is +100V.

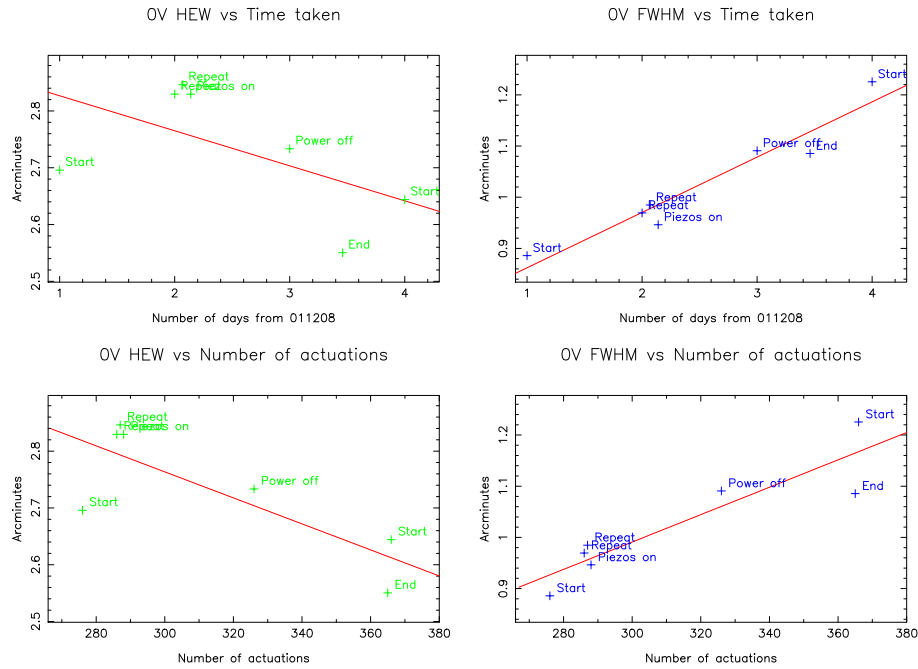


Figure 2.63: Graphs demonstrating the HEW and FWHM changes in each of the images taken with the piezoelectric devices at 0V. The HEW images are on the left and the FWHM are on the right. The top frames show the change over a period of days from the start of testing, whilst the lower frames show the changes over successive actuations of the devices. Both show a trend of decreasing HEW and increasing FWHM over time.

clearly show a decreasing trend over the time period whilst the FWHM results (on the right) show an increasing trend. There is some form of stability problem which is evident and is most likely due to the uneven glue layer which has caused some form of plastic memory in the optic. The temperature within the facility remained constant ($\pm 1^\circ$) throughout the tests so any form of temperature sensitivity is ruled out.

2.11.2 Hartmann test

The Hartmann test was derived in the early part of the 20th century in order to correct for errors in a mirror's form[70]. The process consists of using a pinhole mask in front of the optical system and then taking images at two points, either side of the focus, as shown in figure 2.64. By reconstructing the paths of the rays between the two pinholes, one on each plate, it is possible to calculate the errors in the mirror's form.

A test, similar to the Hartmann test was devised, where groups of actuators were

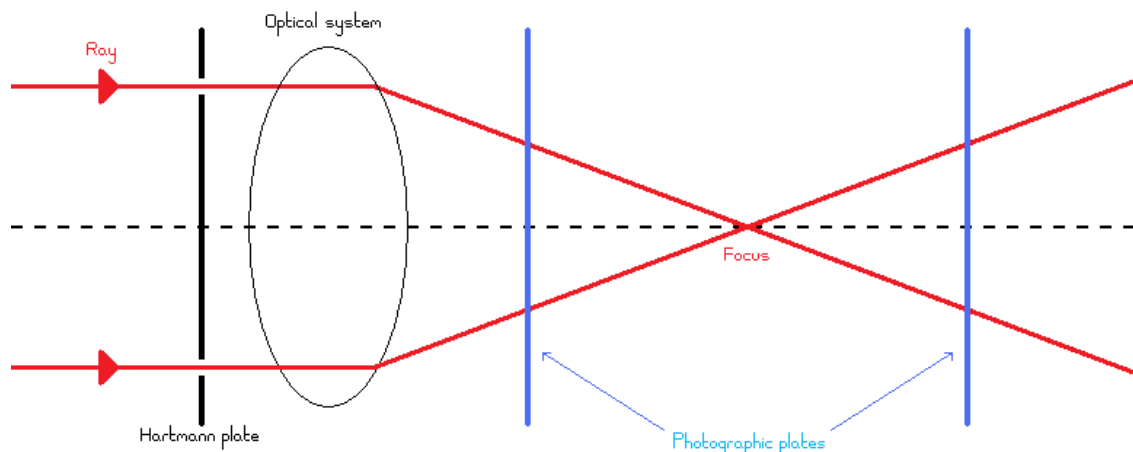


Figure 2.64: An illustration of the Hartmann test, designed to calculate the errors within an optical system. By reconstructing the paths of the rays between two photographic plates, it is possible to calculate the errors in the mirror's form.

used instead of pinholes and only one image was taken with the detector at a position of 559mm in the X axes, into the focus of the mirror. The piezoelectric devices were then actuated in groups of four, creating ten patterns, at $+100\text{V}$ and -100V only, to show how each part of the mirror affected the different areas of the reflected beam. Each of the images had the initial image with no actuation, subtracted off to show the areas which had changed. The central region of the detected flux and the left and right hand sides were studied as each group was actuated. Some selected results are shown in figure 2.65 where histograms of the changes are shown alongside an illustration of the piezoelectric devices being actuated. Each graph consists of three panes with the top representing the left hand side of the image, the middle representing the central region and the bottom representing the right hand side. The data from the $+100\text{V}$ images are shown in black whilst -100V are shown in red. As the ends of the optic could move more freely, these had more of an influence on the detected image and the influence of the middle patterns were almost identical to one another. For this reason, only two patterns from the central area of the mirror are shown. These graphs demonstrate that as the left hand side of the optic is actuated, the left hand side of the image is adjusted and so on, as expected.

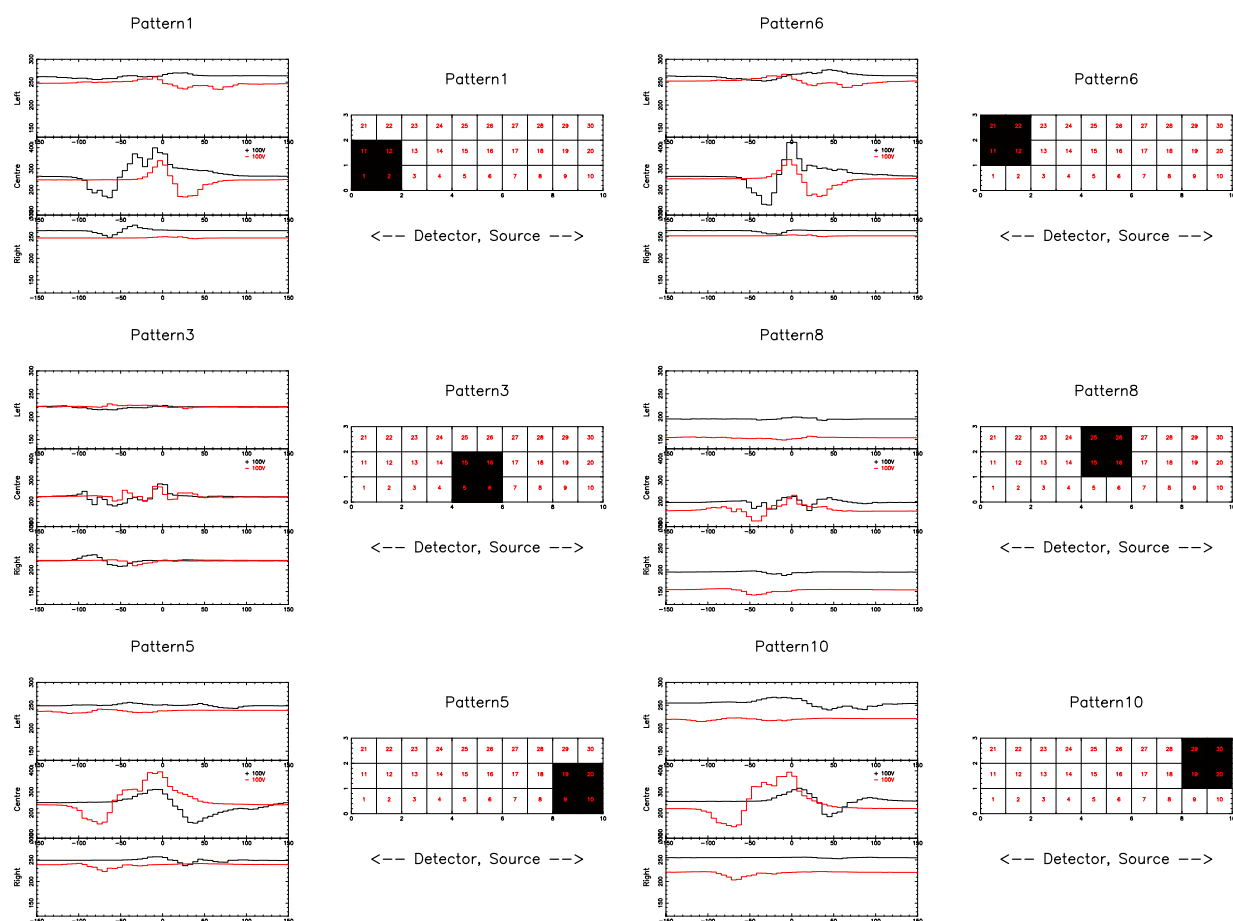


Figure 2.65: The results from the Hartmann test. Histograms of the changes are shown alongside an illustration of the piezoelectric devices being actuated. Each graph consists of three panes with the top representing the left hand side of the image, the middle representing the central region and the bottom representing the right hand side. The data from the +100V images are shown in black whilst -100V are shown in red.

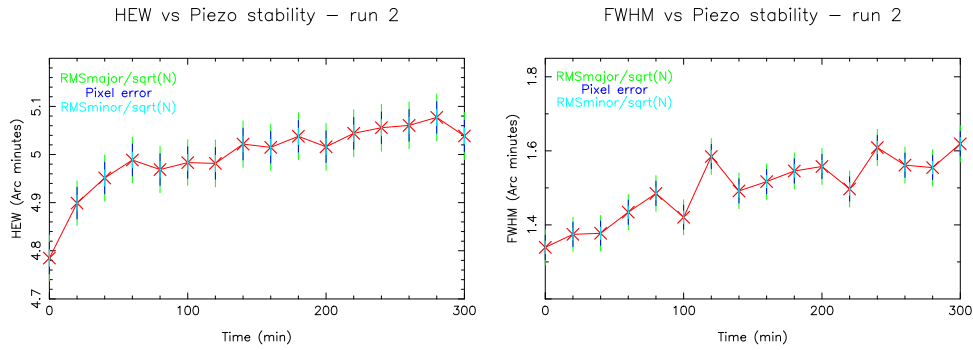


Figure 2.66: Results of the second piezoelectric stability tests. The actuators were held for five hours in a pattern which forced each adjacent actuator into an opposite voltage to its neighbour. The HEW results are on the left and FWHM are on the right and demonstrate a drift of $17.53''$.

2.11.3 Stability of the piezoelectric devices

The stability of the piezoelectric devices is essential for X-ray adaptive optics as the precise mirror figure of large scale X-ray telescopes will need to be maintained for long periods of time. Two tests of the stability of the devices were completed during the testing period, where the actuators were held in a complicated pattern (bottom right of figure 2.40) for a period of time. The first stability test held the actuators in the pattern for one hour with images taken every ten minutes. These images consist of approximately 140,000 counts which means the data and results are governed by statistics. For this reason a second series of images were taken with the actuators held for five hours with an image taken every twenty minutes containing up to 500,000 counts per image. The results are shown in figure 2.66 with the HEW results in the left frame and the FWHM results in the right. The FWHM and the HEW showed a steady increasing drift over the time period of $17.53''$.

The stability of the power supply for the piezoelectric devices was tested at UCL using an oscilloscope, where the voltages were measured over five hours with data taken every ten minutes for the first hour and every twenty minutes for the remaining four hours. The drift of the HEW and FWHM was not due to the power supply fluctuations as this was found to have a stability of $5mV$ over the period, which is equivalent to $1.29 \times 10^{-3}''$. The results obtained from this test are shown in figure 2.67.

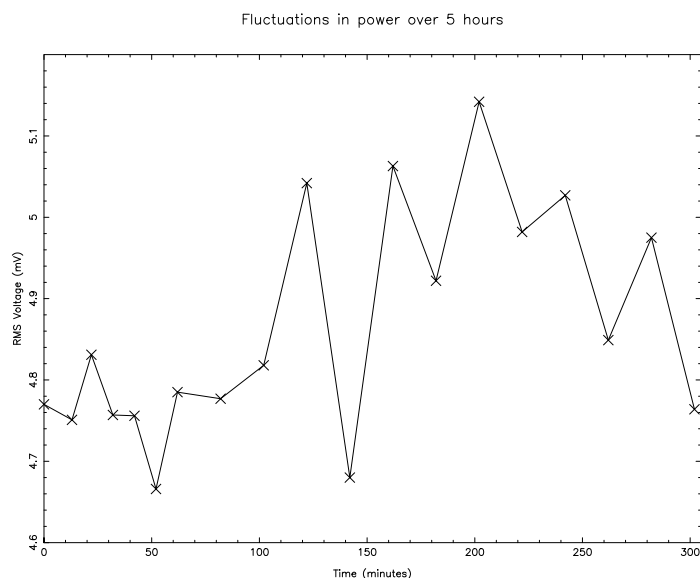


Figure 2.67: The stability of the power supply for the piezoelectric devices over a five hour period tested at UCL. Data was taken every ten minutes for the first hour and every twenty minutes for a further four hours.

2.12 Further tests carried out at STFC Daresbury Laboratory

Once the X-ray tests had been completed at UoL, further experiments were completed at STFC Daresbury Laboratory which involved scans across the optics surface with the piezoelectric devices actuated. The tests were completed in an identical way to those described in section 2.6. Figure 2.68 shows the scan taken across the surface with the piezoelectric devices set to the optimum voltages found during the X-ray tests (as shown in table 2.5). The lower frame in this image shows the change in the mirror's form due to the piezoelectric devices being actuated.

By actuating the piezoelectric devices, “kinks” at the joins of the actuators were created, similar to the junction effect seen on synchrotron mirrors. These kinks are $\sim 3\mu m$ in size and are due to the gaps between the piezoelectric devices and the thickness of the glue layer, as shown in models produced at UCL and UoB and described in section 2.13. This means that any actuation of the piezoelectric devices would be causing deformations which cannot be removed and therefore make the resolution of the optic worse. It is therefore vital to improve the bonding techniques and to control the glue thickness as well as decrease the gaps between the actuators.

Scans across three piezoelectric devices were taken whilst the central piezoelectric

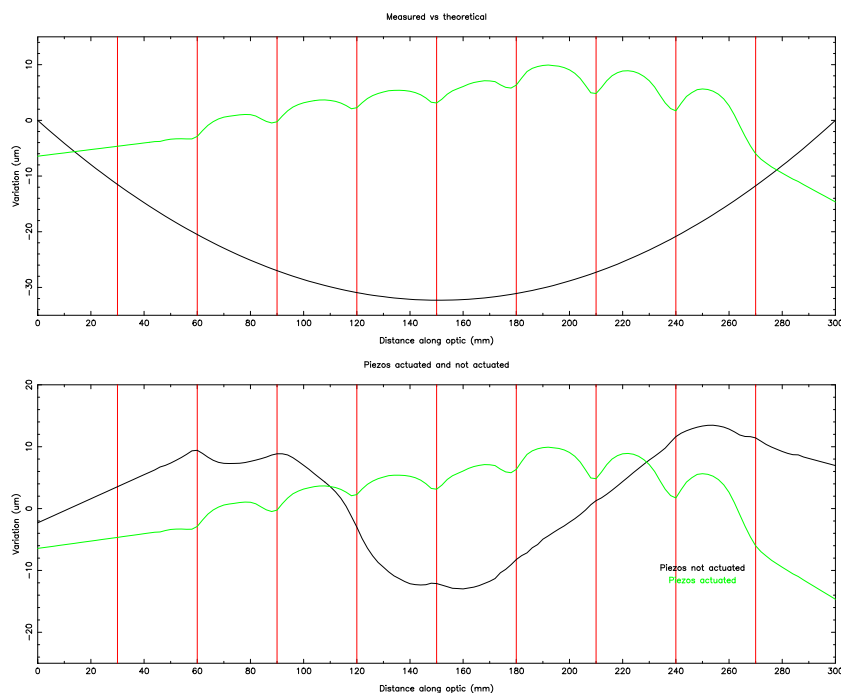


Figure 2.68: Scans of the optic’s surface using the LTP at STFC Daresbury Laboratory with the piezoelectric devices actuated at the optimum voltages determined during the X-ray tests. The top graph shows the single scan with the theoretical curve the optic should have had. The bottom graph shows the change in the figure of the mirror between the piezoelectric devices being actuated and not actuated. The positions of the piezoelectric devices are shown in red.

device of the three was actuated in order to calculate the actual influence function of the devices. Each device would act slightly differently due to the variation in glue thickness and the position on the mirror’s surface as the devices at the ends and edges would have more influence than those in the middle. Piezoelectric device 17 was studied in this way and the results are shown in figure 2.69. Models of the scans were completed at UCL using COMSOL Multiphysics and are also shown in the image. These models did not include the glue thickness and this is clear in the difference in the piezoelectric joins which are shown in black. There is a great similarity in the heights which shows that the influence of the device is very similar to the models. This indicates that the variable glue layer has not affected the influence of the piezoelectric actuator, just the boundaries of the influences is affected. The heights of the models vary from the real data by approximately $2\mu m$, although the real data shows a higher influence achieved at $-50V$ by almost the same amount. There is a definite boundary between the different actuators in the real data, however, the models suggest that the influences of the devices should expand

Actuation of Piezoelectric 17

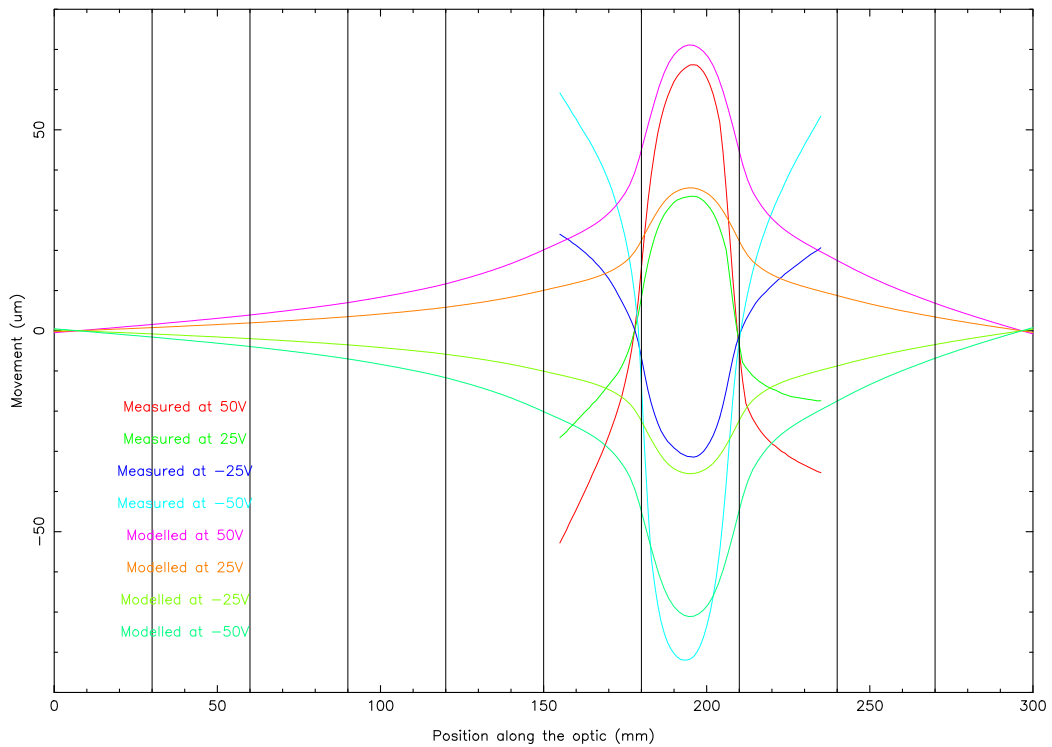


Figure 2.69: Scans taken along the surface of the mirror with piezoelectric 17 actuated, shown alongside the modelled data and the position of the piezoelectric devices shown in black. The difference between the measured and modelled data is due to the glue thickness which causes the kinks in between the actuators but does not appear to change the influence of the device.

across the whole mirror. The lack of glue and the size of the gaps in between the actuators causes those areas to act more strongly against one another than the model predicted, causing the distinct junctions in between the piezoelectric devices. These junctions are on a scale which cannot be removed by the actuators and so must be prevented as these bumps in the surface figure would affect the resolution and performance of the optic.

2.13 Further modelling of the large scale prototype

As the local group patterns were used for the full iteration routine, models were completed in Q to determine whether or not the mirror's resolution could be improved by the piezoelectric devices by simulation. The models described here are identical to those shown in section 2.8 where the patterns were ordered in terms of

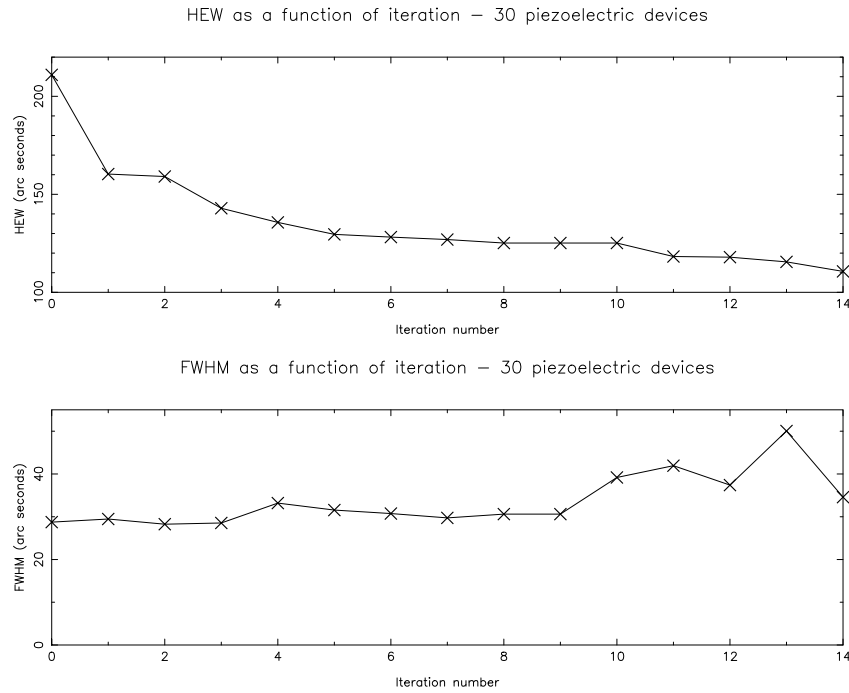


Figure 2.70: The results of the iterative routine in Q using the local group patterns and the LTP data of the optic with the piezoelectric devices turned on. In this routine, the patterns were ordered based on their influence on the HEW. Here the HEW was reduced from 3.46' to 1.84'. The top graph shows the change in HEW and the bottom graph shows the effect on the FWHM based on the pattern iteration.

their influence on the simulated HEW of the optic and then a complete adjustment routine in Q was run. The results are shown in figure 2.70 where the HEW was reduced from 3.46' to 1.84'. This was then repeated with the patterns ordered in terms of their voltages and the HEW was reduced to 1.79' (results in figure 2.71). Both results show a similarity to those found using the FFT patterns. This shows that for any series of patterns, there is no single solution and that for any group of patterns, the number of patterns which have any real effect on the HEW is in the order of two to four. Figure 2.72 shows the initial optic distortion at the top, the actuator distortion shown in figures 2.70 and 2.71 in the middle, with the combination of the two at the bottom. These results also suggest that for any given optical distortion there is no single solution.

A series of models were also completed with an extended voltage range, from -250V to +250V, and reducing the LTP data by a factor of ten, to test the full limits of the influence functions and the adjustment algorithm. The results from these models were limited to a 50% reduction in HEW suggesting this is a real limitation

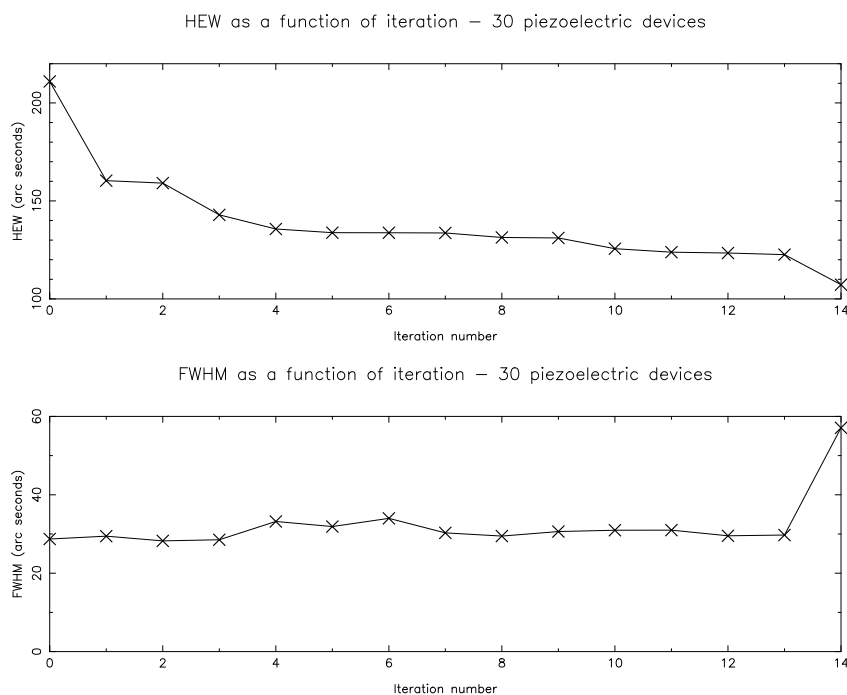


Figure 2.71: The results of the iterative routine in Q using the local group patterns and the LTP data of the optic with the piezoelectric devices turned on. In this routine, the patterns were ordered based on their optimum voltage. Here the HEW was reduced from 3.46' to 1.79'. The top graph shows the change in HEW and the bottom graph shows the effect on the FWHM based on the pattern iteration.

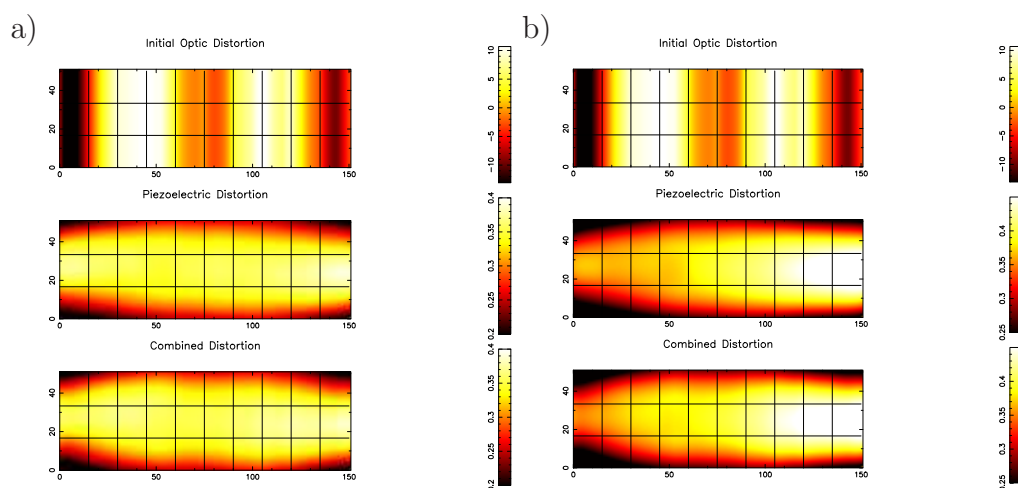


Figure 2.72: The top images represent the starting mirror deformation, the middle figures are the piezoelectric distortion from a) figure 2.70 and b) figure 2.71 and the lower figures are the combination of the top two. These images demonstrate that for any series of patterns and initial mirror figure deformation, there is no single solution.

and not just based on the size of the influence functions, voltage ranges or initial distortion.

A new initial distortion was created for the Q models by randomly summing the FFT patterns at various voltages, creating a distortion whose result was known. The distortion was set to have a simulated HEW of 21.45" and without any distortion, the optic's HEW was measured to be 1.81", a difference of 91.5%. Using the algorithm, the HEW was reduced by 85.6% after all the patterns had been iterated twice, indicating that with enough time, the algorithm can find the result to a distortion which is a linear sum of the FFT patterns. This result indicates that there are gross errors in the optic's form and high frequency errors on the mirror's surface due to the piezoelectric devices, which cannot be removed by the actuators and there is a real limit to the possible reduction with the current quality of the mirror and the patterns being used. It may be possible to create a series of patterns which could reduce the HEW further, however, these would still be limited by the influence functions of the actuators, as each actuator affects a large region around it.

Using the data from the LTP scans of the mirror surface whilst the piezoelectric devices were actuated, it was possible to use Q to model the optic. As with the original LTP data (section 2.7.3), it was added as a deformation matrix with extrapolated edges to cover the full length of the mirror. Q was then used to ray trace the optic and the detector and mirror were adjusted until the lowest HEW was found. Figure 2.73 shows the ray traced result which gave a HEW of 2.14'.

Unfortunately the scan across the optic only covered the central axial area of the mirror and so this scan was expanded over the width of the optic. This was not a true representation of the mirror's figure so more models were completed at UCL using COMSOL Multiphysics. COMSOL Multiphysics requires the mirror to be fixed by at least two points and cannot be floating in free space. Two models were produced by setting the fixed points at the four corners (4 corner mounting) and then at two points at the centre of the radial edges (2 point mounting). The simulated piezoelectric devices were actuated at the optimum voltages calculated during the X-ray tests at UoL (table 2.5). A glue layer of 0.5mm was added to the model between the optic and the piezoelectric devices as this was shown to give $\sim 3\mu\text{m}$ kinks in the joins between the actuators, as was seen in the LTP data. These

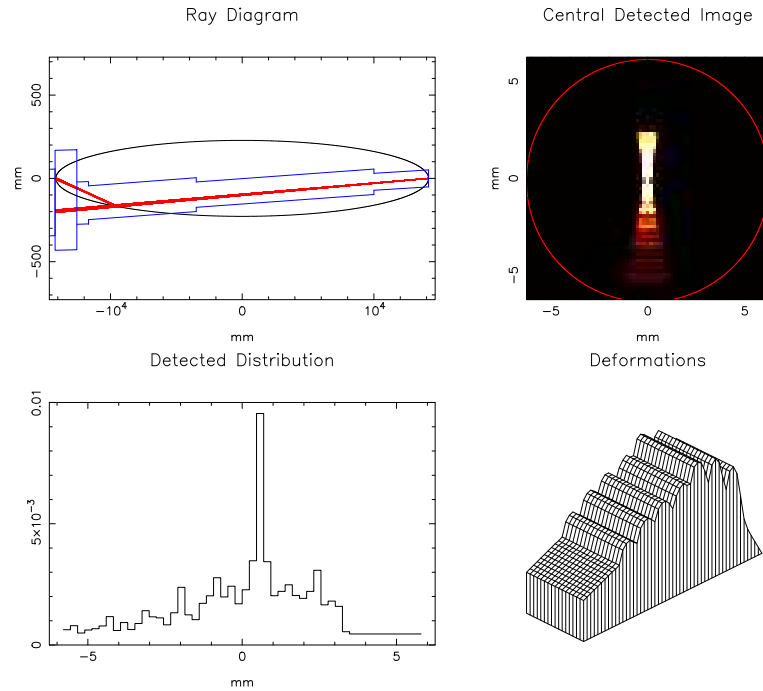


Figure 2.73: Ray traced model in Q of the LTP data taken with the piezoelectric devices actuated at the optimum voltages found during the X-ray tests, table 2.5. The simulated HEW for this deformation matrix was found to be 2.14'.

models were included in the Q models using deformation matrices and the HEWs calculated for the four point mounting and two point mounting were calculated by simulation to be 2.92' and 2.07' respectively and the results are shown in figures 2.74 and 2.75.

After analysing all the results from the X-ray tests, it is believed that the majority of the error in the figure of the mirror was due to the errors in the curvature of the segment. Further segments have been produced and used to analyse the shape of the mirror and have shown that for some reason the mirror's curvature tightened up when released from the mandrel. This means that instead of having a radius of curvature from $165.3mm$ to $169.8mm$ it had a radius from $155mm$ to $160mm$. This has been modelled in Q and the resultant simulated HEW was found to be 2.44' after the detector's position and orientation of the mirror had been optimised. By combining this error with the error from bonding the piezoelectric devices onto the mirror, the HEW obtained by ray-tracing was 2.62'. The ray traced results are shown in figures 2.76 and 2.77 respectively.

A summary of all the models, the results from the models and results from the X-ray data, are shown in table 2.6. The comparisons between the models produced and

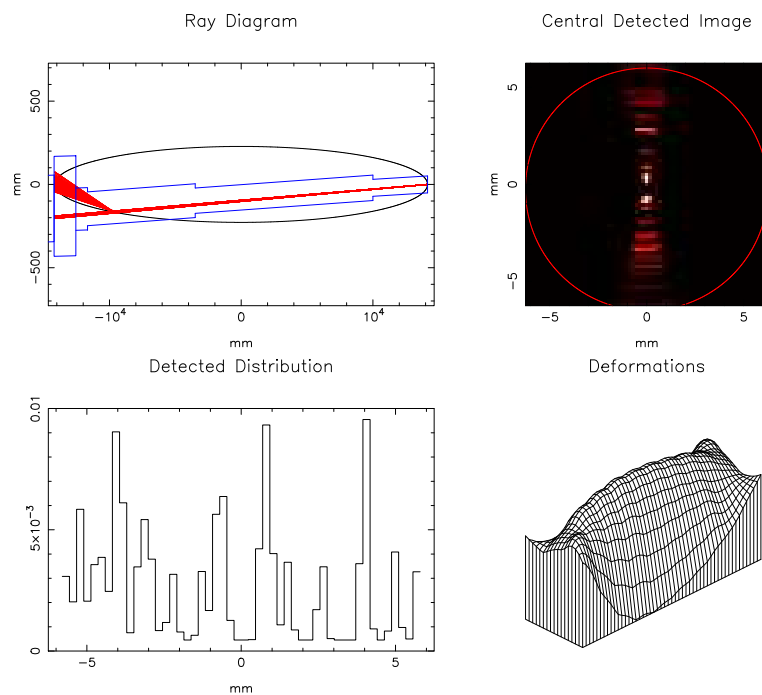


Figure 2.74: Ray trace in Q of the model created with the optic fixed at the four corners and the piezoelectric devices at the optimum voltages found during the X-ray tests. The simulated HEW found with this model was $2.92'$.

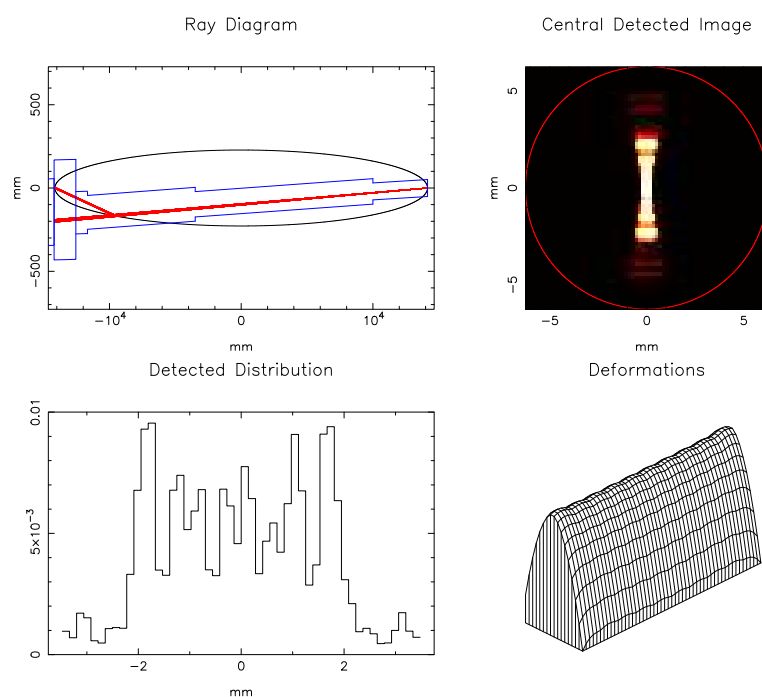


Figure 2.75: Ray trace in Q of the model created with the optic fixed at two points at the centre of the ends of the mirror and the piezoelectric devices at the optimum voltages found during the X-ray tests. The simulated HEW found with this model was $2.07'$.

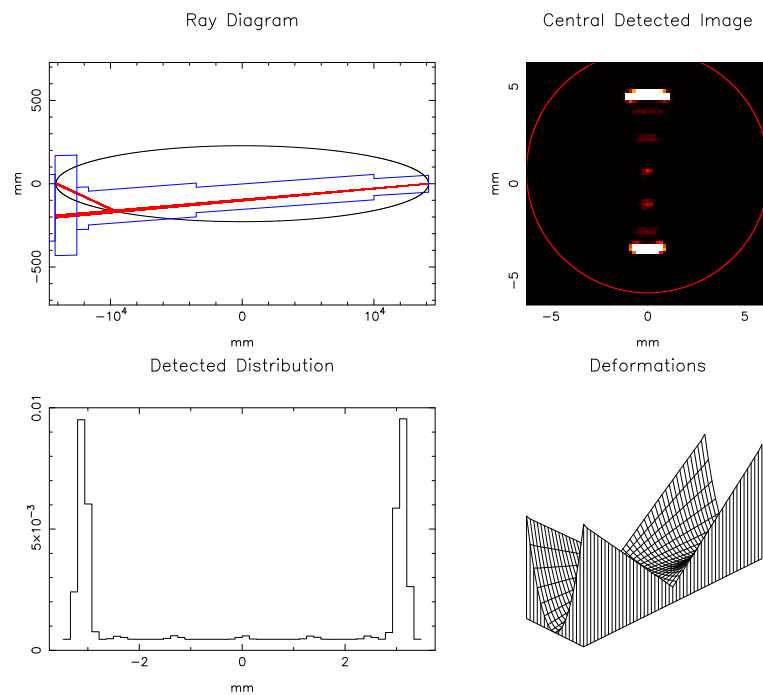


Figure 2.76: Ray traced model in Q of the curvature errors. The optic was modelled as having a radius of curvature from 155mm to 160mm as opposed to 164mm to 169mm . The simulated HEW for this deformation matrix was found to be $2.44'$.

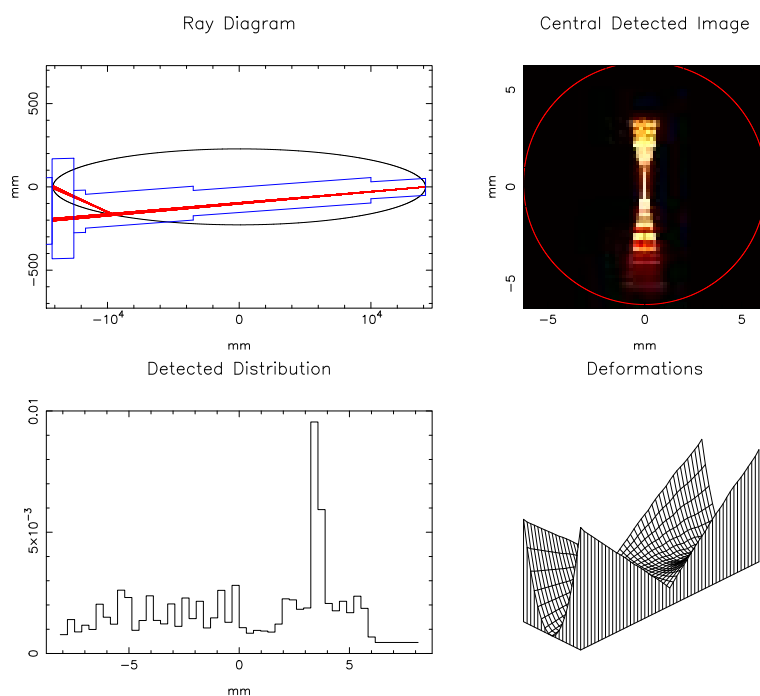


Figure 2.77: Ray traced model in Q of the curvature errors combined with the print-through from bonding the piezoelectric devices. The simulated HEW for this deformation matrix was found to be $2.62'$.

the X-ray data demonstrates a significant amount of similarities. The results from the COMSOL Multiphysics models suggests that the way in which the mirror was mounted was similar to the four corner mounting. This indicates that the models can be used to predict the performance of the mirror, the influences of the actuators and the mounting effectively and accurately. It is also possible to ascertain where the errors on the mirror came from and which elements affected the results the most. The analysis of the results show that the majority of the errors seen were due to the print-through caused by the variable thickness of the glue layer and the curvature errors from the stress in the optic after release from the mandrel. The results shown in table 2.6 illustrate how each stage of production caused additional figure errors seen on the mirror with the largest contribution being the curvature errors.

Model	HEW		FWHM	
	Actual size (mm)	Arc minutes	Actual size (mm)	Arc minutes
Gravitational sag	0.2	0.2	0.1	0.1
Mandrel	1.4	1.1	1.6	1.2
Optic	1.9	1.5	0.4	0.3
Actuators bonded (off)	5.3	4.1	0.9	0.7
Actuators bonded (on)	4.4	3.5	0.6	0.4
Piezoelectric devices being actuated	2.7	2.1	1.4	1.1
Curvature errors	3.1	2.4	3.5	2.7
Curvature errors and piezoelectric devices	3.4	2.6	3.5	2.7
COMSOL Multiphysics Model 2 point mounting	2.6	2.1	0.5	0.4
COMSOL Multiphysics Model 4 corner mounting	3.7	2.9	1.5	1.2
0V with X-rays	4.1	2.8	1.1	0.8
Best HEW image achieved with X-rays	3.9	2.7	1.4	0.9
Pattern 14 at the best voltage	4.3	2.9	0.9	0.7

Table 2.6: Summary of all the results from both the models and the X-ray data. The size of the reflection on the detector is shown in *mm* as well as the results in arcminutes for both the HEW and FWHM of the images.

The result of the model with the curvature errors and the piezoelectric devices was measured by simulation to be 2.6' and the X-ray data with the actuators at 0V achieved was measured practically to be 2.8'. The difference in these two results implies that there was an additional error during the tests, which is likely to have been the pitch and yaw motors and some additional alignment errors. However, the

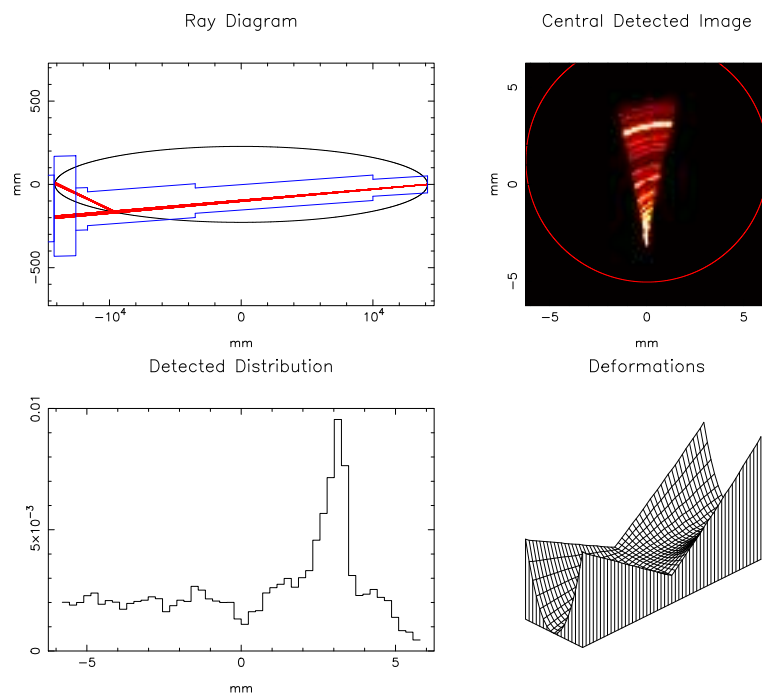


Figure 2.78: A simulation of the X-ray data obtained by combining errors from curvature, bonding the piezoelectric devices and pitch and yaw errors.

similarities between the results obtained practically and those obtained by simulation demonstrates that the models produced in both Q and COMSOL Multiphysics can be used to effectively predict the response of the active X-ray optic.

By combining the curvature errors, the print-through from the piezoelectric devices and errors in the pitch and yaw of the optic, it is possible to simulate the X-ray images that were seen (figure 2.58) during the tests and figure 2.78 shows such a model.

Models at UoB using COMSOL Multiphysics and a grid of three by three piezoelectric devices, have shown that the kinking effect can be significantly reduced or removed by decreasing the size of the gaps between the actuators and by filling the remaining gap with either glue or polyimide. Figure 2.79 shows the conclusions of this model provided by UoB. It has therefore been concluded that the number of joints should be decreased and the gaps between the remaining piezoelectric devices should be reduced and filled.

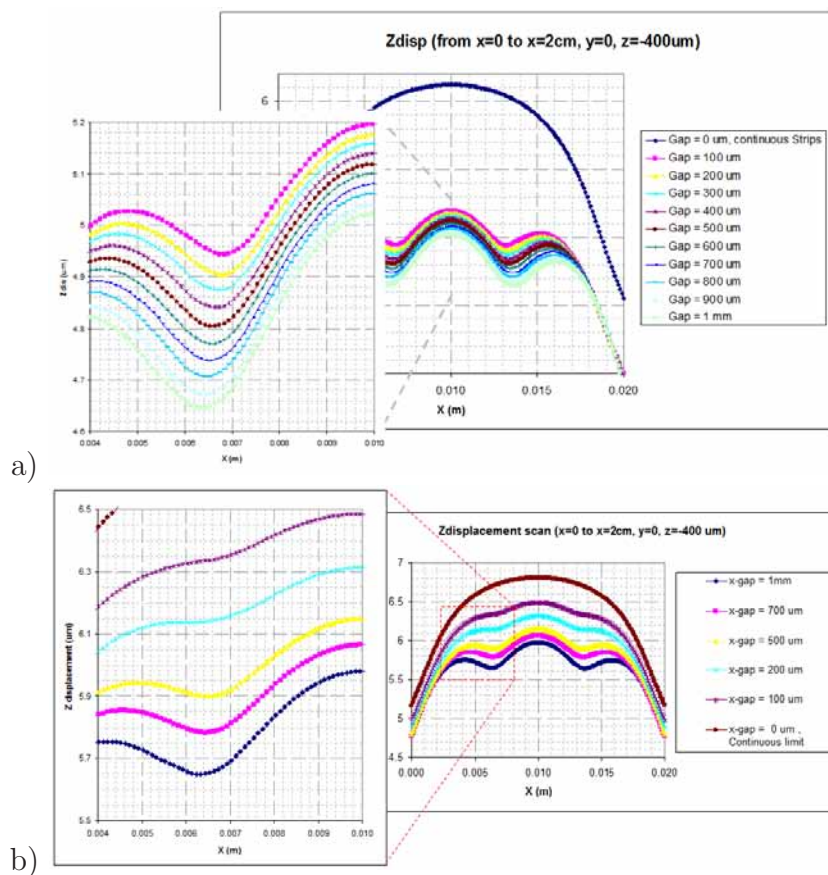


Figure 2.79: Models produced at UoB showing the reduction in the size of the kinks by a) reducing the size of the gaps between the actuators and b) filling the gaps with polyimide. All the models were produced using a three by three actuator grid in COMSOL Multiphysics and were provided by UoB.

2.14 Summary and conclusions

The first prototype optic was designed to be accommodated in the testing facility at the UoL. The facility is 28m long with an X-ray source capable of producing X-ray energies of up to +100keV, and a detector chamber containing an MCP detector system. The LAXRO is an ellipsoidal segment of size 300mm x 100mm x 0.4mm and made from electroformed nickel with a gold reflective surface, designed to provide single reflection, point-to-point focusing when mounted 4.4m from the detector. The optic has thirty curved piezoelectric devices attached to the back to enable active manipulation of the optical surface. These piezoelectric actuators have the same radius of curvature as the optic to minimise the stress applied to the mirror's surface during and after bonding. Metrology was completed on the mandrel surface at UCL and on the mirror's form using the LTP at STFC Daresbury Laboratory. The metrology showed that the optic, when removed from the mandrel, was much flatter than expected but with the piezoelectric devices attached, the optic was closer to the required form. However, the LTP scans confirmed that several of the actuators caused stress on the optical surface and therefore print-through occurred. These data were then inputted into the models at UoL to provide an initial distortion measurement. The results from these models, as shown in tables 2.2 and 2.6, demonstrates that the mirror is limited by its initial shape, after release, and by the print-through from the devices.

The piezoelectric actuators have also been modelled at UoL. To begin with the actuators were modelled as Gaussian bumps, these were then replaced with the influence functions which were calculated using COMSOL Multiphysics at UCL. Metrology performed at STFC Daresbury Laboratory and shown in figure 2.69, confirmed the accuracy of the models and size of the influence functions being used. An iterative subroutine was produced using a series of basic patterns to control the actuators and the results using the Gaussian bumps were very promising, and were improved using the influence functions from UCL. It has been shown that using these patterns, the HEW of the optic could be reduced by almost 50%. Models of the simulated optical distortions, consisting of the FFT patterns where the result is known, have shown that given time, the adjustment algorithm can calculate the correct result and reduce the HEW by up to 85%. Further models completed using

the LTP data but with an extended voltage range and reduced scale of the initial distortion have also been limited to a reduction of 50%. This indicates that there are large scale errors in the optic's form and high frequency errors due to the bonding of the piezoelectric devices which cannot be removed by the actuators or the algorithm and therefore limits the results. It has also been shown that the number of piezoelectric devices on a single given shell should not be too large and a pattern of ten by three is more than enough although fewer may be optimum. The number of actuation patterns of these piezoelectric devices which really make a difference is small, in the order of two to four, but there is a limit to what sort of distortion or figure error in the original mirror that can be corrected for using the actuators. Any distortion of the same size or smaller than the piezoelectric devices cannot be removed, so the distortion from adding the actuators should be reduced. There were also curvature errors due to stress on the optic after release from the mandrel, which produced the largest errors on the optic as shown in the models and metrology.

A series of X-ray tests were performed at UoL using the 28m TTF. A full iterative routine was designed and used a series of local group patterns to control the actuators to try and improve the resolution of the mirror. Due to problems with software and the pitch and yaw motors, the resolution of the mirror was not improved in a predictable way. Subsequent models have shown that it should be possible to reduce the HEW by a factor of 2 using these patterns. The similarities between the models of the optic's response and the results from the X-ray tests demonstrates that the COMSOL Multiphysics and Q models can be used to effectively and accurately predict the mirror's performance. A combination of curvature error, bonding the piezoelectric devices and the pitch and yaw errors created the figure error in the mirror, seen during the X-ray tests, however, it has been shown that the curvature error was the largest contributing factor to the figure error.

Further experiments using the LTP at STFC Daresbury Laboratory showed that when the piezoelectric devices were actuated, a series of $3\mu\text{m}$ kinks were formed at the joins between the actuators. Models completed at UoB and UCL have shown that these kinks were caused by the size of the gaps between the piezoelectric devices and the ratio of the size of the gaps to the thickness of the actuators. This kinking effect is exacerbated by the uneven glue layer caused by the mismatch between the

optic and actuator's radii of curvature. It has been concluded that the number of joins and therefore the number of actuators, should be reduced. The models produced at UoB have also demonstrated that the size of the gaps should be reduced and filled with either glue or polyimide to further reduce the effect.

For the next large adaptive X-ray optic, a series of twelve actuators will be bonded to the mirror with two electrode patterns printed on each, giving a total of twenty four active areas. The gaps between the actuators will be reduced to $100\mu m$ and filled with glue to reduce the gaps and prevent print-through and kinks on the optical surface. New prototypes are also being produced to test the stress on the mirror after release from the mandrel to produce an optic with the correct form. Bonding techniques at UoL are also being improved to remove the print-through seen on the mirror's surface. These will include the use of a vacuum chuck which will hold the actuators in the correct form and tiled formation during the bonding process. The chuck will be made using the form of the mirror so the devices will match it as accurately as possible. This should reduce the level of stress experienced by the optic.

CHAPTER 3

ANALYSIS OF THE MICRO OPTICAL ARRAYS

3.1 Chapter overview

The limitations of current small scale X-ray focusing devices, e.g. zone plates (as described in section 3.3), required the conception of a new class of optic, Micro Optical Arrays (MOAs). MOAs refer to optical systems which consist of a large number of microscopic elements with the ability to focus X-rays to the spot size of a biological cell with sufficient intensity to irradiate biological material. To develop the new devices, the initial design requirements were set out prior to any modelling, production or experimental testing was completed.

A series of reflectivity experiments were carried out at STFC Daresbury Laboratory and at the University of Leicester (UoL) and both of the experiments are discussed. The MOAs used in the test at UoL had an infinite radius of curvature (i.e. flat) and provided vital information about the quality of the etching of the MOA's channels. Both the surface roughness and the quality of the etch needed to be known prior to using the MOAs. In order to determine the quality of the MOA walls, a Field Electron Gun Scanning Electron Microscope (FEGSEM) and an Environmental Scanning Electron Microscope (ESEM) were used to image the MOAs.

This chapter outlines the design, manufacture, metrology, modelling and testing of the small scale adaptive focusing device. The first section of this chapter, section 3.2 gives a background to zone plates, the most commonly used focusing device at

this scale. The subsequent sections outline the introduction to the problem, the design requirements and the design of the optics in sections 3.3 and 3.4 respectively. The theory behind the designs of the 1D and 2D systems are described in section 3.5 and the theory behind the surface features is shown in section 3.6. Images of the MOAs are shown in section 3.7 and the modelling of all the 1D and 2D systems based on the theory are described in section 3.8. The reflectivity experiments are outlined in section 3.9 and the results of the models of the experiments and the experimental results are shown in sections 3.10 and 3.11 respectively. Finally section 3.12 describes the summaries and conclusions from this chapter.

Preliminary work on Micro Optical Arrays (MOAs) was presented at an SPIE meeting in 2001[71]; at the international X-ray microscopy conference in Grenoble in 2002[72]; and further results have been published[73][17]. The next chapter is concerned with the most recent results, which have been published in the refereed literature and conference proceedings as listed in the publications section.

3.2 Background to small scale X-ray focusing devices

Currently, the most commonly used small scale X-ray focusing device capable of creating small spot sizes, is a zone plate[16]. Zone plates are optics which focus using concentric, alternating opaque and transparent zones, which are arranged so that light is diffracted around them, figure 3.1 shows an illustration of a single zone plate. The wavefronts constructively interfere with one another and are brought to the desired focus.

The radius of curvature of the n^{th} zone of a zone plate is given by[16]:

$$r_n^2 = n\lambda f + r_0^2 \quad (3.1)$$

where λ is the wavelength of the X-rays being focused, f is the focal length and r_0 is the radius of the first zone. The width of the n^{th} zone can be calculated using:

$$d_n \approx \frac{\lambda f}{2r_n} = \frac{r_n}{2n} \quad (3.2)$$

The “throughput” of an optic is a common method of describing its efficiency and can be expressed as the product of the optic’s aperture area with the solid angle

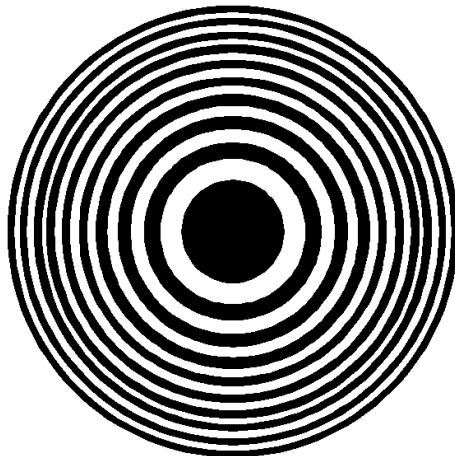


Figure 3.1: An illustration of a single Fresnel zone plate used to focus X-rays via diffraction. It consists of alternating opaque and transparent zones which are arranged so that the X-rays are diffracted around the opaque zones, constructively interfere, and create the desired focus[15].

subtended at the centre of the detector[74]. Zone plates are typically limited by their aperture, usually only a few hundred micrometres and so the throughput efficiency of a zone plate is only $\sim 10\%$.

The efficiency of a zone plate is calculated by:

$$\varepsilon(m) = [A_1^2 + A_2^2 - 2A_1A_2 \cos(\phi_2 - \phi_1)] \frac{\sin^2(m\pi \frac{g}{d})}{m^2\pi^2} \quad (3.3)$$

where a zone with a width of $d - g (\equiv r_{n-1}^2 - r_{n-2}^2)$, transmits a fraction given by $A_1 \exp i\phi_1$ and a neighbouring zone of width $g (\equiv r_n^2 - r_{n-1}^2)$ transmits a fraction of $A_2 \exp i\phi_2$. An ideal zone plate has $A_1 = 0$, $A_2 = 1$, $g = \frac{d}{2}$ and $\phi_1 = \phi_2 = 0$ so equation 3.3 becomes:

$$\varepsilon(m) = \frac{\sin^2(m\pi/2)}{m^2\pi^2} \quad (3.4)$$

The most efficient focus is clearly the first order, taking $m = 1$, $\varepsilon(1) = 10.13\%$.

The study of radiation induced cancers usually involves irradiating biological material using carbon K X-rays ($284eV$), focused using a zone plate to a micrometre sized spot. The low throughput of zone plates means that the number of X-rays which are brought to a focus, is too low to successfully irradiate cells[75].

Using carbon K X-rays restricts the material that can be studied to cell clusters, because the X-rays are almost completely absorbed by single cells, so in order to cause one cell to mutate, ~ 100 cells[17] have to be irradiated. For the research being proposed, single cells would be mutated by supplying a known radiation dose to each cells, instead of an average dose over a group of cells, and the effect on

the surrounding cells would be studied over a distance of $50mm$. Therefore carbon K X-rays are not suitable for this purpose, however, if the energy of the source is increased, then the focused spot size of the zone plate is increased, as demonstrated by equation 3.1. The combination of the type of radiation being used and the current available focusing devices has meant that to date it has only been possible to study cell death as opposed to cell mutations.

The size of the source prior to being focused, limits the spot size which can be produced and with current technology, spot sizes of less than several micrometres are hard to achieve. Consequently, in addition to investigating a new optic design, a new X-ray source providing titanium K_α radiation at an energy of $4.5keV$ is being developed, at Kings College London (KCL), in order to reduce the source spot size. This new source is being developed as a micro-focused source and will provide a very constrained beam of X-rays. The increase in energy from carbon K to titanium K_α X-rays (an increase of $4.2keV$), requires a zone plate with a longer focal length, which would increase the spot size produced[17].

The zones on the zone plate have to be at least $\geq 100nm$ in width to create an efficient diffracting structure. Using equation 3.1, $r_0=0$, $n = 350$, $\lambda=4.5keV=2.75\text{\AA}$ and $f=50mm$, $r_{350}=69.44\mu m$ and $d=99.20nm$. The diameter of the zone plate to focus X-rays at this wavelength would be $D_{350}=138.88\mu m$, making it very difficult to manufacture especially when the width of the outer most zone is only $99.20nm$, and the limited aperture would affect the resolution and efficiency. In addition, in order to achieve a spot size of $10\mu m$ or less, the pores in the optic must be less than $10\mu m$ at X-ray wavelengths, this is impossible to manufacture using zone plates.

Therefore, in order to study cell mutation and smaller cell structures, a focusing device capable of delivering increased intensity per unit time, with a higher throughput, whilst retaining a similar spot size (or smaller) to the zone plate, is required.

The new optic needed to be able to focus both on-axis and off-axis X-rays, thus satisfying the Abbe sine condition[16]. This can be achieved by reflections from two consecutive surfaces (see figure 3.2), but cannot be achieved with a zone plate and it is therefore necessary to move to grazing incidence optics. This method would also increase the efficiency of the optic and the range of the workable X-ray energies.

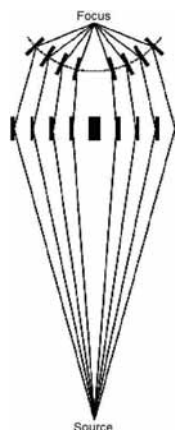


Figure 3.2: A point-to-point focusing device using two reflections of grazing incidence. The source is brought to a focus by consecutive reflections from two surfaces. The grazing angle with which the X-rays hit the optic, depends on the radius of curvature of the optic. By adjusting the radius of curvature, the focal length is adjusted. A device of this type, would satisfy the Abbe sine condition[16] as X-rays both on and off axis would be focused[17].

3.3 Initial design and requirements

As described above, a new form of device is required in order to focus X-rays to the spot size of a single biological cell, $\sim 10\mu m$, at higher X-ray energies than currently used, for radiation studies. It has been concluded that grazing incidence optics would provide the best form of device due to the ability to focus both on-axis and off-axis rays as well as increasing the throughput efficiency and workable energies without altering the focal length.

A device with channels made from a reflective material, such as silicon, would act as an effective grazing incidence optic and by creating an optic with a conical geometry (figure 3.3), it would be possible to focus X-rays to a single spot. In addition, by altering the focal length (i.e. the radius of curvature) and creating very smooth wall surfaces, the precise shape and size of the focused spot could be easily controlled. This optic would be similar to a zone plate and would focus in a very similar way but using grazing incidence reflections instead of diffraction. The optic would be created by etching channels into a silicon chip to reflect the X-rays.

The MOAs are formed from a $20mm \times 10mm \times 0.2mm$ silicon chip with a $4mm^2$ active area in the centre, consisting of a series of etched $10\mu m$ wide channels. Two strips of piezoelectric material are placed either side of the active area to provide active adjustment of the radius of curvature of the device and therefore the focal

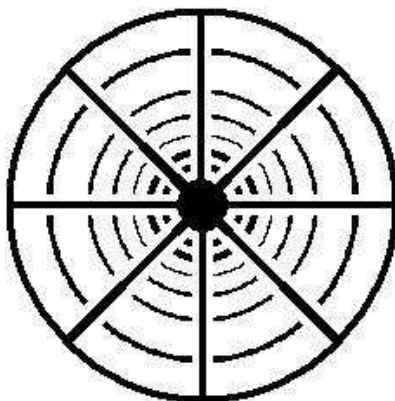


Figure 3.3: A cross section of a proposed system with a cylindrical profile. The channels are attached to the centre stop and outer edge via spindles. The central stop reduces the number of straight through rays which hit the detector. By bending the optic to a spherical profile, it would create a spot focus similar to that of a zone plate but using grazing incidence reflections as opposed to diffraction[17].

length. Using grazing incidence reflections means that the optics are not X-ray energy dependent and by creating an optic with an adaptable radius of curvature, i.e. active, the focal length can be precisely controlled.

Two forms of etching process are currently being investigated, dry etching and wet etching [76]. Wet etching is a process whereby the silicon is immersed in a chemical solution and is dissolved to achieve the desired shape by the use of a mask. The mask has to be made of a material that will not dissolve as quickly as the material being etched. Wet etching can be used to etch along the $\langle 111 \rangle$ or $\langle 110 \rangle$ silicon crystal planes, creating very smooth, straight walls. However, this method cannot be used to produce cylindrical geometry as curved walls cannot be created.

Dry etching involves dissolving the area in the shape of a mask using reactive ions. Once the reacting ions have blasted the surface, the material is passivated and the process is repeated. This process creates two very separate surface features, scallops and curtains, which affect the surface roughness and scattering of the X-rays. A full description of these features and their effects are shown in section 3.6. Shadowing is also seen from the surface roughness features and reduces the number of reflected rays by a small percentage as shown in section 3.6.3.

Many previous attempts have been made to create micro focusing devices by deep silicon etching and examples include [77][78][79]. Creating optics with high

aspect ratios and low surface roughness has been difficult to achieve, however, work still continues at many institutions to perfect this technique.

Several MOA prototypes, both wet and dry etched have been created to be tested and many models have been completed of different configurations of single and tandem MOA systems.

3.4 Micro Optical Arrays design

3.4.1 First prototype design

The design of the MOAs is largely based on polycapillary[80] or Micro Channel Plate optics (MCPs)[81]. For the initial prototype, the MOAs were created using parallel channels forming a simple 1D system, as opposed to the complex conical arrangement (figure 3.3).

The current schematics of the prototype MOA system are a $0.2mm$ thick silicon wafer with a $4mm^2$ ($2mm$ by $2mm$) etched active area. The aperture of the optic has been designed to fit the aperture of the new micro-focusing source. The central active area consists of etched channels, which are $0.01mm$ wide with $0.01mm$ gaps in between them. There is a central stop within the active area to reduce the number of straight through rays which hit the detector. Piezoelectric devices will be used to adjust the curvature of the optic and therefore the focal length. Finite Element Analysis (FEA) models completed at KCL (S. Sahraei, private communication, 2007) have shown that a full coating of piezoelectric material produces less bending than strips of material at the same voltage. For this reason, two piezoelectric strips are placed either side of the channels to enable the MOA to be bent and produce an adjustable focus. The strips are $1mm$ wide and $1mm$ away from the active area to reduce the stress on the corners and edges of the active area as they are actuated.

In order to produce a focused spot of $\sim 10\mu m$ (average size of a biological cell), a focal length of $\sim 50mm$ and a demagnification of $\frac{1}{3}$ of the source, the centre of the MOA needs to be bent by $\sim 0.01mm$. The walls of the channels need to have a surface roughness of $\sim 2nm$ or better across the complete wall of the channel. If the surface roughness is much higher than this, the efficiency of the optic will be too

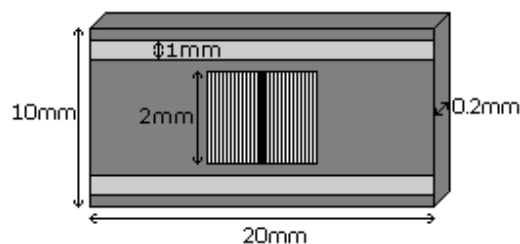


Figure 3.4: Current prototype MOA design, not to scale. The silicon chip is $20\text{mm} \times 10\text{mm} \times 0.2\text{mm}$ with a central active area. The central area is 4mm^2 and consists of 0.01mm wide slots with 0.01mm wide walls. There is a central stop to reduce the number of X-rays which pass straight through the optic and hit the detector. The lighter grey strips are the piezoelectric actuators which are 1mm wide and 1mm from the central area to reduce stress as they are actuated.

low to achieve the intensity per unit time required at the necessary X-ray energy to irradiate the biological material. Figure 3.4 shows the current prototype design. The MOAs are being produced at the Scottish Micro Electronic Centre (SMC) at the University of Edinburgh.

Prototypes have been produced via the dry etch and wet etch processes to compare the surface quality of the channel walls. The design is identical in both cases although the silicon chips used for wet etching are 0.1mm thick as opposed to 0.2mm chips used for the dry etching prototypes. The ends of these channels are also a different shape as the masks used are particular to etching effectively down the crystal planes. This change in shape does not affect the focusing ability of the optic.

3.4.2 Prototype Micro Optical Array mount design

As the MOA has been designed to focus the X-rays produced from a purpose built micro-focus source, a mount to hold the MOAs in place needed to be designed and built. The mount had to be able to hold more than one MOA at a time, to provide two reflections, and allow them to bend whilst still being supported. The position of the MOAs needed to be adjustable for alignment and the piezoelectric actuator electrodes had to be accessible. MSSL have designed and built such a mount, which will be attached to the micro-focus source and fulfills all the above requirements. Figure 3.5 shows the complete structure.

The mount is made up of several units one of which holds the MOA in place and is shown in figure 3.6. The MOA is placed within a groove cut out of the material,

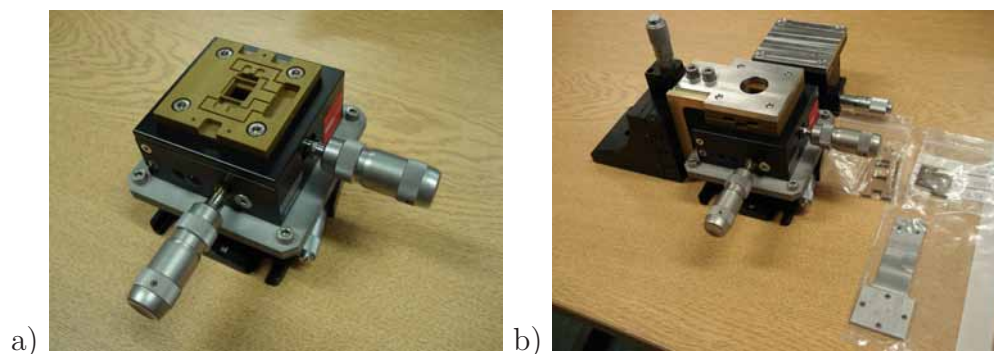


Figure 3.5: The mount designed to hold the MOAs. The handles control the micrometers which allow the MOAs to be moved in the translational directions and to be aligned with each other. The electrodes from the piezoelectric actuators can be attached to the drivers via the connectors on the MOA holder. a) Half of the mount with the area where the MOA will be contained at the top. The channels for the piezoelectric actuator electrodes can be seen. b) The full mount shown with sections for two MOAs. Images provided by MSSL.

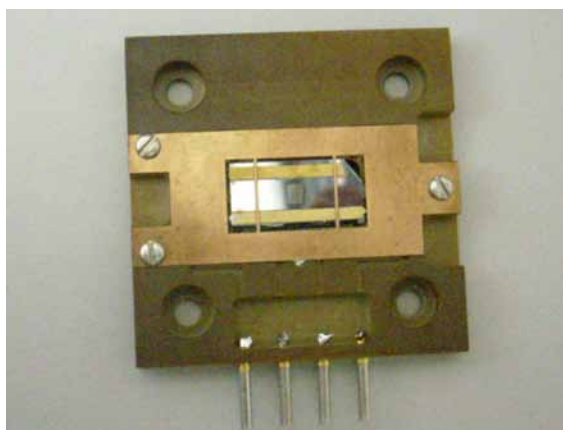


Figure 3.6: The MOA holder component of the mount, shown in figure 3.5, with an MOA in place. This component holds the MOA in place as there is a cut out section which the MOA sits in and the clamp is placed over the top. The clamp has two knife edges which allow the MOA to bend without any stress being added. There are also channels cut into the holder to allow access to the piezoelectric electrodes. The electrodes are connected to the driver via the connectors at the base of the holder.

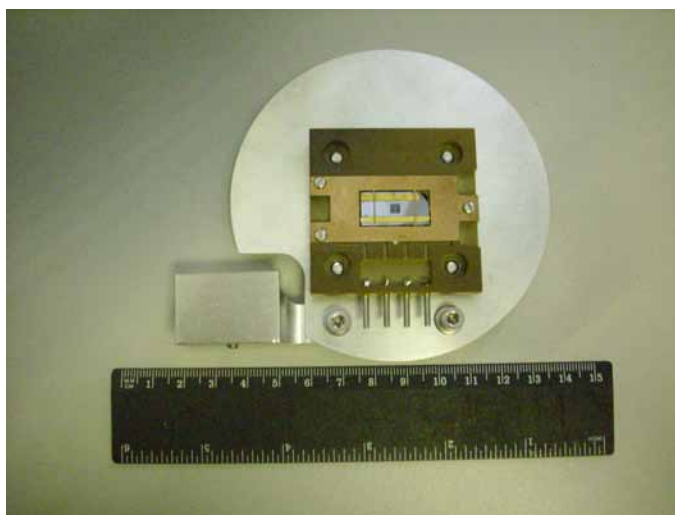


Figure 3.7: An image of the MOA holder for the X-ray tests at UoL. The silver surround is made from steel and acts as a baffle to prevent the rays which do not hit the MOA from travelling through to the CCD. The baffle attaches to the rotation arm to allow rotation of the MOA in one axis. The brown holder is the purpose built MOA holder and an MOA with piezoelectric strips can be seen inside. The MOA holder is attached to the baffle via four screws and the clamp which holds the MOA in place can also be seen over the top of the MOA.

and a clamp placed over the top. Channels are cut into the holder, to allow the actuator electrodes to be attached to the driver. The connections for the electrodes can be seen at the bottom of the MOA holder. The clamp over the holder has two knife edges which allow the MOA to be supported whilst being bent, without applying any stress to the optic. The holder, containing the MOA, is then placed within the mount and can be aligned using micrometers which are controlled by the handles shown in figure 3.5. The whole unit will then attach to the exit aperture of the micro-focus source.

Specific mounting was designed to hold the MOA during the tests within the CCD life test facility at UoL (section 3.9.2), and consisted of an MOA holder and a baffle to reduce the number of rays which miss the optic and hit the CCD. For these tests, the clamp section from the full MOA mount was used (figure 3.6) and figure 3.7 shows the mounting attached to the baffle. The steel baffle was attached to the rotational arm and the clamp section of the MOA holder was attached to the baffle.

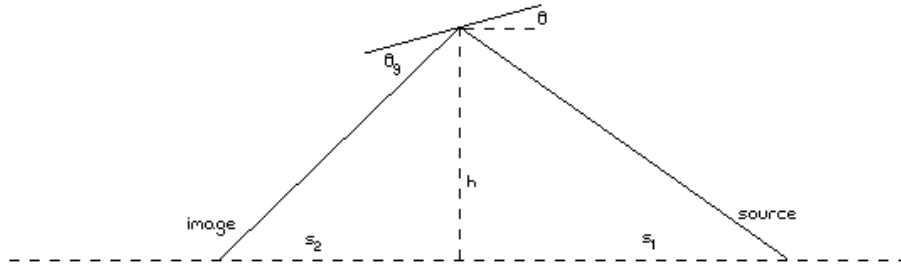


Figure 3.8: Geometry of a single reflection from an MOA channel[18].

3.5 Theory of Micro Optical Arrays

MOAs are small scale, grazing incidence devices, created by etching thin channels into silicon chips, where the X-rays are reflected off the walls of the channels. They can be used as either a collimator, a telescope or for line-to-line focusing as with a cylindrical lens. This is achieved by the combination of reflections from the channel walls which produce a line focus. Below is a description of the designs of various MOA single and tandem systems, based on the design of the channels in the active area. Similar derivations for MCP and capillary arrays can be found in Chapman et al.[82][83] and others.

3.5.1 Single Micro Optical Arrays

The basic geometry of a single MOA channel is shown in figure 3.8 and taking h as the distance of the channel from the optical axis, θ_g as the grazing angle, s_1 as the source to MOA distance and s_2 as the MOA to image distance we have

$$\frac{h}{s_1} = \theta_g - \theta \quad (3.5)$$

$$\frac{h}{s_2} = \theta_g + \theta \quad (3.6)$$

Eliminating θ we get:

$$\frac{1}{s_1} + \frac{1}{s_2} = \frac{2\theta_g}{h} \quad (3.7)$$

which is the standard Gaussian imaging equation:

$$\frac{1}{s_1} + \frac{1}{s_2} = \frac{1}{f} \quad (3.8)$$

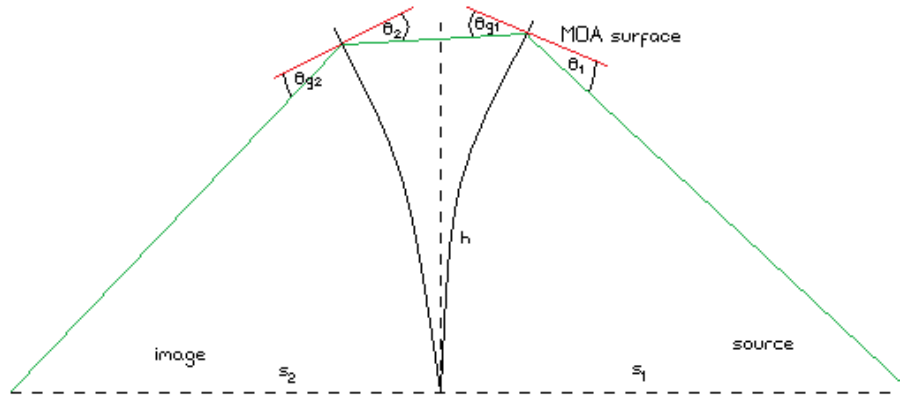


Figure 3.9: Geometry of reflections from a tandem pair of MOAs[18].

This enables the MOA to act as a lens. Taking the above equations, $\frac{h}{\theta} = R$ and eliminating θ_g , the radius of curvature of the MOA is given by

$$R = \frac{2s_1s_2}{s_1 - s_2} \quad (3.9)$$

3.5.2 Tandem Micro Optical Arrays

The aperture of the system described above can be increased by using tandem MOAs i.e. double reflections (figure 3.9), creating a 2D system. The increase in the effective area is dependent on the ratio of the grazing angles between the two MOAs and to illustrate this, three cases have been considered. The first case is where the grazing angles of the two MOAs are the same, whilst in the second case, the first MOA is flat and the subsequent MOA is curved. The final case is where the focal length of the first MOA is set to the object distance s_1 and the focal length of the second MOA is set to the image distance s_2 .

In the last case the rays passing from the first plate to the second are parallel to the optical axis so all the rays reflected by the first MOA will be reflected by the second, which means the total reflected flux is not dependent on the gap between the MOAs. In the other two cases however, this is not true and the number of rays reflected is dependent on the physical set up.

If θ_{g1} is the grazing angle of the first MOA and θ_{g2} is the grazing angle of the second then we have

$$\frac{h}{s_1} = \theta_{g1} - \theta_1 \quad (3.10)$$

$$\frac{h}{s_2} = \theta_{g2} + \theta_2 \quad (3.11)$$

3.5.3 Equal grazing angle tandem Micro Optical Arrays

In this case, $\theta_{g1}=\theta_{g2}=\theta_g$, using $h/R_1=\theta_1$, $h/R_2=\theta_2$ and solving for equations 3.10 and 3.11 gives

$$\frac{1}{R_1} + \frac{1}{R_2} = \frac{1}{s_2} - \frac{1}{s_1} \quad (3.12)$$

and

$$\frac{1}{R_2} - \frac{3}{R_1} = \frac{2}{s_2} \quad (3.13)$$

The radii of curvature for the two plates are then given by

$$R_1 = \frac{4s_1s_2}{s_1 - 3s_2} \quad (3.14)$$

$$R_2 = \frac{4s_1s_2}{3s_1 - s_2} \quad (3.15)$$

3.5.4 Flat-curved tandem Micro Optical Arrays

Equations 3.10 and 3.11 still apply but now $\theta_1 = 0$ (a flat MOA, infinite radius of curvature R_1) and $\theta_2 = \theta_{g1} + \theta_{g2} = h/R_2$ so we have:

$$R_2 = \frac{2s_1s_2}{s_1 + s_2} \quad (3.16)$$

For the flat-curved configuration $\theta_x = \theta_{g1}$ and we have the simpler criterion that the gap between the MOAs must be $\Delta_x \ll L$ to avoid heavy losses, where L is the length of the MOA's channels.

3.5.5 Collimator-telescope tandem Micro Optical Arrays

In this case $R_1=-2s_1$ and $R_2=-2s_2$, so the first plate is curved towards the source and the second is curved towards the image. As all the rays which are reflected from the first plate are parallel to the optical axis on exiting, the gap between the two MOAs can be infinite.

3.5.6 Line Spread Function

The line spread function (LSF) of the detected distribution is the integration of the point spread function which describes the blur of a point source due to the lens. The width of the LSF can be predicted using the formula[18]:

$$w_i = \frac{Lh}{2} \frac{(s_1 + s_2)^2}{s_1^2 s_2} \quad (3.17)$$

for a single MOA and

$$w_i = \frac{Lh}{4} \frac{(s_1 + s_2)^2}{s_1^2 s_2} \quad (3.18)$$

for tandem MOAs, where L is the length of the channel.

Using the equations described above, models and predictions of both single and tandem MOAs were produced and predictions of the efficiencies of the systems were calculated.

3.6 Shadowing and scattering models

The dry etching process (see section 3.3) creates two very separate surface features, scallops and curtains, which affect the surface roughness and scattering of the X-rays. Scallops are caused by the passivation process, which creates a series of curves down the wall. This then causes an in-plane scattering effect (shown in figure 3.10) where the change in the slope of the wall causes the grazing angle of the incoming X-ray to be increased or decreased by a small factor δ (figure 3.10 b)). The second surface effect, curtains, are orthogonal to the scallops down the wall surface and are shown in figure 3.11. It has been named the “curtain effect” as it is similar to ripples in hanging curtains as they become wider down the length of the channel. The effect is due to the mask edges not being perfectly smooth and it causes out-of-plane scattering, which shifts and spreads out the line focus of the MOA. The combination of the scallops and curtains will adversely affect the efficiency of the optic and the intensity of the line focus, therefore, it is essential that these two effects are reduced or eliminated.

Surface roughness also causes shadowing, where part of the surface is hidden from the incoming X-rays by the surface features[19]. This effect reduces the amount of rays which are reflected and focused by the MOA by a small percentage. The

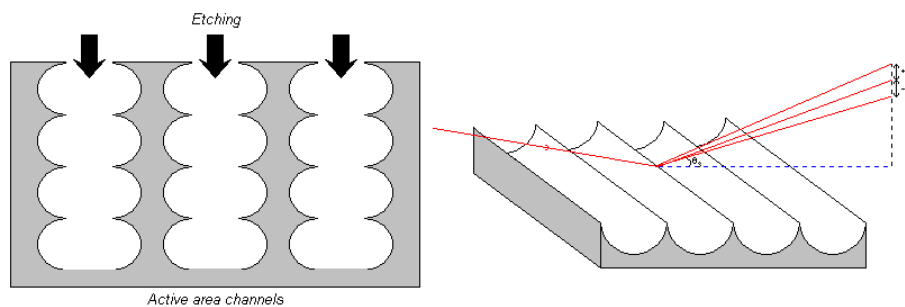


Figure 3.10: A channel wall shown with scallops down its length. Left, an illustration of the MOA wall as it is etched, which creates the scallops during the passivation process. Right, the in-plane scattering caused by these features due to the change in slope, the grazing angle is increased or decreased by a small factor δ .

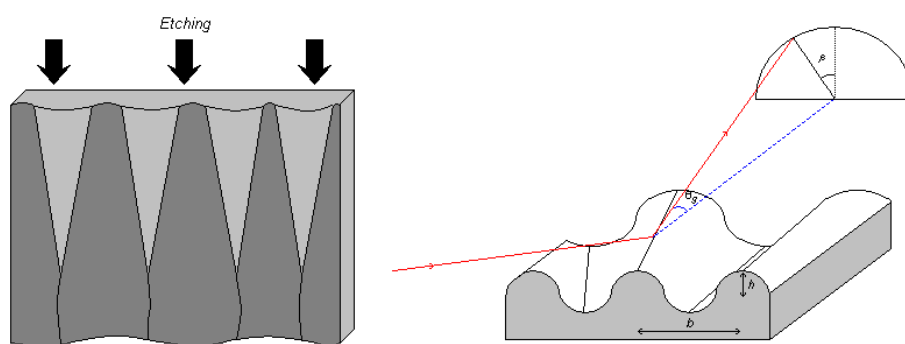


Figure 3.11: A channel wall with the curtain features shown down the length of the wall. Left, the entire length of the channel with the curtain effect which is orthogonal to the scallops, shown in figure 3.10, and is caused by the roughness along the edge of the mask used to etch the channels. Right, the out-of-plane scattering caused by this effect which shifts and spreads out the line focus.

scallops along the walls will either give out-of-plane reflection errors from the sides of the scallops or the X-rays will be diffracted in a conical diffraction model. This will depend on whether the conditions are in the geometric or wave regime. Below is a discussion of the conditions to determine which regime will dominate and the amount of scattering which is caused by the surface roughness.

3.6.1 In-plane scattering

As described in section 1.4, in-plane scattering is conventionally calculated using the Total Integrated Scatter (TIS) which gives the probability that a ray is scattered and is used to calculate the 1st order diffraction. The scattering in higher orders (as $\text{TIS} \rightarrow 1$), can be modelled using a Gaussian distribution approximation where the

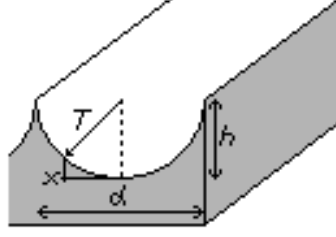


Figure 3.12: A zoomed in image of a single scallop with radius T , height h and width d .

width of the Gaussian is given by equation 3.19[18]:

$$\frac{n\lambda}{d \sin \theta_g} = \sin \beta \quad (3.19)$$

where d is the correlation length of the surface roughness along the channel and β is the width of the Gaussian.

3.6.2 Out-of-plane scattering

Owing to the shape of the scallop features, the walls of an MOA can be approximated to a diffraction grating with the grating spacing being equal to the width of the scallops, b . The grating equation gives a scattering angle β_d from the grating at a given wavelength λ by

$$\sin \beta_d = \frac{\lambda}{b \sin \theta_g} \quad (3.20)$$

where β_d is the diffraction angle out-of-plane, b is the grating spacing and θ_g is the grazing angle of the incoming X-ray. For small angles we get

$$\beta_d = \frac{\lambda}{b\theta_g} \quad (3.21)$$

Taking the scalloping profile to be a sector of a circle (figure 3.12), the radius of the profile can be calculated using the height of the scallops, h , and the width of the scallop, b

$$T \simeq \frac{b^2}{8h} \quad (3.22)$$

Using the radius of the scalloping profile T , and the spacing between the cusps b , the maximum gradient error is then given by

$$\Delta g_{max} = \frac{b}{2T} \quad (3.23)$$

and the average gradient error is then

$$\overline{\Delta g} = \frac{b}{4T} \quad (3.24)$$

Therefore the average deflection error (twice the gradient error) from the scallops is

$$\beta_r = \frac{2b}{4T} = \frac{b}{2T} \quad (3.25)$$

where β_r is the reflection error out-of-plane.

The dividing line between geometric optics (figure error dominated) and wave optics (scattering/diffraction dominated) is given by equating the two angles, β_d and β_r

$$\beta_r = \beta_d \quad (3.26)$$

which gives

$$\frac{b}{2T} = \frac{\lambda}{b\theta_g} \quad (3.27)$$

and rearranging

$$\frac{b^2}{T} = \frac{2\lambda}{\theta_g} \quad (3.28)$$

If b^2/T is larger than this (i.e. T is small or b is large) then the geometric reflection errors dominate the out-of-plane scattering, however, if b^2/T is smaller than this (i.e. T large or b is small) then the diffraction from the scallops dominates. As b and h are fixed by the channel manufacture and λ will be fixed or restricted to a given range, the only varying factor will be θ_g . This will be small for the channels at the centre of the MOA plates and large at the edges. Again rearranging and using equation 3.22, equation 3.28 becomes

$$\theta_g = \frac{\lambda}{4h} \quad (3.29)$$

thus giving the dividing line between geometric reflection errors dominating and diffraction dominating.

For the out-of-plane diffraction, the TIS is dependent on the height of the scallops, h , just as the in-plane TIS is dependent on the RMS surface roughness, σ . The TIS is given by

$$TIS = \left(\frac{4\pi\theta_g\sigma_h}{\lambda} \right)^2 \quad (3.30)$$

where σ_h is the RMS height of the scallops.

The height of the scallops, h , is given by (see figure 3.12)

$$h = T - T\sqrt{1 - \left(\frac{x}{T}\right)^2} \quad (3.31)$$

and using a binomial expansion to obtain the higher terms, equation 3.31 becomes:

$$h = \frac{x^2}{2T} \quad (3.32)$$

The RMS height of the scallops is given by

$$\sigma_h = \sqrt{\overline{h^2} - \bar{h}^2} \quad (3.33)$$

where

$$\bar{h} = \int_0^{d/2} \frac{h}{d/2} dx \quad (3.34)$$

$$\overline{h^2} = \int_0^{d/2} \frac{h^2}{d/2} dx \quad (3.35)$$

and therefore equation 3.33 becomes

$$\sigma_h = \frac{2h}{3\sqrt{5}} \quad (3.36)$$

Substituting this into equation 3.30, setting TIS=1 and rearranging we get

$$\theta_g = c \frac{\lambda}{4h} \quad (3.37)$$

where

$$c = \frac{3\sqrt{5}}{2\pi} = 1.068 \quad (3.38)$$

This result is comparable to the result produced in equation 3.29 and gives the dividing line between reflection error domination and deflection diffraction.

If θ_g is large (at the edges of the MOA) then there will be diffraction and if it is small (at the centre of the MOA) then there will be a geometric reflection error as the geometric reflection error is independent of θ_g and λ . At small grazing angles the phase errors introduced by the height error of the scallops are small, and so the amount of scattering drops and geometry takes over. As θ_g increases, the height errors become important and at some point scattering takes over. This also means that scattering dominates when the projected area of the channel walls is large.

As the out-of-plane deflection should shift the rays out-of-plane, there should be no effect on the focus, just a decrease in the efficiency.

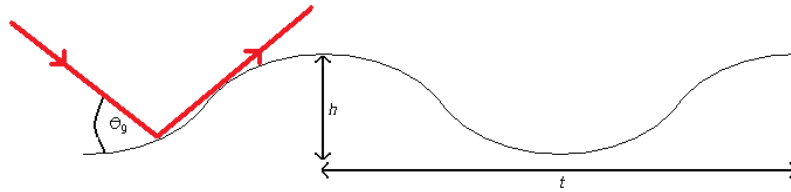


Figure 3.13: A demonstration of shadowing on a reflected surface. The reflective surface is pictured with surface roughness features of length t , and height h . The X-ray is coming from the left of the image and is reflected at an angle θ_g , the grazing angle. Part of the surface is hidden from the incoming X-rays by the surface features thus reducing the efficiency of the optic[19].

3.6.3 Shadowing models

Shadowing is caused by the surface roughness features hiding part of the reflecting surface from the incoming X-rays, which reduces the number of reflected rays. This has more of an effect on the efficiency of the optic the larger the surface features are. The cause of shadowing is demonstrated in figure 3.13[19].

The critical angle at which reflection is no longer achieved is related to the surface roughness by equation 3.39,

$$\tan \theta_c = \frac{h}{t} \quad (3.39)$$

where h is the height of the surface roughness features over a length t . Shadowing was modelled using equation 3.40,

$$\epsilon = \frac{\tan \theta_c}{\tan \theta_g} \quad (3.40)$$

where θ_g is the grazing angle between the X-ray and the optic.

Equation 3.40 reduces the number of rays which are reflected by the optic by a small fraction, ϵ . This therefore reduces the intensity of the focused line or spot but does not affect the focusing ability of the optic. Scalping on the other hand has a more noticeable effect.

3.6.4 Conclusion of surface feature models

The amount of out-of-plane scattering is only dependent on the depth of the channels, h , just as the amount of in-plane scattering depends on σ and not on the correlation length. The scallops along the channel walls will deviate the rays by reflection and the roughness down the scallops causes scattering as h will be large

which leads to a geometric solution and σ will be small which gives scattering. In both cases, h and σ give the TIS and if h or σ are large then $TIS \rightarrow 1$, however, this may not happen at the same point as the reflection and deflection angles, β_d and β_r , become equal.

The amount of shadowing is determined by the height of the features and the grazing angle of the incoming ray.

3.7 Metrology of the Micro Optical Arrays

In preparation for the MOA tests described in section 3.9.2, images of the MOA to be used were taken using the Field Electron Gun Scanning Electron Microscope (FEGSEM) and Environmental Scanning Electron Microscope (ESEM) in the Advanced Microscopy Centre at UoL. Both sides of the wet and dry etched MOAs were imaged as well as down the channel length. The images showed that the dry etched MOA had some surface features of the order of $100nm$ and that some of the channels were broken. The images of both sides of the dry etched MOA can be seen in figure 3.14 and figure 3.15.

Figure 3.14 shows the front side of the dry etched MOA which appeared to have few broken channels and seemed to be cleanly etched. The channel walls appeared to be vertical but displayed the scallop and curtain features which can be clearly seen in figure 3.14 c) and d). The rear side of the MOA (figure 3.15) however, appears very damaged with scratches and chips in the channel walls. In some places the channels do not seem to be fully etched and it appears as though something has dripped down the length of the channel which has caused major surface roughness features. The width and accuracy of the channels on the rear side of the MOA is variable and they appear narrower and uneven in comparison with those on the front side of the MOA. The walls and channels should have both been $0.01mm$ wide, however, this is clearly not the case in the SEM pictures, on the rear side the walls are much narrower so the walls are a trapezium in shape.

The ESEM at UoL was used to image a wet etched MOA and it was found to have much smoother walls and practically no surface features, as shown in figure 3.16. The quality of the wet etched walls is much better than that of the dry etched

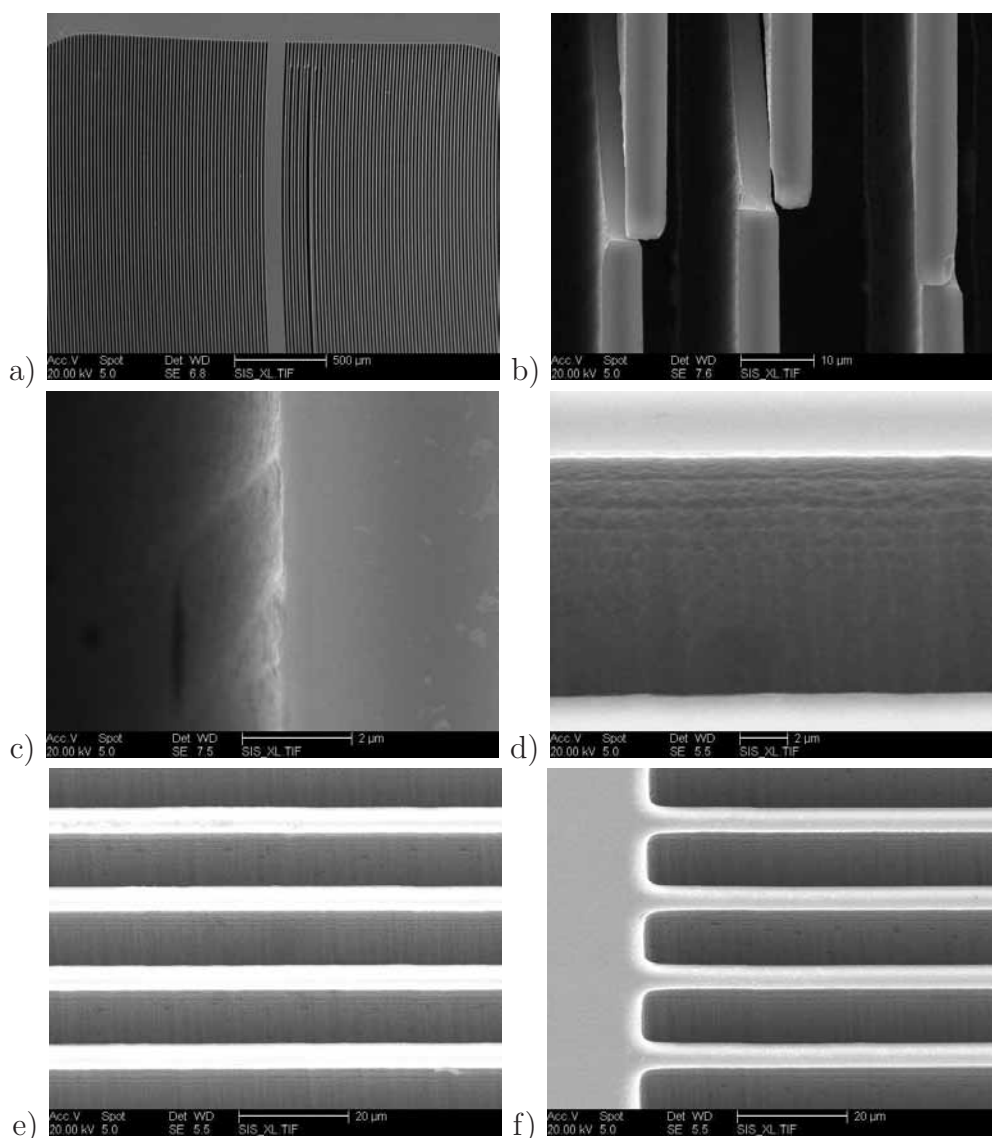


Figure 3.14: Images of the front side of the dry etched MOA taken with the FEGSEM. a) The active area of the MOA, a few broken channels are clearly visible. b) A closer view of the broken channels within the MOA's active area. c) A view down the length of the channel wall where the curtain effect is visible. d) A wider angle view down the MOA channel wall where both scallops and the curtain effect are visible. e) A series of channels, undamaged. The quality of the etch can be seen in this image, the walls are evenly spaced and vertical. f) A view of the edges of the channels which have been curved to improve the quality and ease of the etch. The scales in these images are 500, 10, 2, 2, 20 and $20\mu\text{m}$ for a), b), c), d), e) and f) respectively.

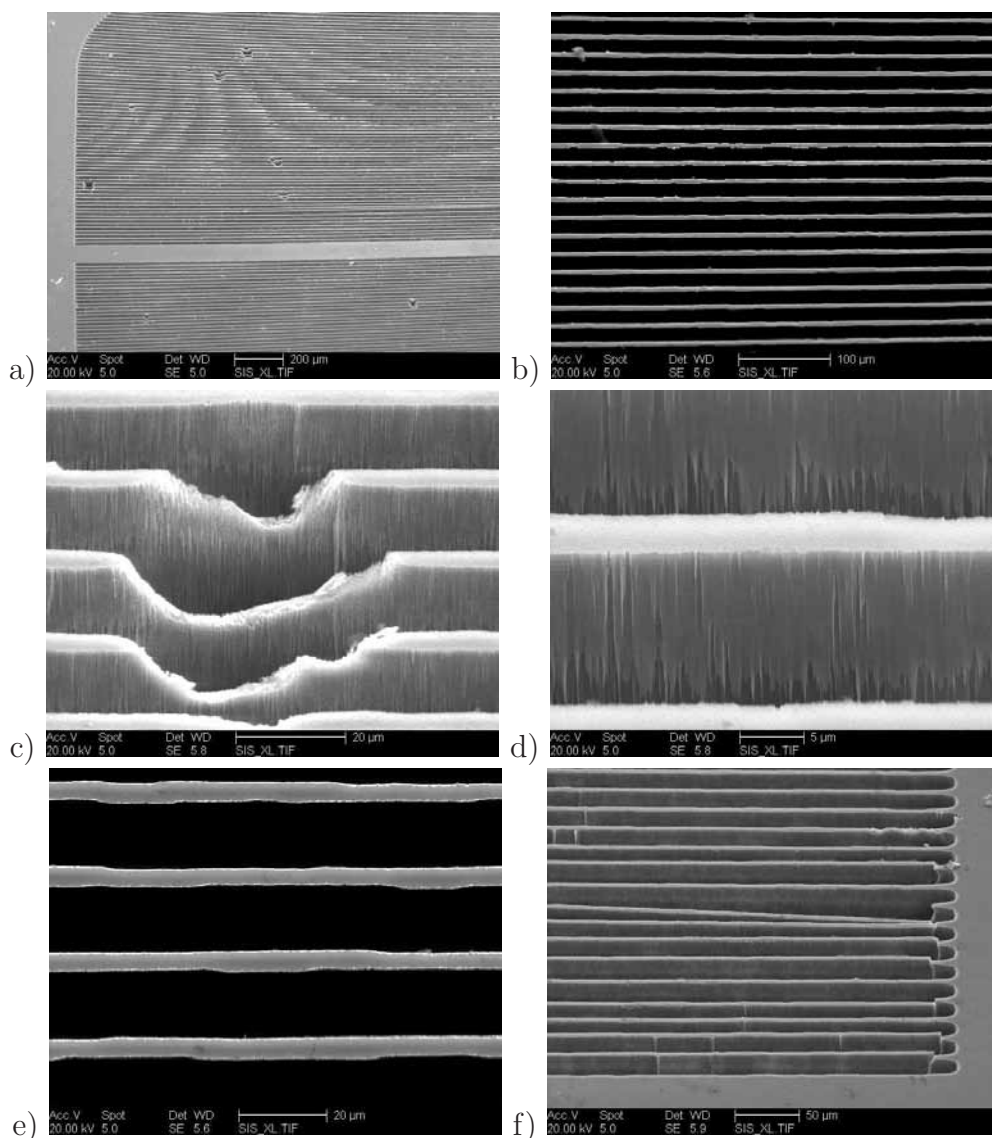


Figure 3.15: Images of the rear side of the dry etched MOA taken with the FEGSEM. a) The rear side of the active area of the MOA. It can be seen that this side of the MOA is very damaged, with broken channels, chips and scratches over the entire area. b) The channels are much narrower, uneven and damaged compared with the front side of the MOA. c) A zoomed in image of the damaged area of the channel walls. d) A closer view down the length of the channel walls where the scallop and curtain effects are less visible, however, it does appear as though a substance has been dripped down the walls creating very high levels of surface roughness. e) A view of the tops of the channel walls which appear uneven and narrow. f) The corners of the channels are very misshapen and damaged and there are a large number of broken channels on this side of the MOA. The scales in these images are 200, 100, 20, 5, 20 and 50 μm for a), b), c), d), e) and f) respectively.

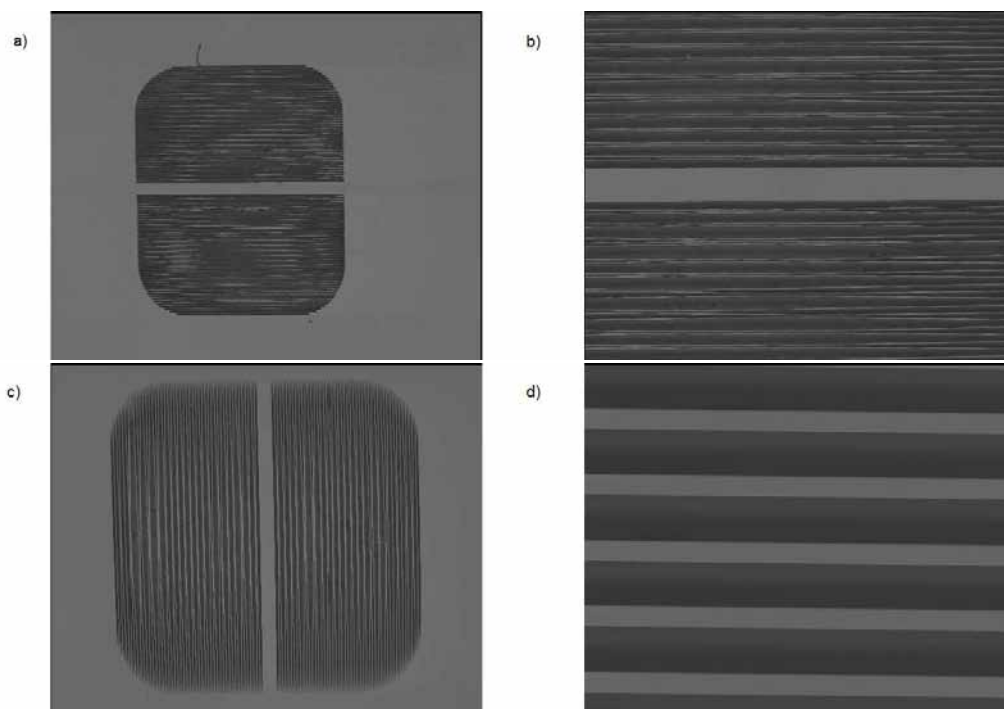


Figure 3.16: A series of images of a wet etched MOA using the ESEM at UoL. The surfaces of the channel walls are much cleaner and show practically no surface features. The channel walls are incredibly straight and even and there are very few broken channels although some do appear to of stuck together. a) and b) show the front side of the MOA and c) and d) show the reverse side. Both sides are practically identical to one another. The scales in these images are $3mm$, $100\mu m$, $2mm$ and $20\mu m$ for a), b), c) and d) respectively.

walls, which would increase the amount of X-ray reflection from the source. Some channels did appear to stick together and bend towards each other, which would reduce the reflecting area, but only by a small fraction.

3.8 Simulation of the Micro Optical Arrays

The models of the optic design have been completed in a ray-tracing program called Q (1.5). Using Q, more than one MOA may be specified at a time to create double reflecting surfaces and a 2D system. Surface properties of the MOAs such as surface roughness and deformations can also be specified which allows alterations to the initial shape of the optic to be added. For instance the piezoelectric devices cause a parabolic shape over the surface as opposed to a cylindrical profile which can be easily added to the models if required. The surface type, source energy and surface coatings can also be set, enabling the creation of accurate models of the MOAs.

The following sections describe the models of single and tandem MOA systems produced. All the systems described in section 3.5 as well as parabolic MOAs and crossed pair MOAs have been modelled and the results are shown.

3.8.1 Line-to-line focusing

Line-to-line focusing, where a finite source is focused using either a single or tandem MOA system, is the simplest form of focusing when using an MOA. Single MOAs will create a line focus from a finite point source because the MOA is made up of narrow channels and the X-rays are reflected off one surface in one axis. In comparison MCPs, which are pore optics, create a point focus with cross arms from consecutive reflections off orthogonal surfaces. If an MOA with an infinite radius of curvature (i.e. flat), is placed halfway between a source and a detector, line-to-line focusing (or point-to-line focusing) can be achieved. Figure 3.17 demonstrates line-to-line focusing with a single flat MOA and a finite source. The X-ray source has an energy of 1.04keV and the MOA has been set up with a perfect silicon surface and no deformations. The whole system is over 40mm and the aperture of the optic is 1.5mm with the source on the right hand side of the image and the detector at 0.0mm , on the left. Figure 3.17 b) is a zoomed-in image of the channels and the interaction of the X-rays with the surface. The red rays represent the X-rays which have come from the source and have not interacted with any surfaces whilst the green rays are those which have been reflected once by the surface. It can be seen that the source is brought to a focus at the detector at 0.0mm . In the zoomed-in image (figure 3.17 b)), it is possible to see the rays (in red) being reflected by the channel walls and becoming green rays. Figure 3.17 also shows that not all rays entering the channels are reflected, but that some pass straight through the optic onto the detector. The same effect can be achieved with a curved MOA, where the radius of curvature is set to twice the distance from the MOA to the detector as can be seen in figure 3.18. In this image, a curved MOA with a radius of curvature of 60mm , positioned at 30mm and curved toward the source, focuses a finite source. The source to detector distance is set to 45mm with the detector at 0.0mm . This model has been set up in the same way as the model shown in figure 3.17.

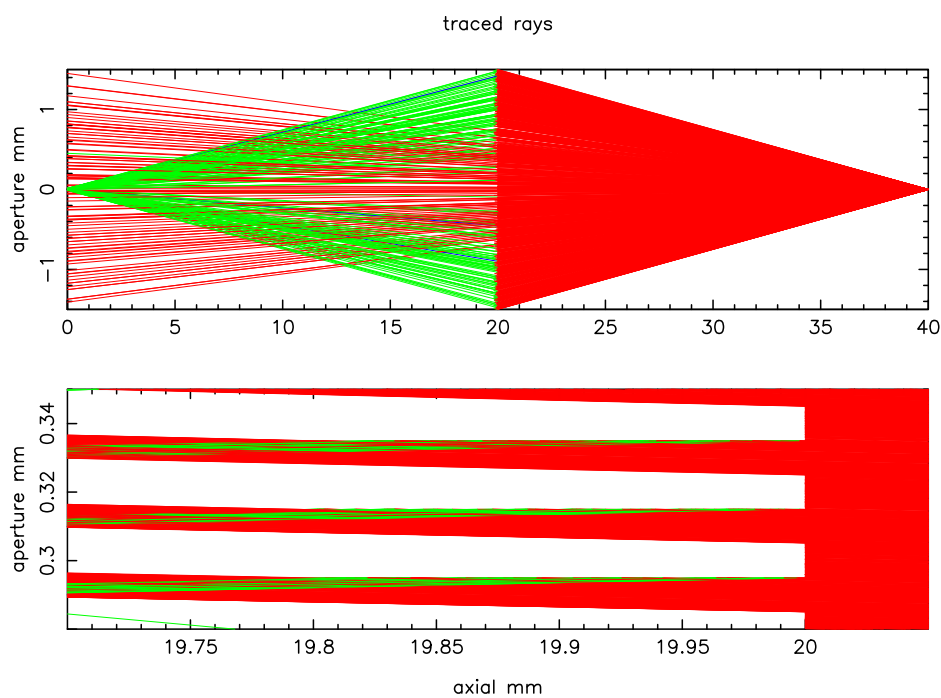


Figure 3.17: Line-to-line focusing of a 1.04 keV source, with a flat MOA. The top image shows the full system with the source positioned on the right of the image and the detector on the left. The red rays are produced by the source and represent the rays which have not been reflected whilst the green rays represent those which have undergone a single reflection. It can be seen in both images that not all the rays produced at the source are reflected by the optic, some pass straight through to the detector. The axes for both frames are in mm and the source to detector distance is $40mm$. The MOA is positioned at $20mm$ and has a focal length of $20mm$. The bottom image shows a zoomed-in section of channels and shows the rays being reflected. The red rays from the source enter the channels from the right and are reflected toward the detector on the left. The MOA has been modelled with a perfect reflecting silicon surface with no deformations.

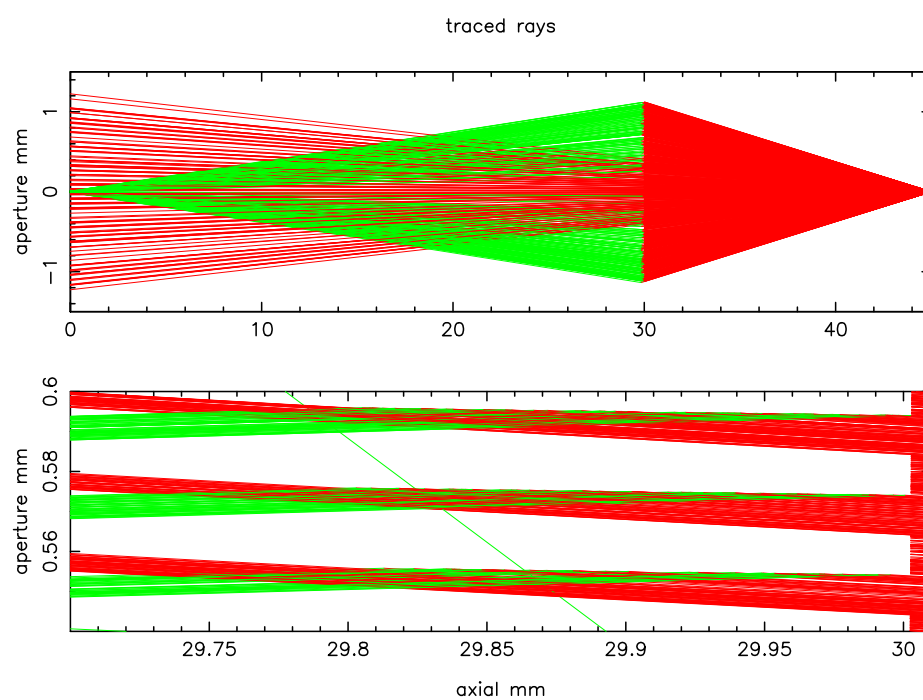


Figure 3.18: Line-to-line focusing with a curved MOA. The top image has a source to detector distance of 45mm and the MOA is positioned at 30mm with a radius of curvature of 60mm , curved toward the source. The bottom image is a zoomed-in section of the channels which shows the rays being reflected. The red rays from the source enter the channels from the right and are reflected toward the detector on the left. The model was produced and set up in the same way as figure 3.17

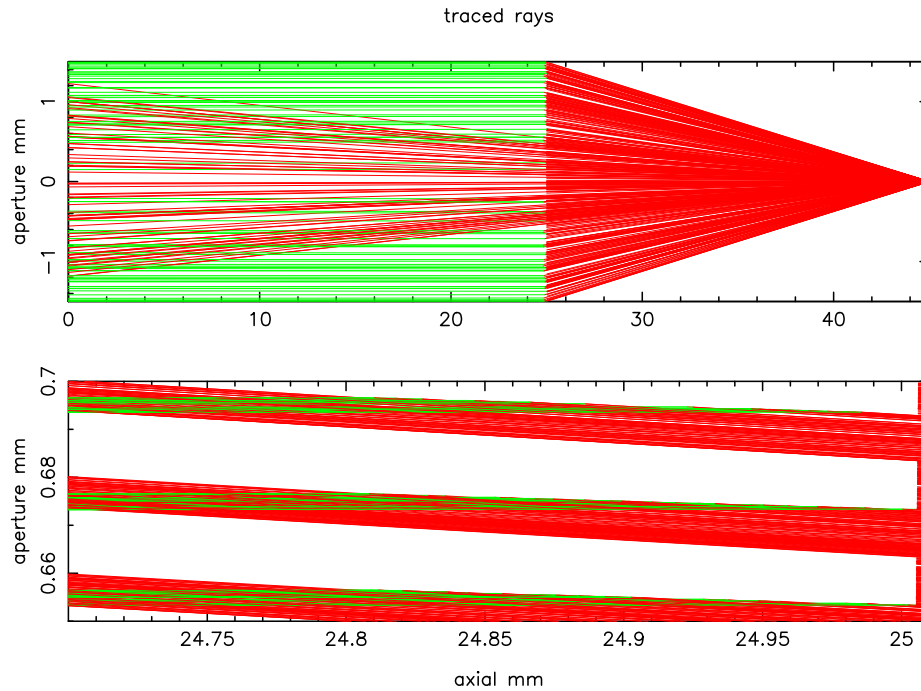


Figure 3.19: A finite source of 1.04 keV being reflected by an MOA acting as a collimator. The figure is set up in the same way as figure 3.17. The focal length of the MOA is 25mm and the radius of curvature of this MOA is 50mm , positioned at 25mm , and curved toward the source. The lower image shows a zoomed-in image of the channels, where the rays enter the channels from the right at an angle, and are reflected toward the left. It can be seen that the reflected rays, in green, are parallel to the optical axis.

3.8.2 Collimator and telescope Micro Optical Arrays

As described in section 3.5.5, a single MOA can act as a collimator or as a telescope and by combining the two in a tandem system, a collimator-telescope providing line-to-line focusing. A collimator creates a parallel beam from a finite source as shown in figure 3.19, whilst a telescope focuses an infinite source (figure 3.20). Line-to-line focusing is demonstrated in figure 3.21 by a collimator-telescope tandem MOA system.

For the collimator system, the radius of curvature of the MOA, R , is set to $R = -2s_1$, where s_1 is the distance from the source to the MOA, and it is curved toward the source. The MOA acting as a telescope, is curved toward the focus with the radius of curvature being $R = -2s_2$, where s_2 is the distance from the focus to the MOA.

By combining a collimator MOA and a telescope MOA, a line-to-line focusing device is created. The gap between the two plates in this instance can be infinite

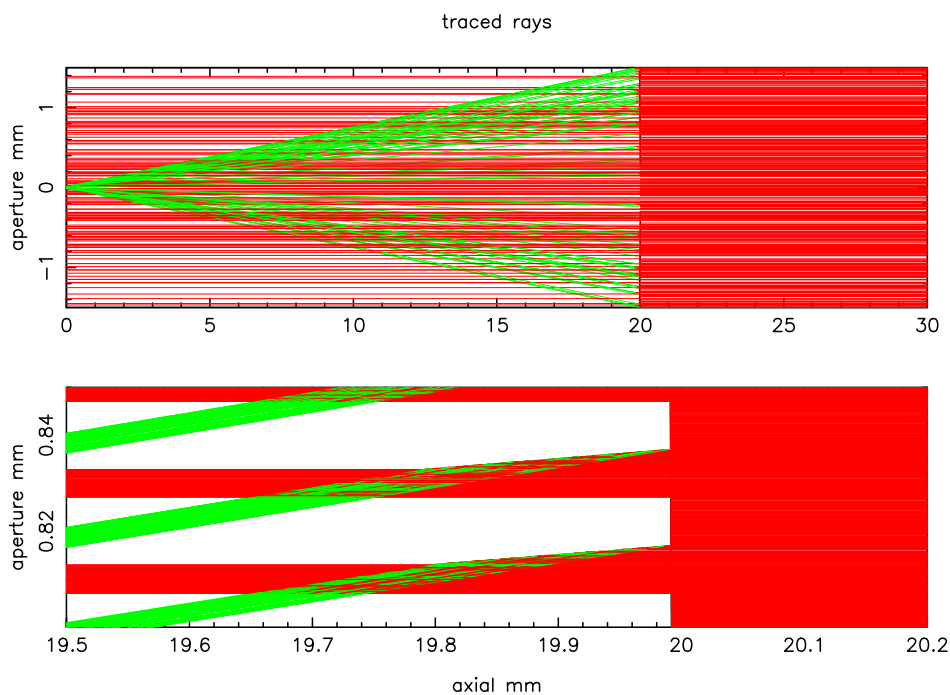


Figure 3.20: An MOA acting as a telescope, focusing an infinite source at an energy of $1.04keV$. The formatting for this figure is the same as in figure 3.17. The focal length of the MOA is $20mm$ and the length of the system is $30mm$. The MOA has a radius of curvature of $40mm$, is positioned at $20mm$ and is curved toward the focus. The lower image shows a zoomed-in image showing that the parallel rays entering the channels from the right, exit the MOA at an angle on the left.

as all the rays reflected by the first MOA are parallel to the optical axis and in line with the channels of the second MOA. If the MOAs are perfectly aligned, then all the rays which have been reflected by the first MOA will be reflected by the second. It can also be seen that there is more than one focus. The first focus is created by rays reflected by the second MOA only and the focus at $0.0mm$ is caused by the rays which are reflected by both MOAs.

3.8.3 Equal grazing angle Micro Optical Arrays

In the collimator-telescope configuration described previously, all the rays reflected by the first MOA will be reflected by the second if the two MOAs are properly aligned. However, in the case of equal grazing angle tandem MOAs, the number of rays reflected is dependent on the physical set up of the MOA system. As shown previously, equation 3.41 describes the case where the rays hit both MOAs at the same angle.

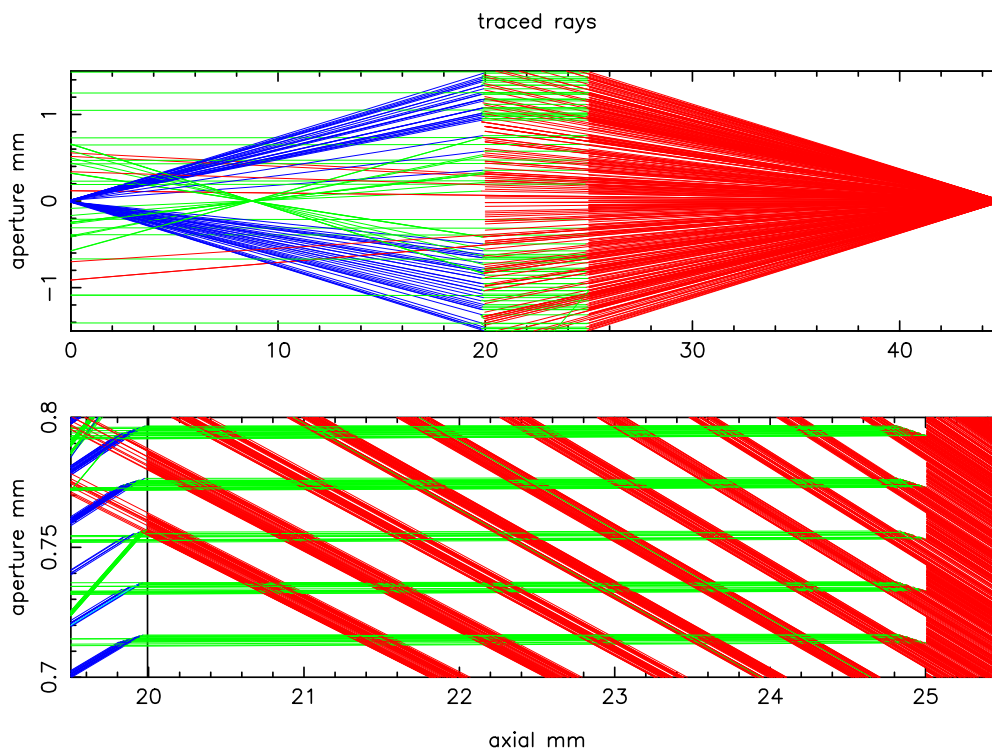


Figure 3.21: Two MOAs acting as a collimator-telescope tandem system. The top image has the finite source with an energy of 1.04keV on the right of the image at 45mm and the detector is on the left at 0.0mm . The image has been produced in the same way as 3.17, with the addition of the blue rays which demonstrate rays which have been reflected twice, once by each MOA. The collimator-telescope system is operating over a distance of 45mm with the two MOAs positioned at 25mm and 20mm respectively. The first is a collimator MOA with a radius of curvature of 40mm curved toward the source. The second MOA is acting as a telescope also with a radius of curvature of 40mm curved toward the detector. The MOAs are separated by 5mm and the rays are parallel to the optical axis between them, this can be seen in the lower image. The rays enter the channels from the right, are reflected by the first MOA and are then reflected by the second MOA as they are perfectly aligned. The majority of the rays reflected by the first MOA are reflected by the second MOA. Two foci can be seen in the top image, the first is at $\sim 8\text{mm}$, the second is at 0.0mm . The first focus is created by rays which have passed through the first MOA and are only reflected and focused by the second MOA and the second focus is created by the rays which have been reflected by both MOAs.

$$\frac{1}{R_1} + \frac{1}{R_2} = \frac{1}{s_2} - \frac{1}{s_1} \quad (3.41)$$

and

$$\frac{1}{R_2} - \frac{3}{R_1} = \frac{2}{s_2} \quad (3.42)$$

where R_1 and R_2 are the radii of curvature of the MOAs, s_1 is the distance from the source to the first MOA and s_2 is the distance from the second MOA to the detector. If the radii of curvature of the first MOA is set to equation 3.43,

$$R_1 = \frac{4s_1s_2}{s_1 - 3s_2} \quad (3.43)$$

and the radius of curvature of the second MOA is set to equation 3.44,

$$R_2 = \frac{4s_1s_2}{3s_1 - s_2} \quad (3.44)$$

it is possible to create a tandem, line-to-line focusing system. Figure 3.22 demonstrates the equal grazing angle tandem system.

As can be seen in figure 3.22, with a gap between the two MOAs, the focus is not positioned as expected at $0.0mm$ but is closer to the MOAs, and the number of rays focused is much less than in figure 3.21. By placing the MOAs close together so they are almost touching, it is possible to move the focus to $0.0mm$ and increase the number of focused rays, thereby increasing the intensity of the focus (see figure 3.23).

As with the collimator telescope MOAs, there are three foci produced by this system and two are shown in figure 3.23. The first, at $\sim 18mm$, is created by the rays which have only been reflected by the first MOA. The focus created at the detector, at $0.0mm$, is created by the rays which have been reflected and focused by both MOAs. The third focus, created by rays only reflected by the second MOA, cannot be seen in this image, but would form behind the detector at $\sim -30mm$.

3.8.4 Flat-curved tandem Micro Optical Arrays

In this configuration, the first MOA is flat, and the second MOA is curved toward the focus with a radius of curvature, R_2 , given by equation 3.45

$$R_2 = \frac{2s_1s_2}{s_1 + s_2} \quad (3.45)$$

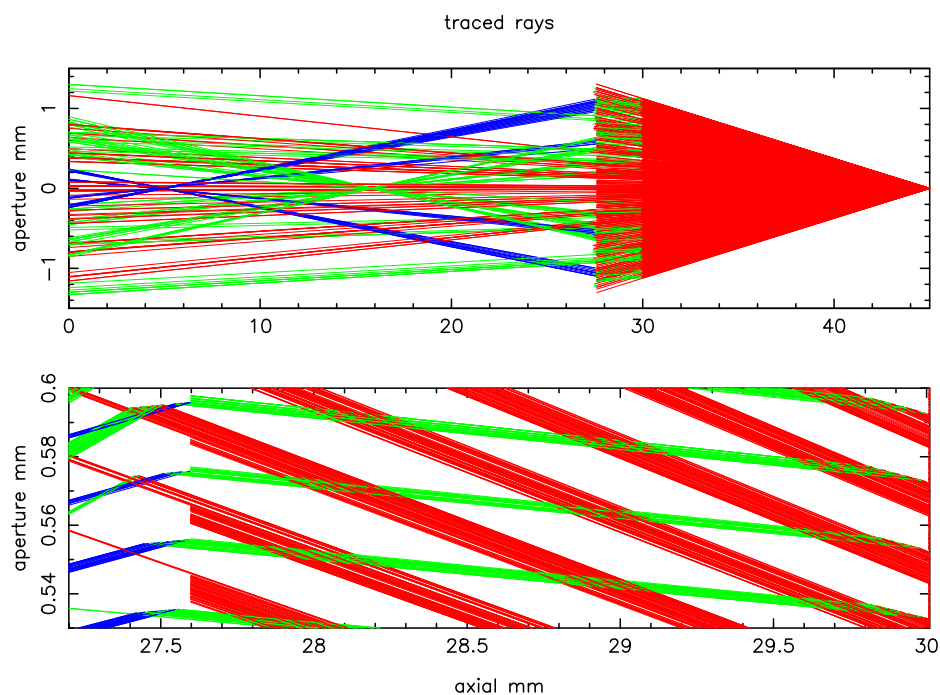


Figure 3.22: Line-to-line focusing with an equal grazing angle tandem MOA system. The system is set up in the same way as figure 3.21. Set over 45mm with the source at 45mm , the MOAs at 30mm and 27.5mm respectively, and the detector at 0.0mm . The full system is shown in the top graph, where the rays are reflected at the same angle by both MOAs. Not all rays reflected by the first MOA are reflected by the second MOA. A zoomed-in image in the lower frame shows the rays being reflected by the two MOAs. There are two foci again in the image, caused by reflections from the first MOA and reflections from both MOAs. The second focus, from the double reflection rays, is not at 0.0mm due to the gap between the MOAs. The intensity of the focus spot is also less than that in figure 3.21, because fewer rays are focused by both MOAs.

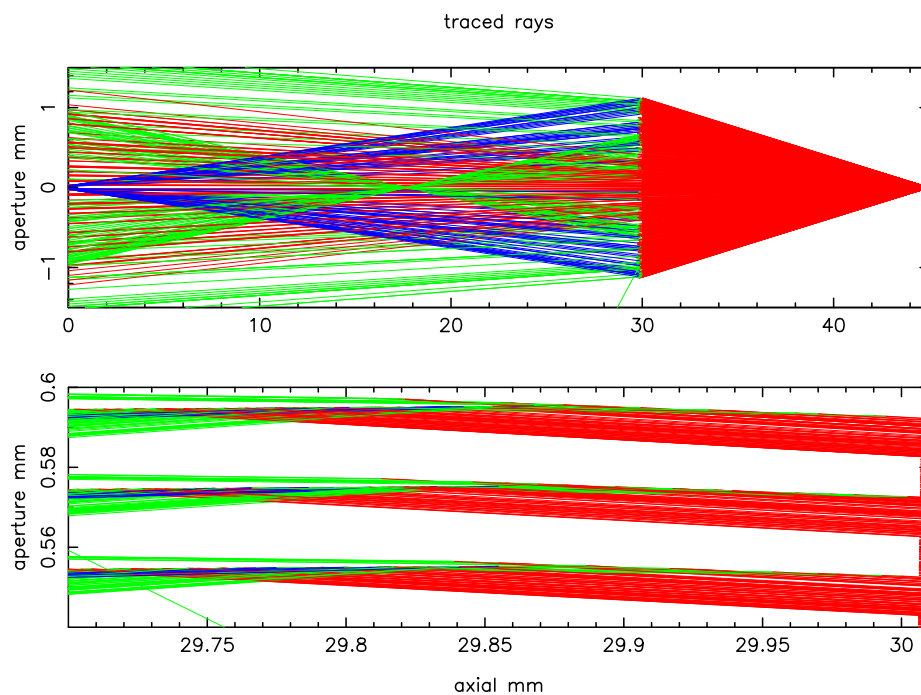


Figure 3.23: Line-to-line focusing with an equal grazing angle tandem system, with no gap between the MOAs. This system is identical to figure 3.22 except the MOAs are almost touching. The number of rays which are focused by both MOAs is greatly increased and the focus has been moved to 0.0mm as expected. In the lower frame, it is clear how close the MOAs are, although some rays reflected by the first MOA are still not reflected by the second.

The number of rays which are focused using this method is lower than that from the other two tandem configurations, due to the alignment of the channels of the MOAs, figure 3.24. In the case of the collimator-telescope system, all the rays which have been focused by the first MOA are focused by the second, as long as the channels are aligned properly. In the other two cases, even the rays focused by the first MOA are not necessarily focused by the second. In the equal grazing angle case, the MOAs need to be almost touching in order to achieve the maximum number of rays reflected by both MOAs. In figure 3.24 b), some of the rays which are reflected by the first MOA are shown to experience a secondary reflection off the opposite wall. These rays, shown in blue, are then not reflected by the second MOA which reduces the efficiency of this configuration.

The maximum number of rays are reflected by the equal grazing angle tandem MOA system, however, the preferred physical set up is the flat-curved tandem system as only one MOA would need to be adaptive thus simplifying the set up and mounting. Ideally an MOA would be created with concentric rings of channels,

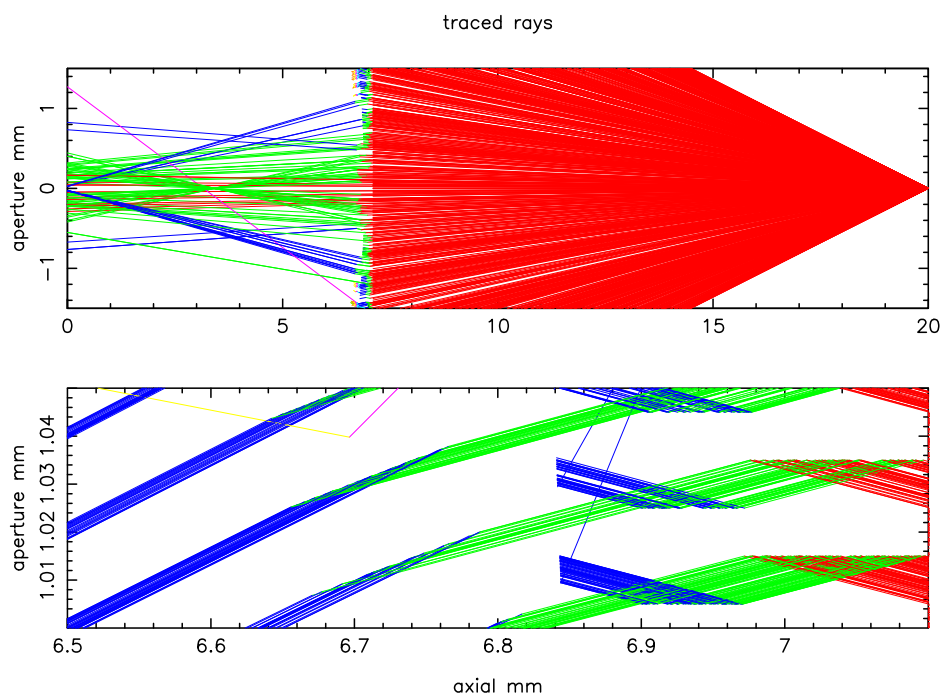


Figure 3.24: A flat-curved tandem MOA system. The source is to the right of the image and the detector is to the left and is configured in the same way as figure 3.21. In the top frame, the MOA closest to the source has an infinite radius of curvature, and the second MOA is curved toward the focus. The source is focused over a distance of 20mm . The MOAs are positioned at 7mm and 6.8mm respectively and can be seen in the lower frame. The number of rays focused by this system is less than that shown in figure 3.23, as fewer rays reflected by the first MOA are focused by the second MOA. Some of the rays which have been reflected off one wall in the first MOA experience a secondary reflection off the opposite wall. These rays, shown in blue, are not reflected by the second MOA which reduces the efficiency of this configuration.

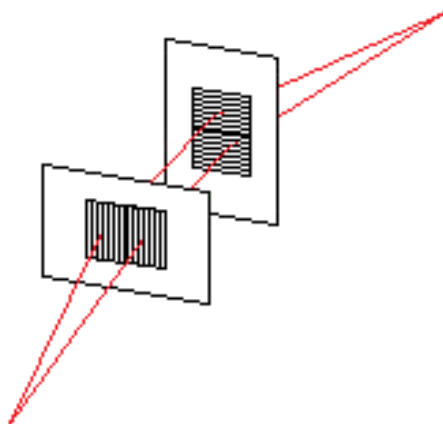


Figure 3.25: An illustration of a crossed pair of MOAs. These MOAs are set up so that they are orthogonal to one another. This creates a focused spot, with cross arms, as opposed to a line focus.

which would provide a focused spot of high intensity, but this is difficult to achieve due to the surface roughness and manufacturing process. A focused spot can be achieved with two 1D MOAs by creating a crossed pair in a 2D system, where the two MOAs are orthogonal to one another, as shown in figure 3.25.

3.8.5 Crossed pair Micro Optical Arrays

A spot focus can be achieved by using a crossed pair of 1D tandem MOAs, creating a 2D system similar to MCPs. This is shown in figure 3.26 with a small aperture of 1mm and over a large distance of 160mm . The size of the focused spot using this method is $\sim 3\mu\text{m}$, much less than the size of an average biological cell ($\sim 10\mu\text{m}$). A similar model is shown in figure 3.27, but with a larger aperture of 4mm and over a shorter distance of 41mm . Using this method, the focused spot is $\sim 15\mu\text{m}$ in diameter which is much larger but is of higher intensity as more rays are focused. Using a combination or one of these two configurations, a spot focus with high intensity is achieved at the point where the two line foci meet. However, crossed arms are also produced, which could create a problem when irradiating the cells as there may be some damage to the surrounding cells. If the intensity of the cross arms can be kept to a minimum, then this method could be easily adopted as an alternative to the cylindrical MOA system. Analysis of the cross arms was completed in Q, and the flux was found to be 1.5% of the flux of the central spot. This is because the second MOA acts as a block to some of the rays which have been focused by the

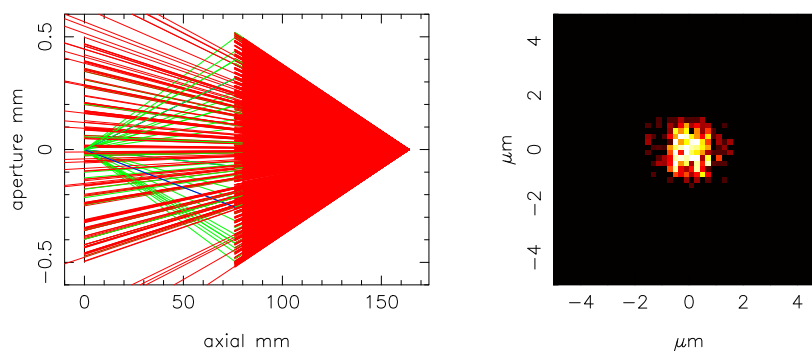


Figure 3.26: A crossed pair of MOAs creating a focused spot. The two MOAs are orthogonal to one another so that each produces a line focus. The point at which the two line foci cross, creates the single point focus. The left hand frame shows the whole system over 160mm , with a gap of 5mm in between the two MOAs. The right hand frame shows the modelled detected image with the axes in μm and the focused spot is $\sim 3\mu\text{m}$ in diameter.

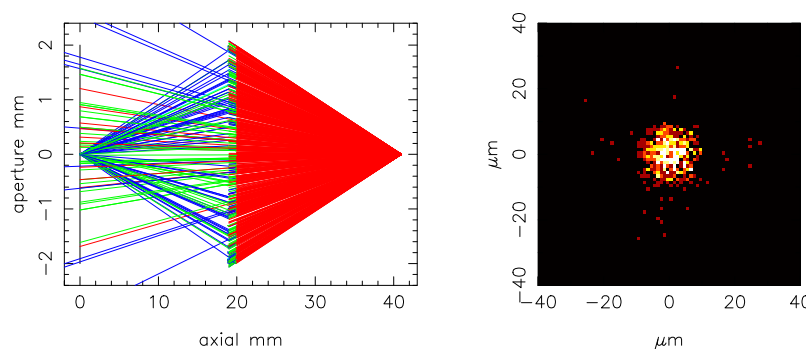


Figure 3.27: A crossed pair of MOAs creating a focused spot of high intensity. The two MOAs are orthogonal to one another so that each produces a line focus. The point at which the two line foci cross, creates the single point focus. The left hand frame shows the whole system over 41mm , with a gap of 1mm in between the two MOAs. The right hand frame is the modelled detected image with the axes in μm and the focused spot is $\sim 15\mu\text{m}$ in diameter. The focused spot is more intense than in figure 3.26 as more rays are focused by both MOAs.

first, which therefore reduces the flux of the cross arms. At this level, the cross arms are effectively negligible.

As described in section 3.3, wet etching provides a much higher surface quality than dry etching as it is possible to etch down the $\langle 111 \rangle$ or $\langle 110 \rangle$ crystal planes, but curved walls and therefore a cylindrical profile cannot be created using this method. Using the crossed pair MOA system, it would be possible to create an approximation to a cylindrical profile using wet etched MOAs with better surface quality and lower surface roughness. The alignment is also not as crucial with this arrangement, as long as multiple channels are in line, a reasonable amount of flux will be focused.

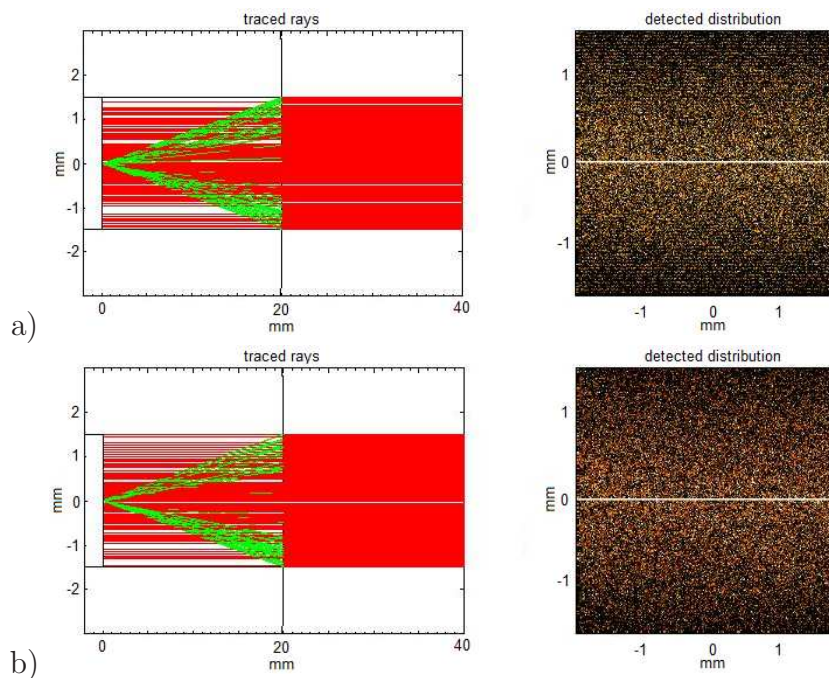


Figure 3.28: Ray tracing and detected images of cylindrical and parabolic MOAs. An infinite source is focused by a curved MOA over a distance of 40mm . The MOA is positioned at 20mm and is curved toward the source with a radius of curvature of 40mm . a) The ray-tracing and detected image of an MOA bent to a parabola. b) An MOA bent to a cylindrical profile. The ray-tracing in both cases is almost identical. The parabolic detected image shows a much cleaner, sharper line focus and the scattered rays are also more coherent.

3.8.6 Parabolic Micro Optical Arrays

The nature of the piezoelectric actuators means that when the MOAs are curved, they create a parabola as opposed to having a cylindrical profile. The parabolic shape has been modelled using the deformation code in Q. The MOAs were modelled in an identical way, with a 1.04keV infinite source and an MOA positioned at 20mm with a radius of curvature of 40mm . The parabolic models showed that although the ray-tracing looked almost identical (figure 3.28), the detected distributions were quite different (figure 3.29). The intensity of the detected distribution for the parabolic MOA is ten times greater than for a cylindrical MOA. This is because a parabola is a perfect solution for focusing an infinite source.

3.8.7 Models of scalloping and shadowing

Low order scattering was already contained within the surface definition routines in Q, however, to be able to model scalloping and shadowing, the routines needed to be

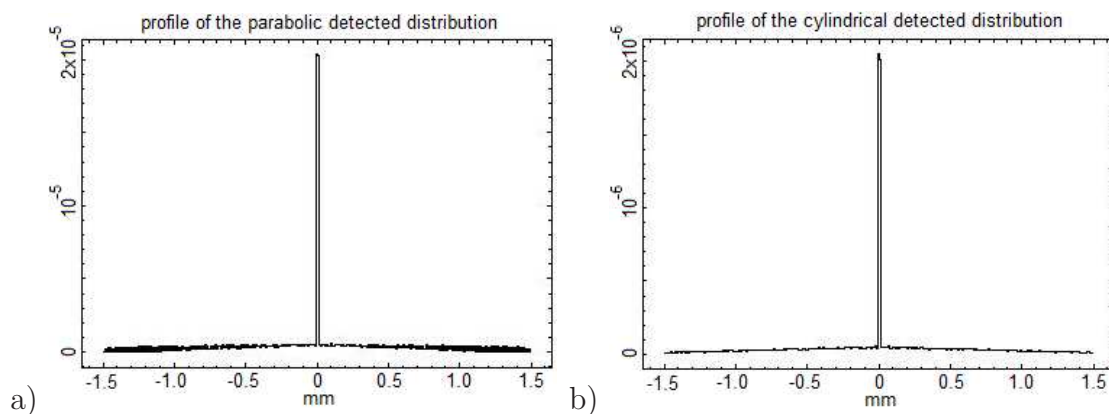


Figure 3.29: Detected distributions of cylindrical and parabolic MOAs as modelled in figure 3.28. a) The distribution of a parabolic MOA and b) the distribution of a cylindrical MOA. The detected distributions are subtly different. The widths of the distributions are very similar, but the intensity of the parabolic line focus is ten times greater than that of a cylindrical MOA.

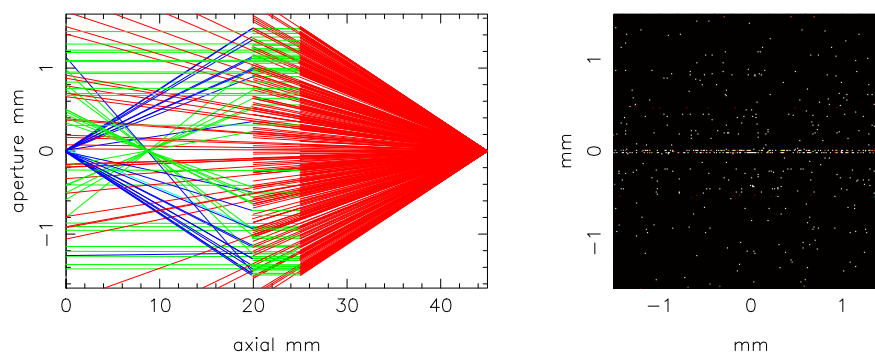


Figure 3.30: A tandem MOA system with scallops and shadowing. The left hand image shows the ray-tracing and the right hand image shows the detected image. This is the same set up as shown in figure 3.21. The number of scattered rays have been increased and the intensity of the line focus has been reduced, but a focus is still produced. The number of rays which are reflected by both MOAs is also reduced.

updated. Here, scalloping includes both the scallop and curtain effects seen on the MOA walls. As described in section 3.6, shadowing was modelled using equations from Klos[19] (as shown in section 3.6.3), and scalloping was modelled by adjusting the power law and deviating the normal of the ray after reflection by a small angle given by the size of the features.

For single and tandem MOA systems, the effect of scalloping simply increases the number of scattered rays and spreads the line focus out (see figure 3.30). However, with the crossed MOAs, unless the optic has a very small aperture and is focusing over a greater distance, a focused spot is not produced. This is demonstrated in figure 3.31 and figure 3.32 respectively.

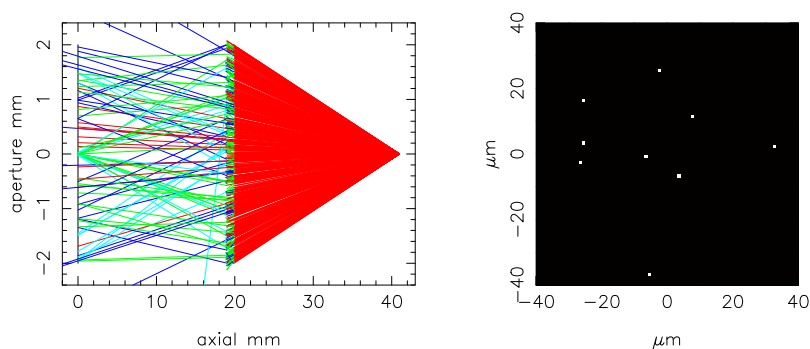


Figure 3.31: A crossed pair of MOAs with scalloping and shadowing included, over a large aperture. The left hand frame shows the ray-tracing and the right hand frame shows the detected image. The MOAs are focusing over a distance of 40mm and the MOAs are at 19mm and 20mm and are orthogonal to one another. There are very few focused rays due to scalloping effects and no focused spot can be seen in the detected image.

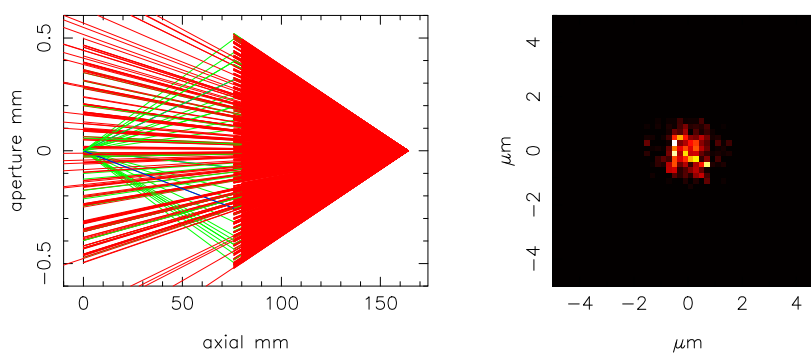


Figure 3.32: A crossed pair of MOAs with scalloping and shadowing, but over a small aperture and longer distance. Left, The ray-tracing and right, the detected image. The MOAs are focusing over a much larger distance of 160mm with the MOAs at 75mm and 80mm and are orthogonal to one another. The number of scattered rays is increased and the intensity of the focused spot is much lower compared to that shown in figure 3.26.

If the curtain effect and scallops can be reduced then crossed MOAs would be a possible solution to approximating the cylindrical profile. If the MOAs are wet etched in the one dimensional profile and combined to create a crossed pair it would remove the scallops and curtain effects completely whilst creating a micrometre focused spot.

3.9 X-ray experiments using Micro Optical Arrays

Two sets of experimental tests were carried out on the MOAs, the first at STFC Daresbury Laboratory and the second at UoL. The experiments carried out at STFC Daresbury Laboratory were simple reflectivity tests on a dry etched MOA whilst the tests performed at UoL tested both dry (the same MOA that was tested at STFC Daresbury Laboratory) and wet etched MOAs but again were simple reflectivity measurements.

3.9.1 Micro Optical Array reflectivity experiments

The reflectivity experiments completed at STFC Daresbury Laboratory were performed using the diffractometer. An MOA was selected at random from a batch which were dry etched and produced at the SMC in Edinburgh. This batch of MOAs were estimated to have a surface roughness of approximately $20nm$. After examining the MOA using a microscope, it was found that one side was in good condition whilst the other seemed discoloured and scratched and this side was placed away from the X-ray beam. A fixed anode X-ray generator at $5kV$, fitted with a carbon source was used as the X-ray source. The MOA was mounted in a temporary aluminium holder within the diffractometer and a carbon filter was placed between the source and diffractometer chamber to reduce the bremsstrahlung flux and the carbon $K\alpha$ emission line. A $1mm$ vertical aperture was also placed within the X-ray beam to reduce the scatter of the beam and the experiments were carried out at a vacuum pressure of $\sim 1 \times 10^{-8} mbar$. The diffractometer comprises of two concentric rotation stages which are driven by stepper motors with an accuracy of 0.001° . The MOA was rotated on one stage, about an angle Ω and the detector was rotated

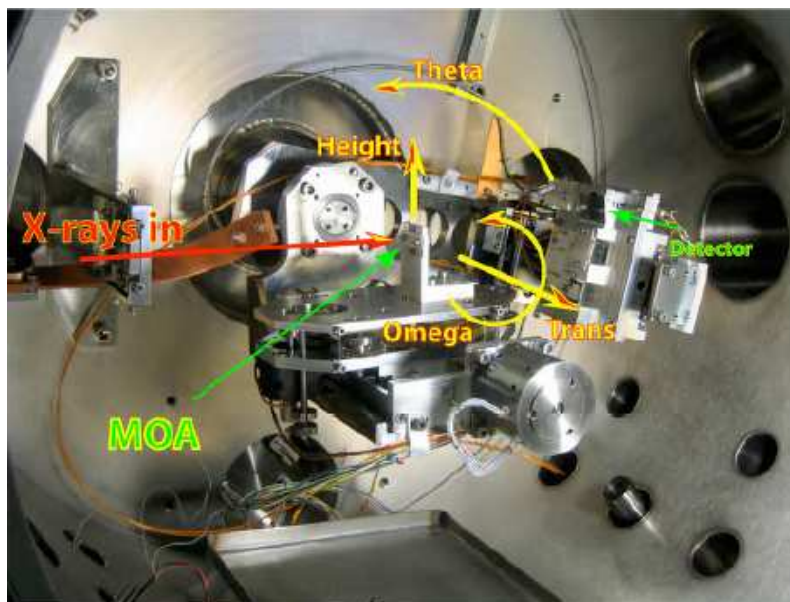


Figure 3.33: The set up of the reflectivity tests performed at STFC Daresbury Laboratory. The MOA was rotated on one stage, about an angle Ω and the detector was rotated on the other, about an angle Θ . Images provided by STFC Daresbury Laboratory.

on the other, about an angle Θ . The MOA could also be moved in two translational stages, height and longitude, thus allowing the best “through” position to be determined. The experimental set up is shown in figure 3.33.

The CEM detector is conical in shape and 2mm wide, which blurs the reflected function as shown in figure 3.33.

A brief measurement of the MOA’s throughput was completed by comparing the detected flux with and without the MOA in position. The results showed that a throughput of 44% was achieved with the MOA. It was scanned in height to determine the optimum vertical position by monitoring the counts after 3 seconds. A dip was found at a height of $H = 1.8\text{mm}$ due to the central stop and a height of $H = 2.5\text{mm}$ was selected for the optimum stage height. A scan through a full range of Ω was completed and it was found that a complete loss of signal occurred at $\Omega = \pm 4^\circ$, giving a length to width ratio of the channels of 15.4:1.

For the reflectivity study, Ω was increased in increments of 0.2° , and for each value of Ω , the detector was scanned through a full range of Θ . The Θ scans were completed at increments of 0.01° with 5 second counting intervals per point. An example of the results obtained from the experiments conducted at STFC Daresbury Laboratory is shown in figure 3.34.

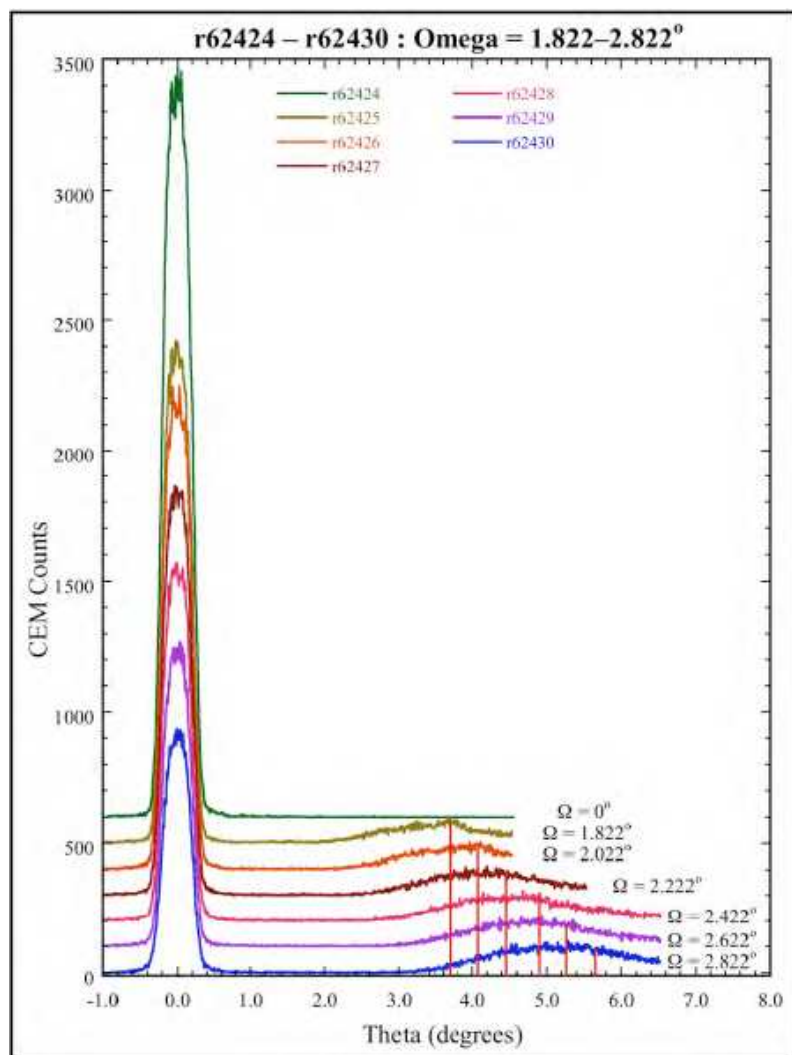


Figure 3.34: An example of the results obtained from the reflectivity tests carried out at STFC Daresbury Laboratory. These results cover an angle range of -1.0° to 8.0° with the straight through flux shown at 0.0° on the X axes and the reflection is seen at approximately 4.0° . Images provided by STFC Daresbury Laboratory.

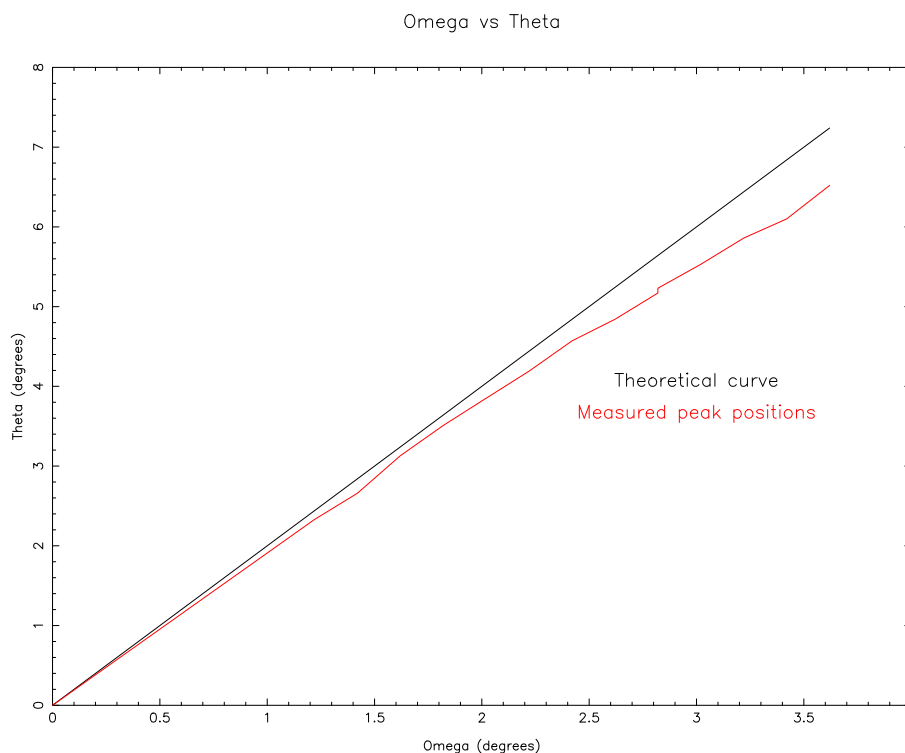


Figure 3.35: The relationship between Θ and Ω . The black line is the expected relationship of $\Theta=2\Omega$, and the red line shows the positions of the peak number of counts at each angle.

In this set up, it is expected that $\Theta=2\Omega$ but this was not the case at the higher angles as shown in figure 3.35, where the trend slowly drops away from the expected trend (shown in black).

Figure 3.36 shows the combination of all the results obtained during these experiments. The blue line indicates the transmitted component detected whilst the red line indicates the reflected component. The vertical lines show the cut or repeat in data obtained. As the transmitted component decreases, the reflected component increases, which is due to the increase in the amount of surface visible to the X-rays as the MOA is rotated. This creates a triangular form in the reflective component and similarly the reduction in the amount of straight through transmission forms a triangular profile in the transmitted component.

From the results it could be concluded that the MOA had a surface roughness of the order of $10nm$ or better but with extensive scalloping. The reflections would therefore be a combination of two distinct elements: wide angular scattering of the X-rays from the micro roughness and micro-lensing from the scalloping effects, where the beam will be reflected at different angles and provide differing foci. The MOA used in the experiments was found to have a low length to width aspect ratio which

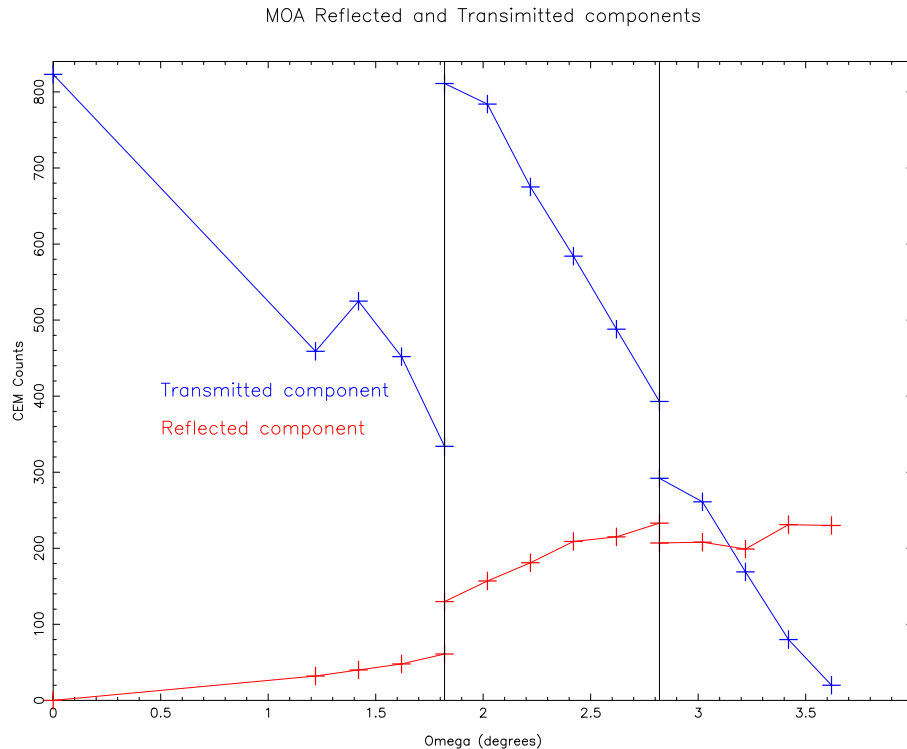


Figure 3.36: Combination of all the results obtained during the experiments at STFC Daresbury Laboratory. The blue line indicates the transmitted component detected whilst the red line indicates the reflected component. The vertical lines show the cut or repeat in data obtained.

would reduce the focusing capability of the optic normal to the optical axis.

There were reflections seen at all angles, but at increasing Ω the counts dropped. There was still a reasonable amount of reflectivity seen at $\Omega \sim 4^\circ$, and it might have been possible to see reflections at larger angles.

3.9.2 The first experimental tests at UoL

The CCD life test facility at UoL has been used to characterise past and present CCDs including the flight spares for XMM-Newton. The facility is $3.1m$ long and has an X-ray source, X-ray CCD and mounting for an optic. The X-ray source can operate at energies between $200eV$ and $4keV$ but these tests were carried out at energies of between $600eV$ to $1keV$. The CCD is a CCD-22, similar to those used on XMM-Newton and is on an $X - Y$ table which allows movement of $\pm 35mm$ in each direction. Figure 3.37 shows the life test facility within the lab. The X-ray source is on the far right of the image (just under the bookcase) with the CCD at the opposite end of the pipeline. The MOA was placed within the tank via the flange which is at the centre of the facility. There is a rotational arm at this point



Figure 3.37: Image of the XMM-Newton CCD life test facility at UoL. The test facility is 3.1m long with an X-ray source, X-ray CCD and mounting at the centre, for an optic. The X-ray source is on the right hand side of the image (by the bookcase) whilst the CCD is on the far left of the image. The MOA was mounted behind the flange which is in the centre of the pipe. The rotation arm can also be seen attached to this flange.

which allows rotation of the optic in one axis and was controlled by a micrometer which allowed for accurate adjustment of the optic's rotation.

The tests were designed to investigate the reflectivity of the channels of the MOAs and so the channels needed to be fully illuminated. To achieve this in the facility described above, the MOA was rotated in between two positions, one where most of the rays passed straight through the optic and the other at an angle of $\sim 2.6^\circ$ where the majority of the length of the channels was illuminated. The first position gave an idea of the spacing and quality of the etch whilst the second position allowed the quality of the surfaces of the channels to be studied.

3.10 Simulated results of the Micro Optical Array experiments

Models of these tests, in the two positions described and two intermediate positions, were produced in Q and the results can be seen in figure 3.38. The model set up was based on the testing facility, with the positions of the source, detector and MOA being set to that of the facility and with a perfect reflecting surface. The

images produced are the same as those for previous models described, and the four positions of the MOA can be seen in the ray-tracing diagrams. Although some rays will be reflected in the first position, the strength of this line focus is very low. A comparison of the distribution of the focus created by the MOA in the four different positions has been completed and can be seen in figure 3.39. The distributions are drawn by taking a cut along the detected image and a histogram is produced of the flux in the pixels within the area selected and the width of the detected distribution represents the width of the line focus. If the line focus is not completely in focus, then the detected distribution will appear wider. This can be seen in figure 3.39 a), which shows the distribution for the rays passing straight through the MOA. There is a line focus produced but it is wider, more scattered, and of less intensity than that shown in figure 3.39 d).

In order to study the effect of the MOA surface roughness, it was added to the models described above by specifying the surface quality in $\text{\AA}/mm$. The results can be seen in figures 3.40 and 3.41. These figures are set up in exactly the same way as figures 3.38 and 3.39, but with surface roughness included. The roughness in these images is not as high as that seen on the surface of the MOA, but they do provide an illustration of the effect of the surface roughness on the results of the tests where the line focus is less intense as more flux has spread into the wings.

3.11 Results from the X-ray experiments performed at UoL

The dry etched MOA, which had been tested at STFC Daresbury Laboratory, was placed within the facility as described in section 3.9.2 and rotated between 0° and 2.1° at increments of 0.14° . An example of an image from the CCD is shown in figure 3.42 with the straight through flux clearly visible. The MOA was calculated to have a throughput of 38.83% which is close to the figure of 44% obtained at STFC Daresbury Laboratory. The number of counts in the central region and to either side of the straight through flux were counted for each of the images taken and a graph was then produced to show the reflection as shown in figure 3.43. These results vary from those produced by the models shown above as the surface quality within

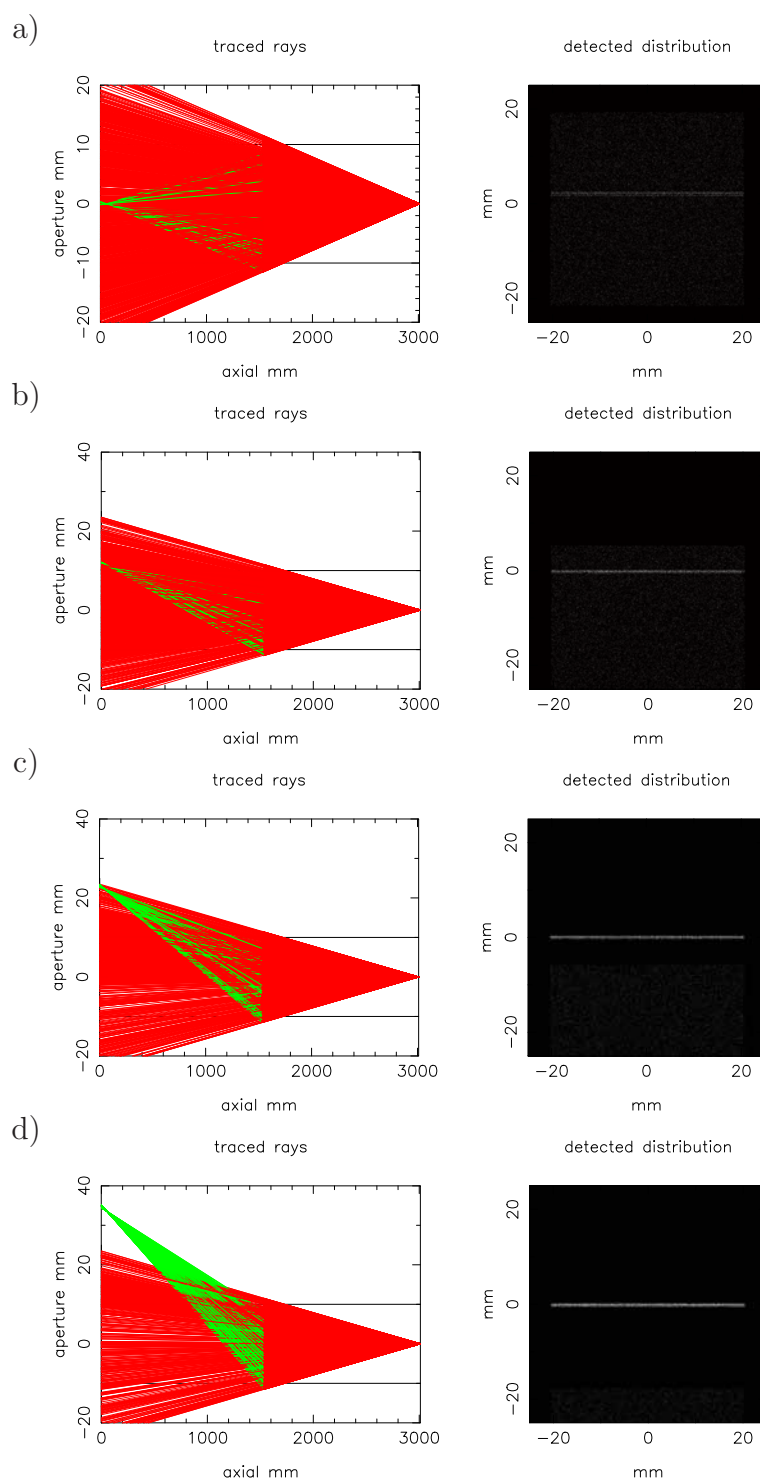


Figure 3.38: Ray tracing of the MOA tests. The source is at an energy of $\sim 1\text{keV}$ and the detector and MOA are positioned as in the testing facility. The ray traced system and detected image are shown for four different angles. a) The initial position of the MOA where the rays passing straight through the optic was studied. b) and c) are intermediate angles between a) and d). d) The angle at which the full length of the MOA channels are illuminated.

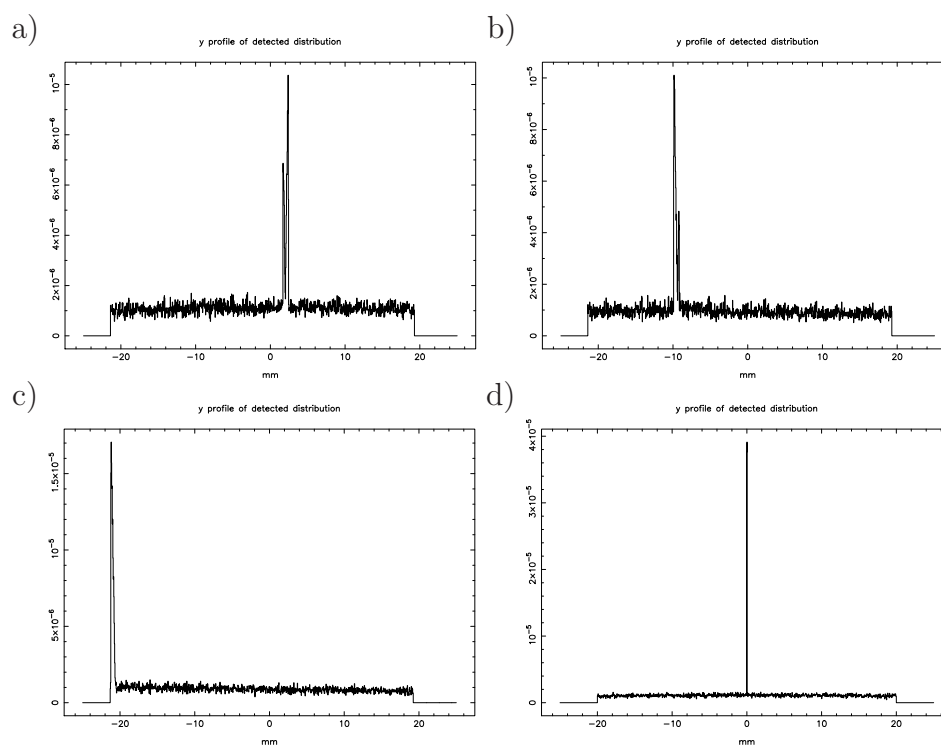


Figure 3.39: Detected distribution of the ray-tracing of the MOA tests. The source is at an energy of $\sim 1\text{keV}$ and the detector and MOA are positioned as in the testing facility. a) The distribution of the initial position of the MOA where the majority of rays pass through the optic, b) and c) show intermediate angles between a) and d). d) The angle at which all the MOA channels are illuminated. The distributions appear off centre as the reflected rays are not in the centre of the detector as the MOA is rotated.

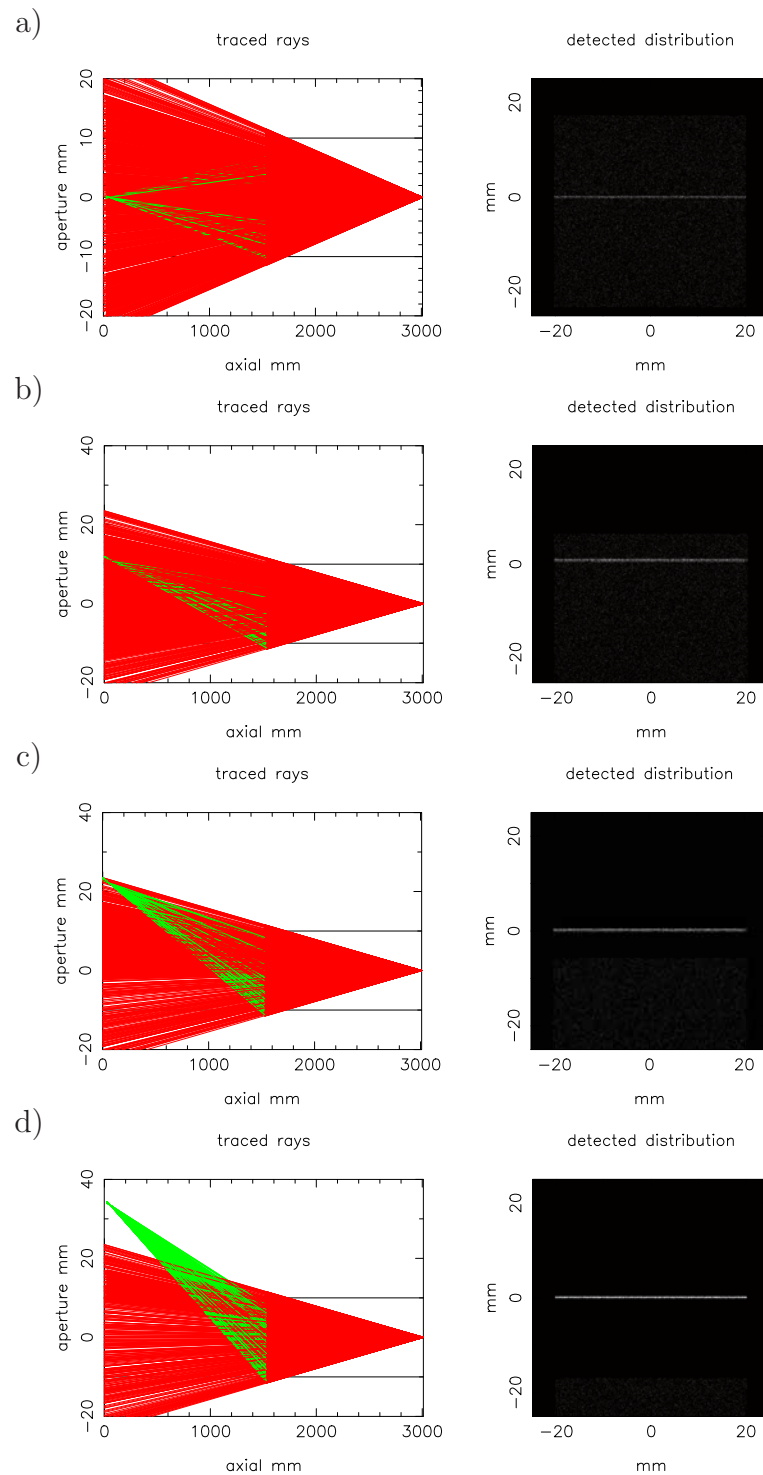


Figure 3.40: Ray tracing of the MOA tests, as in figure 3.38 but with additional surface features and roughness. The source is at an energy of $\sim 1\text{keV}$ and the detector and MOA are positioned as in the testing facility. The ray traced system and detected image are shown at the same four angles as in figure 3.38. Scattering of the beam is clearly visible in all four images. The width of the detected focused line is also wider due to the surface features.

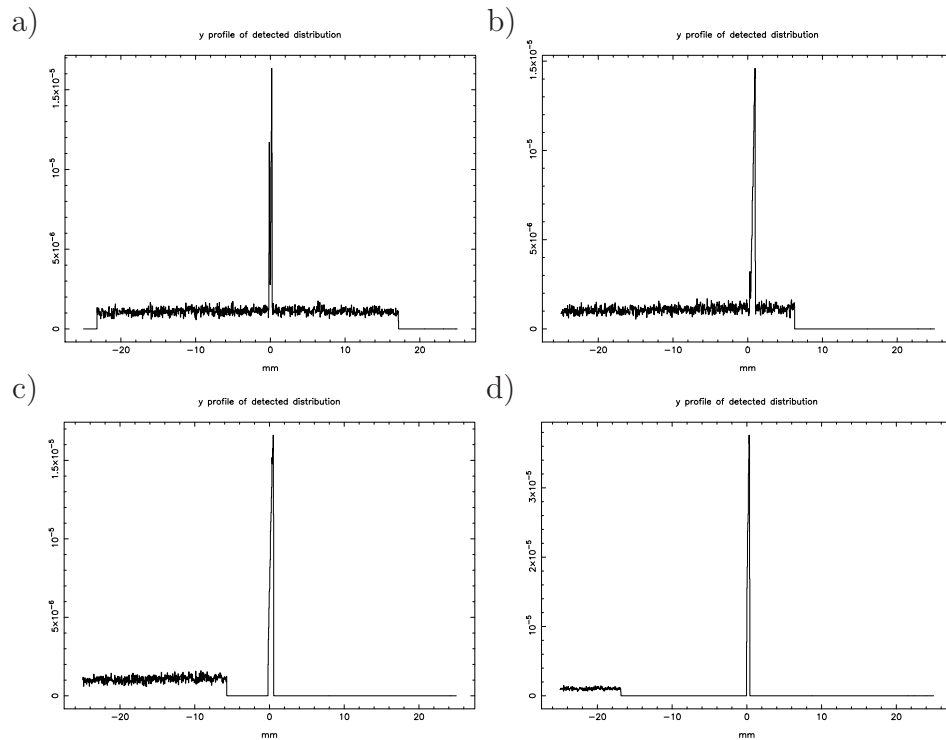


Figure 3.41: Detected distribution of the ray-tracing of the MOA tests, as in figure 3.39 but with surface roughness. The source at an energy of $\sim 1\text{keV}$ and the detector and MOA are positioned as in the testing facility. The width of the distributions is wider than that shown in figure 3.39, this is due to the increased scattering of the beam due to the surface roughness.

the simulations is higher than that of the real MOAs and the detected distributions produced by the simulations show the total number of counts over the entire CCD at a single position, not the peak number of counts at each position.

The number of counts in the central region slowly decreases as the amount of flux which is reflected increases and creates a triangular profile in the data. The reflection component was calculated as a percentage of the maximum number of transmitted counts detected. Unfortunately the amount of reflection was very low at $\sim 3.33\%$ and so the triangular profile is not as clear as it should be. It is also apparent that the two surfaces of the channel walls behave differently because there is asymmetry in the counts between the right and left. This is most likely due to the high surface roughness seen in the FEGSEM images. It was decided that a wet etched MOA would be tested in the same way to see if there was an increase in the amount of reflection. The ESEM at UoL was used to image the MOA and it was found to have much smoother walls and practically no surface features, as shown in figure 3.16.

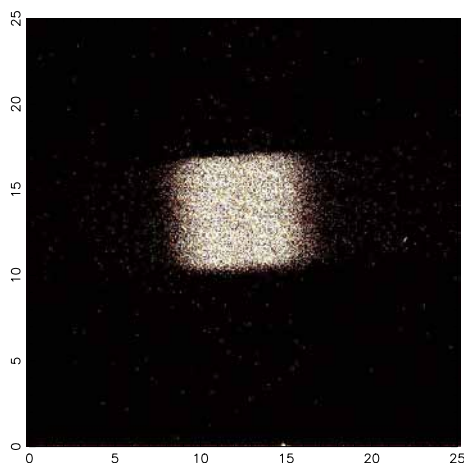


Figure 3.42: An example of a CCD image obtained during the MOA tests within the CCD life test facility at UoL. The central bright region is the straight through flux from the MOA.

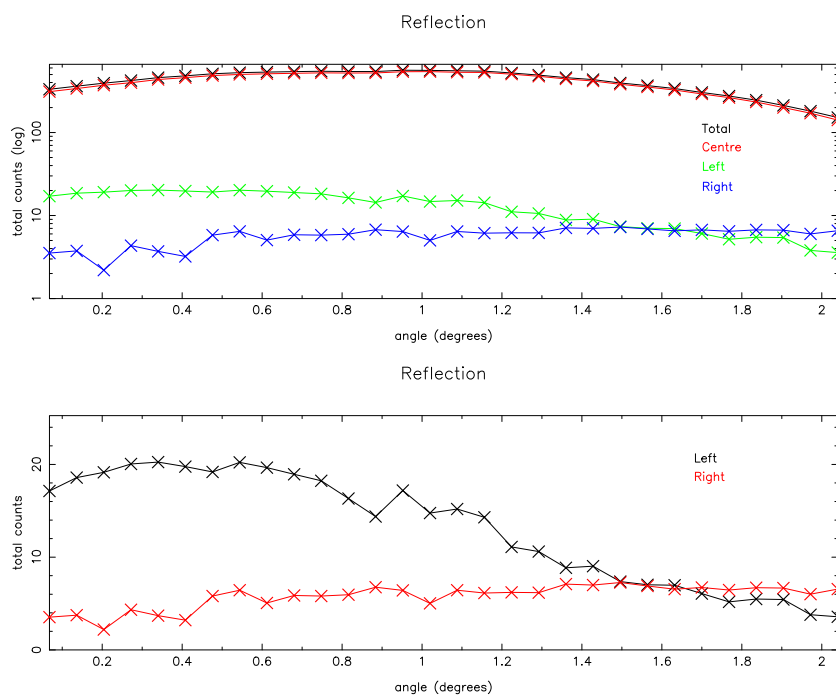


Figure 3.43: Results from the reflectivity tests using a dry etched MOA. There is an increase in the amount of reflected flux as the amount of flux in the central region decreases. The amount of reflection is very low at $\sim 3.33\%$ and has suffered from the surface roughness features as shown by the asymmetry in the left and right hand reflection.

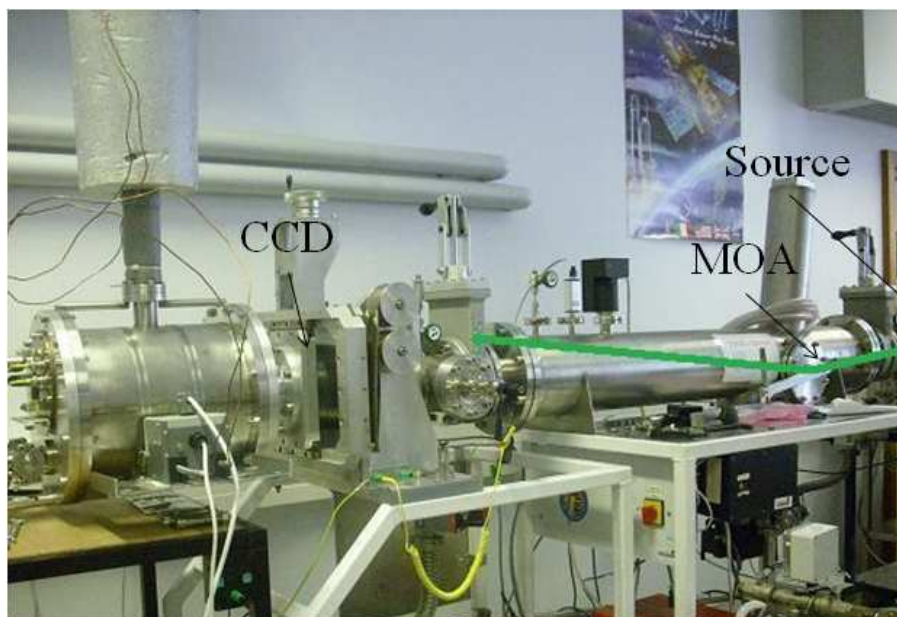


Figure 3.44: A demonstration of why no reflection was seen using the wet etched MOA, with the path of the X-rays shown in green. The reflected flux was being blocked by one of the flanges in the facility.

The wet etched MOA was mounted in an identical way to the dry etched MOA, however, absolutely no reflection was seen. The reason being that the wet etched MOA was half the thickness of the dry etched MOA and so the total reflection angle was double. It was found that one of the flanges towards the detector was too small for any reflected flux to pass to the CCD and this was preventing its detection. This problem is demonstrated in figure 3.44.

The source is mounted on a θ , 2θ turn table to enable accurate alignment of the source, crystal, optic and CCD. It was concluded that the wet etched MOA should be mounted within the crystal housing and rotated by 90° so that the source could be rotated and the reflected flux would go straight down the facility to the detector. This would mean that only reflected flux would be seen above $\sim 1^\circ$ and should therefore increase the amount of reflection. The mounting set up used for the wet etched MOA is shown in figure 3.45.

The reflection was calculated by summing all the counts in the image once the straight through flux had been removed and the results are shown in figure 3.46. The amount of reflection seen was 5.93% which is still reasonably low considering the models showed a reflection of almost 40% would be possible, but more than was seen with the dry etched MOA by almost a factor of 2. The energy at which the source

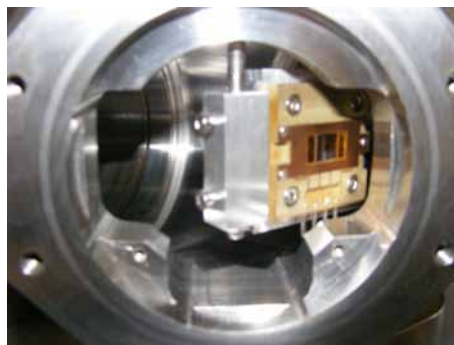


Figure 3.45: The mounting for the wet etched MOA within the crystal holder. A dial on the top allows for accurate alignment of the MOA with the source and a θ , 2θ turn table allows the reflected flux to be studied.

was operating during the tests would mean the maximum amount of reflection from silicon at that energy would be $\sim 18\%$ and the optic is therefore reflecting $\sim \frac{1}{3}$ of the flux available.

3.12 Summary and conclusions

In order to study single cell mutation, by the use of focused X-ray radiation at energies $\geq 1\text{keV}$, a new optic had to be designed and manufactured. The current small scale focusing devices, zone plates, cannot work at energies $\geq 1\text{keV}$ without significantly decreasing the aperture size and increasing the focal length. This research would need to be able to apply a known dose of radiation to each individual cell within a group as opposed to an average dose to the group of cells. The optic needs to be able to produce a focused spot of $\sim 10\mu\text{m}$ in diameter, to irradiate single cells over a distance of no more than 50mm . Micro Optical Arrays (MOAs) were designed to be able to achieve these goals and have been modelled and tested to confirm these predictions.

The initial MOA prototypes have been fully modelled, including single and tandem configurations. Equations have been derived to describe both 1D and 2D systems, including the radii of curvature and positions of each plate, and have been used to investigate the MOA responses by the use of ray-tracing. These combinations included line-to-line focusing with collimator, telescope and equal grazing angle 2D systems. Parabolic MOAs and crossed pair MOAs which are capable of producing a focused spot on the same scale as a biological cell, were also investi-

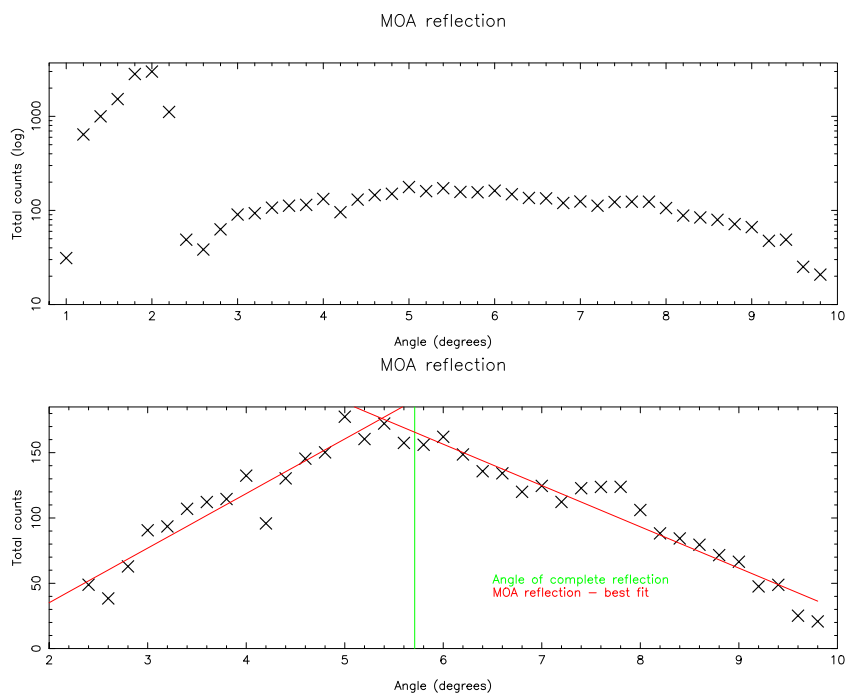


Figure 3.46: The results from the reflectivity tests of the wet etched MOA mounted in the crystal chamber. The triangular shape is very clear and shows reflection of 5.93%.

gated. The results of the models have shown that, if the MOAs can be produced with low surface roughness then they will be suitable for the irradiation of biological material. Prototype optics have been designed and made using both wet and dry etching techniques. If the new prototypes are wet etched and placed in a crossed pair configuration, it would be possible to create an optic which will be able to focus X-rays to a spot size of a biological cell, $\sim 10\mu m$.

Several problems have been identified with the current MOA prototype design. The quality of the surfaces of the dry etched channel walls has led to the consideration of a double sided etch of the MOA. As shown in the FEGSEM images of the dry etched MOA, one side had very cleanly etched, straight channels with $\sim 20nm$ surface roughness. However, on the reverse side the channels were not fully etched, were narrow and had high surface roughness. The reflection tests also showed that the amount of reflection that would be possible would be quite low and could prevent them from being efficient enough for the radiation studies.

It was suggested that by etching the channels from both sides, the channel walls would be smoother, even and with a more consistent surface roughness. There is a possibility that this would cause a small step if the masks of the channels are not properly aligned but this would simply shorten the length of the channel as a

small amount of the channel wall would be hidden from the incoming X-rays. The reflective area efficiencies were calculated for a single MOA, a tandem MOA and a double etched MOA with a step. The results were 1.94% for a single MOA, 3.20% for a tandem MOA and 0.88% for a single double sided etched MOA. Whilst this is possibly a solution for improving the quality of the walls when dry etching the channels, wet etching may provide higher quality surfaces.

As shown in the ESEM images the surface quality of the wet etched MOAs is almost perfect with no surface features at all. An increase from 3.33% to 5.93%, almost a factor of 2, in the amount of reflection was seen in the results from the reflection tests, where the reflection component was calculated as a percentage of the maximum number of transmitted counts detected. As the wet etch method only allows straight walls to be etched, the possible patterns that could be created are limited. However, if two standard prototypes are placed orthogonal to each other to create a crossed pair, then a focused spot of $\leq 15\mu m$ can be achieved from an aperture of $4mm^2$.

A major problem related to the bending of the silicon and the piezoelectric actuators is currently being investigated. Tests into the bending of the MOA, completed at UoB and at KCL, showed that the piezoelectric devices cannot bend the silicon enough to provide the focal length and source demagnification required. The required bending is to displace the central region by $\sim 10\mu m$ but currently only $5\mu m$ is achievable. In order to increase the bending, several new prototype design have been conceived.

A silicon sandwich made of $10\mu m$ silicon, $1\mu m$ silicon oxide and $200\mu m$ silicon would be wet etched along the $\langle 111 \rangle$ plane to create very smooth straight channels. The $200\mu m$ silicon would have a large number of channels etched along the majority of the length of the chip but the $10\mu m$ would have the $4mm^2$ active area as with the previous prototype (figure 3.4). The silicon oxide will not be etched but will act as a bonding layer between the two etched layers. At $4.5keV$, $\sim 50\%$ of the rays will pass through the silicon oxide layer so the throughput and efficiency should be relatively unaffected if the micro-focus source is bright enough. The new prototype design can be seen in figure 3.47. The piezoelectric actuators will be attached to the $10\mu m$ silicon layer after it has been etched. The large number of channels on

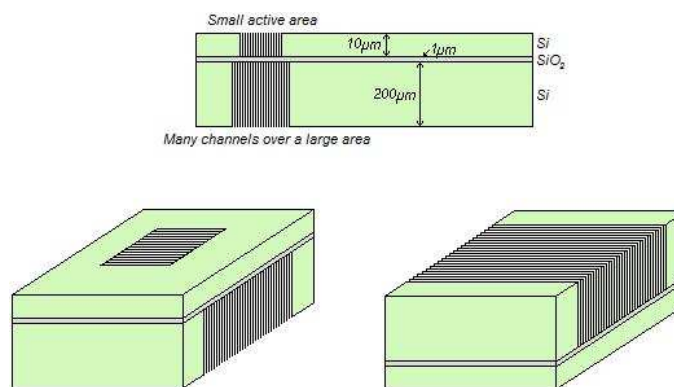


Figure 3.47: A possible new MOA prototype, made from a silicon sandwich chip of $200\mu m$ silicon, $1\mu m$ silicon oxide and $10\mu m$ silicon. The $200\mu m$ silicon layer will be wet etched with many channels over the majority of the length of the chip. The $10\mu m$ layer will have a central active area as with the previous prototype. The silicon oxide layer will act as a bonding layer between the two etched silicon layers.

the $200\mu m$ layer should enable the MOA to bend more easily with the same sized strips made of the same piezoelectric material.

Another possibility, investigated by UoB, is to create a spider MOA, a new arrangement where the piezoelectric devices are used to actuate a series of levers amounting to a mixed piezoelectric and integrated mechanical bending solution. The chip has been redesigned to be $20mm$ x $20mm$ and the levers are made by etching angled channels all the way through the silicon which move independently when the piezoelectric devices are actuated. The actuators have been designed to be $75\mu m$ thick to maximise the bending of the $100\mu m$ thick silicon chip. This form of bending provides a parabolic shape to the MOA, which has been shown with ray-tracing to provide an effective line focus[84]. Figure 3.48 shows a possible prototype design. The legs can either be wet or dry etched and are designed to remove the stress from the active region.

Further possibilities include etching polymers and then coating them with an X-ray reflective coating, or creating a comb where the silicon channels are only attached at one edge. It is vital that the amount of bending required is achieved otherwise the MOAs cannot be used for the radiation studies.

If the MOAs can be wet etched, curved to the correct radius of curvature and mounted in a crossed pair, then they will be able to focus X-rays to less than $10\mu m$ at X-ray energies greater than $1keV$, with enough energy to radiate biological samples.

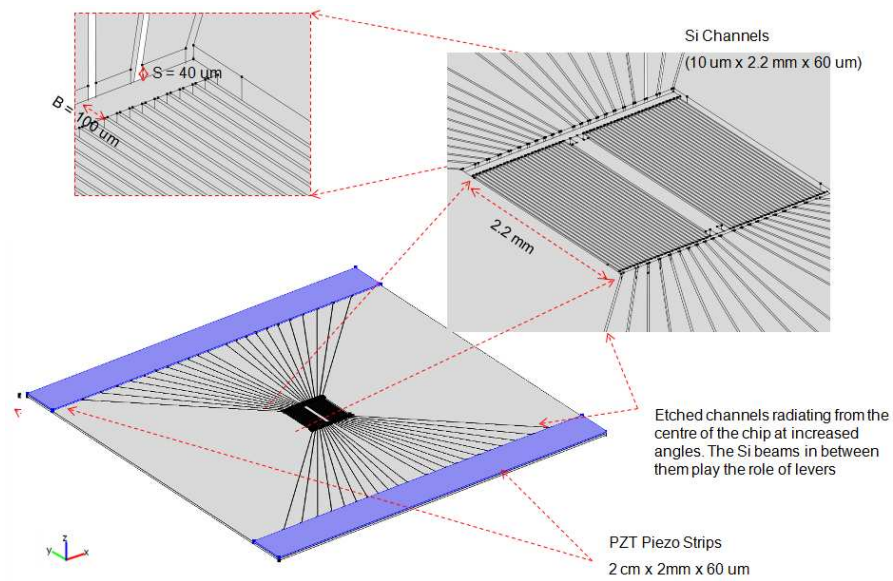


Figure 3.48: A possible prototype design called the spider. A series of channels are etched to make the silicon easier to bend. The legs act as levers which move independently and can either be dry or wet etched and are designed to remove stress from the active region. Provided by UoB.

CHAPTER 4

SUMMARY, CONCLUSIONS AND FUTURE WORK

4.1 Large Adaptive X-ray Optic

The aim of the Large Adaptive X-ray Optic (LAXRO) is to take a standard X-ray shell and improve the resolution of the optic. This is done by actively deforming the figure of the reflecting surface by applying voltages to piezoelectric devices which have been bonded to the reverse. It is hoped that this technology will enable an X-ray telescope with a large collecting area and an improved resolution of $\sim 0.1''$, a factor of five improvement compared to NASA's Chandra observatory.

There are currently two competing ways of achieving this, the first method is being researched at the Harvard Smithsonian Observatory, USA. Here they aim to create a complete, single layer, coating of $\sim 3\mu m$ thick piezoelectric material on the reverse of a glass, iridium coated, X-ray mirror and print the electrode pattern required onto the material to create $10mm^2$ individual active areas. The advantages of this method include the fact that no print-through is created as the material is deposited directly on to the mirror without the need for bonding. Also, each active area is equally bonded and all of the regions are the same thickness so have the same influence on the mirror. The main disadvantage is that the piezoelectric material requires annealing, which in turn requires the whole composite of piezoelectric material and optic to be baked out at high temperatures. The high temperatures would cause the mirror to lose its form and result in irrevocable damage to the optic and so methods to pre-anneal the piezoelectric material are being investigated.

The second method is to have individual piezoelectric actuators tiled and bonded onto the back of the mirror. These individual actuators can be manufactured to be any shape and size required and are annealed prior to bonding. Used in this way, individual actuators have an advantage over a single device as well as having more actuation and currently larger surface areas can be covered with actuators. Bonding individual piezoelectric devices does cause several problems, including curvature mismatch between the optic and the piezoelectric devices if curved actuators are used, glue thickness and consistency of coverage over the surface, gaps between the individual piezoelectric devices and the tiling pattern chosen. Prior to any testing or metrology, the glue thickness and curvature mismatch were identified to be the factors most likely to cause the largest errors and affect the optic's figure and form the most.

During the proof of concept year for the Smart X-ray Optics consortium (SXO), investigations into the effect of piezoelectric devices on flat glass pieces and sections of a spare XMM-Newton mirror shell were completed at University College London (UCL). In conjunction, some initial Finite Element Analysis (FEA) models were produced to show that the mirror's reaction to the actuation of the piezoelectric devices could be accurately predicted.

The initial prototype optic was designed to be a gold coated nickel, electroformed, ellipsoidal segment to provide single reflection, point-to-point focusing and would fit and operate within the Tunnel Test Facility (TTF) at the University of Leicester (UoL). The design and initial modelling of the prototype was carried out by the author. The optic was produced within the Optical Science Laboratory at UCL and the piezoelectric devices were custom made for the project by the School of Metallurgy and Materials at the University of Birmingham (UoB). Electroforming, bonding techniques and the production of pre-curved piezoelectric devices were investigated using cylindrical pre-prototype mirrors. These pre-prototype optics were also used to look into the thickness of both the mirror and the piezoelectric devices to ensure that the optimum amount of movement could be achieved. The facility used for the X-ray tests was the X-ray TTF at UoL, which is a 28m beam line with an X-ray source and MCP detector. The first adaptive X-ray prototype was created by electroforming nickel onto a mandrel of inverse form which had been coated in a

vacuum deposited gold layer to act as a passivation layer and the reflecting surface. Thirty curved piezoelectric actuators were bonded to the back surface of the mirror after electroforming to complete the prototype.

As the Earth's atmosphere absorbs X-rays, X-ray telescopes must be launched and operated in space. The launch restrictions on the weight of the telescopes, restricts the collecting areas and so thin light mirrors are being developed. The aim of the LAXRO was to create a thin light mirror whose resolution could be adjusted through the use of bonded actuators. The mirror was 0.4mm thick and the piezoelectric devices ranged between $165\mu\text{m}$ and $265\mu\text{m}$ in thickness creating a composite optic of less than 1mm (including the glue layer), comparable to the larger XMM-Newton shells. The total weight has been measured to be less than 100g , thus the prototype optic was a thin light segment, although efforts are ongoing to reduce the thickness further.

The optic's surface was measured using the Long Trace Profiler (LTP) at STFC Daresbury Laboratory and was found to be flatter than the original design had specified. This meant that the optic's focal length would be longer than originally calculated; however, it still allowed the influence functions of the piezoelectric devices to be measured. The optic was measured again with the LTP once the piezoelectric devices had been attached and showed a significant amount of print-through from the actuators. Measurements were also taken whilst the piezoelectric devices were actuated and showed it was possible to achieve a significant amount of movement ($\sim 8\mu\text{m}$ at 50V) but it also showed that the gaps in between the actuators caused a $3\mu\text{m}$ kinking effect along the optic. It was shown that the models produced using both FEA and ray-tracing can effectively predict the response of the mirror and the detected image when the piezoelectric devices have been actuated. Furthermore, by incorporating the data obtained using the LTP, accurate predictions of the optical limits of the mirror were assessed and measured. It was hoped that during the alignment of the optic within the TTF, some of the errors in the optics form could be removed using micrometres on the mirror's mounting. Unfortunately the motors were not calibrated correctly and failed to move the optic. This led to the optic being misaligned for the entire length of the X-ray tests which significantly affected the results.

In order to operate the piezoelectric devices during the X-ray tests, several computer controlled routines were set up and tested. A routine was created by the author to cycle through a series of patterns, calculate the voltages required at each stage, set the piezoelectric devices to that voltage, ray trace the result and find the optimum voltage for each pattern and therefore reduce the Half Energy Width (HEW) of the mirror. This routine was used to predict the results of the X-ray tests using varying initial conditions and piezoelectric configuration patterns. These included a series of patterns created using a Fast Fourier Transform (FFT) method, a series of local group patterns which actuated the piezoelectric devices in rows and columns and finally actuated each individual piezoelectric device in turn. This routine was later altered to be used during the X-ray tests in order to calculate the voltages of the piezoelectric devices and to calculate the optimum voltage for each individual pattern. A separate routine developed at UCL was used to set the voltages and control the actuators, and a piece of in-house software was used to obtain the X-ray images from the MCP detector and to calculate the HEW and Full Width Half Maximum (FWHM) of each image.

During the X-ray tests, the first LAXRO prototype demonstrated that it is possible to change the profile and figure of the mirror and thus change the reflection seen by the detector, by actively manipulating the surface using bonded piezoelectric devices. The alteration of the mirror's figure did not improve the resolution or the HEW in a predictable manor and some form of plastic memory was also seen. However, the reasons for this have been investigated and possible solutions have been found. It has also been shown that there was a large amount of curvature errors which were the main contributing factor to the error in the mirror's figure.

A large amount of print-through was seen by the LTP data caused by stress added to the optical surface due to the attachment of the actuators. This was likely to have been caused by the differences in the radii of curvature between the optic and the actuators. The curvature difference caused large air bubbles between the optic and actuators, which were filled with excess glue. This increased the glue thickness and, although a low shrinkage glue was used, would have caused stress on the prototype. It was also shown that the gaps in between the piezoelectric devices caused kinking features on the mirror's surface when the piezoelectric devices were

actuated. Although this problem was predicted, the amount of kinking seen was greater than that originally expected due to the uneven glue layer. The results obtained during the X-ray tests were also hampered by the calculations of the HEW and FWHM which had to be performed by eye, and were then used to calculate the optimum voltage for each piezoelectric configuration. The combination of the glue thickness, gaps between the piezoelectric devices, curvature errors, the calculation of the optimum voltages and the misalignment of the prototype within the facility due to faulty micrometres, prevented the resolution of the optic being improved in a predictable manner. However, further ray-tracing models have shown that if these factors can be reduced then a reduction in the HEW of a factor of two can be achieved. This result is limited by gross figure errors and high frequency terms which cannot be removed by the piezoelectric devices.

It has been concluded that fewer piezoelectric devices with smaller or no gaps between them would be a possible solution, although the optimum configuration would be to have a single coating of piezoelectric material with the electrode pattern printed on to the material. Due to the reduction of movement of a single coating of piezoelectric material compared to individual devices and the problems with annealing the actuators after bonding, individual piezoelectric devices is still the preferred method for this project. Further FEA modelling performed at both UCL and UoB have shown that if the gaps are reduced and filled with either glue or polyimide and fewer devices are bonded with a more consistent glue layer, then the kinking is drastically reduced. It is therefore essential to try and reduce the stress applied to the optic during the bonding of the actuators and reduce the gaps between the individual piezoelectric devices. In conclusion, the first LAXRO prototype aided the understanding of the processes required to create an adaptive optic and has led to investigations to improve the results for the second prototype.

The most immediate work being completed is the investigation to remove the kinking and stress applied to the optic due to the bonding of the piezoelectric devices. This is involving the creation of longer actuators which have the electrode patterns imprinted on to them, to create more active areas whilst reducing the number of joined regions. It is hoped that the joins can be reduced to $\sim 100\mu m$ and then filled with a form of epoxy to reduce the variance in the reaction of the surface in

these areas. The bonding techniques will also be improved to decrease the amount of glue required which in turn will reduce the amount of stress on the optic and should reduce the print-through. This will involve a vacuum chuck to hold the actuators in the correct figure and tessellation required whilst an even glue layer is applied to the optic. Metrology is also ongoing to examine all effects seen with the first prototype including improvements of the production techniques, glue thickness, curvature errors and power stability.

Two new prototype optics with the new piezoelectric design are going to be tested; a new nickel prototype and a glass prototype kindly provided by NASA's Goddard Space Flight Center, USA. Although nickel and glass have very similar Young's moduli, glass has a lower density and is therefore lighter. Both of these optics will be tested in the same way as the previous prototype, however, the in-house software is being improved to perform the analysis automatically on each image. Models of the routines have shown that it is possible to improve the resolution of both a glass and a nickel optic using the piezoelectric devices. Therefore improving all the production techniques should mean that an adaptive optic, whose resolution can be improved via active manipulation of the reflective surface by the actuation of bonded piezoelectric devices, can be created.

4.2 Micro Optical Arrays

In order to be able to irradiate single biological cells with higher energy than is currently possible, and thus study radiation induced cancers by looking at the effect on surrounding material, a grazing incidence device to focus X-rays over a distance of $\sim 50mm$ with a variable focal length needs to be created. Micro Optical Arrays (MOAs) are similar to polycapillary devices or Micro Channel Plate (MCP) optics and are created by etching vertical channels within silicon wafers.

By bending an optic with etched channels, the channels are forced into a curved or fanned out configuration which can then focus the X-rays to a precise spot or line. A micro-focusing source is also being developed in order to decrease the size of the focused spot further. By combining the MOAs with the micro-focus source it is hoped that a focused spot of a few microns can be achieved. The current

technology, zone plates, used for this research can only be used at energies $\leq 1keV$ without significantly increasing the focal length and decreasing the aperture. At this energy, only cell death can be studied as the radiation is completely absorbed. By moving to a grazing incidence optic, higher energies can be used which allows for radiation induced mutations to be studied and a known dose can be applied to each individual cell as opposed to an average dose to a group of cells. In addition, by creating a device with two reflections, both on and off axis rays are focused increasing the power of the focused spot. In order to achieve source demagnification of $\frac{1}{3}$, the MOA would need to be bent to a radius of curvature of $50mm$. The original design was to have concentric rings of channels with spindles to hold them together. This would be similar to a Fresnel Zone plate in design but still focus the X-rays by reflection not diffraction. The radius of curvature of the optic would be controlled by attaching small amounts of piezoelectric material which would allow a variable focal length. Two MOAs would be placed in series to provide two surfaces of reflection and both would have variable focal lengths. Several areas were identified to cause problems prior to any testing. The first was the surface roughness of the channels, as this would determine how much radiation could be focused and would limit the amount of scattering. The second problem would be the amount of bending, although this was seen to be less of a problem than the surface roughness.

The MOAs are created by etching silicon wafers at the Scottish Microelectronics Centre (SMC) at the University of Edinburgh. A series of etching techniques have been investigated, both wet and dry, to try and create a series of channels in the thin silicon wafer with low surface roughness. The first prototype Micro Optical Arrays (MOAs) were $20mm \times 10mm$ silicon wafers, $0.2mm$ thick, with a $4mm^2$ active area comprising of the etched channels. A small strip of piezoelectric was placed either side of the active area in order to bend the MOA and to control the focal length of the optic.

The first reflectivity tests performed at both STFC Daresbury Laboratory and at UoL showed that very little flux would be reflected with the dry etched MOA, due to the high surface roughness. Although the dry etching technique would allow a circular arrangement of channels to be created into the silicon and form a focused spot, the quality of the surface roughness would prevent enough X-rays being focused

to irradiate the biological material. Reflection was seen up to 4° at a large range of energies during the dry etched MOA reflection tests, performed at STFC Daresbury Laboratory and 3.33% reflection was seen during the tests completed at UoL. This was much less than the 40% predicted with the models, however the condition of the surfaces of the walls was much worse than had been predicted, as shown in the images taken with the FEQSEM. Wet etched MOAs were produced with a higher quality of surface wall roughness which was confirmed by reflectivity tests performed at UoL. With the wet etched MOA, $\sim 6\%$ reflection was seen, which again was lower than the amount predicted with the models, but the maximum amount of reflection possible by silicon at the working energy is only 18%. Single reflection, shown as a peak in the reflection, was seen at the correct angles for both wet and dry MOAs.

Due to the nature of the wet etching process, only patterns which follow the $\langle 110 \rangle$ or $\langle 111 \rangle$ silicon crystal planes can be created which would prevent a circular arrangement of channels. Several theoretical arrangements of single and tandem, dry and wet etched MOAs were modelled at UoL and showed that a series of MOAs could be used to focus the X-rays effectively. It was found that a crossed pair of MOAs could produce a focused spot, of $\leq 15\mu m$, with enough flux to be able to irradiate cells. Although crossed arms are created with this method, the amount of flux in the arms is so low that this should not affect the radiation studies. This would prevent the need for a circular arrangement of channels, therefore allowing wet etched channels to be used and thus increase the amount of flux focused.

Investigations at Kings College London (KCL) and at UoB, have shown that it will not be possible to bend the MOAs enough to focus the X-rays at the correct distance of $\sim 50mm$. Models at the School of Metallurgy and Materials at UoB have optimised the thickness, size and type of piezoelectric to provide the maximum amount of bending possible but it is still not as much as required. The required bending is to displace the central region by $\sim 10\mu m$ but currently only $5\mu m$ is achievable. For this reason many new prototypes have been modelled and are being considered including combs and spiders, where material is removed from the chip to make it easier to bend without applying further stress to the MOA or active area. Another possibility is to have one of the MOAs pre-curved and the secondary MOA is then bent by the piezoelectric devices to create the correct focal length. All

these possibilities are being investigated via FEA models and bending tests using the piezoelectric actuators.

In conclusion, the first prototype MOAs have shown reflection at the predicted angles is possible but with less flux than expected and the amount of bending required is still not achievable. New MOA arrangements are being investigated and new designs are being considered to try and achieve the correct focal length and the correct amount of reflection.

Currently, alternative bending techniques are the most significant piece of work being undertaken. At present, the MOAs will not be suitable for the type of radiation studies being proposed if the scale of bending cannot be improved. In order to aid the bending of the MOA structure, new designs of prototypes with removed sections of silicon are being investigated and new designs of piezoelectric devices are also being considered. The pre-curving of MOAs is also being tested to see if this can increase the bending movement in addition to the piezoelectric devices. A new micro-focus source is also being designed and built to try and create a smaller spot size to reduce the focal length of the device. The etching processes are also being improved to try and decrease the RMS surface roughness and therefore increase the flux being reflected.

The new designs, which are being studied and modelled at both UoB and KCL, would significantly complicate the manufacture processes of the MOAs and so the current design is preferred. If the surfaces of the MOA channel walls can be made sufficiently smooth, and a pre-curved adjustable MOA tandem pair with a $50mm$ focal length are produced, then these devices can be used for studies into radiation induced cancers.

BIBLIOGRAPHY

- [1] IMTEK: Institut für Mikrosystemtechnik. http://www.imtek.de/micro-optics/content/upload/projekt/2005/mirror_photo.jpg, May 2004.
- [2] The Centre for X-ray Optics. <http://www-cxro.lbl.gov/>, November 2009.
- [3] P. Kirkpatrick and A. Baez. Formation of optical images by x-rays. *Journal of the Optical Society of America*, 38:776, 1948.
- [4] B. Aschenbach. X-ray telescopes. *Rep. Prog. Phys.*, 48:579, 1985.
- [5] Flickr. http://farm4.static.flickr.com/3161/3004411379_54b965b76e.jpg?v=0, November 2008.
- [6] NASA Chandra information. http://www.nasa.gov/images/content/155429main_chandra_330x255.jpg.
- [7] HEA Group Harvard University The Chandra observatory image gallery. http://chandra.harvard.edu/photo/2007/ngc4258/ngc4258_comp.jpg.
- [8] ESA XMM-Newton image gallery. http://xmm.esac.esa.int/external/xmm_science/gallery/images/ngc4258_lrg.jpg.
- [9] The XMM satellite schoolpage. <http://www.sr.bham.ac.uk/xmm/images/telescopes/mirrors.jpg>.
- [10] ESA XMM-Newton image gallery. http://xmm.esac.esa.int/external/xmm_science/gallery/images/xmm_mirror.gif.

- [11] UK Space Research Centre, University of Leicester.
<http://www2.le.ac.uk/departments/physics-and-astronomy/research/src/missions/xmm-newton/instrument/chandramirrors2.jpg>.
- [12] Caltech: NuSTAR Nuclear Spectroscopic Telescope Array.
<http://www.nustar.caltech.edu>.
- [13] UBE America Inc. Aerospace Materials: Upilex Foam.
<http://northamerica.ube.com/content.php?pageid=137>.
- [14] P. Takacs, E. Church, C. Bresloff, and L. Assoufid. Improvements in the accuracy and the repeatability of long trace profiler measurements. *Applied Optics*, 38:5468, 1999.
- [15] C. Patton. <http://glsmyth.com/pinhole/aticles/zoneplate/image43.gif>.
- [16] A. Michette and C. Buckley. *X-ray science and technology*. Institute Of Physics Publishing, 1993.
- [17] M. Al Aioubi, P. Prewett, S. Huq, V. Djakov, and A. Michette. A novel moems based adaptive optics for x-ray focusing. *Microelectronic Engineering*, 83:1321, 2006.
- [18] R. Willingale, C. Feldman, A. Michette, T. Button, C. Dunare, M. Folkard, D. Hart, C. McFaul, G. Morrison, W. Parkes, S. Pfauntsch, A. Powell, D. Rodriguez Sanmartin, S. Sahraei, T. Stevenson, B. Vojnovic, and D.Zhang. Active micro-structured optical arrays of grazing incidence reflectors. *JXOI*, 2009.
- [19] R. Klos. *Scattering from X-ray mirrors*. PhD thesis, University of Leicester, 1987.
- [20] Proof of concept, research on smart x-ray optics. *submitted to EPSRC*, EP/D04880X/1, 2005.
- [21] *The penguin dictionary of Physics*. Penguin, third edition, 2000.
- [22] NASA Student site and The electromagnetic spectrum.
<http://science.hq.nasa.gov/kids/imagers/ems/xrays.html>, March 2007.

- [23] H. Young and R. Freedman. *University Physics*. Addison-Wesley, tenth edition, 2000.
- [24] P. Lena. Adaptive optics: a breakthrough in astronomy. *Experimental astronomy astrophysical instrumentation and methods*, 26:35, 2009.
- [25] R. Signorato, D. Hausermann, M. Somayazulu, and J. Carre. Performance of an adaptive u-focusing kirkpatrick-baez system for high-pressure studies at the advanced photon source. *Proc. of SPIE*, 5193:112, 2004.
- [26] A. Habenschuss, G. Ice, C. Sparks, and R. Neiser. The ornl beamline at the national synchrotron light source. *National synchrotron radiation instrumentation conference*, 1987.
- [27] B. Jaffe, W. Cook, and H. Jaffe. Piezoelectric ceramics. *Journal of sound and vibration*, 20:562, 1971.
- [28] J. Sirohi and I. Chopra. Fundamental understanding of piezoelectric strain sensors. *Journal of Intelligent Material Systems and Structures*, 11:246, 2000.
- [29] Smart Material Corp. Actuator development. <http://www.smart-material.com/smart-choice.php?from=mfc>.
- [30] B. Su, D. Pearce, and T. Button. Routes to net shape electroceramic devices and thick films. *Journal of the European Ceramic Society*, 21:2005, 2001.
- [31] C. Bowen, R. Stevens, L. Nelson, A. Dent, G. Dolman, B. Su, T. Button, M. Cain, and M. Stewart. Manufacture and characterization of high activity piezoelectric fibres. *Smart Mater. Struct.*, 15:295, 2006.
- [32] R. James. *The optical principles of the diffraction of X-rays*, volume Second. G. Bell and Sons LTD., 1962.
- [33] A. Compton and S. Allison. *X-rays in theory and experiment*. Van Nostrand Company Inc., 1935.
- [34] B. Henke, E. Gullikson, and J. Davis. X-ray interactions: Photoabsorption, scattering, transmission and reflection at e=50-30,000ev, z=1-92. *Atomic data and nuclear data tables*, 54:181, 1993.

- [35] P. Beckmann and A. Spizzichino. *The scattering of EM waves from rough surfaces*. Pergamon press, 1963.
- [36] S. Rice. Reflection of electromagnetic waves from slightly rough surfaces. *Communication in Pure and Applied Mathematics*, 4:351, 1951.
- [37] B. Lai and F. Cerrina. Shadow: A synchrotron radiation ray tracing program. *Nuclear instruments and methods in physics research*, 246:337, 1986.
- [38] X ray Oriented Programs. <http://www.esrf.eu/computing/scientific/xop2.1/>, November 2009.
- [39] J. Bahrtdt. Wave-front propagation: design code for synchrotron radiation beam lines. *Applied Optics*, 36:4367, 1997.
- [40] G. Geloni, E. Saldin, E. Schneidmiller, and M. Yurkov. Transverse coherence properties of x-ray beams in third-generation synchrotron radiation sources. *Opt. Comm.*, 276:167, 2007.
- [41] Modelling software ZEMAX: Software For Optical System Design. <http://www.zemax.com/>.
- [42] Lambda Research: Oslo Optical Design Software. http://www.lambdare.com/software_products/oslo/oslo/.
- [43] COMSOL: COMSOL Multiphysics Modeling and Simulation. <http://www.comsol.com/>.
- [44] D. Schwartz, R. Brissenden, M. Elvis, G. Fabbiano, T. Gaetz, D. Jerius, M. Juda, P. Reid, S. Wolk, S. O'Dell, J. Kolodziejczak, and W. Zhang. On-orbit adjustment calculation for the generation-x x-ray mirror figure. *Proc. of SPIE*, 7011:70110W, 2008.
- [45] J. Gribbin. *Companion to the cosmos*. Pheonix Giant, second edition, 1997.
- [46] R. Giacconi and B. Rossi. A 'telescope' for soft x-ray astronomy. *Journal of Geophysical Research*, 65:773, 1960.

- [47] M. Weisskopf. The chandra x-ray observatory: an overview. *Adv. Space Res.*, 32(10):2005, 2003.
- [48] F. Jansen, D. Lumb, B. Altieri, J. Clavel, M. Ehle, C. Erd, C. Gabriel, M. Guainazzi, P. Gondoin, R. Much, R. Munoz, M. Santos, N. Schartel, D. Texier, and G. Vacanti. Xmm-newton observatory. *Astronomy and Astrophysics*, 365:L1, 2001.
- [49] E. White and A. Hornschemeier. International x-ray observatory (ixo). *American Astronomical Society*, 41:388, 2008.
- [50] P. Reid, R. Cameron, L. Cohen, M. Elvis, P. Gorenstein, D. Jerius, R. Petre, W. Podgorski, D. Schwartz, and W. Zhang. Constellation-x to generation-x: Evolution of large collecting area, moderate resolution grazing incidence x-ray telescopes to larger area, high resolution, adjustable optics. *Proc. SPIE*, page 325, 2004.
- [51] H. Wolter. Generalized schwarzschild mirror systems with glancing incidence as optics for x-rays. *Annalen de Physik*, 445:286, 1952.
- [52] W. Reidy, G. Vaiana, T. Zehnpfennig, and R. Giacconi. Study of x-ray images of the sun at solar minimum. *The Astrophysical Journal*, 151:333, 1968.
- [53] R. Giacconi, G. Branduardi, U. Briel, A. Epstein, D. Fabricant, and E. Feigelson. The einstein (heao2) x-ray observatory. *The Astrophysical Journal*, 230:540, 1979.
- [54] R. Giacconi, G. Branduardi, U. Briel, A. Epstein, D. Fabricant, E. Feigelson, S. Holt, R. Becker, E. Boldt, and P Serlemitsos. The einstein /heao 2/ x-ray observatory. *Astrophysical Journal*, 230:540, 1971.
- [55] M. Weisskopf, B. Brinkman, C. Camizares, G. Garmire, S. Murray, and L. Van Speybroeck. An overview of the performance and scientific results from the chandra x-ray observatory. *Publications of the astronomical society of the pacific*, 114:1, 2002.
- [56] IXO NASA, Goddard Space Flight Center. <http://ixo.gsfc.nasa.gov/>.

- [57] P. Reid, W. Davis, S. O'Dell, D. Schwartz, S. Tolier-McKinstry, R. Wilke, and W. Zhang. Generation-x mirror technology development plan and the development of adjustable x-ray optics. *Proc. of SPIE*, 7437:74371F, 2009.
- [58] Gen-X science Harvard Center for Astrophysics, High Energy Astrophysics group. <http://www.cfa.harvard.edu/hea/genx/science/>.
- [59] F. Jansen, D. Lumb, B. Altieri, J. Clavel, M. Ehle, C. Erd, C. Gabriel, M. Guainazzi, P. Gondoin, R. Much, R. Munoz, M. Santos, N. Schartel, D. Textier, and G. Vacanti. Xmm-newton observatory, 1. the spacecraft and operations. *Astronomy & Astrophysics*, 365:L1, 2001.
- [60] D. Burrows, J. Hill, J. Nousek, J. Kennea, A. Wells, J. Osborne, A. Abbey, A. Beardmore, K. Mukerjee, A. Short, G. Chincarini, S. Campana, O. Citterio, A. Moretti, C. Pagani, G. Tagliaferri, P. Giommi, M. Capalbi, F. Tamburelli, L. Aangelini, G. Cusumano, H. Braauninger, W. Burkert, and G. Hartner. The swift x-ray telescope. *Space science reviews*, 120:165, 2005.
- [61] NASA Chandra X ray Observatory. http://chandra.harvard.edu/about/telescope_system.html.
- [62] W. Zhang. Manufacture of mirror glass substrates for the nustar mission. *Proc. of SPIE*, 7437:74370N, 2009.
- [63] R. Canestrari, M. Ghigo, G. Pareschi, S. Basso, G. Motta, M. Doro, E. Giro, and L. Lessio. Techniques for the manufacturing of stiff and lightweight optical mirror panels based on slumping of glass sheets: concepts and results. *Proc. of SPIE*, 7437:74371, 2009.
- [64] M. Collon, R. Guenther, M. Ackermann, R. Partapsing, C. Kelly, M. Beijersbergen, M. Bavdaz, K. Wallace, M. Olde Riekerink, P. Mueller, and M. Krumrey. Stacking of silicon pore optics for ixo. *Proc. of SPIE*, 7437:74371A, 2009.
- [65] A. Martindale, J. Pearson, C. Whitford, G. Fraser, D. Rothery, D. Talboys, J. Carpenter, T. Stevenson, E. Bunce, R. Fairbend, J. Seguy, E. Sclater, I. Delgado, A. Dixon, J. Treis, J. Mas-Hesse, J. San Juan, K. Muinonen, C. Sawyers,

- C. Bulloch, and E. Schyns. The mercury imaging x-ray spectrometer: instrument overview. *Proc. of SPIE*, 7441:744115, 2009.
- [66] G. Fraser. *X-ray detectors in astronomy*. Cambridge, 1989.
- [67] C. Atkins, H. Wang, P. Doel, D. Brooks, S. Thompson, C. Feldman, R. Willingale, T. Button, D. Rodriguez Sanmartin, D. Zhang, A. James, and C. Theobald. Future high-resolution x-ray telescope technologies: prototype fabrication methods and finite element analysis. *Proc. of SPIE*, 7011:70110X, 2008.
- [68] J. Wyant. White light interferometry. *Proc. of SPIE*, 4737:473712, 2002.
- [69] K. Von Bieren. Interferometry of wave fronts reflected off conical surfaces. *Applied Optics*, 22:2109, 1983.
- [70] J. Schwiegerling and D. Neal. <http://www.wavefrontsciences.com/historical%20development.pdf>.
- [71] P. Prewett and A. Michette. Moxi: a novel microfabricated zoom lens for x-ray imaging. *Proc. of SPIE*, 4145:180, 2001.
- [72] A. Michette, P. Prewett, A. Powell, S. Pfauntsch, K. Atkinson, and B. Boonliang. Novel micro-structured adaptive x-ray optics. *J. Phys. IV France*, 104:277, 2003.
- [73] M. Al Aioubi, P. Prewett, S. Huq, V. Djakov, and A. Michette. Design and fabrication of micro optical system for x-ray analysis of biological cells. *Proc. of SPIE*, 5825:640, 2005.
- [74] R. Longhurst. *Geometrical and Physical Optics*. Longman, third edition, 1973.
- [75] M. Folkard, K. Prise, C. Shao, S. Gilchrist, G. Schettino, A. Michette, and B. Vojnovic. Understanding radiation damage to cells using microbeams. *Acta Physica Polonica A*, 109:257, 2006.
- [76] MEMS and Nanotechnology Clearinghouse. <http://www.memsnet.org/mems/processes/etch.html>, July 2007.

- [77] R. Heilmann, M. Ahn, E. Gullikson, and M. Schattenburg. Blazed high-efficiency x-ray diffraction via transmission through arrays of nanometer-scale mirrors. *Optics Express*, 16:8658, 2008.
- [78] J. Bhardwaj and H. Ashraf. Advanced silicon etching using high-density plasmas. *Proc. of SPIE*, 2639:224, 1995.
- [79] A. Hynes, H. Ashraf, J. Bhardwaj, J. Hopkins, I. Johnston, and J. Shepherd. Recent advances in silicon etching for mems using the ase process. *Sensors and Actuators A: Physical*, 74:13, 1999.
- [80] C. MacDonald and W. Gibson. Applications and advances in polycapillary optics. *X-ray spectrometry*, 32:258, 2003.
- [81] G. Price, A. Brunton, G. Fraser, M. Bavdaz, M. Beijersbergen, J. Boutot, R. Fairbend, S. Flyckt, A. Peacock, and E. Tomaselli. Hard x-ray imaging with microchannel plate optics. *Nucl. Instrum. and Methods Phys. Res A*, 490:290, 2002.
- [82] H. Chapman, K. Nugent, and S. Wilkins. X-ray focusing using cylindrical-channel capillary arrays, i. theory. *Applied Optics*, 32:6316, 1993.
- [83] H. Chapman and A. Rode. Geometric optics of arrays of reflective surfaces. *Applied Optics*, 33:2419, 1994.
- [84] D. Rodriguez-Sanmartin, D. Zhang, T. Button, C. Meggs, C. Atkins, H. Wang, P. Doel, D. Brooks, C. Feldman, R. Willingale, A. Michette, S. Pfauntsch, S. Sahraei, A. James, C. Dunare, T. Stevenson, W. Parkes, and A. Smith. Progress on the development of active micro-structured optical arrays for x-ray optics. *Proc. of SPIE*, 7448:744807, 2009.